Modelling Electron Tunnelling in the Presence of Adsorbed Materials

A Thesis presented for the degree of
Doctor of Philosophy
by

Rainer Christian Hoft
B. Sc. : University of Cape Town
B. Sc. Hons. (Theoretical Physics): University of Cape Town

Institute for Nanoscale Technology
Faculty of Science
University of Technology, Sydney

November 2007

Certificate of Originality

I certify that the work in this thesis has not previously been submitted for a degree nor has it been submitted as part of the requirements for a degree except as fully acknowledged within the text.

I also certify that the thesis has been written by me. Any help that I received in my research work and the preparation of the thesis itself has been acknowledged. In addition, I certify that all information sources and literature used are indicated in this thesis.

Chapter 1 contains a literature review prepared by me. Chapter 2 describes the theoretical foundations needed for the work presented in this thesis. This theory can be found in many text books and other publications. It has been presented here in my own treatment in a way that best conveys my understanding of the material. Where the treatment of another author has been followed closely, this is acknowledged. Chapters 3 to 6 describe work done by me under the guidance of my supervisor and co-supervisor and advice from other colleagues. Two exceptions should be noted. The work under the heading *Surface adsorption* in section 4.2.2 and the work in section 4.5 was contributed mainly by my supervisor and is detailed in publications of which I am co-author, as cited in the text. Chapter 7 contains my concluding remarks and suggestions for future work.

Rainer C. Hoft

Acknowledgements

Firstly, a sincere thanks to my supervisor, Prof. Michael Ford, whose guidance, enthusiasm and unparallelled availability was paramount to this work and my development as a researcher. Many thanks also to my co-supervisor, Prof. Michael Cortie for countless discussions and support. The Institute for Nanoscale Technology under leadership of Mikes Cortie and Ford, has provided a stimulating and vibrant environment in which to do research. I am priviledged to have been a part of the relaxed and intellectually challenging atmosphere at INT, and to have been supported to attend many conferences. I am indebted to all its members, past and present, especially those who have been directly involved in my research. Benjamin Soulé de Bas and Carl Masens were instrumental in getting me started on the SIESTA software package. Benjamin was also a great help in my acquaintance with density functional theory. Andrew McDonagh's patience in supplementing my knowledge of chemistry is commendable. I had many fruitful discussions with Nicholas Armstrong. Special thanks also to my fellow PhD students, Xiaoda (David) Xu, Don Maclurcan, Dakrong Pissuwan, Nadine Harris, Burak Cankurtaran, Nicholas Stokes, Martin Blaber, Jonathan Edgar and of course Benjamin. The Z-matrix work was carried out in close collaboration with Julian Gale at Curtin, who co-authored the SIESTA package and whose knowledge of the software and DFT in general is inspiring. My PhD was made possible by funding and facilities provided by the University of Technology Sydney, the Faculty of Science and INT at UTS. Very generous computational resources were made available by the Australian Centre for Advanced Computing and Communications (AC^3) and the Australian Partnership for Advanced Computing (APAC). All those mentioned above, I consider friends as well as colleagues, and have contributed greatly to my first three very enjoyable years in Australia. Finally, and wholeheartedly, I thank Senena, whose love and support during the second half of my PhD has made this a truly exceptional experience.

Contents

List of Figures

List of Tables

Glossary of Acronyms

AE	All-Electron
BDT	benzenedithiol
BFGS	Broyden-Fletcher-Goldfarb-Shanno
BSSE	Basis Set Superposition Error
C-AFM	Conducting Atomic Force Microscope/y
CC	Coupled Cluster
CG	Conjugate Gradients
DEB	diethynylbenzene
DFT	Density Functional Theory
DOS	Density Of States
DZP	Double-ζ plus Polarisation
EB	ethynylbenzene
EPM	1,4-ethynylphenylenemethanethiol
GGA	Generalised Gradient Approximation
HOMO	Highest Occupied Molecular Orbital
LB	Langmuir-Blodgett
LCAO	Linear Combination of Atomic Orbitals
LDA	Local Density Approximation
LDOS	Local Density Of States
LEED	Low Energy Electron Diffraction
LUMO	Lowest Unoccupied Molecular Orbital

MCB	Mechanically Controllable Break junction
NDR	Negative Differential Resistance
NEGF	Non-Equilibrium Green's Functions
PBE	Perdew-Burke-Ernzerhof (GGA parametrisation)
PDOS	Projected Density Of States
PES	Potential Energy Surface
PS	Pseudopotential
PW	Plane Wave
PZ	Perdew-Zunger (LDA parametrisation)
SAM	Self-Assembled Monolayer
SCF	Self-Consistent Field
STM	Scanning Tunnelling Microscope/y
STS	Scanning Tunnelling Spectroscopy
SZP	Single-ζ plus Polarisation
TDDFT	Time-Dependent Density Functional Theory
WKB	Wenzel-Kramers-Brillouin
XYL	phenylenedimethanethiol

Abstract

The transport characteristics of single-molecule Au(111) junctions are investigated using density functional theory (DFT) together with the non-equilibrium Green's functions formalism (NEGF). DFT optimisations of the adsorption of various molecules on a Au(111) surface are used as starting points for the equilibrium junction geometries. Test calculations are performed to find a recommended set of parameters for the final DFT results. The interaction energies of several molecules with the Au(111) surface obtained within the same level of theory are compared. Amine compounds bind preferentially in an adatom geometry and weakly in the ontop site. A Z-matrix optimiser is implemented in the SIESTA code as a useful tool for future surface and molecular junction optimisations.

Transport properties are calculated for molecular junctions in their equilibrium geometry. While the conductances are orders of magnitude larger than experimental data, the sizes are in line with expectation. The junction geometries are altered in various ways. Changing the binding site or altering the nature of the sulphur-gold interaction in a phenylenedimethanethiol junction, reduces the conductance by a factor of two. Orders of magnitude reduction of conductance is only observed when increasing the distance between a physisorbed molecule and the surface. Increasing this distance for a chemisorbed molecule, results in a surprising increase in conductance. This is attributed to an interplay between the coupling strength of the molecule with the surface and the location of the molecular energy levels relative to the Fermi level. When the chemical bond is broken, the system is spin-polarised and the conductances for electrons of opposite spin types are different by a factor of 250 – the junction acts as a spin-filter. When stretching a diethynylbenzene junction, the strong gold-carbon bond does not break, but rather extracts a gold atom from the surface. In this case the

conductance decreases rapidly with stretching.

A WKB tunnel barrier model is used as an alternate much faster method for calculating $I(V)$ characteristics. With the surface work functions acting as barrier heights, the relative junction conductances are in good agreement with the DFT results. However, the direction of asymmetry in the $I(V)$ characteristics predicted by the two levels of theory are opposite. More sophisticated barrier shapes may be needed to correctly predict the asymmetries. The tunnelling model is used in conjunction with the DFT results to quantify the effect a gap between an STM tip and monolayer may have on STS measurements.

Chapter 1

Introduction

1.1 Overview and motivation

Molecular electronics is one of the major modern research endeavours falling under the general banner of nanotechnology. The ultimate goal in this field is the development of a new-generation technology to follow on from the current semiconductor based architectures used in microchips. The vision is to build an integrated circuit of which the components, e.g. wires and transistors, consist of small molecules, or arrays of such molecules [6]. To date only modest advances have been made on the manufacturing side. Perhaps the largest hurdle is the problem of tremendous heat dissipation when current is driven through such small devices [7].

However, rapid progress has been made in the last three decades on the theoretical understanding and experimental characterisation of the basic architecture required for such a technology. This involves understanding the charge transport properties of a single molecule attached to macroscopic components. The experimental drive was boosted by the invention of the scanning tunnelling microscope (STM) in the early 1980's by Binnig and Rohrer [8]. The STM allows imaging of surfaces with atomic resolution. It operates by measuring the tunnelling current between the STM tip, ideally with a single atom at its apex, and the substrate under study. It is therefore intuitively an appropriate tool for measuring the current passing through a molecule connected between the tip and substrate

under an applied bias. In addition, the current between the STM tip and substrate can be measured at given bias voltages. Such scanning tunnelling spectroscopy (STS) measurements have been reported by various authors [2,3,9–19]. Other techniques used to achieve such electrode-molecule-electrode junctions are conducting atomic force microscopy (C-AFM) [20–22], mechanically controllable break junctions (MCBs) [23–25], nanopores [26–29], metallic crossbars [30] and large-area molecular junctions using a lithographically patterned photoresist [31].

It is now well established that the corresponding $I(V)$ characteristics in such experiments cannot be ascribed to the molecule alone, but is a function of the entire junction, i.e. the electrode material, the nature of the molecule-electrode contact and the details of the molecule itself [32,33]. This makes the interpretation of experimental results problematic, as it is very difficult to characterise the nature of the coupling or the electrode-molecule binding geometry.

A physical understanding of the mechanism of charge transport across nanoscale molecular junctions has been advanced through sophisticated computational modelling. The difficulties associated with experimental work in the field described above, makes modelling particularly important. Density functional theory (DFT) [34,35] provides a relatively inexpensive, yet fairly accurate *ab-initio* discription of the electronic structure of a system consisting of ~ 100 atoms. The non-equilibrium Green's function (NEGF) formalism allows this description to be extended to the case of an open (aperiodic) system driven out of equilibrium by an applied bias. These formalisms in combination therefore provide an efficient method for computing the transmission properties of small molecular junctions to a reasonable accuracy [36–38].

More realistic descriptions can be obtained by using higher levels of theory. Dynamical effects have been included through time-dependent DFT (TDDFT) [39–41] and electron correlation effects through coupled cluster (CC) or configuration interaction (CI) [42] theories. However, these calculations demand extremely high computational resources and their application to systems with ~ 100 atoms is limited.

Empirical approaches such as tunnel barrier models [10, 43–47] can provide a qualitative picture. The advantage is that a systematic understanding of the

effect of varying the fundamental junction parameters can be obtained, which is not feasible in *ab-initio* appoaches.

Using the tools introduced above, many experimental measurements of the current through single molecule junctions are now available. Using largely the DFT-NEGF formalism, many computational calculations of $I(V)$ characteristics have been reported. Calculations based on the DFT-NEGF theory generally overestimate experimentally measured currents by one or two orders of magnitude. Some authors have attributed this discrepancy to certain shortcomings of DFT for the purpose of transport calculations [48–52]. While there is concern as to the appropriateness of the level of theory, another contributing factor is almost certainly differences in geometry between computational idealisations and actual experimental setups. This issue has been addressed in several computational studies [49,53–60] by calculating the $I(V)$ characteristics of junctions with geometries different from the idealised binding geometries previously assumed. Much better agreement between experiment and computation was demonstrated.

In the present study we add to the literature on computational analysis of charge transport through molecular junctions in three related topics:

- Adsorption of molecules on Au(111) surfaces, specifically comparing the adsorption of thiol and non-thiol terminated molecules [61–66].

- $I(V)$ characteristics of molecular junctions of the form Au(111)-X-Au(111), where X is one of several selected molecules. We focus on the effect of changing the adsorption geometry [67]. Specifically we perform a detailed investigation of the process of stretching the junction [68,69].

- Describing the system with a tunnel barrier model. We compare results obtained using the DFT-NEGF approach and the tunnel barrier approach [70–73].

A detailed analysis is performed of the computational parameters required for accurate DFT adsorption studies and DFT-NEGF transport calculations [74].

1.2 Background

1.2.1 The origin of molecular electronics

The semiconductor industry has undergone a process of constant miniaturisation over the last few decades driven by Moore's law, with device characteristics currently in the tens of nanometer scale. However, for this trend to continue the industry will need to manufacture devices where new quantum phenomena enter into the picture. To this end, the conduction of electric current through single molecules is the subject of considerable interest.

This relatively new field, "molecular electronics", was inspired by the 1974 paper by Aviram and Ratner [75] in which they proposed that a molecule consisting of a donor-spacer-acceptor (D-s-A) structure can behave as a molecular rectifier when connected to two electrodes. Under bias, electrons will flow easily in the direction cathode-A-s-D-anode, but will require a higher threshold voltage to flow in the opposite direction, hence giving the molecule its rectifying behaviour.

Experimental investigation of this possibility was slow to follow due to a lack of tools to perform electrical measurements at such a small scale. The invention [8] of the STM in 1982 by Binnig and Rohrer, was therefore crucial to the development of the field. STS measurements of the $I(V)$ characteristic of the electrode-molecule-electrode system is the fundamental quantity needed for analysis of possible rectification or other interesting behaviour.

1.2.2 Self-assembled monolayers

The experimental breakthrough enabling electrical measurements on single molecules between an STM tip and substrate, was the discovery of techniques for forming self-assembled monolayers (SAMs) on surfaces. In 1983 Nuzzo and Allara first adsorbed alkanethiols onto gold sufaces from solution [76]. The field has grown substantially and the most widely studied system remains alkane thiols on gold [77]. More recently, conjugated aryl thiol and dithiol SAMs have been reported [78]. Ref. [79] contains a thorough review of the application of such systems in the context of nanotechnology. The chemical stability of gold and its strong interaction with thiols makes it an ideal surface for the study of SAMs. In

addition, it is the most widely studied metal in nanotechnology due to catalytic properties that emerge at the nanoscale, unique optical properties and a range of processing technologies [79, 80].

Studies of SAMs anchored to gold surfaces by groups other than thiols are sparse. Examples of such work are diisocyanide [81] and ethynylbenzene monolayers [82]. Acetylenes have also been shown to bond to gold surfaces [83]. The energetics and candidate geometries for adsorption of ethynylbenzene on gold was studied at the DFT level [64]. Other computational studies include the adsorption of ammonia [84] and phosphines [80] on gold (111).

1.2.3 Experimental progress

Early attempts at experimental verification of the Aviram-Ratner proposal were unable to distinguish between rectifying properties intrinsic to the molecule and Schottky barrier effects at the molecule-metal interface. In 1993 Martin, Sambles and Ashwell were able to attribute rectification to the donor-spacer-acceptor structure of the molecule forming a Langmuir-Blodgett (LB) film sandwiched between metal electrodes [85]. This was confirmed in 1997 by Metzger *et al.* [86]. Asymmetric $I(V)$ characteristics of asymmetric molecules with non-DsA structure have also been observed [24, 87]. Of critical importance here is not only the inherent asymmetry of the molecule, but also the nature of the coupling to the two electrodes.

An important consideration is the mechanism by which "through"-molecule current flow occurs. A related question is the meaning of the conductance of a molecule and whether it can be measured. If the Aviram-Ratner through-bond tunnelling picture is correct, one would expect the conductivity of molecules to be strongly correlated with the degree of conjugation of the molecular orbitals. In 1996 Bumm *et al.* performed STS measurements on a SAM of dodecanethiol molecules with embedded conjugated, 4,4′-di(phenylene-ethynylene) benzenethiolate derivatives on a Au(111) surface [9]. The alkane chains forming the SAM have a low level of conjugation due to the localised nature of the σ-orbitals on the backbone. They found that the conjugated molecules were indeed far more conductive than the alkanethiols.

An inherent difficulty with interpreting STS measurements is the gap that is present between the top of the SAM and the STM tip. A group at Purdue University devised a method for assembling a monolayer of gold nanoparticles onto a substrate through aryl-dithiol linkages [11]. STS $I(V)$ curves were obtained while systematically varying the gap distance between the STM tip and a gold nanoparticle adsorbed on a SAM of phenylenedimethanethiol (XYL) molecules [10]. They found Coulomb blockade behaviour at low voltages and "Coulomb staircase" behaviour at increased voltages. By fitting the data to a model consisting of two tunnelling capacitors in series, they obtained the resistance of the XYL molecule as 18 ± 12 MΩ. Datta *et al.* used an STM to measure the $I(V)$ characteristics of a monolayer of XYL molecules on Au(111) without any gold nanoparticles, thereby eliminating the Coulomb blockade effect. They used the tip-SAM height as a fitting parameter to support their theoretical model of transport through a molecular monolayer [13].

One of the seminal experiments in molecular electronics is the first direct measurement of the conductance of a molecular junction by Reed *et al.* [23]. They introduced the technique of obtaining single-molecule contact between two metal electrodes by using a mechanically controllable break junction. Their measured resistance of benzenedithiol (BDT) was ~ 22 MΩ.

Another important technique invented by the same group at Yale, is the silicon nanopore structure [26, 27]. A SAM of molecules is sandwiched between metal contacts inside a silicon structure. This again allows direct measurement of molecular conduction, but through an active area containing ~ 1000 molecules. The area is smaller than the domain size of the SAM, leading to a very ordered structure [27]. Measurements on a SAM of 4-thioacetylbiphenyl molecules yielded strong rectification due to the asymmetry of the metal-molecule-metal heterostructure [26]. Subsequent nanopore experiments resulted in very large negative differential resistance (NDR), with an on-off ratio of 1000:1 [27,28]. The molecule in this study contained a redox centre and the NDR was attributed to a two-step reduction process switching the conductivity of the molecule. Much weaker NDR was observed by Datta *et al.* in STS measurements on a SAM of 4-p-terphenylthiol molecules on Au(111) [12]. They attributed the NDR to an

interplay between the electrostatic potential profile across the system and narrow features in the local density of states (LDOS) of the STM tip apex atom.

Meanwhile conducting atomic force microscopy (C-AFM) was also being used as a valuable tool for molecular conductance measurements [20]. For example, carotenoid molecules embedded in a SAM of insulating alkanethiols were studied with a conducting AFM, measuring a resistance of 4.2 ± 0.7 GΩ, six orders of magnitude smaller than an alkanethiol of the same length [21]. The same group later used a C-AFM to measure the conductance of a single octanedithiol molecule [22]. The dithiols were embedded in a SAM of single-ended octanethiols incubated with a suspension of gold nanoparticles, that bind selectively to the molecules with a thiol endgroup. The AFM tip was brought into contact with the nanoparticles in order to measure the $I(V)$ characteristics of the junction. A statistical analysis of thousands of such measurements resulted in five distinct curves that were integer multiples of a fundamental curve, interpreted as the $I(V)$ characteristic of a single alkanedithiol molecule. The resistance of the molecule was measured as 900 ± 50 MΩ.

This statistical approach was arguably the strongest evidence thus far that the $I(V)$ characteristic of a single molecule can be probed. The technique may still suffer from the Coulomb blockade effect due to the use of a gold nanoparticle to contact the top of the SAM. Accordingly a series of experiments followed, also based on a statistical approach, but using an STM and circumventing the need for the nanoparticle acting as second electrode. This new technique is attributed to Tao at Arizona State University [2,3]. The STM tip was plunged into a substrate in a solution of molecules and gradually retracted. Conductance histograms of thousands of measurements were constructed. Clear peaks in the histograms could be identified at integer multiples of the quantum of conductance, the limiting conductance for pure metallic contacts [88]. These were attributed to strands of gold bridging the substrate and tip as the tip was initially retracted. Lower-level conductance peaks were identified at integer multiples of some significantly smaller conductance value, which were interpreted as the conductance through parallel molecular connections. In this way Tao *et al.* measured the resistance of hexane-, octane-, and decanedithiol as 10.5 ± 0.5, 51 ± 5, and 630 ± 50 MΩ

respectively [2], of 4,4′-bipyridine as 1.3 ± 0.1 MΩ [2] and of BDT and XYL as 1.2 and 22 MΩ respectively [3].

Recently this technique was used on thiols as well as amines [14–16] by two groups who independently found that single-molecule conductance values could far more readily be extracted from conductance histograms for amines than for thiols. They did not make use of a filtering technique, but rather included all measured data points in the histrograms. This led to significantly more diffuse histograms in the case of thiols, making the extraction of a single-molecule conductance troublesome. However in the case of amines, the conductance values could be extracted. This was attributed to much more selective binding of the amines on the gold surface, thereby limiting the number of distinct bonding configurations and hence conductance values observed over the range of measurements. For a series of biphenyl-amines, the extracted conductances corresponded very well to a theoretical model of the conductance as a function of the twist angle between the phenyl rings [16]. Subsequent measurements by Tao's group showed two distinct sets of peaks in the conductance histogram for octanedithiol, attributed to two different binding geometries [17, 18]. They also repeated the measurements for amines and carboxylic acids [19].

The 1999 Reed *et al.* experiment [27] has not been reproduced, which raises doubts as to whether the large NDR was indeed an intrinsic molecular property. However, other experimental demonstrations of molecular switching behaviour [30, 89–93] indicate that devices that rely on molecular control may in future become a reality [94].

It seems evident that experimentalists are indeed able to observe $I(V)$ characteristics pertaining to a single molecule. This is further confirmed by inelastic electron tunnelling spectroscopy (IETS) measurements, where peaks in the second derivative of the $I(V)$ curve can be attributed to vibrational modes of the molecule [29, 95].

1.2.4 Theoretical progress

Parallel to the advances made in probing the $I(V)$ characteristics and other interesting properties pertinent to achieving a molecular electronic device, much

effort has been invested in the modelling of these systems. Besides the task of building future nano-electronic devices, the problem of charge transport at the nanoscale is a very interesting theoretical challenge, leading to new physical insights and lying at the boundary between the fields of physics, chemistry and materials science [37].

The problem of describing electron transfer through a molecule linked to two charge reservoirs on the left and right lies somewhere inbetween two extreme cases. On one hand the current through a perfect metallic wire connecting the two reservoirs should be essentially independent of the wire length. On the other hand through-space tunnelling across the junction would decrease exponentially with tunnelling distance. For the present situation a theory was needed which allows treatment of the molecule with a discrete Hamiltonian, coupled to the continuous density of states of the reservoirs.

Lang developed a DFT based approach to obtain the tunnelling current density in the vacuum region between two metal electrodes with an adsorbed atom on each [96]. He used his technique to investigate the theory of STM imaging of single atoms on a substrate [97, 98].

More general methods were established by groups under Ratner [99, 100] and Datta [88, 101], who developed a Green's function based approach for calculating the transmission across a molecule connected to electrodes. This Green's function formalism used widely today, is based on the techniques originally developed by Kadanoff and Baym [102] and Keldysh [103]. Alternative methods were developed by Emberly and Kirczenow, who solved the Schrödinger equation directly for the scattered wavefunctions [104] and Joachim *et al.*, who used a transfer matrix technique [105]. The transmission function resulting from any of these techniques can be used to calculate the current according to the Landauer formula. This ubiquitous relation was originally proposed by Landauer [106] and Büttiker [107] for the current across a non-interacting electron region and later extended by Meir and Wingreen for the case of interacting electrons [108].

In the Landauer derivation, it was assumed that dissipation occurs deep within the reservoirs. It has been shown by Das and Green [109, 110] that the same formula can be derived from a quantum kinetic point of view, which fully takes

into account elastic and inelastic processes within the device.

Datta *et al.* used their model to fit STS $I(V)$ curves with the tip-molecule distance as fitting parameter. They established the importance of the location of the Fermi level relative to the molecular orbitals as well as the potential drop across the molecular region [13,111]. These early computational results made use of extended Hückel tight binding approaches for the molecular Hamiltonian. An important consideration in this work was to treat several of the gold electrode atoms closest to the molecule on the same footing as the molecule, thereby giving rise to the idea of an "extended molecule". This treatment is important to capture the molecule-electrode coupling. Ratner *et al.* studied BDT and XYL between Au(111) electrodes, treating the extended molecule within the Hartree-Fock level of theory [112]. This was one of the first calculations to treat the molecule at an *ab-initio* level. However, the electrode Fermi energy was still a parameter.

As early as 1995, Lang calculated the resistance of a 3-atom molecular wire by treating the molecular charge density using a self-consistent plane-wave DFT approach [113]. The electrodes however, were treated using a jellium model, i.e. interacting electrons within a uniform positively charged background. In 2000 they extended this work to calculate the $I(V)$ characteristics of BDT between metal electrodes [114]. They found that the current was two orders of magnitude larger than the experimental values of Reed *et al.* [23], but that this could be reduced by more than an order of magnitude by including gold adatoms at the metal-molecule interfaces [114]. Emberly and Kirczenow showed that the magnitude of the currents can be brought into close agreement with experiment if an alternate geometry is considered, where transport does not occur through an individual molecule, but through pairs of molecules bonded to opposite electrodes and aligned orthogonal to each other [60, 115].

Derosa and Seminario developed the first Green's function based approach using a density functional theory (DFT) description of the extended molecule [116]. Subsequently much work has been done developing and applying codes that treat the molecule and electrodes on an equal *ab-initio* footing. DFT approaches to the self-consistent electronic structure together with the NEGF formalism to obtain the transmission spectrum were developed by Datta *et al.* [117, 118],

Taylor *et al.* in the form of the package MCDCAL [119], Brandbyge *et al.* in the TranSIESTA package [120] and Rocha *et al.* in SMEAGOL [121]. The latter software is based on the widely used SIESTA DFT electronic structure code [122, 123].

These methods reproduce the theoretical conductance for a one-dimensional gold nanowire, $G_0 = \frac{2e^2}{\hbar}$ [118, 120], which has been confirmed experimentally [124]. However, as in the earlier results of Di Ventra, Pantelides and Lang [114], the calculated conductance of a BDT molecule was about two orders of magnitude larger than experimental data [118, 125].

Much work has been done to understand the origin of the large differences between experimental and calculated current and conductance values. There are various considerations that may account for the discrepancies. Firstly, the calculations are performed after specifying a model geometry which does not necessarily correspond to the actual experimental geometry. Hu *et al.* performed a statistical analysis of calculated currents for bipyridine and alkanedithiol junctions [55]. They found that the effects of the contact geometry on the conductance is much larger for the bipyridine molecule than for the alkanedithiol. For the alkanedithiol, the ensemble average corresponds to experimental values. For bipyridine, some configurations give conductances close to experiment, but the ensemble average is still much larger [55]. Müller found that by adding gold adatoms to a alkanethiol junction, agreement can be obtained between calculated [56] and experimental conductances [2] for certain geometries. Ratner *et al.* [54] and Solomon *et al.* [49] also found that changes in interfacial geometry of the thiol-gold contact can lead to orders of magnitude changes in the predicted conductance.

A particular aspect of the junction geometry which is expanded on in the present work, is stretching of the gold-sulfur bond or the junction as a whole. This is particularly relevant in describing the series of recent experiments outlined previously in this chapter, where an STM tip is plunged into the substrate and retracted while conductance measurements are taken. In their statistical analysis, Hu *et al.* found that increasing the gold-surfur bond length beyond the equilibrium value may result in an increase or decrease in conductance [55].

Xue and Ratner [53] found a surprising increase in conductance with increased gold-sulfur distance. This could be attributed to the highest occupied molecular orbital (HOMO) of the isolated molecule being very close in energy to the metal Fermi level. As the coupling between molecule and surface decreases, the orbital mixing reduces and hence the HOMO moves closer to the Fermi level, thereby facilitating resonant tunnelling. Ke *et al.* [57] obtained a similar result. Ferry *et al.* [59, 126] predicted an increase in conductance for the XYL molecule between gold electrodes for certain stretching distances of the molecule, using their transfer matrix method. The conductance resonance was attributed to the more delocalised nature of the HOMO and lowest unoccupied molecular orbital (LUMO) for certain stretched geometries, leading to a larger conductance. Romaner *et al.* [127] used DFT to calculate the band structure of a stretched junction and found that the HOMO shifts upward and aligns with the Fermi level of the metal, in agreement with the results of Ratner. They predicted that the gold-sulphur bond breaks before detaching a chain of gold atoms from the surface, contrary to the Carr-Parrinello molecular dynamics simulations of Kruger *et al.* [128]. However it was pointed out that the energy difference between the two scenarios is very small and hence the actual stretching behaviour may depend strongly on the initial geometry.

The Au-S interaction has been well characterised (see for example Ref. [79]). The Au/thiol SAM forms by an annealing process [129] and it is therefore reasonable to assume that experimental measurements of the conductance of gold-thiol-gold junctions will probe a range of actual geometries, resulting in a lack of reproducibility between measurements [54]. Recent experiments involving amine junctions showed less variability in conductance [14–17, 19]. It was postulated that the reproducibility of the amine conductance measurements is due to a much smaller spectrum of possible binding geometries. The amine-gold bond is far weaker than its thiol counterpart and only stable when the amine is coordinated with a single gold adatom [15].

Another reason for the unusually large calculated currents could be errors inherent in the DFT approximation, in particular the fact that this is a static mean-field theory, which does not account for dynamical effects and includes only

an approximate treatment of electron correlation. Delaney and Greer [42] used a configuration interaction (CI) expansion of the wavefunctions to calculate transport characteristics of a gold-BDT-gold junction and showed that this level of theory predicts currents close to the experimental measurements of Reed [23]. Sai *et al.* [40] calculated dynamical corrections to the conductance of molecular junctions using time-dependent DFT (TDDFT). They found that such corrections reduce the conductance of a metal-BDT-metal junction by about 10%. Solomon *et al.* investigated errors specific to the treatment of open systems, which could occur if proper account of the open shell nature of the system is not taken [48].

A further consideration which is not included in standard DFT-NEGF approaches, is inelastic scattering due to electron-phonon interactions. This has been investigated by Solomon *et al.* [130] and the peaks in the vibrational spectrum agree well with experiment [29].

1.3 Present study

In this work we present computational simulations of the adsorption of small organic molecules on the Au(111) surface as well as the current and conductance characteristics of these molecules between two Au(111) electrodes. Particular emphasis is placed on the effect of the interface geometry of the molecular junction on the conductance or current. The geometry optimisations are performed within the DFT level of theory with the SIESTA package. The transport calculations use the DFT-NEGF implementations in the TranSIESTA-C and SMEAGOL packages as well as a simpler tunnel barrier model approach.

The background theory needed for these computations is presented in chapter 2. In DFT equilibrium calculations of periodic systems, as well as the NEGF extension to allow treatment of open systems under finite bias, there are several computational parameters which will affect the accuracy of the results within the level of theory. In chapter 3 several test calculations are presented in order to find a suitable set of parameters.

Surface adsorption studies of thiols, ethynyls and amines are presented in chapter 4. The implementation of a new ZMATRIX module in SIESTA is described.

This is a tool for optimising geometries using a Z-matrix internal coordinate system and is particularly useful for optimising molecules on surfaces, as required in this work.

Chapter 5 describes the DFT-NEGF transport calculations. Current-voltage $[I(V)]$ curves are presented with the systems in their "equilibrium" geometries (the molecule is bonded to both electrodes in the position obtained using a DFT geometry optimisation). In addition some perturbed geometries are investigated. These include introducing a gap distance between the molecule and electrode on one side, positioning the molecule on different binding sites on the surfaces and an analysis of the process of stretching and breaking the molecular junction.

Chapter 6 deals with the description of the junction using a tunnel barrier model. The model is defined and used to calculate the $I(V)$ characteristics of some of the junction geometries already introduced in chapter 5. The model is applied to a typical STM setup and the implications for STS measurements investigated.

Chapter 7 contains a summary and concluding remarks as well as suggestions for extensions of the research described in this work.

Chapter 2

Theory

In this work we need to solve the electronic and ionic structure of systems consisting of molecules and surfaces. Periodic boundary conditions will be used to make the problem tractable with the number of atoms in the systems of interest limited to ~ 100. We opt for a quantum mechanical treatment of the system and the first step to finding a solution is writing down the Hamiltonian. All stationary solutions to the many particle wave function Ψ may then in principle be found by solving the Schrödinger equation

$$\hat{H}\Psi = E\Psi. \tag{2.1}$$

The Hamiltonian is written as the sum of several components

$$\begin{aligned} \hat{H} &= -\frac{1}{2}\sum_{i=1}^{N}\nabla_i^2 - \frac{1}{2}\sum_{I=1}^{M}\frac{1}{M_I}\nabla_I^2 + \sum_{i=1}^{N}\sum_{j>i}^{N}\frac{1}{|\vec{r}_i - \vec{r}_j|} \\ &- \sum_{i=1}^{N}\sum_{I=1}^{M}\frac{Z_I}{|\vec{r}_i - \vec{R}_I|} + \sum_{I=1}^{M}\sum_{J>I}^{M}\frac{Z_I Z_J}{|\vec{R}_I - \vec{R}_J|} \end{aligned} \tag{2.2}$$

where the number of electrons and nuclei are N and M respectively, M_I is the mass of nucleus I relative to the mass of an electron and Z_I is the positive charge of nucleus I. $\vec{r}_i$ are the electron positions and $\vec{R}_I$ are the nuclear positions. As in the rest of this work, we have made use of atomic units where $\hbar = m_e = e = 1$. The first two terms represent the kinetic energy of the electrons and nuclei

respectively, and the third, fourth and fifth terms represent the electron-electron, electron-nuclear and internuclear interaction energies. Solving such a many-body problem is currently beyond the scope of mainstream computational methods and a series of approximations have to be made before the theory can be applied to systems of interest.

The first approximation makes use of the fact that the electrons move significantly faster than the nuclei due to their much smaller mass. On the time scale of electronic motion we therefore treat the nuclei as stationary and their only contribution to the electronic Hamiltonian is to set up an external potential $V_{\text{nuc}}(\vec{r})$ in which the electrons move. This is known as the Born-Oppenheimer approximation [131,132] and decouples the nuclear and electronic motion. We thus rewrite (2.2), noting that it is no longer the Hamiltonian for the entire system, but describes only the electron motion

$$\hat{H} = -\frac{1}{2}\sum_{i=1}^{N}\nabla_i^2 + \sum_{i=1}^{N}\sum_{j>i}^{N}\frac{1}{|\vec{r}_i - \vec{r}_j|} + \sum_{i=1}^{N} v_{\text{nuc}}(\vec{r}_i) \tag{2.3}$$

$$= \hat{T} + \hat{V}_{\text{ee}} + \hat{V}_{\text{Ne}} \tag{2.4}$$

where the external potential due to the field of the nuclei is given by

$$v_{\text{nuc}}(\vec{r}) = -\sum_{I=1}^{M}\frac{Z_I}{|\vec{r} - \vec{R}_I|}. \tag{2.5}$$

Note that in the presence of other external potentials such as an applied electric field, equation (2.3) will be modified by replacing v_{nuc} with a general external potential v_{ext} which includes the field set up by the nuclei. The corresponding operator in (2.4) will be $\hat{V}_{\text{ext}}$. The energy given by using this electronic Hamiltonian in (2.1) is the electronic energy of the system, and since the nuclear kinetic energy is assumed to be 0, the total energy is given by

$$E_{\text{tot}} = E_{\text{elec}} + E_{\text{nuc}} \tag{2.6}$$

where E_{nuc} is the *constant* internuclear repulsion energy

$$E_{\text{nuc}} = \sum_{I=1}^{M} \sum_{J>I}^{M} \frac{Z_I Z_J}{|\vec{R}_I - \vec{R}_J|}. \tag{2.7}$$

We will from now on write $E_{\text{elec}} = E$, the quantity we need to minimise in order to find the ground state electronic structure for a given and fixed set of nuclear coordinates.

This is the starting point for all modern *ab-initio* electronic structure methods. In order to solve the electronic structure of a particular many-body system, many more approximations are needed; inevitably there is a trade-off between the accuracy of the method and the complexity and hence computational efficiency with which the method can be implemented. For our purposes and indeed for the majority of electronic structure and transport calculations, Density Functional Theory (DFT) provides a quantitatively accurate solution, while being feasible given the available computational resources.

2.1 Density Functional Theory

Parr and Yang [133] give a thorough account of DFT and a more introductory treatment can be found in Koch and Holthausen [134].

The main problem in solving (2.1) subject to the Hamiltonian (2.3) is that the many-body wavefunction Ψ is a function of $4N$ variables, being the three spatial and one spin coordinate of each electron. Knowledge of Ψ povides us with all properties of the system, but in order to determine the minimum energy electronic structure it may not be necessary to have this full knowledge. Already in 1927 attempts were made by Thomas [135] and Fermi [136] to describe the kinetic energy of the system as a functional of the electron density alone. The electron density $\rho(\vec{r})$ is a function of the three spatial coordinates, describing the probability of finding any electron at a *particular* point in space. Accordingly it is defined from the N-particle wavefunction as

$$\rho(\vec{r}) = N \int \cdots \int |\Psi(\vec{x}_1, \vec{x}_2, \ldots, \vec{x}_N)|^2 \mathrm{d}s_1 \mathrm{d}\vec{x}_2 ... \mathrm{d}\vec{x}_N \tag{2.8}$$

so that $\rho(\vec{r})\mathrm{d}\vec{r}_1$ is the probability of finding any electron within the volume element $\mathrm{d}\vec{r}_1$. Due to the probabilistic interpretation of the square of the wavefunction, the integral represents the probability of finding a particular electron in the volume element $\mathrm{d}\vec{r}$ and since the electrons are indistinguishable this is multiplied by N to find the probability of finding *any* electron in the same volume element. From the normalisation constraint on the wavefunction

$$\int \cdots \int |\Psi(\vec{x}_1, \vec{x}_2, \ldots, \vec{x}_N)|^2 \mathrm{d}\vec{x}_1 \mathrm{d}\vec{x}_2 \ldots \mathrm{d}\vec{x}_N = 1, \tag{2.9}$$

it follows that the electron density integrates to the number of electrons in the system

$$\int \rho(\vec{r})\mathrm{d}\vec{r} = N. \tag{2.10}$$

In the above the $\vec{x}_i$ are four-dimensional variables defining the three space and one spin coordinates of the electrons, $\vec{x}_i = (\vec{r}_i, s_i)$ where s_i takes one of the spin-values α or β.

The expectation value of the external potential energy can be written simply in terms of the electron density and the one-particle potential v_{ext}. Since $\langle\Psi|\Psi\rangle = \int \Psi^*\Psi \mathrm{d}\vec{x}^N = 1$,

$$\begin{aligned}
\langle\hat{V}_{\mathrm{ext}}\rangle &= \langle\Psi|\sum_{i=1}^{N} v_{\mathrm{ext}}(\vec{r}_i)|\Psi\rangle \\
&= \int \Psi^* \left(\sum_{i=1}^{N} v_{\mathrm{ext}}(\vec{r}_i)\right) \Psi \mathrm{d}\vec{x}^N \\
&= \sum_{i=1}^{N} \int \Psi^* v_{\mathrm{ext}}(\vec{r}_i) \Psi \mathrm{d}\vec{x}^N \\
&= \sum_{i=1}^{N} \int \frac{1}{N} \rho(\vec{r}_i) v_{\mathrm{ext}}(\vec{r}_i) \mathrm{d}\vec{r}_i \\
&= \int \rho(\vec{r}) v_{\mathrm{ext}}(\vec{r}) \mathrm{d}\vec{r}
\end{aligned} \tag{2.11}$$

where the shorthand notation $\mathrm{d}\vec{x}^N = \mathrm{d}\vec{x}_1 \mathrm{d}\vec{x}_2 \ldots \mathrm{d}\vec{x}_N$ has been used. The expressions for $\langle\hat{T}\rangle$ and $\langle\hat{V}_{\mathrm{ee}}\rangle$ cannot be written in this straightforward manner.

In 1964 the idea of Thomas and Fermi was formally justified in a seminal

paper by Hohenberg and Kohn [34] in which they proved that the ground state wavefunction and hence ground state energy of the system is a functional of the ground state electron density alone. The proof requires a widely used concept in quantum mechanics, known as the variational principle.

2.1.1 Variational principle

The variational principle states that the expectation value $\langle E \rangle$ of the energy of any trial wavefunction is an upper bound to the true ground state energy E_0 corresponding to the ground state wavefunction Ψ_0 of a system with a given Hamiltonian $\hat{H}$. This follows from the expansion of the trial wavefunction Φ as a linear combination of the orthogonal eigenfunctions of $\hat{H}$

$$\begin{aligned}
\langle E \rangle &= \frac{\langle \Phi | \hat{H} | \Phi \rangle}{\langle \Phi | \Phi \rangle} \\
&= \frac{\langle \sum_i c_i \Psi_i | \hat{H} | \sum_j c_j \Psi_j \rangle}{\langle \sum_i c_i \Psi_i | \sum_j c_j \Psi_j \rangle} \\
&= \frac{\sum_i \sum_j c_i^* c_j \langle \Psi_i | \hat{H} | \Psi_j \rangle}{\sum_i \sum_j c_i^* c_j \langle \Psi_i | \Psi_j \rangle} \\
&= \frac{\sum_i \sum_j c_i^* c_j E_j \delta_{ij}}{\sum_i \sum_j c_i^* c_j \delta_{ij}} \\
&= \frac{\sum_i |c_i|^2 E_i}{\sum_i |c_i|^2} \\
&\geq E_0
\end{aligned}$$

where the last line results because E_0 is the ground state energy and hence $E_i \geq E_0$ for all the other eigenenergies E_i.

This principle can be used in quantum chemistry as a tactic for finding the ground state wavefunction: if we search over all possible wavefunctions, then the one that yields the lowest energy is the ground state wavefunction. Of course in practice the search will be limited to a particular subset of wavefunctions.

2.1.2 Hohenberg-Kohn theorems

The first Hohenberg-Kohn theorem states that *the ground state electron density uniquely defines the external potential, up to a trivial additive constant.* Since the other terms in the electronic Hamiltonian, namely the kinetic energy and electron-electron repulsion operators are universal for all N-electron systems and N is fixed by the density through (2.10), this implies that the Hamiltonian is uniquely defined by the ground state electron density $\rho_0(\vec{r})$. In the case of a non-degenerate ground state, the ground state wavefunction is also uniquely defined by $\rho_0(\vec{r})$.

The remarkably simple proof of Hohenberg and Kohn uses the technique of *reductio ad absurdum*. Suppose that there are two external potentials $v_{\text{ext}}(\vec{r})$ and $v'_{\text{ext}}(\vec{r})$ which both give rise to the same ground state electron density $\rho_0(\vec{r})$. Denote the Hamiltonians associated with these external potentials by $\hat{H}$ and $\hat{H}'$ respectively (obtained by adding the universal kinetic energy and electron-electron repulsion operators). Furthermore denote by Ψ_0, E_0 and Ψ'_0, E'_0 the ground state wavefunctions and ground state energies obtained by solving the respective Schrödinger equations. Then by the variational principle and (2.11)

$$\begin{aligned} E_0 &\leq \langle \Psi'_0 | \hat{H} | \Psi'_0 \rangle \\ &= \langle \Psi'_0 | \hat{H}' | \Psi'_0 \rangle + \langle \Psi'_0 | \hat{H} - \hat{H}' | \Psi'_0 \rangle \\ &= E'_0 + \langle \Psi'_0 | \hat{V}_{\text{ext}} - \hat{V}'_{\text{ext}} | \Psi'_0 \rangle \\ &= E'_0 + \int \rho_0(\vec{r}) \left[v_{\text{ext}}(\vec{r}) - v'_{\text{ext}}(\vec{r}) \right] \mathrm{d}\vec{r} \\ \implies E_0 - E'_0 &\leq \int \rho_0(\vec{r}) \left[v_{\text{ext}}(\vec{r}) - v'_{\text{ext}}(\vec{r}) \right] \mathrm{d}\vec{r} \end{aligned} \tag{2.12}$$

Similarly

$$\begin{aligned} E'_0 &\leq \langle \Psi_0 | \hat{H}' | \Psi_0 \rangle \\ &= E_0 + \int \rho_0(\vec{r}) \left[v'_{\text{ext}}(\vec{r}) - v_{\text{ext}}(\vec{r}) \right] \mathrm{d}\vec{r} \\ &= E_0 - \int \rho_0(\vec{r}) \left[v_{\text{ext}}(\vec{r}) - v'_{\text{ext}}(\vec{r}) \right] \mathrm{d}\vec{r} \\ \implies E_0 - E'_0 &\geq \int \rho_0(\vec{r}) \left[v_{\text{ext}}(\vec{r}) - v'_{\text{ext}}(\vec{r}) \right] \mathrm{d}\vec{r} \end{aligned} \tag{2.13}$$

Comparing (2.12) and (2.13) shows that equality holds in both equations and hence $\Psi_0 = \Psi_0'$. However Ψ_0 and Ψ_0' are solutions to distinct Schrödinger equations ($\hat{H}$ and $\hat{H}'$ differ by more than a constant) and cannot be equal. This provides the contradiction and hence the external potential, Hamiltonian, ground state wave function and ground state energy are all uniquely defined by the ground state electron density. Also, the energy contributions by the individual parts of the Hamiltonian can therefore be written as functionals of $\rho_0(\vec{r})$. Equation (2.11) already provides this for the external potential energy. Hohenberg and Kohn thus defined a universal functional of the density

$$F[\rho_0(\vec{r})] = \langle \Psi | \hat{T} + \hat{V}_{\mathrm{ee}} | \Psi \rangle \tag{2.14}$$

which is valid for any external potential and any number of particles (since $\rho_0(\vec{r})$ fixes the number of particles through (2.10)). Adding (2.11) and (2.14) gives the total ground state electronic energy as a functional of the electron density for a given external potential v_{ext}

$$E_v[\rho_0(\vec{r})] = \int \rho_0(\vec{r}) v(\vec{r}) \mathrm{d}\vec{r} + F[\rho_0(\vec{r})]. \tag{2.15}$$

Next Hohenberg and Kohn proved that a variational principle applies here as well and follows in a straightforward manner from the standard variational principle. This is known as the second HK theorem. Suppose that $\rho_0'(\vec{r}) \neq \rho_0(\vec{r})$ is the ground state density corresponding to another external potential $v'(\vec{r}) \neq v(\vec{r})$ with Hamiltonian $\hat{H}'$ and ground state energy E_0'; then

$$\begin{aligned} E_v[\rho_0'(\vec{r})] &= \langle \Psi' | \hat{H} | \Psi' \rangle \\ &\geq \langle \Psi | \hat{H} | \Psi \rangle \\ &= E_v[\rho_0(\vec{r})] \\ &= E_0. \end{aligned} \tag{2.16}$$

Note that the input density to the functionals $F[\rho]$ and $E_v[\rho]$ above are assumed to be the ground state density associated with some external potential $v(\vec{r})$. The HK theorems only apply to such v-representable densities. The second HK theorem

therefore states that the energy obtained by applying the functional (2.15) to any v-representable trial density is an upper bound to the true ground state energy.

2.1.3 Kohn-Sham equations

While the Hohenberg-Kohn theorems establish the fact that in order to solve the electronic structure of a many-electron system, we need to find only the electron density and not the many-body wavefunction, it does not describe any method for finding this density. It proves the existence of the functional $E_v[\rho]$ but gives no indication of its form. What it does prove, is that the ground state electron density, is the density that minimises $E_v[\rho]$. It is therefore instructive to write this functional as the sum of several components

$$E_v[\rho] = T[\rho] + E_H[\rho] + V_{\text{ext}}[\rho] + E_{\text{cor}}[\rho] \tag{2.17}$$

$$E_H[\rho] = \frac{1}{2}\iint \frac{\rho(\vec{r})\rho(\vec{r}')}{|\vec{r}-\vec{r}'|}\mathrm{d}\vec{r}\mathrm{d}\vec{r}' \tag{2.18}$$

$$V_{\text{ext}}[\rho] = \int \rho(\vec{r})v(\vec{r})\mathrm{d}\vec{r} \tag{2.19}$$

where T is the kinetic energy functional, V_{ext} the potential energy due to the nuclei and any other external field and the electron-electron interaction energy has been split into the Hartree energy, E_H, and an unknown correction term, E_{cor}. The Hartree energy defined in (2.18) represents the energy due to the interaction of each electron with the averaged field of all the electrons. There are three distinct contributions to the correction term, namely the exchange, correlation and self-interaction energies. The exchange energy arises due to the Pauli exclusion principle, or equivalently the antisymmetric nature of the wavefunction. This forbids two electrons in the same spin state to occupy the same region in space, and has the effect of depleting the probability density for electrons around a reference electron of like spin. It has no effect on the interaction between electrons of opposite spin.

Secondly the correlation energy is the energy due to the instantaneous Coulomb repulsion of all electrons with one another. It corrects for the fact that electrons are not just moving in the averaged field of all other electrons and depletes the

probability density of all electrons close to the region of a reference electron.

Furthermore the expression for $E_H[\rho]$ includes a non-physical self-interaction where each electron is interacting with its own probability density. The correction term $E_{\rm cor}[\rho]$ must also serve to remove this self-interaction.

As seen above, it is possible to write explicit expressions for the Hartree energy and the external potential energy functionals, but it is not known what the form of the kinetic energy functional or the Coulomb correction functional should be.

In 1965 Kohn and Sham [35] proposed a practical method for finding the ground state electron density. Their idea was to construct a fictitious non-interacting reference system with the same ground state density as the real system. The simplest wavefunction that describes N non-interacting electrons and obeys the antisymmetry requirement due to the Pauli principle, is an antisymmetrised product of one-electron wavefunctions $\psi_i(\vec{r})$. One can write this antisymmetric product most conveniently as a Slater determinant

$$\Psi_{\rm S}(\vec{x}_1,\vec{x}_2,\ldots,\vec{x}_N)=\frac{1}{\sqrt{N!}}\begin{vmatrix}\psi_1(\vec{x}_1) & \psi_2(\vec{x}_1) & \ldots & \psi_N(\vec{x}_1)\\ \psi_1(\vec{x}_2) & \psi_2(\vec{x}_2) & \ldots & \psi_N(\vec{x}_2)\\ \vdots & \vdots & \ddots & \vdots\\ \psi_1(\vec{x}_N) & \psi_2(\vec{x}_N) & \ldots & \psi_N(\vec{x}_N)\end{vmatrix} \tag{2.20}$$

where the scale factor is chosen to normalise $\Psi_{\rm S}$. These one-electron wavefunctions, commonly referred to as orbitals, are chosen to be orthonormal so that the resulting electron density is given by

$$\begin{aligned}\rho(\vec{r}) &\equiv N\int\cdots\int|\Psi_S(\vec{x}_1,\vec{x}_2,\cdots,\vec{x}_N)|^2{\rm d}s_1{\rm d}\vec{x}_2\cdots{\rm d}\vec{x}_N\\ &= \sum_{i=1}^{N}|\psi_i(\vec{r})|^2.\end{aligned} \tag{2.21}$$

The last line follows by examining the terms resulting from the product of two Slater determinants in the integrand and eliminating those that integrate to 0 according to the orthonormality condition $\int\psi_i(\vec{x}_k)^*\psi_j(\vec{x}_k){\rm d}\vec{x}_k=\delta_{ij}$.

The next important step is to separate the kinetic energy functional into

the contribution of a non-interacting system of electrons and a correction term. The non-interacting part can be written down exactly and will form the major contribution to the kinetic energy of the system

$$\begin{aligned} T[\rho] &= \langle\Psi|\sum_{i=1}^{N} -\frac{1}{2}\nabla_i^2|\Psi\rangle \\ &\equiv \widetilde{T}[\rho] + \langle\Psi_{\mathrm{S}}|\sum_{i=1}^{N} -\frac{1}{2}\nabla_i^2|\Psi_{\mathrm{S}}\rangle \\ &= \widetilde{T}[\rho] + \sum_{i=1}^{N}\langle\psi_i(\vec{r})| - \frac{1}{2}\nabla^2|\psi_i(\vec{r})\rangle \\ &\equiv \widetilde{T}[\rho] + T_{\mathrm{S}}[\rho]. \end{aligned} \tag{2.22}$$

where the third line follows again by examining the product of Slater determinants and using the orthonormality condition. The kinetic energy correction, $\widetilde{T}[\rho]$ and the Coulomb correction, $E_{\mathrm{cor}}[\rho]$ are absorbed into one term describing all the unknown parts of the HK functional;

$$\begin{aligned} E_v[\rho] = &- \frac{1}{2}\sum_{i=1}^{N}\langle\psi_i(\vec{r})|\nabla^2|\psi_i(\vec{r})\rangle + \frac{1}{2}\iint\frac{\rho(\vec{r})\rho(\vec{r}')}{|\vec{r}-\vec{r}'|}\mathrm{d}\vec{r}\mathrm{d}\vec{r}' \\ &+ \int\rho(\vec{r})v(\vec{r})\mathrm{d}\vec{r} + E_{\mathrm{XC}}[\rho] \end{aligned} \tag{2.23}$$

with

$$E_{\mathrm{XC}}[\rho] = \widetilde{T}[\rho] + E_{\mathrm{cor}}[\rho]. \tag{2.24}$$

The method of Lagrange multipliers can be used to minimise the energy given by (2.23) subject to the constraints

$$\int\psi_i^*(\vec{r})\psi_j(\vec{r})\mathrm{d}\vec{r} = \delta_{ij} \tag{2.25}$$

introduced already. Note that through (2.21) this implies that the normalisation constraints on the wavefunction (2.9) and density (2.10) are satisfied. To this

end we define the functional

$$\Omega[\psi_1, \psi_2, \ldots, \psi_N] \equiv E_v[\rho] - \sum_{i=1}^{N}\sum_{j=1}^{N} \varepsilon_{ij} \left[\int \psi_i^*(\vec{r})\psi_j(\vec{r})\mathrm{d}\vec{r} - \delta_{ij} \right] \tag{2.26}$$

and solve the corresponding Euler equations $\frac{\delta\Omega}{\delta\psi_i^*} = 0$. First note that

$$\frac{\delta X}{\delta\psi_i^*} = \frac{\delta X}{\delta\rho} \cdot \frac{\partial\rho(\vec{r})}{\partial\psi_i^*(\vec{r})} = \frac{\delta X}{\delta\rho} \cdot \psi_i(\vec{r}) \tag{2.27}$$

from (2.21). Then

$$\begin{aligned}
0 &= \frac{\delta\Omega}{\delta\psi_i^*} \\
&= \frac{\delta E_v}{\delta\psi_i^*} - \sum_{j=1}^{N} \varepsilon_{ij}\psi_j(\vec{r}) \\
&= \frac{\delta}{\delta\rho}\int \rho(\vec{r})v(\vec{r})\mathrm{d}\vec{r} \cdot \frac{\partial\rho}{\partial\psi_i^*} + \frac{\delta T_\mathrm{S}}{\delta\psi_i^*} + \frac{\delta E_H}{\delta\rho} \cdot \frac{\partial\rho}{\partial\psi_i^*} + \frac{\delta E_\mathrm{XC}}{\delta\rho} \cdot \frac{\partial\rho}{\partial\psi_i^*} - \sum_{j=1}^{N} \varepsilon_{ij}\psi_j(\vec{r}) \\
&= v(\vec{r})\psi_i(\vec{r}) - \frac{1}{2}\nabla^2\psi_i(\vec{r}) + \int \frac{\rho(\vec{r}')}{|\vec{r} - \vec{r}'|}\mathrm{d}\vec{r}' \cdot \psi_i(\vec{r}) + V_\mathrm{XC}(\vec{r})\psi_i(\vec{r}) - \sum_{j=1}^{N} \varepsilon_{ij}\psi_j(\vec{r})
\end{aligned}$$

where we have made use of the definition of the non-interacting part of the kinetic energy, $T_\mathrm{S}[\rho]$ (2.22) and defined the exchange-correlation potential as the functional derivative of the exchange-correlation energy with respect to the electron density

$$V_\mathrm{XC}(\vec{r}) \equiv \frac{\delta E_\mathrm{XC}}{\delta\rho}. \tag{2.28}$$

Rearranging leads to the equations

$$\hat{f}^\mathrm{KS}\psi_i(\vec{r}) = \left(-\frac{1}{2}\nabla^2 + V_\mathrm{eff}(\vec{r}) \right) \psi_i(\vec{r}) = \sum_{j=1}^{N} \varepsilon_{ij}\psi_j(\vec{r}) \tag{2.29}$$

where an effective one-particle potential has been defined

$$\begin{aligned} V_{\text{eff}}(\vec{r}) &\equiv v(\vec{r}) + V_H(\vec{r}) + V_{\text{XC}}(\vec{r}) \\ V_H(\vec{r}) &\equiv \int \frac{\rho(\vec{r}')}{|\vec{r} - \vec{r}'|} \mathrm{d}\vec{r}'. \end{aligned} \tag{2.30}$$

Since $\varepsilon_{ij} = \langle\psi_j|\hat{f}^{\text{KS}}|\psi_i\rangle = \langle\psi_i|\hat{f}^{\text{KS}}|\psi_j\rangle^* = \varepsilon^*_{ji}$, the matrix defined by the Lagrange multipliers ε_{ij} is Hermitian and can thus be transformed into diagonal form by a unitary transformation of the orbitals ψ_i. This leads to the canonical form of the Kohn-Sham equations

$$\hat{f}^{\text{KS}}\psi_i = \varepsilon_i\psi_i. \tag{2.31}$$

This is a set of eigenvalue equations that can be solved once the exchange-correlation potential $V_{\text{XC}}(\vec{r})$ is known. Although the one-electron "orbitals" ψ_i are purely fictional, a solution of (2.31) leads to the electron density from (2.21) which minimises the total energy (2.23) and therefore corresponds to the ground state elecron density and total energy of the exact solution to the non-relativistic Schrödinger equation within the Born-Oppenheimer approximation.

The one-particle Kohn-Sham operator $\hat{f}^{\text{KS}}$ depends through (2.30) on the orbital solutions ψ_i and the set of equations (2.31) must therefore be solved self-consistently. This is known as the self-consistent cycle and hence DFT is an SCF method. In section 2.2 we will discuss the computational method used to implement the DFT solution of the electronic structure of our systems of interest. Having now established the DFT method, we briefly discuss in the next section some exchange-correlation potentials that are used in practice.

2.1.4 Exchange-correlation potentials

The form of V_{XC} is not known and finding better approximations to it, is the subject of much research in the field of density functional theory. Apart from the further approximations neccessary to perform actual computational implementations of DFT, "guessing" V_{XC} is the only obstacle to making DFT an exact theory. Unfortunately there is no systematic way of approaching better and better XC potentials.

Spin polarisation

In the formal derivation of DFT, there is no dependence on the spin of the electrons s_i or on the corresponding spin-densities $\rho^\alpha(\vec{r})$ and $\rho^\beta(\vec{r})$ (as long as the external potential is not spin-dependent). Therefore, if the exact V_{XC} were known, the solution to the electronic structure problem would proceed without taking account of the spin-densities. However in practice V_{XC} is approximated and it is found that these approximations are vastly improved if V_{XC} is a functional of both ρ^α and ρ^β. In particular, when there is an odd number of electrons or when bond dissociation is described, it is essential to treat the α and β electrons separately.

Local density approximation

The simplest approximation to V_{XC} is the local density approximation (LDA), which was already proposed by Kohn and Sham in their 1965 paper [35]. Accordingly the exchange and correlation potentials at each point in space are assumed to be identical to those of a uniform electron gas with constant density equal to the actual density at that point in space; to wit

$$E_{\mathrm{XC}}^{\mathrm{LDA}}[\rho] = \int \rho(\vec{r})\varepsilon_{\mathrm{XC}}^{\mathrm{LDA}}[\rho(\vec{r})]\mathrm{d}\vec{r} \tag{2.32}$$

where $\varepsilon_{\mathrm{XC}}^{\mathrm{LDA}}[\rho]$ is the exchange correlation energy per particle of an electron gas with uniform density ρ, which is decomposed into exchange $\varepsilon_{\mathrm{X}}^{\mathrm{LDA}}$ and correlation $\varepsilon_{\mathrm{C}}^{\mathrm{LDA}}$ terms. The exchange term is known exactly due to Dirac [137]

$$\varepsilon_{\mathrm{X}}^{\mathrm{LDA}}[\rho] = -\frac{3}{4}\sqrt[3]{\frac{3\rho}{\pi}}. \tag{2.33}$$

No analytical expression for the correlation term is avaliable. However, Ceperly and Alder [138] performed highly accurate quantum Monte-Carlo simulations of a homogeneous electron gas and based on their results other authors have developed parametrised forms for $\varepsilon_{\mathrm{C}}^{\mathrm{LDA}}$. The most widely used are those by Vosko, Wilk and Nusair [139], Perdew and Wang [140] and Perdew and Zunger [141]. The latter will be used in the present work. These parametrisations allow for spin

polarisation and in this case the exchange energy can be written as

$$E_{\mathrm{X}}^{\mathrm{LDA}}[\rho] = -\frac{3}{4}\sqrt[3]{\frac{3}{\pi}}\int \left(\rho^{\alpha}(\vec{r})^{4/3} + \rho^{\beta}(\vec{r})^{4/3}\right) \mathrm{d}\vec{r}. \tag{2.34}$$

Generalised gradient approximation

The next logical step for a better approximation to the true E_{XC} is to use an exchange correlation potential that takes into account not only the local density at each point in space, but also the gradient of the density at that point. First attempts at this idea produced results that were counterintuitively worse than those obtained using LDA. The reason for this involves the concept of the exchange correlation hole, which has not been discussed thus far. Briefly, the XC hole describes the change in electron density around a reference electron due to the effects of exchange and correlation. The total hole function can be written as the sum of the exchange and correlation hole functions, $h_{\mathrm{XC}}(\vec{r},\vec{r}') = h_{\mathrm{X}}(\vec{r},\vec{r}') + h_{\mathrm{C}}(\vec{r},\vec{r}')$. It can be shown that the mathematical expression for the exact h_{X} and h_{C} obey certain rules. As it happens the exchange and correlation holes corresponding to $E_{\mathrm{XC}}^{\mathrm{LDA}}$ obey these rules and this is a large part of the reason that LDA performs better than expected from such a basic approximation. The reason for the bad performance of the original gradient corrected XC energies was that these rules were not obeyed by the corresponding hole functions, and the XC potentials were therefore unphysical. However, the rules can be crudely enforced in order to drastically improve the performance of the functional. Such functionals are known as generalised gradient approximations (GGA). In general they have the form

$$E_{\mathrm{XC}}^{\mathrm{GGA}}[\rho^{\alpha},\rho^{\beta},\nabla\rho^{\alpha},\nabla\rho^{\beta}] = \int \rho(\vec{r})\varepsilon_{\mathrm{XC}}^{\mathrm{GGA}}(\rho^{\alpha},\rho^{\beta},\nabla\rho^{\alpha},\nabla\rho^{\beta})\mathrm{d}\vec{r}. \tag{2.35}$$

Again several parametrisations are available. In this work we shall use that due to Perdew, Burke and Ernzerhof [142].

Hybrid functionals and Hartree-Fock theory

An alternative to DFT, known as Hartree-Fock theory uses the wavefunction resulting from the Slater determinant in (2.20) as an approximation to the actual

many-electron wavefunction. This completely neglects electron correlation, but the antisymmetric nature of the wavefunction exactly accounts for electron exchange. LDA DFT results are usually slightly better than Hartree-Fock results, and using GGA further improves performance. However, the exchange energy is generally about an order of magnitude larger than the correlation energy. Therefore it makes sense to incorporate the exact exchange energy from Hartree-Fock theory into DFT, and approximate only the correlation energy. Again early attempts at such a scheme performed worse than expected because the resulting expressions for the exchange-correlation holes were unphysical. However several parametrisations have been suggested whereby a certain amount of exact exchange energy is mixed in with LDA or GGA approximations to exchange and correlation energy, thereby improving the hole functions and hence the performance of the potential. The resulting functionals are known as hybrid functionals and the most widely used is B3LYP, due to Stephens *et al.* [143].

2.2 Computational implementation of DFT

In the previous section, the theoretical foundation and a practical scheme for implementing DFT was outlined. Here we describe some of the practical issues that arise in an actual computational implementation. In this work the SIESTA[a] package was used for all calculations not involving transport and hence many of the concepts will be explained as they are dealt with therein. The SIESTA method is described in Refs. [122, 123, 144–146] with Ref. [122] being the most complete. A review of the applications of the method can be found in Ref. [147].

The computational issues deal largely with a number of approximations that are made to provide an implementation that can realistically be performed on the computational resources available. There is always a tradeoff between efficiency and accuracy. Unlike the choice of exchange-correlation potential described in section 2.1.4, the approximations described in the current section can be systematically changed to improve accuracy (but decrease efficiency). In chapter 3, we describe the tests that were performed in order to find a set of parameters defin-

[a] Acronym for Spanish Initiative for Electronic Simulations with Thousands of Atoms. website: www.uam.es/departmentos/ciencias/fismateriac/siesta/

ing these remaining approximations that provide us with quantitatively accurate results that can realistically be performed with our resources.

2.2.1 Basis sets

Equations (2.20) and (2.21) suggest a way to represent the electron density as the sum of the probability densities of a number of one-electron orbitals. Rather than allowing complete freedom for the spatial form of these orbitals, it is convenient to define them as a linear combination of pre-defined basis functions. Two main types of basis functions are used in practice: plane-waves and atomic orbitals. For solid-state systems plane-waves are normally used since they automatically obey Bloch's theorem. However for molecular sysems, atomic orbitals provide an intuitive framework for interpreting the resulting electronic structure. Furthermore, atomic orbitals are localised around atoms whereas plane-waves extend through space. This localisation is a desirable property for more efficient algorithms, as fewer pairs of functions overlap and hence fewer matrix elements need to be calculated in (2.38) and (2.39) below.

Atom centred Gaussian functions (Gaussian-type-orbitals or GTO's) are often used for the atomic orbitals due to their computational efficiency. Slater-type-orbitals (STO's) are also used as they consist of exponential functions similar to the eigenfunctions of a hydrogen atom and are therefore physically intuitive. The analytical expressions for these types of basis functions are

$$\begin{aligned} \phi^{\mathrm{PW}} &= e^{i\vec{k}\cdot\vec{r}} \\ \phi^{\mathrm{GTO}} &= N x^i y^j z^k e^{-\alpha r^2} \\ \phi^{\mathrm{STO}} &= N r^{n-1} e^{-\zeta r} \mathrm{Y}_{lm}(\Theta, \phi) \end{aligned}$$

with n, l, m the quantum numbers, $\mathrm{Y}_{lm}(\Theta, \phi)$ the usual spherical harmonics, $r = |\vec{r}|$, $\vec{r} = (x, y, z)$, N a normalisation factor, $\vec{k}$ the wave-vector and α and ζ constants. For the GTO's, $l = i + j + k$ specifies the angular momentum of the orbital. Alternatively purely numerical functions can be pre-defined and used as a basis, as is the case in the SIESTA method.

Linear combination of atomic orbitals

The linear combination of atomic orbitals (LCAO) ansatz states that the single-electron orbitals in (2.21) can be written as a linear combination of atom-centred orbitals

$$\psi_i(\vec{r}) = \sum_{\mu=1}^{L} c_{\mu i}\phi_\mu(\vec{r}) \tag{2.36}$$

where there are L basis functions labeled ϕ_μ. Substituting this into the Kohn-Sham equations (2.31), multiplying by an arbitrary basis function $\phi_\nu(\vec{r})$ and integrating over space leads to

$$\sum_{\mu=1}^{L} c_{\mu i} \int \phi_\nu(\vec{r})\hat{f}^{\mathrm{KS}}\phi_\mu(\vec{r})\mathrm{d}\vec{r} = \varepsilon_i \sum_{\mu=1}^{L} c_{\mu i} \int \phi_\nu(\vec{r})\phi_\mu(\vec{r})\mathrm{d}\vec{r} \tag{2.37}$$

where the basis functions ϕ_μ are assumed to be real. These integrals can be seen as the matrix elements of the Hamiltonian and overlap matrices

$$H_{\nu\mu} = \int \phi_\nu(\vec{r})\hat{f}^{\mathrm{KS}}\phi_\mu(\vec{r})\mathrm{d}\vec{r} \tag{2.38}$$

$$S_{\nu\mu} = \int \phi_\nu(\vec{r})\phi_\mu(\vec{r})\mathrm{d}\vec{r} \tag{2.39}$$

and (2.37) becomes

$$\sum_{\mu=1}^{L} c_{\mu i} H_{\nu\mu} = \varepsilon_i \sum_{\mu=1}^{L} c_{\mu i} S_{\nu\mu}. \tag{2.40}$$

Further defining the matrices

$$C = \begin{pmatrix} c_{11} & c_{12} & \cdots & c_{1L} \\ c_{21} & c_{22} & \cdots & c_{2L} \\ \vdots & \vdots & \ddots & \vdots \\ c_{L1} & c_{L2} & \cdots & c_{LL} \end{pmatrix} \tag{2.41}$$

and

$$\varepsilon = \begin{pmatrix} \varepsilon_1 & 0 & \cdots & 0 \\ 0 & \varepsilon_2 & \cdots & 0 \\ \vdots & \vdots & \ddots & \vdots \\ 0 & 0 & \cdots & \varepsilon_L \end{pmatrix} \tag{2.42}$$

gives a set of linear equations in matrix form

$$(H - \varepsilon S)C = 0 \tag{2.43}$$

which can be solved for C and ε by diagonalisation. This is an $\mathcal{O}(n^3)$ problem where n is the dimension of the square matrices. SIESTA offers an alternative $\mathcal{O}(n)$ solution method, but this does not work for metals [122] and hence is not utilised in this work.

Basis set size

The quality of the basis set used in electronic structure calculations is of critical importance to the accuracy of the results. In the limit of a complete basis set, the molecular orbitals $\psi_i(\vec{r})$ are free to take on any form and within the XC approximation, the minimum energy will be exact. However an infinite number of basis functions are required for completeness, and in practice a tradeoff between accuracy and efficiency is needed.

In the context of atomic orbitals, the smallest basis set used, is one function per angular momentum channel for each principle quantum number of each atom. These are named single-ζ (SZ) basis sets and the corresponding functions are the first-ζ orbitals $\phi^{1\zeta}_{Inl}$, where I is the atomic index and n and l are the principal and angular momentum quantum numbers. In SIESTA the functions $\phi^{1\zeta}_{Inl}$ correspond to the numerical eigenfunctions of an isolated pseudo-atom in a spherical box [148]. The eigenenergy of ϕ_{Inl} is raised by a small amount $\delta\varepsilon_{Inl}$ so that the first node occurs at the radius of the box. The functions are cut off at this radius r_{Inl} and thus have finite spacial extent. This localisation ensures that the matrices H and S are sparse. The sparseness of the matrices is needed to provide linear scaling of the algorithms which is central to the SIESTA methodology. The cutoff

radii r_{Inl} can be specified manually, but we use the option provided in SIESTA where a single *energyshift* parameter $\delta\varepsilon$ is specified. This provides a consistent way to define the confinement for all orbitals and is a convenient parameter for testing the convergence of results. Table 2.1 lists the cutoff radii r_{Inl} for the valence orbitals of gold, sulphur, carbon and hydrogen atoms for various choices of $\delta\varepsilon$.

		$\delta\varepsilon$		
species	orbital	5 mRy	1 mRy	0.1 mRy
Au	6s	3.84	4.46	5.44
	5d	2.70	3.30	4.03
S	3s	2.56	2.98	3.55
	3p	3.21	3.82	4.67
C	2s	2.58	3.07	3.66
	2p	3.15	3.84	4.82
H	1s	3.12	3.72	4.65

Table 2.1: Cutoff radii, r_{Inl} in Ångstrom for the valence orbitals of gold, sulphur, carbon and hydrogen atoms corresponding to various choices of the energyshift parameter in SIESTA.

Using an SZ basis set is only good for qualitative analysis and a second ζ orbital per angular momentum channel $\phi^{2\zeta}_{Inl}$ can be specified to give a double-ζ (DZ) basis set. In SIESTA this second orbital has the same tail as $\phi^{1\zeta}_{Inl}$ but takes on a polynomial form $a - br^2$ inside a "split" radius r^s_{Inl}. The values of r^s_{Inl} are similarly fixed by a single parameter, specifying the norm of $\phi^{1\zeta}_{Inl}$ for $r > r^s_{Inl}$. In this work the SIESTA suggested default value of 0.15 is used throughout.

In order to account for the polarising effect bonding has on the orbitals, so-called polarisation functions should be included in the basis. It is possible to use solutions to the pseudo-atom in a spherical box corresponding to states with higher angular momentum than the valence orbitals of the atom. However in SIESTA the polarisation functions are generated by projecting out the higher angular momentum component of the solution when the pseudo-atom is placed in an electric field. Basis sets that include polarisation orbitals for each n are SZP, DZP, SZDP (for doubly polarised), DZDP etc.

Basis set superposition error

There is a complication that arises due to the use of atomic basis functions when calculating interaction energies as energy differences between reactants and products. Since the energy differences are calculated from systems with different stoichiometry, the number of basis functions available is not the same. The product system, with additional basis functions, provides greater variational freedom for the one–electron wavefunctions. This lowers the DFT total energy of the product and leads to an overestimation of the interaction energy, and is known as the basis set superposition error (BSSE). The counterpoise correction due to Boys and Bernardi [149] is used in this work. Accordingly, the calculations of the total energy of the reactant systems is done with the addition of "ghost atoms" replacing the atoms that would be present in the product. The basis functions of these ghost atoms are used in the calculation, but for all other purposes the atoms are not present. This places the wavefunctions of the reactant and product systems on the same variational footing.

2.2.2 Spin polarisation and Fermi smearing

By introducing the basis set $\phi_\mu(\vec{r}), 1 \leq \mu \leq L$ with L basis functions, and solving the matrix equation (2.43), the result is L molecular orbitals $\psi_i(\vec{r}), 1 \leq i \leq L$ and their corresponding eigenvalues ε_i. Since there are only N electrons, the lowest possible eigenstates will be occupied, i.e. $\psi_i(\vec{r}), 1 \leq i \leq N$ where the states have been arranged with increasing eigenvalue ε_i. The electron density is then given by (2.21).

As mentioned in section 2.1.4, if the system is expected to be spin-polarised (i.e. $\rho^\alpha \neq \rho^\beta$), the XC potential is parametrised as a functional of ρ^α and ρ^β. Separate sets of orbitals are then required for α and β spin electrons, $\psi_i^\alpha(\vec{r})$ and

$\psi_i^\beta(\vec{r})$. The total electron density is the sum of the two spin-densities

$$\begin{aligned} \rho^\alpha(\vec{r}) &= \sum_{i=1}^{N_\alpha} |\psi_i^\alpha(\vec{r})|^2 \\ \rho^\beta(\vec{r}) &= \sum_{i=1}^{N_\beta} |\psi^\beta(\vec{r})|^2 \\ \rho(\vec{r}) &= \rho^\alpha(\vec{r}) + \rho^\beta(\vec{r}) \end{aligned} \tag{2.44}$$

and the eigenvalues corresponding to the spin α and spin β orbitals are in general different. The α- and β-spin basis functions are also independent, $\phi_\mu^\alpha(\vec{r})$ and $\phi_\mu^\beta(\vec{r})$.

To aid convergence of the self-consistent cycle, a finite electronic temperature is usually introduced. This plays the role of a physical temperature in smearing the occupation of eigenstates according to the Fermi function. The electron density is then given by

$$\rho(\vec{r}) = \sum_{i=1}^{L} n_i^\alpha |\psi_i^\alpha(\vec{r})|^2 + \sum_{i=1}^{L} n_i^\beta |\psi_i^\beta(\vec{r})|^2$$

according to the orbital occupation numbers

$$n_i^s = f(\varepsilon_i^s - E_F) = \frac{1}{e^{(\varepsilon_i^s - E_F)/kT} + 1} \tag{2.45}$$

and the spin polarisation is defined as

$$\begin{aligned} \gamma &= N^\alpha - N^\beta \\ &= \sum_{i=1}^{L} n_i^\alpha - \sum_{i=1}^{L} n_i^\beta. \end{aligned} \tag{2.46}$$

The Fermi level E_F is found by enforcing the normalisation of the electron density (2.10). In a spin unpolarised system with an odd number of electrons, the spin α and spin β eigenvalues will match up, and hence the value of E_F will imply partial occupation of orbitals ψ_i^α and ψ_i^β with eigenvalues $\varepsilon_i^\alpha = \varepsilon_i^\beta \sim E_F$, such that the number of electrons in each spin state is half-integer.

The theoretical justification for finite temperature DFT was given in 1965 by Mermin [150] in which he proved that the Hohenberg-Kohn theorems hold also for $T \neq 0$.

2.2.3 Pseudopotential

The pseudopotential approximation makes use of the fact that the core electrons of an atom play essentially no part in chemical bonding. The core electronic structure of a free atom is therefore assumed to remain unchanged in any environment. Accordingly, the potentials due to the nuclei, $v_I(\vec{r}) = -\frac{Z_I}{|\vec{r}-\vec{R}_I|}$, are replaced by pseudopotentials corresponding to the electrostatic potential of the nuclei together with their core electrons. The electronic structure problem then has to be solved only for the valence electrons. The reduced number of electrons in the system greatly lightens the computational load. For calculations with plane-wave basis sets, the number of basis (plane-wave) functions needed is also reduced, because the rapidly oscillating valence wave functions near the atomic cores are replaced with pseudo-wavefunctions with no nodes. When using pseudopotentials, it is important that they have good *transferability*, i.e. the approximation based on a free atom remains good when the atom is placed in a different chemical environment.

A pseudopotential has to be generated for each atomic species in the calculation. The first step is solving the "all-electron" Schrödinger equation for the ion together with all its core and valence electrons. This is done within the Kohn-Sham approach, using an appropriate XC functional. For consistency the same functional should be used as in the calculation of the entire system. Assuming a spherically symmetric atom, the Kohn-Sham equations (2.31) are solved in radial form

$$\left(-\frac{1}{2}\frac{\mathrm{d}}{\mathrm{d}r^2} + \frac{l(l+1)}{2r^2} + V(r)\right) u_{nl} = \varepsilon u_{nl} \tag{2.47}$$

with the potential $V(r) = V_{\mathrm{XC}}(r) + V_H(r) - \frac{Z}{r}$. For heavy atoms, it is advisable that the Hamiltonian include scalar-relativistic terms for the kinetic energy [151], which account for the relativistic motion of the core electrons (but does not

include spin-orbit coupling),

$$\left[\frac{1}{2m_e(r)}\left(-\frac{\mathrm{d}^2}{\mathrm{d}r^2}-\frac{1}{2m_e(r)c^2}\frac{\mathrm{d}V(r)}{\mathrm{d}r}r\frac{\mathrm{d}}{\mathrm{d}r}\frac{1}{r}+\frac{l(l+1)}{r^2}\right)+V(r)\right]u_{nl}=\varepsilon u_{nl} \quad (2.48)$$

where the relativistic electron mass is $m_e(r) = 1 + \frac{\varepsilon - V(r)}{2c^2}$. A self-consistent solution to this all-electron problem is obtained after specifying the occupancies of the atomic energy levels, $0 \leq f_{nl} \leq 2(2l+1)$. Due to spherical symmetry, the energy levels with different m are degenerate. In most cases the atomic ground state is chosen, but sometimes it is desirable to generate a pseudopotential corresponding to an atomic excited state.

The next step is to construct the valence pseudo-wavefunctions from the resulting valence all-electron wavefunctions. For transition metals care should be taken as to which orbitals are considered valence. Including more electrons in the valence will drastically increase computational cost, but not necessarily improve results. For each angular momentum component l a valence pseudo-wavefunction u_l^{ps} is constructed from a reference all-electron wavefunction u_{nl}^{ae} where n is such that u_{nl}^{ae} is either a valence or virtual orbital.

The pseudo-wavefunctions are constructed to be nodeless and match the respective all-electron wavefunctions beyond a core cutoff radius, $u_l^{\mathrm{ps}}(r) = u_{nl}^{\mathrm{ae}}(r)$ for $r > r_l^c$, and have the same eigenvalues, $\varepsilon_l^{\mathrm{ps}} = \varepsilon_{nl}^{\mathrm{ae}}$. Norm-conserving peudopotentials where $\int_0^\infty |u_l^{\mathrm{ps}}(r)|^2 \mathrm{d}r = \int_0^\infty |u_{nl}^{\mathrm{ae}}(r)|^2 \mathrm{d}r = 1$ were shown to have good scattering properties [152], an essential feature for good transferability. This was therefore the standard until Vanderbilt introduced so-called ultrasoft pseudopotentials [153]. These obey a modified norm-conservation condition which preserves the scattering properties and are smoother for $r < r_l^c$. The increased smoothness means that fewer plane-waves are needed to represent the wavefunctions when planewave basis sets are used. This is not relevant in SIESTA and norm-conserving pseudopotentials are used.

The screened angular momentum dependent pseudopotential $V_l^{\mathrm{ps,scr}}(r)$ is constructed by inverting the non-relativistic radial Schrödinger equation (2.47) with the corresponding pseudo wavefunction u_l^{ps}. Each pseudopotential component is now unscreened by subtracting the Hartree and XC potential due to the valence

charge density. The latter is obtained from the valence pseudo-wavefunctions, assuming the same occupancy as specified for the all-electron calculation. This results in the ionic pseudopotential (the quantity needed to replace the ion plus core electrons) in semi-local form, i.e. a different pseudopotential for each angular momentum component,

$$V_l^{\rm ps}(r) = V_l^{\rm ps,scr}(r) - V_{\rm H}[\rho^{\rm ps}(r)] - V_{\rm XC}[\rho^{\rm ps}(r)] \quad (2.49)$$

$$\rho^{\rm ps}(r) = \sum_{l=0}^{l_{\rm max}} f_l |u_l^{\rm ps}(r)|^2. \quad (2.50)$$

The electronic energy of the entire system (2.23) can now be rewritten

$$E_v[\rho] = \sum_{i=1}^{L} n_i \langle\psi_i| -\frac{1}{2}\nabla^2 |\psi_i\rangle + E_{\rm H}[\rho] + E_{\rm XC}[\rho] + \sum_{i=1}^{L} n_i \langle\psi_i|\hat{V}^{\rm ps}|\psi_i\rangle \quad (2.51)$$

where ρ refers to the charge density of the valence electrons included in the self-consistent calculation. The pseudopotential operator $\hat{V}^{\rm ps}(r) = \sum_l \hat{V}_l^{\rm ps}(r)$ needs to project out the l-component of the wavefunction. The Hartree and XC energies of the interaction between the valence and core charge densities is included in the pseudopotential energy term which depends linearly on the valence charge density ρ. This is valid for the Hartree energy, but the XC energy is not a linear functional of charge density. In most cases this does not lead to substantial errors, but becomes important for calculations on alkali metals [154] and spin-polarised systems [155, 156]. Louie *et al.* [155] suggested a partial core correction to the pseudopotential. In stead of subtracting the XC potential of only the valence electrons from the screened pseudopotential, the XC potential of the valence density plus a partial core density $\tilde{\rho}$ is subtracted. The corresponding partial core density $\tilde{\rho}$ is then added to the density used to evaluate the $E_{\rm XC}$ contribution to the total energy. $\tilde{\rho}$ is defined by specifying a cutoff radius $r^{\rm nlc}$. For $r > r^{\rm nlc}$, $\tilde{\rho} = \rho^{\rm core}$ and for $r < r^{\rm nlc}$, $\tilde{\rho}$ is given by a polynomial function in r. Equations

(2.49) and (2.51) thus become

$$\begin{aligned} V_l^{\rm ps}(r) &= V_l^{\rm ps,scr}(r) - V_{\rm H}[\rho^{\rm ps}(r)] - V_{\rm XC}[\rho^{\rm ps}(r) + \tilde{\rho}] \\ E_v[\rho] &= \sum_{i=1}^{L} n_i \langle\psi_i| - \frac{1}{2}\nabla^2|\psi_i\rangle + E_{\rm H}[\rho] + E_{\rm XC}[\rho + \tilde{\rho}] + \sum_{i=1}^{L} n_i \langle\psi_i|\hat{V}^{\rm ps}|\psi_i\rangle \end{aligned} \tag{2.52}$$

In this work norm-conserving pseudopotentials constructed according to the scheme of Troullier and Martins [157] are generated with the ATOM package. This package is independent of SIESTA but is distributed freely with the latter. It generates pseudopotentials in semi-local form, compatible with the required input for SIESTA. An arbitrary local pseudopotential $V_{\rm local}^{\rm ps}$ is chosen so that $V_l^{\rm ps}(r) = V_{\rm local}^{\rm ps}(r) + \delta V_l^{\rm ps}(r)$ in order to keep the angular momentum dependent parts short-range, $\delta V_l^{\rm ps}(r) = 0$ for $r > r_l^c$. They are then transformed into the nonlocal Kleinman-Bylander (KB) form [158], where the pseudopotential operator is written as

$$\begin{aligned} \hat{V}^{\rm ps} &= V_{\rm local}(r) + \hat{V}^{\rm KB} \\ \hat{V}^{\rm KB} &= \sum_{l=1}^{l_{\rm max}} \sum_{m=-l}^{l} |\chi_{lm}\rangle E_l \langle\chi_{lm}|. \end{aligned} \tag{2.53}$$

The KB projector functions χ_{lm} and energies E_l are constructed from the pseudo-wavefunctions $u_l^{\rm ps}$ and semi-local pseudopotentials $\delta V_l(r)$ according to a scheme proposed by Blöchl [159]. This representation preserves the pseudo wavefunctions and energies. However spurious "ghost" states with lower energies may be introduced by the transformation. Such states are unphysical and jeopardise the transferability of the pseudopotential. SIESTA chooses the local component of the peudopotential $V_{\rm local}$ in such a way as to avoid these ghost states. Nonetheless the presence of ghost states is still possible. This can be detected and if present, the semi-local form of the pseudopotential has to be regenerated.

The above treatment largely follows that of Ref. [154] which gives a good overview of pseudopotential generation and transferability issues.

2.2.4 Integrations and grid point sampling

The overlap matrix elements (2.39) and the kinetic energy and KB parts of the Hamilonian matrix elements (2.38) are calculated as two-centre integrals, i.e. they depend only on the relative positions of the two atoms on which the known basis functions ϕ_μ and ϕ_ν are centred. These integrals can be calculated once for each pair of basis functions, and tabulated as a function of the distance between the two atoms, up to a maximum distance given by the sum of the spacial cutoffs r_{Inl} of the two orbitals.

The Hartree, XC and local pseudopotential contributions to the Hamiltonian matrix elements as well as the electron density are evaluated on a real-space grid in the unit cell. The fineness of this grid is defined by an energy parameter E_{cut}, which specifies the maximum kinetic energy of a plane-wave that could be represented on the grid without aliasing [122].

2.2.5 Periodic boundary conditions and k-point sampling

In order to calculate the properties of infinite systems such as bulk crystals or surfaces, a unit cell is defined and periodic boundary conditions imposed. This introduces the complication of dispersion and all appropriate quantities need to be sampled in k-space. In SIESTA k-point sampling is performed at a set of $\vec{k}$ vectors chosen according to the scheme of Monkhorst and Pack [160].

In order to expand the k-dependent wavefunctions, the basis set ϕ_μ must be redefined to include this k-dependence. One can define the new basis functions $\widetilde{\phi}_\mu(\vec{k},\vec{r})$ as the sum over all the periodic translations of the unit cell basis functions $\phi_\mu(\vec{r})$ with the k-dependence introduced through a phase factor

$$\widetilde{\phi}_\mu(\vec{k},\vec{r}) \equiv \sum_{\mu' \equiv \mu} e^{i\vec{k}\cdot\vec{R}_{\mu'}} \phi_{\mu'}(\vec{r}) \tag{2.54}$$

where $\mu' \equiv \mu$ indicates all the equivalent periodic translations of the basis function labeled μ and $\vec{R}_{\mu'}$ is the position of the atom on which $\phi_{\mu'}$ is centred. These k-dependent basis functions are by construction periodic and hence so are the

wavefunctions

$$\psi_i(\vec{k},\vec{r}) = \sum_{\mu=1}^{L} c_{\mu i}(\vec{k})\widetilde{\phi}_\mu(\vec{k},\vec{r}). \tag{2.55}$$

The Hamiltonian matrix elements are

$$\begin{aligned} H_{\mu\nu}(\vec{k}) &= \langle\widetilde{\phi}_\mu(\vec{k},\vec{r})|\hat{f}^{\mathrm{KS}}|\widetilde{\phi}_\nu(\vec{k},\vec{r})\rangle \\ &= \sum_{\mu'\equiv\mu}\sum_{\nu'\equiv\nu}\langle e^{i\vec{k}\cdot\vec{R}_{\mu'}}\phi_{\mu'}(\vec{r})|\hat{f}^{\mathrm{KS}}|e^{i\vec{k}\cdot\vec{R}_{\nu'}}\phi_{\nu'}(\vec{r})\rangle \\ &= \sum_{\mu'\equiv\mu}\sum_{\nu'\equiv\nu} e^{i\vec{k}\cdot(\vec{R}_{\nu'}-\vec{R}'_{\mu})}\langle\phi_{\mu'}(\vec{r})|\hat{f}^{\mathrm{KS}}|\phi_{\nu'}(\vec{r})\rangle \end{aligned} \tag{2.56}$$

and similarly for the overlap matrix elements $S_{\mu\nu}(\vec{k})$. Since the Hamiltonian is required only within the unit cell, the integrals on the right that correspond to two-centre integrals are only calculated for pairs where at least one orbital is centred inside the unit cell, and for integrals that are calculated on the real-space grid only contributions for positions $\vec{r}$ within the unit cell are summed. In SIESTA a supercell is defined which includes the unit cell and all basis functions that contribute to $H_{\mu\nu}$. The electron density becomes

$$\rho(\vec{r}) = \sum_{i=1}^{L}\int_{\mathrm{BZ}} n_i(\vec{k})|\psi_i(\vec{k},\vec{r})|^2\mathrm{d}\vec{k} \tag{2.57}$$

where the integral is over the first Brillouin zone.

2.2.6 Quantities of interest

In this section we describe the physical quantities which are calculated from the self-consistent electronic structure obtained with SIESTA, as required in the current work. This is by no means an exhaustive list of properties that can be calculated. The electric current and conductance requires solution of the system in non-equilibrium which lies beyond the capabilities of SIESTA. These calculations are discussed in section 2.4. The calculation of the atomic forces in SIESTA required for geometric structure optimisation is discussed in section 2.3.

Density matrix and electron density

The quantity used to track all the information about the electronic structure and determine when self-consistency is reached, is the density matrix defined as

$$D_{\mu\nu} = \sum_i \int_{\mathrm{BZ}} n_i(\vec{k}) c_{\mu i} c_{\nu i} e^{i\vec{k}\cdot(\vec{R}_\nu - \vec{R}_\mu)} \mathrm{d}\vec{k}. \tag{2.58}$$

Accordingly the electron density can be written as

$$\rho(\vec{r}) = \sum_\mu \sum_\nu D_{\mu\nu} \phi_\mu(\vec{r}) \phi_\nu(\vec{r}) \tag{2.59}$$

where the summations run over all μ, ν with $\vec{R}_\mu$ and $\vec{R}_\nu$ in the supercell. In SIESTA the self-consistent cycle is terminated when the maximum change in any element of the density matrix is below a given tolerance, typically 10^{-4}.

Total and free energy

For geometry optimisations (i.e. finding the optimum ionic coordinates of the system, discussed in section 2.3), the quantity that is minimised is the total energy E_{tot}, given by the electronic energy, equation (2.51), plus the internuclear repulsion energy, equation (2.7). In practice the major part of the electronic energy can conveniently be calculated as the sum of the eigenvalues of the occupied states, called the band structure energy

$$\begin{aligned} E_{\mathrm{BS}} &= \sum_{i=1}^{L} \int_{\mathrm{BZ}} n_i(\vec{k}) \langle \psi_i | \hat{f}^{\mathrm{KS}} | \psi_i \rangle \\ &= \sum_{i=1}^{L} \int_{\mathrm{BZ}} n_i(\vec{k}) \langle \sum_{\mu=1}^{L} c_{\mu i}(\vec{k}) \widetilde{\phi}(\vec{k}, \vec{r}) | \hat{f}^{\mathrm{KS}} | c_{\nu i}(\vec{k}) \widetilde{\phi}_\nu(\vec{k}, \vec{r}) \rangle \mathrm{d}\vec{k} \\ &= \sum_{i=1}^{L} \int_{\mathrm{BZ}} n_i(\vec{k}) \sum_{\mu=1}^{L} \sum_{\nu=1}^{L} c^*_{\mu i}(\vec{k}) c_{\nu i}(\vec{k}) H_{\mu\nu}(\vec{k}) \mathrm{d}\vec{k} \end{aligned} \tag{2.60}$$

which at the Γ-point reduces to $\sum_\mu \sum_\nu D_{\nu\mu} H_{\mu\nu} = \mathrm{Tr}(HD)$. However the Hartree and XC contributions to the total energy differ from the corresponding contribu-

tions to the band structure energy:

$$\begin{aligned}\sum_{i=1}^{L}\int_{\mathrm{BS}} n_i\langle\psi_i|\hat{V}_H|\psi_i\rangle \mathrm{d}\vec{k} &= \sum_{i=1}^{L}\int_{\mathrm{BZ}} n_i \int \psi_i^* \int \frac{\rho(\vec{r}')}{|\vec{r}-\vec{r}'|}\mathrm{d}\vec{r}'\psi_i \mathrm{d}\vec{r}\mathrm{d}\vec{k} \\ &= \sum_{i=1}^{L}\int_{\mathrm{BZ}} \iint \frac{\rho(\vec{r})\rho(\vec{r}')}{|\vec{r}-\vec{r}'|}\mathrm{d}\vec{r}\mathrm{d}\vec{r}'\mathrm{d}\vec{k} \\ &= 2E_{\mathrm{H}} \end{aligned} \tag{2.61}$$

and

$$\begin{aligned}\sum_{i=1}^{L}\int_{\mathrm{BZ}} n_i\langle\psi_i|\hat{V}_{\mathrm{XC}}|\psi_i\rangle \mathrm{d}\vec{k} &= \sum_{i=1}^{L}\int_{\mathrm{BZ}} n_i \int \psi_i^* V_{\mathrm{XC}}(\vec{r})\psi_i \mathrm{d}\vec{r}\mathrm{d}\vec{k} \\ &= \int \rho(\vec{r}) V_{\mathrm{XC}}(\vec{r})\mathrm{d}\vec{r} \\ &= E_{\mathrm{XC}} - \int \rho(\vec{r})\left(\varepsilon_{\mathrm{XC}} - V_{\mathrm{XC}}\right)\mathrm{d}\vec{r}. \end{aligned} \tag{2.62}$$

With these correction terms the total energy can be calculated as

$$E_{\mathrm{tot}} = E_{\mathrm{BS}} - E_{\mathrm{H}} + \int \rho(\vec{r})\left(\varepsilon_{\mathrm{XC}}(\vec{r}) - V_{\mathrm{XC}}(\vec{r})\right)\mathrm{d}\vec{r} + E_{\mathrm{nuc}}. \tag{2.63}$$

When a finite temperature T is applied the free energy should be minimised and this is related to the internal energy E_{tot} by [122]

$$F = E_{\mathrm{tot}} - E_{\mathrm{F}}\sum_{i=1}^{L}\int_{\mathrm{BZ}} n_i \mathrm{d}\vec{k} - kT\sum_{i=1}^{L}\int_{\mathrm{BZ}}\left(n_i \ln n_i + (1-n_i)\ln(1-n_i)\right)\mathrm{d}\vec{k}. \tag{2.64}$$

When the finite temperature is introduced merely as a convenience to enable partial occupation of states, the total energy in the athermal limit can be approximated by [161]

$$E_{\mathrm{tot}}(T=0) = \frac{1}{2}\big[E_{\mathrm{tot}}(T) + F(T)\big]. \tag{2.65}$$

Mulliken population analysis

Within the LCAO ansatz, it is intuitively pleasing to interpret the overall electron density as the sum of the electron population of the individual basis functions. There are different ways of doing this; in SIESTA the populations are calculated following the scheme of Mulliken [162]. A population matrix is defined in terms of the density and overlap matrices as $P_{\mu\nu} = D_{\mu\nu}S_{\mu\nu}$. Importantly the elements of the population matrix sum to the number of electrons in the system

$$\begin{aligned}\sum_{\mu=1}^{L}\sum_{\nu=1}^{L} P_{\mu\nu} &= \sum_{i=1}^{L}\int_{\mathrm{BZ}} n_i \sum_{\mu=1}^{L}\sum_{\nu=1}^{L} c^*_{\mu i}c_{\nu i}e^{i\vec{k}\cdot(\vec{R}_\nu-\vec{R}_\mu)}\int \phi_\mu(\vec{r})\phi_\nu(\vec{r})\mathrm{d}\vec{r}\mathrm{d}\vec{k} \\ &= \sum_{i=1}^{L}\int_{\mathrm{BZ}} n_i \int \psi^*_i(\vec{r})\psi_i(\vec{r})\mathrm{d}\vec{r}\mathrm{d}\vec{k} \\ &= N \end{aligned} \tag{2.66}$$

Four levels of Mulliken population are defined. The matrix elements $P_{\mu\nu}$ give the overlap population between basis orbitals ϕ_μ and ϕ_ν. The sum of a row (or column) $P_\mu = \sum_\nu P_{\mu\nu}$ defines the population of a basis orbital ϕ_μ. The atomic population M_I is determined by summing the P_μ for all basis functions ϕ_μ centred on the atom I. The mulliken charge on the atom is then defined as the excess charge over the electronic charge on the neutral atom, $C_I = M_I - Z_I$. Finally the overlap population between two atoms I and J is given by $M_{IJ} = \sum_{\substack{\nu\in I\\ \mu\in J}} P_{\mu\nu}$. Unfortunately this analysis is dependent on the basis set used, but gives a valuable intuitive view of the electronic structure.

Density of states

The total density of electronic states (DOS) is calculated in terms of the eigenvalues and in practice the delta function is replaced by a Gaussian broadening of

width typically $\sigma \sim 0.1$ eV:

$$\begin{aligned} D(E) &= \sum_{i=1}^{L} \int_{\mathrm{BZ}} \delta\left(E - \varepsilon_i(\vec{k})\right) \mathrm{d}\vec{k} \\ &\approx \sum_{i=1}^{L} \int_{\mathrm{BZ}} \frac{1}{\sigma\sqrt{\pi}} \exp\left[\frac{(E - \varepsilon_i(\vec{k}))^2}{\sigma^2}\right] \mathrm{d}\vec{k}. \end{aligned} \tag{2.67}$$

The projected density of states (PDOS) onto a basis orbital ϕ_μ is calculated as

$$D_\mu(E) = \sum_{i=1}^{L} \int_{\mathrm{BZ}} \delta\left(E - \varepsilon_i(\vec{k})\right) |c_{\mu i}(\vec{k})|^2 \mathrm{d}\vec{k}. \tag{2.68}$$

Projecting onto combinations of orbitals, e.g. onto an atom, is additive; in particular projecting onto *all* the orbitals recovers (2.67) by virtue of the normalisation of the expansion coefficients. Finally the local density of states (LDOS) at a particular point in space is given by

$$D(E, \vec{r}) = \sum_{i=1}^{L} \int_{\mathrm{BZ}} \delta\left(E - \varepsilon_i(\vec{k})\right) |\psi_i(\vec{k}, \vec{r})|^2 \mathrm{d}\vec{k} \tag{2.69}$$

which when integrated over space again recovers (2.67) due to the normalisation of the wavefunctions. In order to evaluate (2.67)-(2.69), the integration is replaced by a sum over the sampled k-points and the Gaussian broadening is applied in each case.

2.3 Geometric structure optimisation

Thus far a prescription has been given for solving the electronic structure and total energy after an electronic Hamiltonian is defined through the set of pseudopotentials corresponding to the nuclear coordinates. These coordinates have been considered stationary by virtue of the Born-Oppenheimer approximation. The task of geometry optimisation is then to minimise the total energy $E_{\mathrm{tot}}(\vec{R}_1, \ldots, \vec{R}_M)$ given by equation (2.63) with respect to the nuclear coordinates. At each step in the minimisation, the DFT self-consistent electronic structure is found as de-

scribed in sections 2.1 and 2.2 and used to evaluate E_{tot}.

The minimisation is performed in a series of steps i with variables $\vec{x}_i$, starting at $i = 0$ and terminating when some convergence criteria are reached. In SIESTA, as in most cases, this will be in the form of a maximum force on any of the nuclear coordinates.

The most efficient algorithms require knowledge of the function values $f(\vec{x})$ as well as the gradient values $\vec{g}_i = -\nabla f(\vec{x})$. In the context of relaxing the nuclear geometry, these are the forces on the nuclei,

$$\vec{F}_n = -\frac{\partial E}{\partial \vec{R}_n} \tag{2.70}$$

and can be calculated by differentiating equation (2.63) with respect to the nuclear coordinates. When a finite temperature is applied, the free energy needs to be minimised. From equation (2.64),

$$\frac{\mathrm{d}F}{\mathrm{d}\vec{R}_i} = \frac{\partial F}{\partial \vec{R}_i} + \frac{\partial F}{\partial n_i}\frac{\partial n_i}{\partial \vec{R}_i} + \frac{\partial F}{\partial \psi_i}\frac{\partial \psi_i}{\partial \vec{R}_i} = \frac{\partial F}{\partial \vec{R}_i} = \frac{\partial E_{\mathrm{tot}}}{\partial \vec{R}_i} \tag{2.71}$$

where the "total" derivative indicates that the effect of changes in position on n_i and ψ_i need to be taken into account. However, $\frac{\partial F}{\partial \psi_i} = \frac{\partial E_{\mathrm{tot}}}{\partial \psi_i} = 0$, since the total energy is minimised with respect to the choice of the wavefunction by virtue of the DFT formalism. Also, $\frac{\partial F}{\partial n_i} = 0$, since the free energy is chosen as minimised with respect to the occupation numbers. Thus the introduction of a finite temperature does not complicate the force calculation. The forces can be derived analytically from the expressions for the different energy contributions, and in SIESTA are generally calculated in the same portion of code [122].

Amongst the most widely used minimisation algorithms are molecular dynamics (MD), conjugate gradients (CG) and the Broyden-Fletcher-Goldfarb-Shanno (BFGS) algorithm. In MD the minimisation is achieved by moving the variables $\vec{x}_i$ according to the equations of motion given by the forces (gradients) in each iteration. Ref. [163] contains a complete outline of the MD and CG techniques. The CG and BFGS algorithms are used in this work and therefore discussed in more detail.

2.3.1 Conjugate gradients minimisation

In this method each iteration consists of selecting a direction of descent $\vec{h}_i$, finding the distance λ_i that minimises the function *along that direction* and then setting the new point accordingly, $\vec{x}_{i+1} = \vec{x}_i + \lambda_i \vec{h}_i$. This step is known as line minimisation and is essentially the problem of finding the minimum of a one-dimensional function. This can be done in various ways, for example the algorithm due to Brent which can be modified to make use of derivative information [164]. It is tempting to decide that the direction of steepest descent, $\vec{g}_i = -\nabla f(\vec{x}_i)$, is the best choice for $\vec{h}_i$ at each iteration. However the gradient at the current position is always perpendicular to the previous direction $\vec{h}_{i-1}$, by virtue of the line minimisation along that direction. Therefore in the steepest descent method, successive directions are forced to be perpendicular, which is not necessarily the most efficient option [164].

The CG algorithm ensures in stead that successive directions are *conjugate* to each other and to all previous minimisation directions. This means that the gradient at each point $\vec{x}_i$ remains perpendicular to all previous minimisation directions. In addition the set of successive directions are linearly independent. The function $f(\vec{x})$ is assumed to have an approximately quadratic form and written as the second order Taylor expansion about the origin

$$f(\vec{x}) \approx f(0) + \nabla f(0)\vec{x} + \frac{1}{2}\vec{x} \cdot A\vec{x} \tag{2.72}$$

where A is the matrix of partial second derivatives known as the Hessian matrix $A_{mn} = \frac{\partial^2 f}{\partial x_m \partial x_n}\Big|_{\vec{x}=0}$. It follows that

$$\begin{aligned} \nabla f(\vec{x}) &= \nabla f(0) + \frac{1}{2}A\vec{x} + \frac{1}{2}A^{\mathrm{T}}\vec{x} \\ &= \nabla f(0) + A\vec{x} \end{aligned} \tag{2.73}$$

since A is symmetric.

If equation (2.72) is exact the minimum will be found in at most $3M$ line minimisations, since $\nabla f(\vec{x}_{3M})$ has to be perpendicular to $3M$ linearly independent directions in the coordinate space and therefore $\nabla f(\vec{x}_{3M}) = 0$. When $f(\vec{x})$

is not quadratic, more iterations may be necessary, but the algorithm is said to be quadratically convergent.

In order to generate a sequence of directions $\vec{h}_i$ that satisfy the conjugacy and linear independence conditions, a recurrence relation for $\vec{h}_i$ is constructed. First note that (2.73) already implies a recurrence relation for the gradients

$$\begin{aligned} \vec{g}_{i+1} &= \vec{g}_i - A(\vec{x}_{i+1} - \vec{x}_i) \\ &= \vec{g}_i - \lambda_i A\vec{h}_i. \end{aligned} \tag{2.74}$$

Since $\vec{h}_i$ is perpendicular to $\vec{g}_{i+1}$,

$$\begin{aligned} 0 &= \vec{h}_i \cdot \vec{g}_{i+1} = \vec{h}_i \cdot \vec{g}_i - \lambda_i \vec{h}_i \cdot A\vec{h}_i \\ \Rightarrow \lambda_i &= \frac{\vec{h}_i \cdot \vec{g}_i}{\vec{h}_i \cdot A\vec{h}_i} \end{aligned} \tag{2.75}$$

A natural guess for $\vec{h}_{i+1}$ would be a linear combination of the current gradient and previous direction

$$\vec{h}_{i+1} = \vec{g}_{i+1} + \gamma_i \vec{h}_i. \tag{2.76}$$

Starting the sequence with $\vec{h}_0 = \vec{g}_0$ and setting $\gamma_i = \frac{|\vec{g}_{i+1}|^2}{|\vec{g}_i|^2}$ results in the desired properties. It can be shown inductively [165] that the gradients are mutually orthogonal

$$\vec{g}_i \cdot \vec{g}_j = 0 \quad \text{for all } i \neq j \tag{2.77}$$

and that the conjugacy condition holds

$$\vec{h}_i \cdot \vec{g}_j = 0 \quad \text{for all } i < j \ . \tag{2.78}$$

The conjugacy together with equation (2.76) ensures that the directions $\vec{h}_i$ are linearly independent, for suppose we can write

$$\vec{h}_i = \sum_{j=0}^{i-1} \alpha_j \vec{h}_j, \tag{2.79}$$

then

$$0 = \vec{g}_i \cdot \sum_{j=0}^{i-1} \alpha_j \vec{h}_j = \vec{g}_i \cdot \vec{h}_i = \vec{g}_i \cdot \vec{g}_i + \gamma_{i-1} \vec{g}_i \cdot \vec{h}_{i-1} = |\vec{g}_i|^2, \tag{2.80}$$

and we have already reached a minimum.

2.3.2 BFGS minimisation

In the BFGS algorithm, the second order Taylor expansion is centred in stead at the current point $\vec{x}_i$ and Newton's method used to find a solution for $\nabla f(\vec{x}) = 0$ in equation (2.73). Thus the solution of

$$\vec{x} - \vec{x}_i = -A^{-1} \nabla f(\vec{x}_i) \tag{2.81}$$

is used as the next point $\vec{x}_{i+1}$. The problem is that one generally does not know the inverse Hessian matrix A^{-1} and BFGS is therefore known as a quasi-Newton method. The crux of the BFGS algorithm is that a series of approximations $H_i \approx A^{-1}$ are generated by an *updating formula*

$$H_{i+1} = H_i + \widetilde{H}\left(\vec{x}_i, \vec{x}_{i+1}, \nabla f(\vec{x}_i), \nabla f(\vec{x}_{i+1}), H_i\right). \tag{2.82}$$

Moreover, it has been shown that with the BFGS updating formula $\widetilde{H}$ the approximations converge to the true inverse Hessian within $3M$ steps if $f(\vec{x})$ is quadratic [164]. In practice a reasonable point on the line $\vec{x} - \vec{x}_i$ is chosen. This does not have to be the point $\vec{x}$ that satisfies (2.81) nor is it necessary to perform a line minimisation.

2.3.3 Z-matrix coordinates

The above minimisation algorithms can be used for any set of coordinates which define the total energy of the system. Cartesian coordinates can be a natural choice, since they are used to carry out the electronic structure calculation and find the internuclear energy term. However, when describing molecular geometries, it is often more intuitive to use internal coordinates, such as the Z-matrix system. In Z-matrix coordinates successive atoms are described in terms of any

three preceding atoms by a bond length, an angle and a dihedral (torsion) angle.

Let $E(\vec{R})$ and $E(\vec{Z})$ denote the total energy as a function of Cartesian and Z-matrix coordinates respectively. The total energy will be calculated as usual from the Cartesian geometry $\vec{R}$. In order to minimise the energy in the Z-matrix coordinate space, we require the corresponding gradient vector (the forces on the Z-matrix coordinates),

$$\nabla E(\vec{Z}) = M \nabla E(\vec{R}) \tag{2.83}$$

where $M_{mn} = \frac{\partial R_n}{\partial Z_m}$ is the matrix of partial derivatives, describing the infinitesimal changes in Cartesian coordinates resulting from changes in the Z-matrix coordinates. These derivatives can be evaluated by the method of finite differences.

2.4 Non-equilibrium Green's function formalism

Section 2.1 established the DFT for determining the electronic structure of systems in equilibrium and in section 2.2 the computational implementation of such a scheme was discussed. In this work, we require not only the equilibrium electronic and geometric structure, but also the electronic transport across a junction. Such a junction is assumed to consist of two semi-infinite electrodes to the left and right of a device region. A bias is applied between the left and right electrodes such that the voltage drop occurs entirely within the device region. Only transport in the longitudinal (z-) direction is considered.

There are two significant differences between this system and that treated in the preceding sections. Firstly, the system is no longer closed as the electrodes are infinite and aperiodic. Secondly, the application of a bias between the electrodes drives the system out of equilibrium. The first problem can be overcome by defining the device region to include sufficient electrode layers on the left and right so that the remaining electrode parts can be treated as bulk. The properties of these infinite periodic bulk electrodes are then calculated separately from those of the finite device region. The second issue is central to the problem we aim to solve, i.e. calculating the current flow through the device for a given bias. Electrons are injected into the system from an external source and extracted by an external drain in order to keep the electrodes at distinct chemical potentials,

μ_1 and μ_2. The electrodes are assumed to be at equilibrium with these chemical potentials, but the flow of current drives the device part of the system out of equilibrium. The effect of the external source and drain is added by including a source term in the usual Schrödinger equation describing the electrodes. The result is a modification of the device Hamiltonian which, together with the source term, accounts for the non-equilibrium nature of the device.

The non-equilibrium Green's function (NEGF) formalism is used as a tool to employ these techniques. Other approaches such as the transmission formalism of Büttiker [166] can be taken. The NEGF technique appears to be the most widely implemented, since together with the current through the device, the density matrix can be readily evaluated. Another advantage is that the NEGF formalism is more generally applicable than the single-particle framework described in this work. Any theory that provides the Hamiltonian and wavefunctions of the system can be used in conjunction with the NEGF formalism. In particular, inelastic scattering amongst electrons or between electrons and phonons inside the device can be taken into account in a completely analagous manner as the treatment of the coupling to the electrodes described here.

In this work the TranSIESTA-C/ATK[b] [120] and Smeagol[c] [121,167] packages were used to calculate the electronic transport using the NEGF formalism. In both cases the electronic structure methods of DFT are employed, based on the SIESTA methodology described in section 2.2. The Kohn-Sham prescription for obtaining the Hamiltonian in terms of the electron density is used. The electrostatic potential associated with the voltage bias across the device region is incorporated into the boundary conditions when solving the Poisson equation for the Hartree potential. It is important to note [120] that the fictional single-particle wavefunctions of equation (2.21) are used as the actual wavefunctions of the system. This is a departure from the formalism of DFT and the non-equilibrium electron density obtained does not minimise the Hohenberg-Kohn functional, equation (2.14) [167].

[b]Based on an extension of SIESTA, now a commercial package. website: www.atomistix.com

[c]Acronym for Spin and Molecular Electronics Algorithm on a Generalized atomic Orbital Landscape. Academic licence package that can be integrated with SIESTA. website: www.smeagol.tcd.ie

2.4.1 Modified Schrödinger equation

As alluded to above, the Schrödinger equation for the isolated electrodes is modified by adding source terms to account for the fact that electrons can be injected into the electrodes:

$$(E - \hat{H_{1,2}})\Phi_{1,2} = S_{1,2}, \tag{2.84}$$

where the wavefunctions, Hamiltonians and source terms of the isolated electrodes are labeled with the indices 1 and 2. The Schrödinger equation of the electrode-device-electrode system can be decomposed into separate device and electrode regions,

$$\begin{pmatrix} E - H_1 & -\tau_1^\dagger & 0 \\ -\tau_1 & E - H & -\tau_2 \\ 0 & -\tau_2^\dagger & E - H_2 \end{pmatrix} \begin{pmatrix} \Phi_1 + \chi_1 \\ \Psi \\ \Phi_2 + \chi_2 \end{pmatrix} = \begin{pmatrix} S_1 \\ 0 \\ S_2 \end{pmatrix} \tag{2.85}$$

where H and Ψ are the Hamiltonian and wavefunction respectively of the device region and χ_1 and χ_2 are the excitations in the electrodes due to the coupling with the device. τ_1 and τ_2 define the coupling between the electrodes and device and can be written as $|\mu\rangle \langle\alpha|$ where μ and α are basis functions of the device and electrode respectively. The source terms in (2.85) are assumed to be the same as defined in (2.84). The equations resulting from the top and bottom rows of (2.85) become

$$\begin{aligned} (E - H_{1,2})\chi_{1,2} - \tau_{1,2}^\dagger \Psi &= 0 \\ \implies \chi_{1,2} &= g_{1,2}\tau_{1,2}^\dagger \Psi \end{aligned} \tag{2.86}$$

where (2.84) was used to eliminate $\Phi_{1,2}$ and $S_{1,2}$ and the Green's functions for the electrodes have been defined as the inverse of the operators

$$g_{1,2}(E) \equiv \lim_{\eta \to 0} (E - H_{1,2} + \eta i)^{-1}. \tag{2.87}$$

An infinitesimal imaginary number, ηi was added to the Hermitian operators $(E - H_{1,2})$, otherwise the Green's functions would not be defined at the eigenvalues of the electrode wavefunctions, $E = \varepsilon_\alpha$. The equation for the device region from

(2.85) is

$$\begin{aligned} -\tau_1(\Phi_1+\chi_1)+(E-H)\Psi-\tau_2(\Phi_2+\chi_2) &= 0 \\ \implies (E-H-\tau_1 g_1\tau_1^\dagger-\tau_2 g_2\tau_2^\dagger)\Psi &= \tau_1\Phi_1+\tau_2\Phi_2 \end{aligned}$$

or

$$(E-H-\Sigma_1-\Sigma_2)\Psi = S \tag{2.88}$$

where the "self-energy" terms of the electrodes and the source term for the device have been defined as

$$\Sigma_{1,2} \equiv \tau_{1,2} g_{1,2} \tau_{1,2}^\dagger \tag{2.89}$$

$$S = S_1 + S_2 \equiv \tau_1\Phi_1 + \tau_2\Phi_2. \tag{2.90}$$

The Green's function for the device is thus defined as

$$G(E) \equiv (E-H-\Sigma_1-\Sigma_2)^{-1} \tag{2.91}$$

so that

$$\Psi = G(S_1+S_2) \tag{2.92}$$

2.4.2 Equilibrium Green's functions and spectral function

Two distinct solutions exist for the electrode Green's functions defined in (2.87), corresponding to the sign of the infinitesimal η. These are named the "retarded" and "advanced" Green's functions,

$$\begin{aligned} g_{1,2}^R &= \lim_{\eta\to 0^+}(E-H_{1,2}+\eta i) \\ g_{1,2}^A &= \lim_{\eta\to 0^-}(E-H_{1,2}+\eta i) \end{aligned}$$

and correspond to different boundary conditions. Assuming that the eigenfunctions of an electrode form a complete orthonormal set, the electrode Green's function can be written as a sum over the eigenfunctions, Φ_1^α, of the electrode

wavefunction

$$g_1(E) = \sum_\alpha c_1^\alpha \left|\Phi_1^\alpha\right\rangle \left\langle\Phi_1^\alpha\right| \tag{2.93}$$

for some set of coefficients c_1^α. The orthonormality condition ensures that a unitary transformation of the basis can be applied in order to work in the basis of eigenfunctions, where $\sum_\alpha \left|\Phi^\alpha\right\rangle \left\langle\Phi^\alpha\right| = 1$. The coefficients can thus be determined from

$$\begin{aligned}
\sum_\alpha \left|\Phi_1^\alpha\right\rangle \left\langle\Phi_1^\alpha\right| = I &= (E - H_1 + \eta i) g_1(E) \\
&= (E - H_1 + \eta i) \sum_\alpha c_1^\alpha \left|\Phi_1^\alpha\right\rangle \left\langle\Phi_1^\alpha\right| \\
&= \sum_\alpha (E - \varepsilon_1^\alpha + \eta i) c_1^\alpha \left|\Phi_1^\alpha\right\rangle \left\langle\Phi_1^\alpha\right| \\
\implies c_1^\alpha &= \frac{1}{E - \varepsilon_1^\alpha + \eta i} \\
\implies g_1^R(E) &= \lim_{\eta \to 0^+} \sum_\alpha \frac{\left|\Phi_1^\alpha\right\rangle \left\langle\Phi_1^\alpha\right|}{E - \varepsilon_1^\alpha + \eta i}
\end{aligned} \tag{2.94}$$

and similarly for electrode 2. This expression can be used to evaluate the electrode Green's functions using contour integration in the complex plane. The analogous expression for the advanced Green's function shows that $g_{1,2}^R$ and $g_{1,2}^A$ are in fact Hermitian adjoints,

$$g_1^A(E) = \lim_{\eta \to 0^+} \sum_\alpha \frac{\left|\Phi_1^\alpha\right\rangle \left\langle\Phi_1^\alpha\right|}{E - \varepsilon_1^\alpha - \eta i} = (g_1^R)^\dagger. \tag{2.95}$$

The spectral function is defined as the anti-Hermitian part of the Green's function

$$\begin{aligned}
a_1(E) &= i \left[g_1^R(E) - g_1^A(E) \right] \\
&= \lim_{\eta \to 0^+} \sum_\alpha i \left|\Phi_1^\alpha\right\rangle \left\langle\Phi_1^\alpha\right| \left(\frac{1}{E - \varepsilon_1^\alpha + \eta i} - \frac{1}{E - \varepsilon_1^\alpha - \eta i} \right) \\
&= \lim_{\eta \to 0^+} \sum_\alpha \left|\Phi_1^\alpha\right\rangle \left\langle\Phi_1^\alpha\right| \frac{2\eta}{(E - \varepsilon_1^\alpha)^2 + \eta^2} \\
&= \sum_\alpha \left|\Phi_1^\alpha\right\rangle \left\langle\Phi_1^\alpha\right| 2\pi \delta(E - \varepsilon_1^\alpha).
\end{aligned}$$

In the last step the factor 2π was obtained from the known normalisation of the Lorentzian function. The trace of the spectral function yields the density of states

$$\begin{aligned} \mathrm{Tr}\left[a_1(E)\right] &= 2\pi \sum_{\alpha} \delta(E - \varepsilon_1^{\alpha}) \\ &= 2\pi D(E) \end{aligned} \tag{2.96}$$

as can be seen on comparison with equation (2.67), ignoring integration over the Brillouin zone for ease of exposition. For a general basis set the expression for the density of states is modified by multiplying the spectral function by the overlap matrix defined in (2.39),

$$\mathrm{Tr}\left[a_1(E)S_1\right] = 2\pi \sum_{\alpha} \delta(E - \varepsilon_1^{\alpha}). \tag{2.97}$$

Moreover the density matrix, equation (2.58), can be found from

$$\begin{aligned} \frac{1}{2\pi}\int f(E-\mu_1)a_1(E)\mathrm{d}E &= \int \sum_{\alpha} f(E-\mu_1)\delta(E-\varepsilon_1^{\alpha}) \left|\Phi_1^{\alpha}\right\rangle \left\langle\Phi_1^{\alpha}\right| \mathrm{d}E \\ &= \sum_{\alpha} f(\varepsilon_1^{\alpha}-\mu_1) \left|\Phi_1^{\alpha}\right\rangle \left\langle\Phi_1^{\alpha}\right| \\ &= \sum_{\alpha} n_1^{\alpha} \left|\Phi_1^{\alpha}\right\rangle \left\langle\Phi_1^{\alpha}\right| \\ &= D \end{aligned} \tag{2.98}$$

2.4.3 Non-equilibrium Green's function and spectral function

In a similar way the device Green's function can be written in terms of the eigenvectors, Φ_i, and complex eigenvalues, ε_i, of the non-Hermitian effective Hamiltonian, $(H + \Sigma_1 + \Sigma_2)$. The eigenvectors of a non-Hermitian operator do not form an orthonormal set, but rather form a bi-orthonormal set with the eigenvectors, Ψ_i, of the adjoint operator, $(H + \Sigma_1^{\dagger} + \Sigma_2^{\dagger})$. The device Green's function can thus be written

$$G(E) = \sum_i \left|\Phi_i\right\rangle \left\langle\Psi_i\right| \frac{1}{E - \varepsilon_i}. \tag{2.99}$$

Note that the electrode Green's functions and hence the self-energy operators are energy dependent. Therefore the complex eigenvalues, ε_i, are also energy dependent; they are written as

$$\varepsilon_i(E) = \varepsilon_0^i + \Delta_i(E) - i\frac{\gamma_i(E)}{2}, \tag{2.100}$$

with ε_0^i the real eigenvalues of the isolated device Hamiltonian. The spectral function can be evaluated as

$$\begin{aligned} A &\equiv i\left(G - G^\dagger\right) \\ &= \sum_i |\Phi_i\rangle \langle\Psi_i| \left(\frac{i}{E - \varepsilon_0^i - \Delta_i(E) + i\gamma_i(E)/2} - \frac{i}{E - \varepsilon_0^i - \Delta_i(E) - i\gamma_i(E)/2} \right) \\ &= \sum_i |\Phi_i\rangle \langle\Psi_i| \frac{\gamma_i(E)}{\left(E - \varepsilon_0^i - \Delta_i(E)\right)^2 + \left(\gamma_i(E)/2\right)^2}. \end{aligned} \tag{2.101}$$

The density of states on the device can be found from the trace of the spectral function, after multiplying by the overlap matrix when using a general basis set

$$\mathrm{Tr}[A(E)S] = \sum_i \frac{\gamma_i(E)}{\left(E - \varepsilon_0^i - \Delta_i(E)\right)^2 + \left(\gamma_i(E)/2\right)^2} = D(E). \tag{2.102}$$

This expression for the density of states shows that the imaginary part of the eigenvalues resulting from the non-Hermitian nature of the effective Hamiltonian is responsible for the broadening due to coupling to the electrodes. Furthermore, the eigenvalues of the isolated device are shifted by an amount $\Delta_i(E)$.

Broadening matrices are defined corresponding exactly to the non-Hermitian part of the effective Hamiltonian,

$$\Gamma_{1,2} = i\left(\Sigma_{1,2} - \Sigma_{1,2}^\dagger\right). \tag{2.103}$$

We now prove two useful identities. Observe that $G^{-1} = (E - H - \Sigma_1 - \Sigma_2)$ and

$(G^\dagger)^{-1} = \left(E - H - \Sigma_1^\dagger - \Sigma_2^\dagger\right)$, so that

$$\begin{aligned} G(\Gamma_1 + \Gamma_2)G^\dagger &= iG(\Sigma_1 + \Sigma_2 - \Sigma_1^\dagger - \Sigma_2^\dagger)G^\dagger \\ &= iG\left((G^\dagger)^{-1} - G^{-1}\right)G^\dagger \\ &= i(G - G^\dagger) \\ &= A \qquad (2.104) \\ &\equiv A_1 + A_2 \qquad (2.105) \end{aligned}$$

where the spectral function has been split naturally into left and right parts,

$$\begin{aligned} A_1 &\equiv G\Gamma_1 G^\dagger \\ A_2 &\equiv G\Gamma_2 G^\dagger \qquad (2.106) \end{aligned}$$

Also,

$$\begin{aligned} \Gamma_{1,2} &= i\left(\Sigma_{1,2} - \Sigma_{1,2}^\dagger\right) \\ &= i\tau\left(g_{1,2}^R - g_{1,2}^A\right)\tau^\dagger \\ &= \tau a_{1,2}\tau^\dagger \qquad (2.107) \end{aligned}$$

2.4.4 Device density matrix

All the quantities necessary to derive the device density matrix have now been established.

$$\begin{aligned}
D &\equiv \sum_i n_i \left|\Psi_i\right\rangle \left\langle\Psi_i\right| \\
&= \int \sum_i n_i(E) \left|\Psi_i\right\rangle \left\langle\Psi_i\right| \mathrm{d}E \\
&= \int \sum_i n_i(E) \left|G(S_1^i + S_2^i)\right\rangle \left\langle G(S_1^i + S_2^i)\right| \mathrm{d}E \\
&= \int \sum_\alpha n_\alpha(E) \left|G\tau(\Phi_1^\alpha + \Phi_2^\alpha)\right\rangle \left\langle G\tau(\Phi_1^\alpha + \Phi_2^\alpha)\right| \mathrm{d}E \\
&= \int G\tau \left[\sum_\alpha n_\alpha(E) \left|\Phi_1^\alpha\right\rangle \left\langle\Phi_1^\alpha\right| + n_\alpha(E) \left|\Phi_2^\alpha\right\rangle \left\langle\Phi_2^\alpha\right|\right] \tau^\dagger G^\dagger \mathrm{d}E \\
&= \frac{1}{2\pi} \int G\tau \left[f(E-\mu_1)a_1(E) + f(E-\mu_2)a_2(E)\right] \tau^\dagger G^\dagger \mathrm{d}E \\
&= \frac{1}{2\pi} \int G \left[f(E-\mu_1)\Gamma_1 + f(E-\mu_2)\Gamma_2\right] G^\dagger \mathrm{d}E \\
&= \frac{1}{2\pi} \int \left[f(E-\mu_1)A_1 + f(E-\mu_2)A_2\right] \mathrm{d}E
\end{aligned} \tag{2.108}$$

which can be seen as a generalisation of equation (2.98) where the left and right spectral functions are competing to fill up the device density matrix. The above derivation makes use of the results in equations (2.98), (2.106) and (2.107). Notice also that the summation changed from being over i, the eigenfunctions of the device region, to being over α, the eigenfunctions of the electrodes. This is intuitive when making substitutions from device quantities to electrode quantities. A more rigorous argument requires the second quantised formalism [168]. Finally, cross terms between eigenfunctions on different electrodes are zero since they do not interact, $\left|\Phi_1^\alpha\right\rangle \left\langle\Phi_2^\alpha\right| = \left|\Phi_2^\alpha\right\rangle \left\langle\Phi_1^\alpha\right| = 0$.

2.4.5 Current flow

Thus far the Green's functions and related quantities have been described in the energy domain only. Equivalently, the operators can be defined in the time do-

main and depend on two time-coordinates, e.g. $G(t,t')$ is the Green's function at time t due to a perturbation at time t'. At steady state all quantities depend only on the difference between the two time-coordinates, $\tau = t - t'$. The switch between the energy and time domains is then made by the relevant Fourier transforms

$$\begin{aligned} X(\tau = t - t') &= \frac{1}{2\pi\hbar}\int X(E)e^{iE\tau/\hbar}\mathrm{d}E \\ X(E) &= \int X(\tau)e^{iE\tau/\hbar}\mathrm{d}\tau \end{aligned} \tag{2.109}$$

from which it follows that setting the two time-coordinates equal is equivalent to integrating over energy

$$\begin{aligned} X(t) = X(t,t) &= X(\tau = 0) \\ &= \frac{1}{2\pi\hbar}\int X(E)\mathrm{d}E \end{aligned} \tag{2.110}$$

In order to evaluate the current, we will start in the time domain and use this relation to switch to an integration over energy. We will also make use of the time-dependent version of the compound Schrödinger equation (2.85). For the device part this leads to (c.f. equation (2.88))

$$i\hbar\frac{\mathrm{d}}{\mathrm{d}t}\Psi = (H + \Sigma_1 + \Sigma_2)\Psi + S_1 + S_2 \tag{2.111}$$

and the Hermitian conjugate equation gives

$$-i\hbar\frac{\mathrm{d}}{\mathrm{d}t}\Psi^\dagger = (H + \Sigma_1^\dagger + \Sigma_2^\dagger)\Psi^\dagger + S_1^\dagger + S_2^\dagger. \tag{2.112}$$

The current flow is then evaluated by considering the rate of change of the prob-

ability density of the eigenfunctions inside the device region,

$$\begin{aligned}
\frac{\mathrm{d}}{\mathrm{d}t}\sum_i \langle\Psi_i(t)|\Psi_i(t)\rangle &= \frac{1}{i\hbar}\sum_i \left[\langle\Psi_i(t)|i\hbar\frac{\mathrm{d}}{\mathrm{d}t}\Psi_i(t)\rangle - \langle i\hbar\frac{\mathrm{d}}{\mathrm{d}t}\Psi_i(t)|\Psi_i(t)\rangle\right] \\
&= \frac{1}{i\hbar}\sum_i \Big[\langle\Psi_i(t)|(H+\Sigma_1+\Sigma_2)\Psi_i(t) + S_1^i + S_2^i\rangle] \\
&\quad -\langle(H+\Sigma_1+\Sigma_2)\Psi_i(t) + S_1^i + S_2^i|\Psi_i(t)\rangle\Big] \\
&= \frac{1}{i\hbar}\sum_i \Big[\Psi_i^\dagger(t)\left(\Sigma_1 - \Sigma_1^\dagger\right)\Psi_i(t) + \Psi_i^\dagger(t)S_1^i - S_1^{i\dagger}\Psi_i(t) \\
&\quad +\Psi_i^\dagger(t)\left(\Sigma_2 - \Sigma_2^\dagger\right)\Psi_i(t) + \Psi_i^\dagger(t)S_2^i - S_2^{i\dagger}\Psi_i(t)\Big] \quad (2.113)
\end{aligned}$$

The total probability density inside the device will remain constant. The expression (2.113) can be interpreted as the sum of the current flows at the two electrodes, which is zero. In order to find the size of the current, we thus evaluate the flow at electrode 1 only. Equation (2.110) is used to switch to the energy domain. The following properties of the trace function will be invoked:

$$\mathrm{Tr}\left[|\phi\rangle\langle\psi|\right] = \langle\phi|\psi\rangle \quad (2.114)$$

$$\mathrm{Tr}\left[AB\right] = \mathrm{Tr}\left[BA\right] \quad (2.115)$$

$$\mathrm{Tr}\left[A \pm B\right] = \mathrm{Tr}\left[A\right] \pm \mathrm{Tr}\left[B\right]. \quad (2.116)$$

Furthermore, the source terms are eliminated using

$$\begin{aligned}
\sum_i S_1^i S_1^{i\dagger} &= \sum_\alpha \tau_1 \Phi_1^\alpha \Phi_1^{\alpha\dagger}\tau_1^\dagger \\
&= \int \tau_1 f_1(E) a_1(E)\tau_1^\dagger \mathrm{d}E \\
&= \int f_1(E)\Gamma_1(E)\mathrm{d}E \quad (2.117)
\end{aligned}$$

and

$$\sum_i S_1^i S_2^{i\dagger} = \sum_i S_2^i S_1^{i\dagger} = 0. \quad (2.118)$$

Finally, we are ready to evaluate the current,

$$\begin{aligned}
I &= \frac{e}{i\hbar}\sum_i \left[\Psi_i^\dagger(t)\left(\Sigma_1-\Sigma_1^\dagger\right)\Psi_i(t)+\Psi_i^\dagger(t)S_1^i-S_1^{i\dagger}\Psi_i(t)\right] \\
&= \frac{e}{i\hbar}\sum_i \int \left[\Psi_i^\dagger\left(\Sigma_1-\Sigma_1^\dagger\right)\Psi_i+\Psi_i^\dagger S_1^i-S_1^{i\dagger}\Psi_i\right]\mathrm{d}E \\
&= \frac{e}{i\hbar}\sum_i \int \mathrm{Tr}\left[\left(\Sigma_1-\Sigma_1^\dagger\right)^\dagger\Psi_i\Psi_i^\dagger+\Psi_i S_1^{i\dagger}-S_1^i\Psi_i^\dagger\right]\mathrm{d}E \\
&= \frac{e}{i\hbar}\sum_i \int \mathrm{Tr}\left[\left(\Sigma_1^\dagger-\Sigma_1\right)G\left(S_1^i+S_2^i\right)\left(S_1^i+S_2^i\right)^\dagger G^\dagger+GS_1^iS_1^{i\dagger}-S_1^iS_1^{i\dagger}G^\dagger\right]\mathrm{d}E \\
&= \frac{e}{i\hbar}\int \mathrm{Tr}\left[\left(\Sigma_1^\dagger-\Sigma_1\right)G\Big(f_1\Gamma_1+f_2\Gamma_2\Big)G^\dagger+Gf_1\Gamma_1-f_1\Gamma_1G^\dagger\right]\mathrm{d}E \\
&= \frac{e}{i\hbar}\int \mathrm{Tr}\left[-\frac{1}{i}\Gamma_1G(f_1\Gamma_1+f_2\Gamma_2)G^\dagger+f_1\Gamma_1\left(G-G^\dagger\right)\right]\mathrm{d}E \\
&= \frac{e}{\hbar}\int \mathrm{Tr}\left[\Gamma_1G\left(f_1\Gamma_1+f_2\Gamma_2\right)G^\dagger-f_1\Gamma_1A\right]\mathrm{d}E \\
&= \frac{e}{\hbar}\int \mathrm{Tr}\left[\Gamma_1G\left(f_1\Gamma_1+f_2\Gamma_2\right)G^\dagger-f_1\Gamma_1G\left(\Gamma_1+\Gamma_2\right)G^\dagger\right]\mathrm{d}E \\
&= \frac{e}{\hbar}\int \mathrm{Tr}\left[\Gamma_1G\Gamma_2G^\dagger\Big(f(E-\mu_2)-f(E-\mu_1)\Big)\right]\mathrm{d}E \\
&= \frac{e}{\hbar}\int T(E)\Big(f(E-\mu_2)-f(E-\mu_1)\Big)\mathrm{d}E. \qquad (2.119)
\end{aligned}$$

By defining the transmission function $T(E) = \mathrm{Tr}\left[\Gamma_1G\Gamma_2G^\dagger\right]$, equation (2.119) has been reconciled with the Landauer formula in the transmission formalism [166]. If the Fermi functions are assumed to be step functions, then the current can be written in terms of the applied bias V, with $eV = \mu_1 - \mu_2$

$$I(V) = \frac{e}{\hbar}\int_{-eV/2}^{eV/2} T(E)\mathrm{d}E \qquad (2.120)$$

and the conductance is given by

$$\begin{aligned}
G(V) &= \frac{\mathrm{d}I(V)}{\mathrm{d}V} \\
&= \frac{e^2}{2\hbar}\Big[T(eV/2)+T(-eV/2)\Big] \qquad (2.121)
\end{aligned}$$

where the quantum of conductance can be identified

$$G(0) = \frac{e^2}{\hbar} = G_0 \tag{2.122}$$

A factor 2 to account for spin up and spin down electrons, recovers the usual expression for G_0.

2.5 WKB solution to tunnelling problem

The majority of electronic transport results in this work are based on the DFT-NEGF formalism. However, we also make use of a much simpler picture: the device is viewed as a tunnelling region described by a barrier shape $U(x)$ between the electrode-device interfaces at $x = 0$ (left) and $x = d$ (right). In general the barrier shape is determined by the details of the molecule in this region.

We treat this tunnelling problem with the well-known Wentzel-Kramers-Brillouin (WKB) approximation (Ref. [169] deals with its application in a range of quantum mechanics problems). As such one starts with the one-dimensional time-independent Schrödinger equation

$$-\frac{\hbar^2}{2m}\frac{\mathrm{d}^2}{\mathrm{d}x^2}\psi(x) + U(x)\psi(x) = E\psi(x). \tag{2.123}$$

This can be rewritten as

$$\psi''(x) + k(x)^2\psi(x) = 0 \tag{2.124}$$

in terms of the wave vector $k(x) \equiv \frac{1}{\hbar}\sqrt{2m\left[E - U(x)\right]}$. In the case of a constant potential barrier $U(x) = V_0$, the most general solution is $\psi(x) = Ae^{ik_0x} + Be^{-ik_0x}$. When $U(x)$ is not constant, one nonetheless looks for approximate solutions of the form $\psi(x) = e^{T(x)+iS(x)}$. Substituting into (2.124) and equating real and imaginary parts yields

$$(T')^2 - (S')^2 + T'' + k^2 = 0 \tag{2.125}$$

$$2T'S' + S'' = 0. \tag{2.126}$$

Under the assumption that the potential $U(x)$ is slowly varying so that the rate of change in amplitude is small compared with that of the phase, or $T', T'' \ll S'$, the equation for the real part (2.125) becomes $(S')^2 = k^2$, whence $S(x) = \pm \int k(x)\mathrm{d}x$. Using $S' = \pm k$ and $S'' = \pm k'$ in equation (2.126) gives $T' = -\frac{1}{2}\frac{k'}{k} \rightarrow T = -\frac{1}{2}\ln k$ plus a constant of integration, or $e^{T(x)} = A[k(x)]^{-\frac{1}{2}}$. This gives a general solution within this approximation of

$$\psi(x) = \frac{1}{\sqrt{k}}\left[Ae^{i\int k(x)\mathrm{d}x} + Be^{-i\int k(x)\mathrm{d}x}\right]. \tag{2.127}$$

In the case where $E < U(x)$, setting $\kappa = k/i$ leads to

$$\psi(x) = \frac{A}{\sqrt{\kappa}}e^{\int \kappa(x)\mathrm{d}x + i\pi/4} + \frac{B}{\sqrt{\kappa}}e^{-\int \kappa(x)\mathrm{d}x + i\pi/4} \tag{2.128}$$

and the approximation $T', T'' \ll S'$ in fact implies a rapidly varying amplitude $\frac{A}{\sqrt{\kappa}}e^{\pm\int \kappa(x)\mathrm{d}x}$ as compared with the phase $\frac{A}{\sqrt{\kappa}}e^{i\pi/4}$, consistent with the fact that we expect an exponentially decaying wavefunction in this classically forbidden region.

The approximate solutions given by equations (2.127) and (2.128) become unphysical in the region $U(x) \approx E$, where $k \rightarrow 0$. In order to obtain a global approximate solution for $\psi(x)$, the solutions in the two regions $U(x) > E$ and $U(x) < E$ have to be connected in the region $U(x) \approx E$. This can be done rigorously by assuming a linear variation in $U(x)$ around the point $x_0, V(x_0) = E$, and hence obtaining the solution to the differential equation in this region. The solution is given by Airy functions and can be matched to the solutions of (2.127) and (2.128) on the left and right (see for example Ref. [169]).

The complication of connecting solutions can be circumvented by assuming the electron is tunnelling through a potential $U(x) > E$ for $0 < x < d$ and considering the wavefunction at positions just to the right of 0 and to the left of d. Using the fact that we expect an exponential decay in $\psi(x)$ in the barrier region, we put $A = 0$ in equation (2.128) and find the transmission coefficient

from left to right as

$$\begin{aligned} T(E) &= \left|\frac{\psi(d-\delta)}{\psi(0+\delta)}\right|^2 \\ &= \left|e^{-\int_\delta^{d-\delta}\kappa(x)\mathrm{d}x}\sqrt{\frac{V(\delta)-E}{V(d-\delta)-E}}\right|^2 \\ &\approx e^{-2\int_\delta^{d-\delta}\kappa(x)\mathrm{d}x} \\ &\approx e^{-\frac{2\sqrt{2}}{\hbar}\int_0^d\int\sqrt{m[U(x)-E]}\mathrm{d}x}. \end{aligned} \tag{2.129}$$

This expression for the WKB transmission function and the corresponding Landauer expression for the current [168]

$$I(V) = \frac{2e}{h}\int_{-eV/2}^{eV/2} T(E)\mathrm{d}E \tag{2.130}$$

will be used as an alternative evaluation of the transport properties of the systems under study.

Chapter 3

Validation

Before using DFT as a predictive tool, one should ensure that the level of theory used produces suitably accurate results compared with known experimental data and reliable computational data from other sources. Furthermore, the results should be well converged with respect to the computational parameters used.

In chapter 2 various parameters were described that alter the accuracy of a DFT calculation. In this chapter, we will demonstrate how suitable parameters were chosen for the calculations in the remaining chapters and demonstrate the validity of our results by comparing a series of test calculations against established experimental and computational data.

3.1 Pseudopotentials

The generation of pseudopotentials involves a choice of XC potential, a core cutoff radius r_l^c for each angular momentum component, a suitable choice of valence electrons, and possible inclusion of relativistic and non-linear core corrections (see section 2.2.3). A pseudopotential has to be generated for each atomic species. In this work these include the metal Au and organic elements H, C, N, O and S.

GGA XC potentials are generally regarded as an improvement over LDA. However the TranSIESTA-C software package does not support GGA calculations and therefore the TranSIESTA-C transport calculations were done with an LDA XC potential, parametrised by Perdew and Zunger (PZ) [141]. The SIESTA

geometry relaxations were performed using the GGA parametrised by Perdew, Burke and Ernzerhof (PBE) [142].

Unfortunately there is no formula for producing good pseudopotentials. Since the pseudopotentials are generated for an isolated atom, the main concern is that they remain good approximations for a vaiety of different chemical environments, i.e. have good *transferability*. The best test is therefore to check that results from pseudopotential calculations closely reproduce all-electron calculations and experimental data. This will be the focus of sections 3.3-3.5. There are also some standard checks that can be done on the raw pseudopotential data and these will be discussed in this section.

For each angular momentum component, the pseudo-wavefunction must match the all-electron wavefunction beyond the cutoff radius r_l^c, and be smooth and nodeless below r_l^c. A desirable property for pseudopotentials is *softness*, i.e. smooth decay of the pseudo-wavefunction below r_l^c. The pseudopotential becomes softer with increased r_l^c due to the enhanced freedom in constructing the pseudo-wavefunction in the region $0 < r < r_l^c$ subject to the norm-conservation constraint. However, increasing r_l^c reduces the transferability, since the approximation becomes more severe as the pseudo-core is enlarged. Clearly r_l^c has to be beyond the last node of the all-electron wavefunction. For good transferability, r_l^c should be small enough that the pseudo-wavefunction matches the all-electron wavefunction in the vicinity of the peak.

A good indicator of the softness of the pseudopotential $V_l(r)$ is rapidly decaying oscillations of the Fourier transform $V_l(q)$.

The pseudopotential produces good scattering properties if the logarithmic derivative of the pseudo-wavefunction matches that of the all-electron wavefunction. For $r > r_l^c$ this is true by construction at the eigenenergy ε_l, but should remain true for energies close to the eigenvalue. The radius at which to test the logarithmic derivatives r^d is not uniquely defined but should be similar to the covalent or ionic radius of the atom - a likely distance for scattering events.

Table 3.1 indicates the parameters used to generate the pseudopotentials, as well as the radii r^{d} at which the logarithmic derivatives were evaluated. Note that this does not affect the pseudopotential generation.

species	XC functional	cutoff radii r_0^c	r_1^c	r_2^c	r_3^c	corrections rel	nlc	r^d
Au	GGA	2.35	2.35	1.50	1.50	Y	N	2.80
Au	LDA	2.25	2.25	2.25	2.25	Y	N	2.80
H	GGA	1.25	1.25	1.25	1.25	N	N	0.70
C	GGA	1.33	1.33	1.33	1.33	N	N	1.50
N	GGA	1.14	1.14	1.14	1.14	N	N	2.00
O	GGA	1.14	1.14	1.14	1.14	N	N	1.70
S	GGA	1.50	1.50	1.50	1.50	N	N	2.10

Table 3.1: Data used to generate the pseudopotentials. All radii are given in Bohr.

The Au pseudopotentials used with the GGA-PBE and LDA-PZ functionals are shown in figures 3.1-3.4 and 3.5-3.8 respectively. Four plots for each angular momentum component l are used. These show (a) the all-electron and pseudo-wavefunctions u_{nl}^{ae} and u_l^{ps}, (b) the logarithmic derivative of the pseudowavefunction $\frac{\mathrm{d}}{\mathrm{dr}} \ln u_l^{\mathrm{ps}}(r)$ at a chosen r^{d}, (c) the pseudopotential $V_l(r)$ and (d) the Fourier transform of the pseudopotential $V_l(q)$. The core cutoff radius r_l^{c} is indicated in each case on plots (a) and (c) and the eigenenergy on plot (b). Non-linear core corrections are not used and relativistic corrections are used only for gold. The pseudopotential plots for the remaining elements are given in Appendix A.

In all cases the all-electron wavefunction is well reproduced in the vicinity of the function peak. The logarithmic derivatives for the gold s and p and the sulphur s wavefunctions are not well reproduced, but the disparities occur at energies about 1.5 Rydberg from the corresponding eigenenergies. Thus the effect on transferability should not be substantial. The logarithmic derivatives in all other cases are well reproduced by the pseudo-wavefunctions.

3.2 Other parameters

Apart from the XC functional and pseudopotential, the other parameters described in section 2.2 which affect the accuracy of results are the basis set size, the energyshift parameter $\delta\varepsilon$, defining the spatial extent of all basis functions, the meshcutoff parameter E_{cut}, defining the fineness of the real-space grid and the

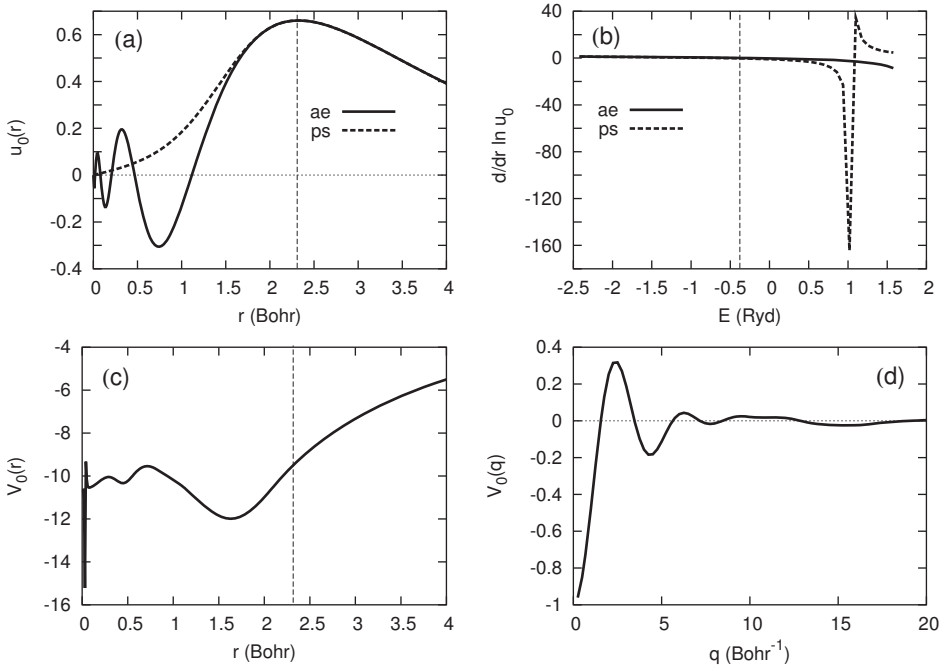

Figure 3.1: Gold GGA pseudopotential for $l = 0$

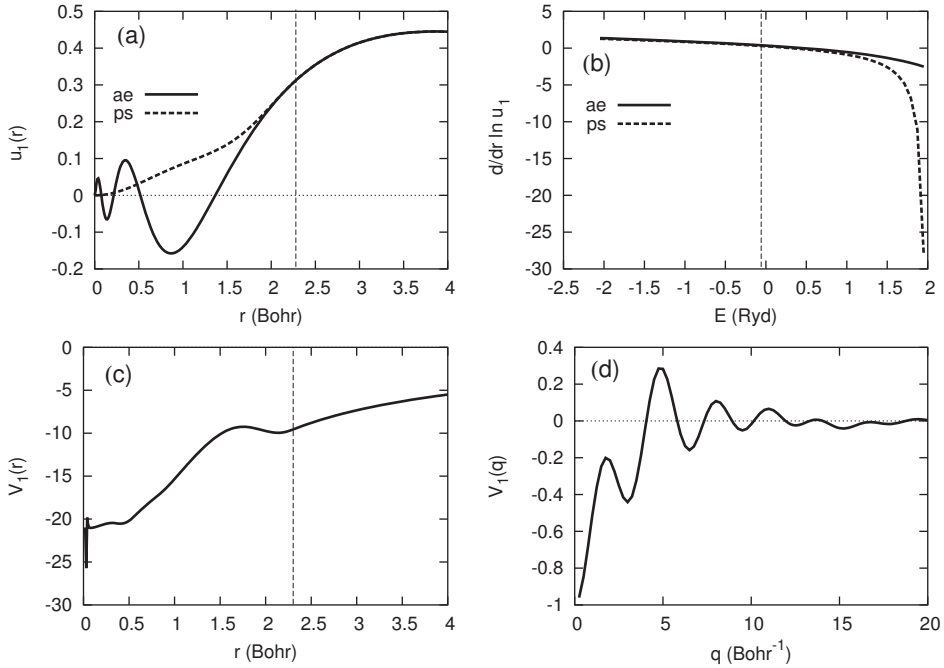

Figure 3.2: Gold GGA pseudopotential for $l = 1$

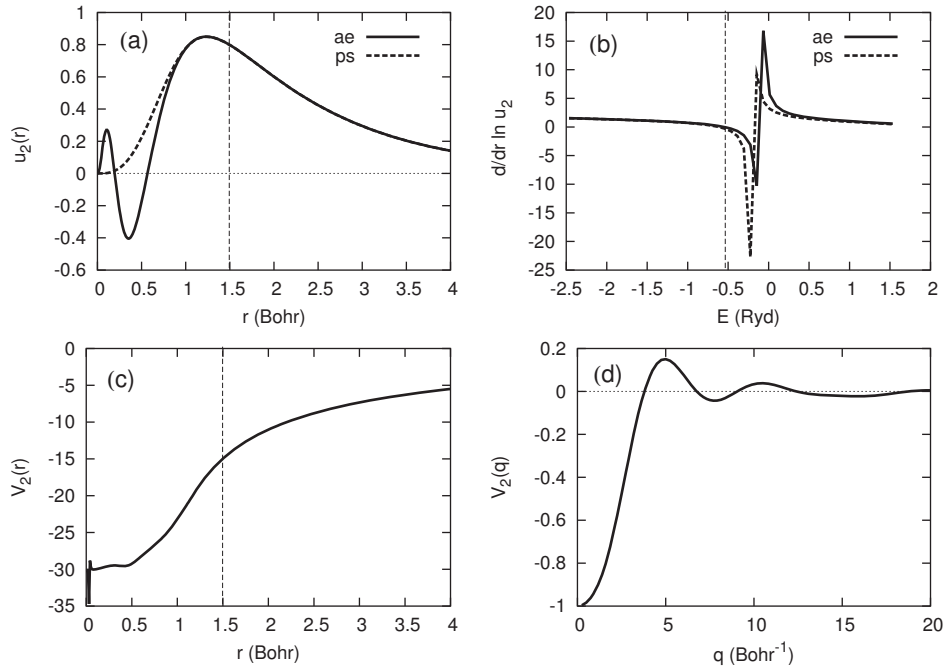

Figure 3.3: Gold GGA pseudopotential for $l = 2$

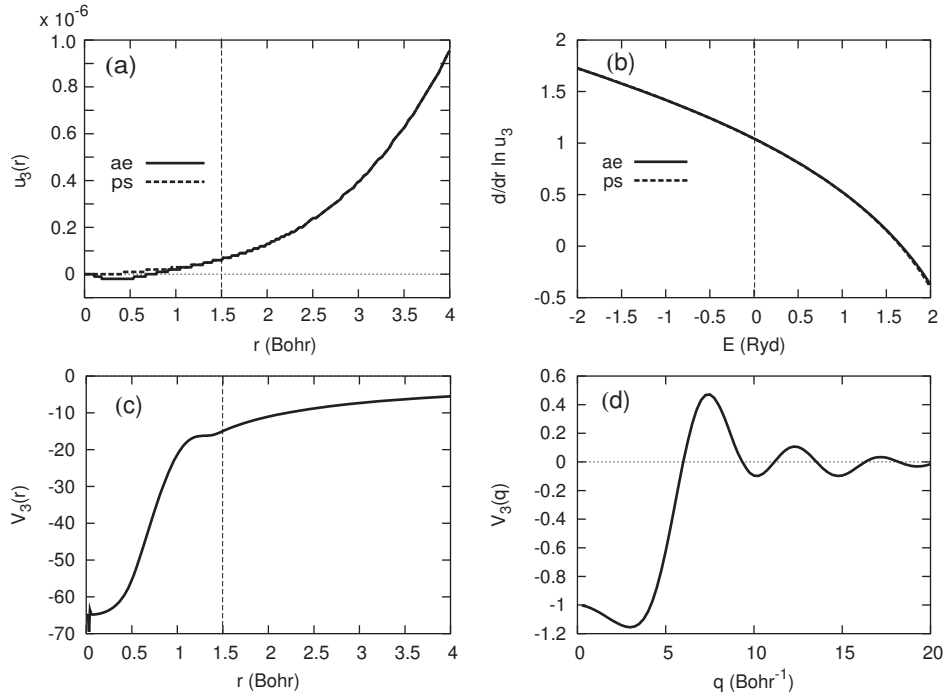

Figure 3.4: Gold GGA pseudopotential for $l = 3$

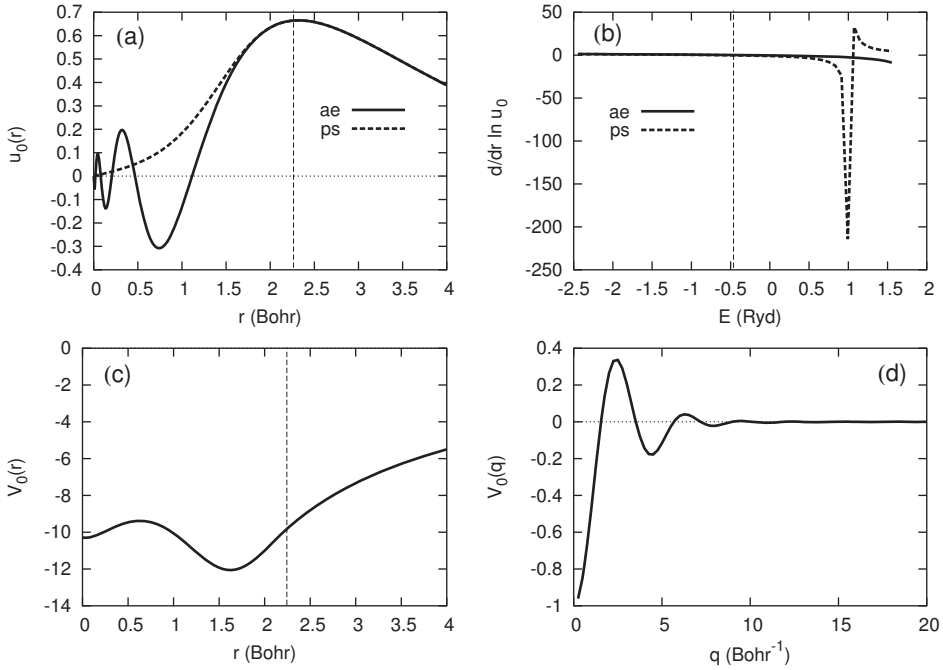

Figure 3.5: Gold LDA pseudopotential for $l = 0$

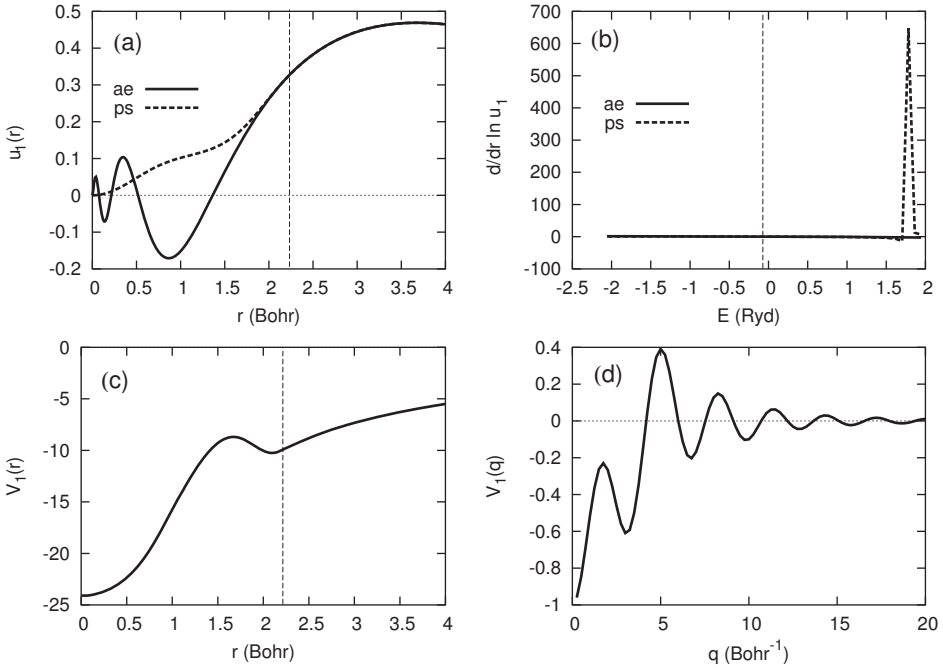

Figure 3.6: Gold LDA pseudopotential for $l = 1$

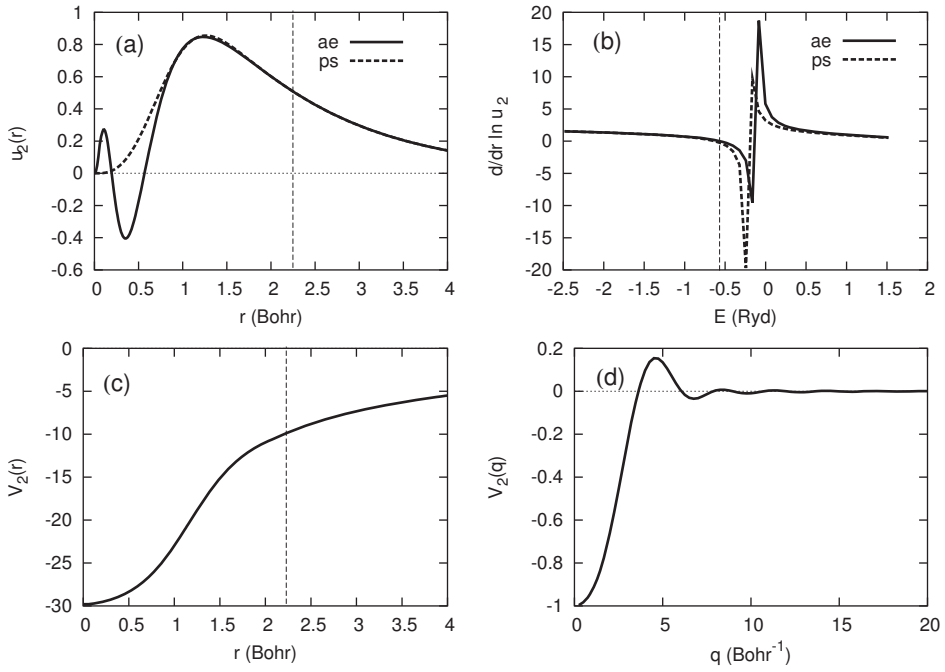

Figure 3.7: Gold LDA pseudopotential for $l = 2$

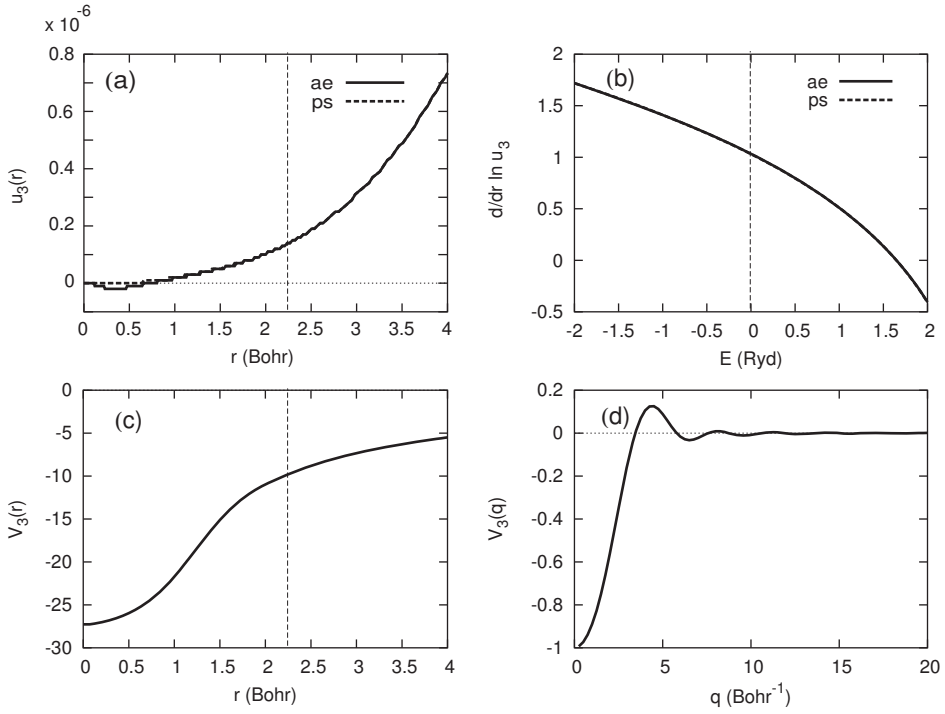

Figure 3.8: Gold LDA pseudopotential for $l = 3$

Monkhorst-Pack (MP) grid used for k-point sampling. The number of k-points, N_{k}, in each periodic direction are chosen to be equal. In the slab calculations in the following chapters a finite number of layers are used to approximate a semi-infinite surface. It is therefore necessary to determine how many surface layers give an accurate representation of the true surface.

In the remaining sections of this chapter we demonstrate test calculations that validate the pseudopotentials and other approximations used. We take the point of view that the convergence of results with respect to one parameter can be tested while keeping the other parameters fixed at reasonable, but not necessarily optimal values. This prevents the parameter space from being inaccessibly large.

3.3 Au bulk

Calculations of bulk gold were performed using the primitive fcc unit cell shown in figure 3.9 and periodic boundary conditions (PBC's) in SIESTA.

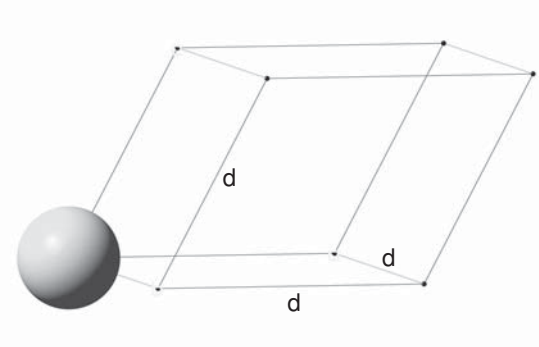

Figure 3.9: Au bulk primitive fcc unit cell.

3.3.1 Total energy and cohesive energy

The total and cohesive energies per atom in Au bulk were evaluated with different parameters. The cohesive energy was calculated as $E_{\mathrm{c}} = E_{\mathrm{bulk}} - E_{\mathrm{atom}}$. E_{bulk} is the total energy per atom of bulk gold calculated as the total energy of the unit cell shown in figure 3.9. E_{atom} is the total energy of an isolated atom calculated by placing a Au atom in the centre of a large unit cell, so that there are no

interactions between periodic images. E_c is corrected for the BSSE by including the basis functions centred at the first, second and third bulk nearest neighbours of the isolated Au atom in the E_{atom} calculation. Figure 3.10 shows that this yields a converged value with respect to the number of neighbours ghosted. The bulk unit cell is defined by the Au nearest neighbour distance (Au-Au bond length) $d = 2.96$ Å. This will be varied in the next section. The present calculations are performed using the GGA-PBE XC functional.

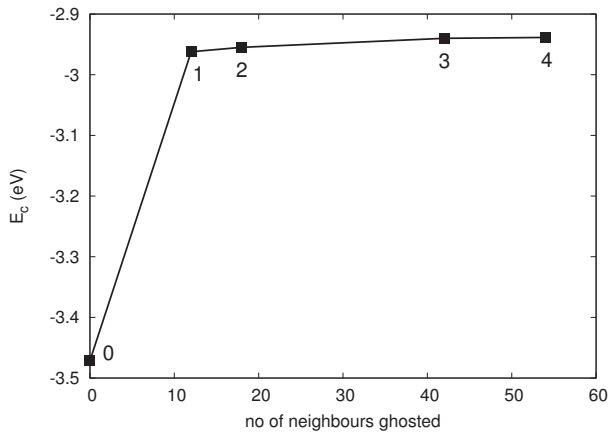

Figure 3.10: Convergence of cohesive energy of bulk Au with respect to the number of nearest neighbours ghosted in the isolated atom calculations. The x-axis indicates the number of ghost atoms while the data point labels indicate the number of groups of nearest neighbours included.

Figure 3.11 shows the total and cohesive energies as a function of the energyshift parameter, using a DZP basis, an MP grid of 7x7x7 k-points and a meshcutoff, $E_{cut} = 300$ Ry. The total energy is well converged at $\delta\varepsilon = 5$ mRy, however the BSSE corrected cohesive energy is only converged at $\delta\varepsilon = 1$ mRy. As expected the BSSE error approaches zero as the basis orbitals are enlarged. The uncorrected (raw) cohesive energy is converged at $\delta\varepsilon = 0.2$ mRy.

Figure 3.12 shows the total and cohesive energy evaluated with different basis set sizes where $\delta\varepsilon = 5$ mRy. The energies are reasonably converged with an SZP basis set and well converged with a DZP basis set. Clearly the inclusion of a polarisation orbital (SZP) is more important than a second orbital for each angular momentum component (DZ).

Figure 3.13 shows the cohesive energies with an increasing number of k-points

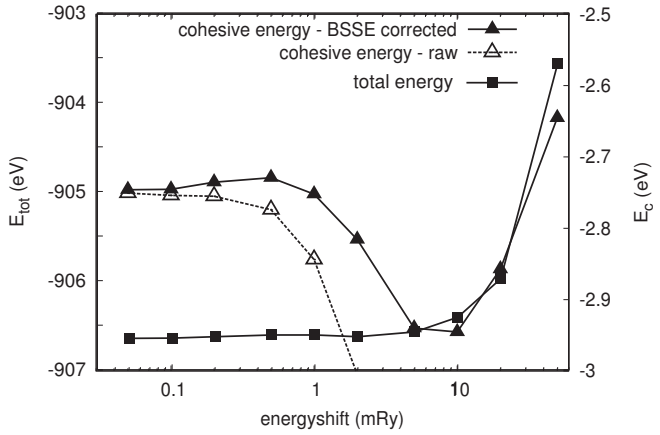

Figure 3.11: Convergence of total and cohesive energies of bulk Au with energyshift parameter, using a DZP basis set with $N_{\mathrm{k}} = 7$ and $E_{\mathrm{cut}} = 300$ Ry.

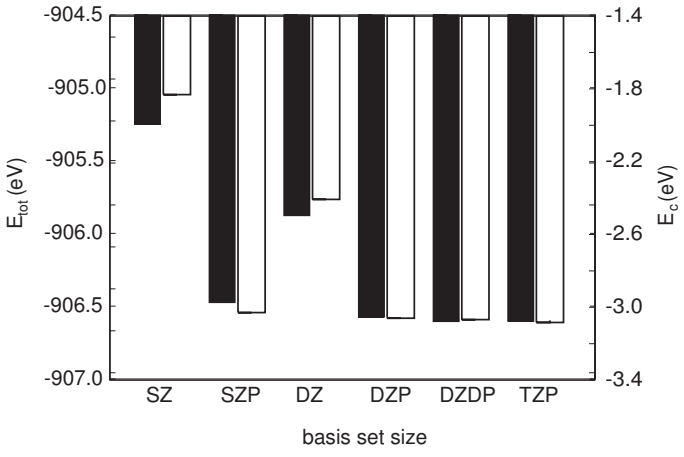

Figure 3.12: Convergence of total (dark rectangles) and cohesive (light rectangles) energy of bulk Au with basis set size. $\delta\varepsilon = 5$ mRy, $N_{\mathrm{k}} = 7$ and $E_{\mathrm{cut}} = 300$ Ry.

used for the bulk calculation. For the isolated atom, only the Γ-point is used, since this is not a periodic system. The value of E_{atom} is therefore constant and the convergence of total and cohesive energy is identical. The energy is converged for $N_k = 10$.

Figure 3.14 shows the variation in the total energy with the meshcutoff parameter as well as the number of cpu seconds used for the calculation. The total energy is converged at $E_{\text{cut}} \sim 70$ Ry. However, the fineness of the real-space grid has a much larger effect on the interatomic forces and stresses on the unit cell, since the discrete grid breaks the translational invariance of the total energy. In the next section we show the effect this has on a calculation of the bulk lattice constant.

3.3.2 Lattice constant and bulk modulus

The Au nearest neighbour distance d and bulk modulus B_0 are determined by calculating the total energy for the primitive fcc unit cell for a series of unit cell sizes and fitting the energy versus volume curve to the Murnaghan equation of state [170]

$$E(V) = E_0 + \frac{B_0 V}{B_0'}\left(\frac{(V_0/V)^{B_0'}}{B_0' - 1} + 1\right) - \frac{B_0 V_0}{B_0' - 1} \tag{3.1}$$

where V_0 is the equilibrium unit cell volume, $B_0 = -V\frac{\partial P}{\partial V}\Big|_{V=V_0}$ is the bulk modulus and $B_0' = \left(\frac{\partial B}{\partial P}\right)_T$ is assumed to be a constant. The nearest neighbour distance is related to the unit cell volume by $d = \left(\sqrt{2}V\right)^{\frac{1}{3}}$. The fcc lattice constant is $l = \sqrt{2}d$.

Figure 3.15 shows the relative energy vs volume curve using our standard pseudopotential from table 3.1 as well as one with non-linear core corrections added. The parameters from a fit to equation 3.1 as well as the resulting Au nearest neighbour distance $d = \left(\sqrt{2}V_0\right)^{\frac{1}{3}}$ are shown in table 3.2. Clearly the change in pseudopotential has very little effect on the results.

Figure 3.16 shows the Au nearest neighbour distance and bulk modulus as the energyshift parameter is varied. A comparison with a different k-point grid is also indicated. Convergence is only reached for a very accurate energyshift parameter. However for $\delta\varepsilon = 5$ mRy, the error with respect to the limiting value is $< 1\%$ for

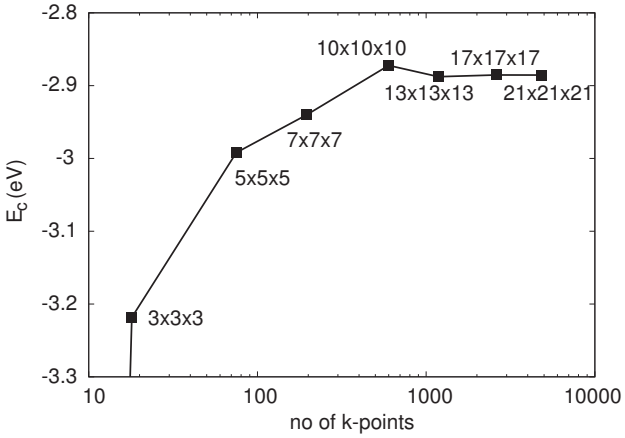

Figure 3.13: Convergence of Au cohesive energy with number of k-points. The k-grid is indicated at each data point. A DZP basis is used with $\delta\varepsilon =$ 5 mRy and $E_{\rm cut} = 300$ Ry.

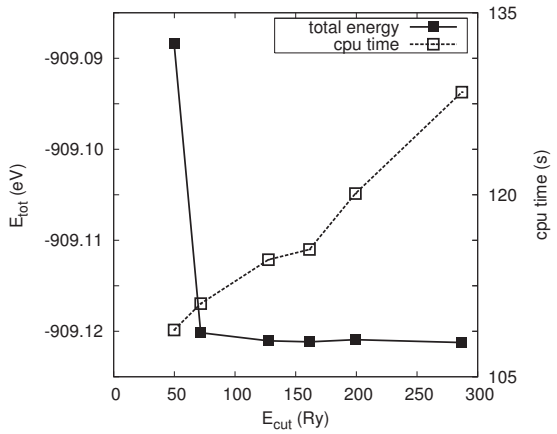

Figure 3.14: Convergence of total energy of bulk Au with meshcutoff parameter. DZP basis set with $\delta\varepsilon = 5$ mRy, $N_{\rm k} = 7$ and $E_{\rm cut} = 300$ Ry.

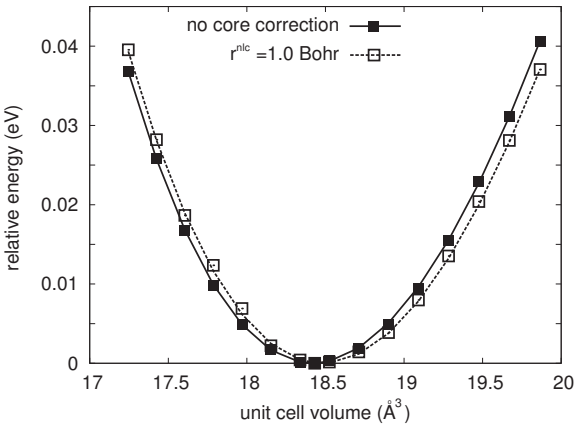

Figure 3.15: Calculation of the Au nearest neighbour distance and bulk modulus using a GGA peudopotential with and without a non-linear core correction, $r^{\mathrm{nlc}} = 1.0$ Bohr. DZP basis set with $\delta\varepsilon = 5$ mRy, $N_{\mathrm{k}} = 7$ and $E_{\mathrm{cut}} = 300$ Ry.

pseudopotential	V_0 (Å^3)	B_0 (GPa)	B_0'	d (Å)
no core corrections	18.42	136	5.89	2.964
$r^{\mathrm{nlc}} = 1.0$ Bohr	18.48	132	5.15	2.968

Table 3.2: Parameters from figure 3.15 data fit to Murnaghan's equation.

the nearest neighbour distance. The bulk modulus is less well converged and the corresponding error is $\sim 20\%$ when $\delta\varepsilon = 5$ mRy.

Figure 3.17 illustrates how a coarse spatial grid causes a decrease in the smoothness of the curve of energy vs cell size. Even though the total energy is seen to converge at a meshcutoff as low as 70 Ry (see figure 3.14), a much finer grid is required to obtain accurate forces and stresses. A meshcutoff of 300 Ry is seen to produce a smooth E vs d curve, indicating that the effect of the broken translational invariance is minimal. We therefore use $E_{\mathrm{cut}} = 300$ Ry in most cases, unless memory requirements prevent this. As seen in figure 3.14, the increased computational cost is about 20%.

3.3.3 Comparison with literature

Table 3.3 compares our LDA and GGA values for the Au bulk cohesive energy, nearest neighbour distance and bulk modulus with experiment and other calculations from the literature. Our results are consistent with all electron calculations

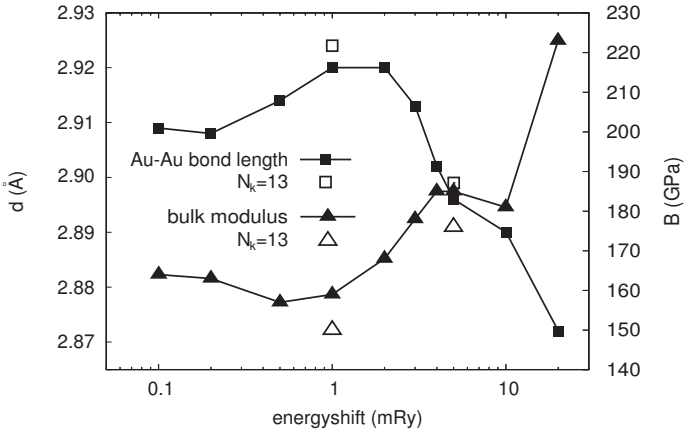

Figure 3.16: Au nearest neighbour distance and bulk modulus for different energyshift parameters. LDA-PZ XC functional, DZP basis set, $N_k = 7$, $E_{\rm cut} = 300$ Ry. The hollow data points show comparative results for $N_k = 13$.

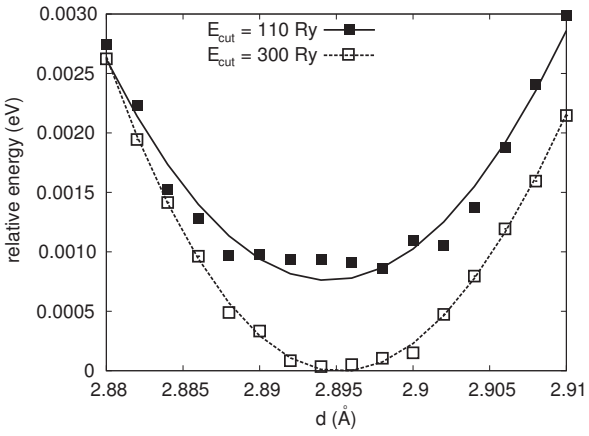

Figure 3.17: Total energy vs Au nearest neighbour distance for an insufficient meshcutoff parameter, $E_{\rm cut} = 110$ Ry, resulting in a decreased smoothness, compared to the finer grid with $E_{\rm cut} = 300$ Ry. DZP basis with $\delta\varepsilon = 5$ mRy and $N_{\rm k} = 7$.

using linear muffin tin orbitals (AE-LMTO) [171] and planewaves [172] as well as pseudopotential planewave (PS-PW) calculations [173] where LDA tends to cause overbinding and GGA overcompensates to cause underbinding. Note that Ref. [173] uses the PBE GGA functional, whereas Ref. [172] uses the PW91 GGA functional.

	E_c (eV)		d (Å)		B (GPa)	
	GGA	LDA	GGA	LDA	GGA	LDA
present work	2.94	4.08	2.964	2.896	136	185
AE-LMTO [171]	-	4.32	-	2.87	-	193
AE-PW [172]	-	-	2.94	2.87	142	198
PS-PW [173]	3.15	4.43	2.93	2.87	-	-
experiment [5]	3.81		2.88		173	

Table 3.3: Bulk Au cohesive energy, nearest neighbour distance and bulk modulus calculated in the present work using a DZP basis set, $\delta\varepsilon = 5$ mRy, $E_{\text{cut}} = 300$ Ry and $N_k = 7$, compared with experiment and calculations from the literature.

3.4 Atoms and molecules

To check the validity of the pseudopotentials used for the organic atoms, H, C, N, O and S, we calculated various bond lengths and interaction energies for comparison with experimental and calculated all-electron results from the NIST database [4], given in table 3.4.

Our calculations use pseudopotentials generated with GGA-PBE XC functionals. These functionals are also used in the electronic structure calculations. DZP basis sets with $\delta\varepsilon = 5$ mRy are used for all atomic species. The real-space grid is defined by $E_{\text{cut}} = 300$ Ry. Since these systems are not periodic, a large unit cell is used without k-point sampling.

The bond lengths in our calculations tend to be slightly larger, but are nevertheless in good agreement with the all-electron calculations. When compared to the NIST all-electron data, our calculated interaction energies are better than the NIST pseudopotential data.

In addition, our calculated first (IE^1) and second (IE^2) ionisation energies for

	present work		all electron [4]		pseudopotential [4]		experiment [4]	
molecule	r (Å)	E_{I} (eV)	r (Å)	E_{I} (eV)	r (Å)	E_{I} (eV)	r (Å)	E_{I} (eV)
H_2O	0.977	-9.45	0.973	-9.63	0.974	-9.40	0.958	-9.51
C_2	1.345	-6.53	1.2637	-6.27	1.2964	-4.22	1.243	-6.22
N_2	1.132	-9.33	1.1168	-10.33	1.1321	-8.68	1.098	-9.76
O_2	1.239	-6.66	1.2285	-6.34	1.2329	-4.82	1.208	-5.12
S_2	1.959	-4.93	1.9356	-4.69	1.9417	-4.09	1.889	-4.37

Table 3.4: Calculated bond lengths and interaction energies compared with data taken from the NIST database [4]. The all-electron calculations use the 6-31G** basis set and a GGA-PBE XC functional while the pseudopotential calculations use the CEP-31G* basis set and a B3LYP XC functional.

the various atoms used, compare very well to experimental values, as seen in table 3.5.

	present work		experiment [5]	
atom	IE^1	IE^2	IE^1	IE^2 (eV)
Au	9.27	30.28	9.22	29.7
C	11.65	36.41	11.26	35.64
N	14.86	45.28	14.54	44.14
O	13.29	49.10	13.61	48.76
S	10.08	33.68	10.36	34.0

Table 3.5: Calculated first and second ionisation energies of various atomic species. Experimental values are from Kittel [5].

3.5 Au slabs

In chapter 4 we perform structure optimisations of various molecules on a Au(111) surface. The surface is approximated by n layers of Au atoms. In the plane parallel to the surface, periodic boundary condition ensure the infinite extent of the surface. Enough gold atoms per layer are used and a large enough vacuum gap included in the unit cell above the slab, to ensure that the molecule does not interact with its periodic images or with the periodic image of the slab (see figure 3.18).

Additional tests are required to assess the accuracy of these calculations. Firstly we test for a value of n that gives a reasonable representation of a true

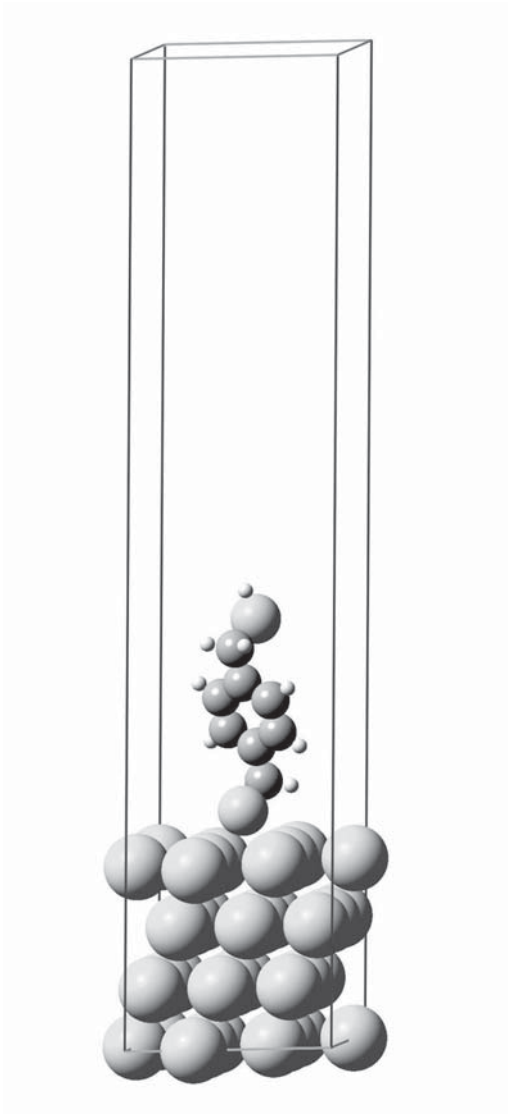

Figure 3.18: Unit cell for in calculations of a molecule on a Au(111) surface. 3x3 Au atoms per layer are used and 4 layers approximate the surface.

semi-infinite surface. To this end, we investigate how the charge density at a height of 1 Å above the surface changes as the number of layers is increased. The charge density is sampled at a grid of 100x100 points above the surface, with 3x3 Au atoms per layer in the unit cell. Figure 3.19 shows the root-mean squared (RMS) and maximum difference in charge density at the sampled points between an n-layer slab and a 13-layer slab. The charge density is well converged for a 4-layer slab.

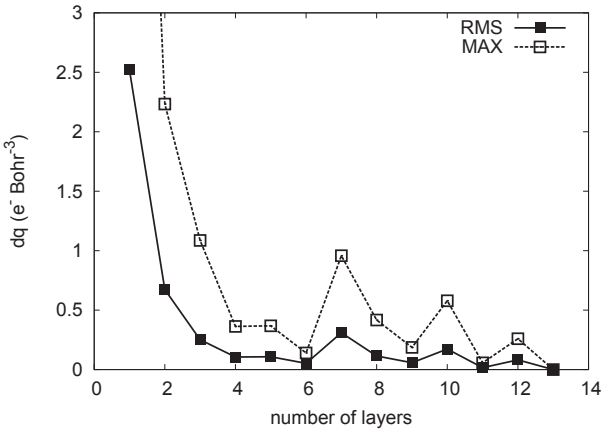

Figure 3.19: Convergence of charge density at a height of 1 Å above the Au(111) surface. The y-values are the RMS and maximum difference between the charge densities above an n-layer and 13-layer slab at the sampled points.

The calculations in chapter 4 were performed with a reference set of parameters summarised in table 3.6. Note that only one k-point is needed in the direction perpendicular to the slab as this direction is not periodic. Also, since there are three gold atoms in each periodic direction, the number of k-points required in each direction is about three times smaller than for the bulk calculation with only one atom in the unit cell.

The interaction energy of 1,4-phenylenedimethanethiol (XYL) on a Au(111) surface is given in table 3.7, together with the interaction energies obtained after changing one of the parameters, but keeping the geometry fixed. The methods used to obtain the optimised geometry will be detailed in chapter 4; here we merely point out that the change in interaction energy is very small and justifies the set of parameters used. The choice of XC functional does however have a

substantial effect on the calculated interaction energy. This is not unexpected; LDA functionals are known to overestimate binding energies, as seen in section 3.3. Each functional should however give consistent trends for interaction energies of different molecules or on different surface binding sites.

parameter	reference value
pseudopotential	as in table 3.1
XC functional	GGA-PBE
basis set size	DZP
energyshift $\delta\varepsilon$	5 mRy
MP grid	3x3x1
meshcutoff E_{cut}	300 Ry
slab layers n	4
electronic temperature T	300 K

Table 3.6: Default set of parameters to use for slab calculations.

changed parameter	new value	E_{I} (kcal/mol)
none	-	-30.0
energyshift $\delta\varepsilon$	1 mRy	-30.6
MP grid	7x7x1	-31.7
slab layers n	7	-33.2
meshcutoff E_{tot}	200 Ry	-30.0
XC functional	LDA-PZ	-49.2

Table 3.7: Effect of changing various computational parameters on XYL-Au(111) interaction energy, E_{I}.

3.6 Transport calculations

In Chapter 5 we describe electronic transport calculations on junctions consisting of a molecule sandwiched between two Au(111) electrodes. Here the system is not periodic; however, the calculation is done on a finite device region with periodic boundary conditions imposed. The coupling to the semi-infinite electrodes is taken into account by including self-energy terms in the system Hamiltonian, which is found from a separate calculation of the bulk electrodes (see section 2.4).

In this section we discuss calculations performed with the TranSIESTA-C and SMEAGOL codes on three representative systems: a gold chain (figure 3.20), 1,4-benzenedithiol (BDT) sandwiched between Au(111) electrodes (figure 3.26) and 1,4-phenylenedimethanethiol (XYL) between Au(111) electrodes (figure 3.30).

Since the gold chain is not periodic in the direction perpendicular to transport (transverse direction), only the Γ-point is needed in this plane. For the molecular junctions, the gold slab is periodic in the tranverse direction and hence the importance of the k-point sampling grid used in this plane is assessed. In all cases the number of k-points used in the direction of transport should be large for the leads calculation in order to simulate metallic leads; generally 100 k-points are used. However, the device region is not periodic in the transport direction and hence only the Γ-point is needed. The large number of k-points in the electrode calculations is not of great concern, since this part of the calculation is relatively cheap compared to the calculation of the device region electronic structure.

3.6.1 Linear gold chain

$I(V)$ characteristics

The $I(V)$ characteristics of a gold chain were evaluated for -1.0 V $\leq V \leq$ 1.0 V with both TranSIESTA-C and SMEAGOL, using different basis sets and XC functionals. Strictly speaking it is unphysical to apply a finite bias across an ideal gold chain with no scattering. However by partitioning the system into electrode and device regions, a contact resistance between the electrodes and device is effectively introduced (see for example toy examples in Ref. [168]). The conductance for such a system is expected to equal the quantum of conductance,

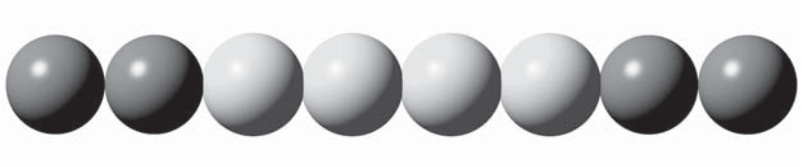

Figure 3.20: Au chain configuration for transport calculations. The dark atoms form part of the semi-infinite leads and the light atoms constitute the device region.

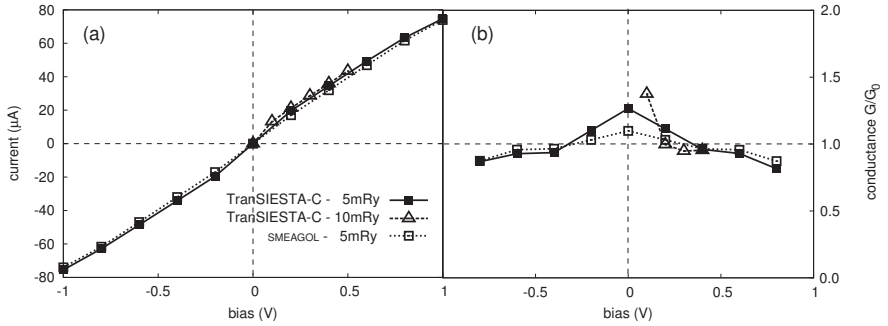

Figure 3.21: (a) Current and (b) conductance for Au chain. Both SMEAGOL and TranSIESTA-C calculations use an SZP basis set. $\delta\varepsilon$ in SMEAGOL is fixed at 5 mRy and in TranSIESTA-C interchanged between 5 and 10 mRy. Since there is no interaction between adjacent unit cells in the transverse direction, only the Γ-point is needed for the transport calculation. An LDA XC functional is used.

$G_0 \approx 77.5\ \mu$S [88].

The results for the current and conductance are plotted in figures 3.21-3.23. Figure 3.21 compares the current and conductance given by TranSIESTA-C and SMEAGOL. TranSIESTA-C calculations with different energyshift parameters are also compared. The effect on the current is minimal; the conductance is changed more substantially, but remains close to G_0.

Figure 3.22 compares the SMEAGOL results with different basis set sizes and also a different energyshift parameter. Again the current is virtually unaffected while the changes in conductance are more noticeable.

Figure 3.23 compares the SMEAGOL results using either an LDA or GGA XC functional. This also has very little effect on the current, and a more pronounced effect on the conductance. An SZP basis set with $\delta\varepsilon = 5$ mRy is used.

The $I(V)$ curves for the gold chain show almost Ohmic behaviour, but the conductance decreases slightly at higher voltages. This has been observed in previous calculations and experiments [120].

Zero bias conductance results

From the above it is clear that the $I(V)$ curve is almost unaffected by the computational parameters, whereas the effect on the conductance is more pronounced. In fact, there are two ways in which the conductance can be calculated. Firstly the

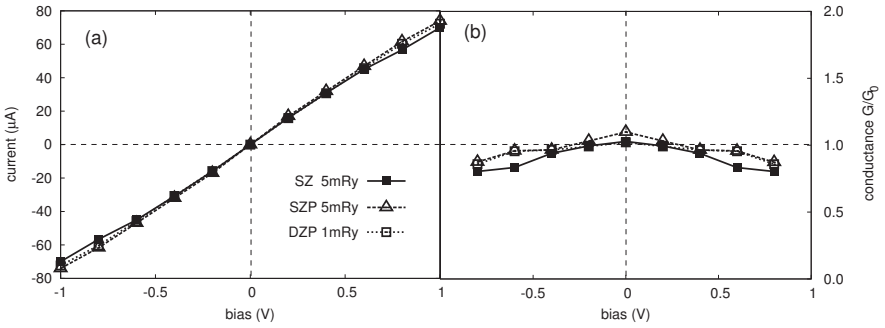

Figure 3.22: (a) Current and (b) conductance for Au chain. SMEAGOL calculations using an LDA XC functional and varying basis set size and $\delta\varepsilon$.

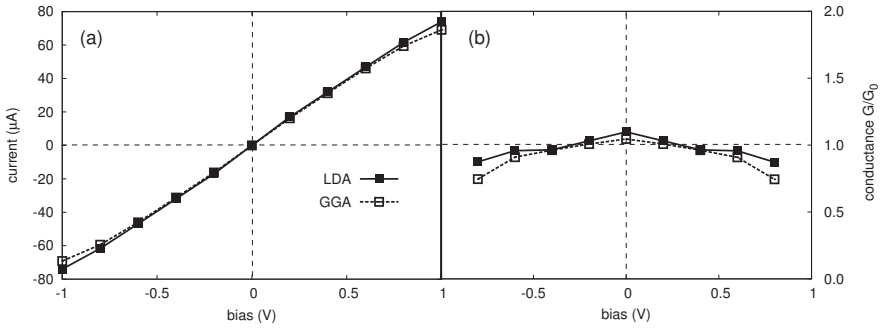

Figure 3.23: (a) Current and (b) conductance for Au chain. SMEAGOL calculations using either an LDA or GGA XC functional with an SZP basis set and $\delta\varepsilon = 5$ mRy.

analytical derivative of the Landauer formula for the current, equation (2.119), yields

$$G(V) = \frac{2e^2}{h} \int_{-\infty}^{\infty} T(E) \frac{1}{2kT} \left[\frac{e^{\frac{E+eV/2}{kT}}}{\left(1 + e^{\frac{E+eV/2}{kT}}\right)^2} + \frac{e^{\frac{E-eV/2}{kT}}}{\left(1 + e^{\frac{E-eV/2}{kT}}\right)^2} \right] \mathrm{d}E \tag{3.2}$$

which reduces to

$$G(V) = \frac{e^2}{h} \left[T\left(\frac{eV}{2}\right) + T\left(-\frac{eV}{2}\right) \right] \tag{3.3}$$

when $T = 0$ K. Alternatively, the conductance can be estimated from successive evaluations of the current

$$G(V) = \frac{I(V + \Delta V) - I(V - \Delta V)}{2\Delta V}. \tag{3.4}$$

The conductance given in figures 3.21-3.23 were based on equation (3.4) with $\Delta V = 0.2$ V and $T = 300$ K.

While equation (3.2) is exact, it is not necessarily the better option, since discontinuities in the transmission function at energies close to the chemical potentials of the electrodes can lead to an unreliable conductance value. This is illustrated in the transmission functions plotted in figure 3.24. At 0 V the transmission function is discontinuous at $E \approx 0$ where the number of transmission channels changes between one and three. Therefore the conductance given by equation (3.3) can be either 1 or 3, depending on the exact location of the discontinuity, $E = \varepsilon$. Introducing a finite temperature into equation (3.2) reduces the sensitivity to ε. The sensitivity is further reduced by using equation (3.4) where the evaluations of the current integrals occur over an interval spanning $E = \varepsilon$.

Figure 3.25 compares the zero bias conductance results evaluated with equations (3.2) and (3.4) at $T = 0$ K and $T = 300$ K, using both TranSIESTA-C and SMEAGOL with an LDA XC functional and SZP basis set with varying energyshift parameter. The conductance is very sensitive to $\delta\varepsilon$ and approaches the expected value of $G_0 \approx 77.5$ μS as the orbitals become less confined. The hollow data points at $\delta\varepsilon = 1$ mRy and 10 mRy in figure 3.25a indicate calculations with a

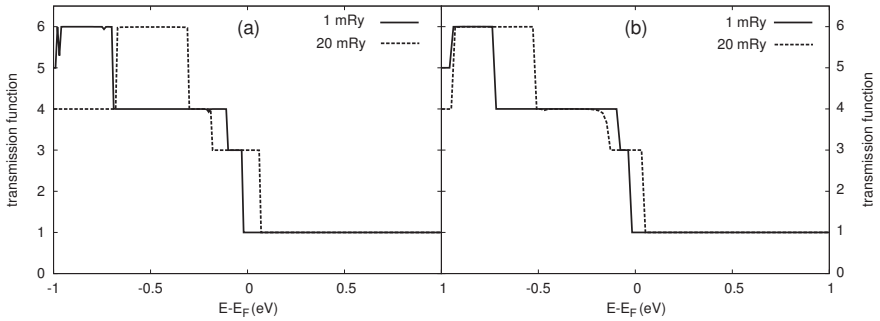

Figure 3.24: Transmission functions at 0 V calculated with (a) TranSIESTA-C and (b) SMEAGOL, with an LDA XC functional, SZP basis set and either $\delta\varepsilon = 1$ mRy or $\delta\varepsilon = 20$ mRy.

DZP basis set and shows that the inclusion of a second ζ orbital is not as important as a larger spatial extent for the first ζ orbital. This will be considered in chapter 5 when an SZP basis set is used throughout. A DZP basis set represents a significant increase in computational resources, since for gold this implies an increase in the number of basis functions per atom from 9 to 15.

Convergence of the zero bias conductance with respect to the orbital confinement is generally faster at zero temperature than at finite temperature. However, when using equation 3.3, a sufficiently small energyshift parameter should be used to ensure that a discontinuous transmission function does not result in an incorrect conductance value.

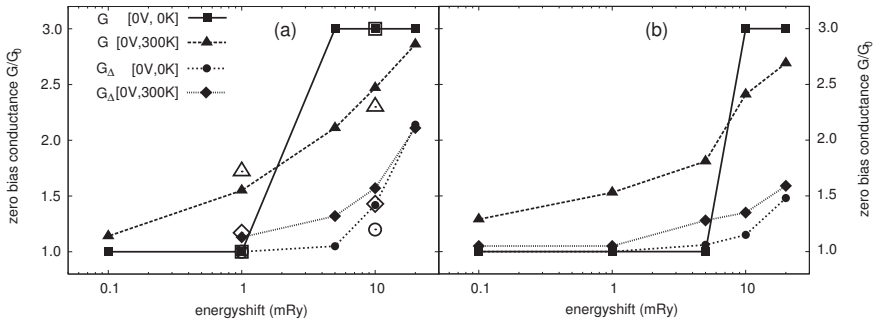

Figure 3.25: Zero bias conductance results of a gold chain calculated using (a) TranSIESTA-C and (b) SMEAGOL using an LDA XC functional and SZP basis set with varying $\delta\varepsilon$. Hollow data points indicate a DZP basis set.

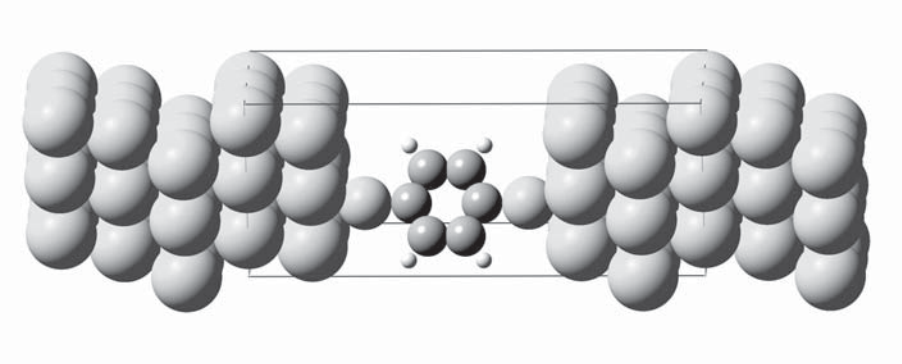

Figure 3.26: Computational setup of the twoprobe transport calculations for the Au(111)-BDT-Au(111) junction. The device unit cell contains the molecule with two surface layers of 3x3 Au atoms on each side. The electrode unit cells contain three layers of 3x3 Au atoms each.

3.6.2 BDT junction

Figure 3.26 shows the left electrode, device region and right electrode unit cells for a Au(111)-BDT-Au(111) junction. The device region contains two surface layers on either side of the molecule. This is to ensure that the electrodes are accurately represented by a bulk calculation, i.e. all surface effects are contained within the device unit cell. Comparative calculations of the current were done including *three* surface layers on the right side of the molecule in the device region. As seen in figure 3.27, the resulting current shows virtually no change.

As the calculation of the $I(V)$ characteristics can be quite computationally expensive, a less accurate set of parameters is usually used than for the geometry optimisations. The complexity of the calculations can be greatly reduced by using a smaller basis set. As seen in section 3.3.1, an SZP basis set on gold atoms yields a similar cohesive energy to a DZP basis set. In section 3.6.1, the $I(V)$ characteristics of a gold chain were only affected very slightly when the basis set was changed beween DZP, SZP and SZ. Figure 3.28 compares the $I(V)$ curves of the BDT junction, using SZP, DZP and a basis set with two orbitals per s-channel and one orbital per d-channel, labeled DZ(s)-SZ(d), on the Au atoms. In all cases DZP basis sets are used for the molecule. This suggests that we are justified in using an SZP basis set for the Au atoms in the transport calculations.

In figure 3.29 the transmission spectra of the BDT junction calculated with

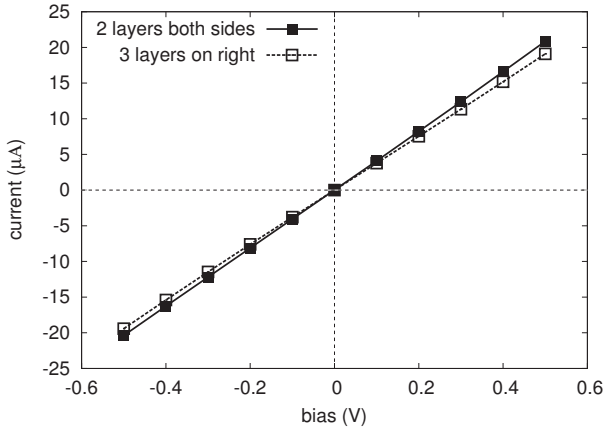

Figure 3.27: $I(V)$-curves for the BDT junction, where two surface layers are included in the device region to the left of the molecule, and either two or three surface layers on the right.

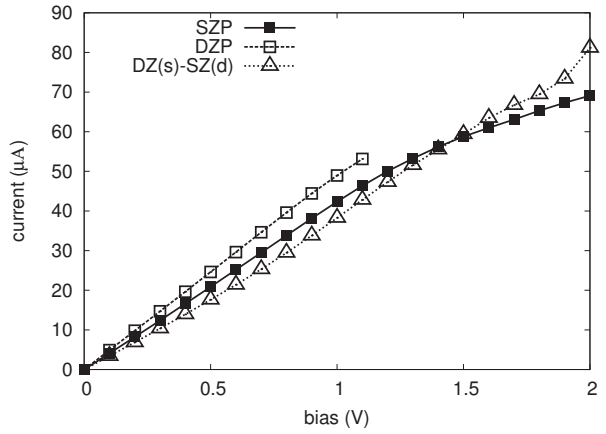

Figure 3.28: $I(V)$-curves for the BDT junction, using different basis sets on the Au atoms. A DZP basis set is used for the molecule. The other parameters are $\delta\varepsilon = 10$ mRy, $E_{\text{cut}} = 150$ Ry and only the Γ-point is used in the calculation.

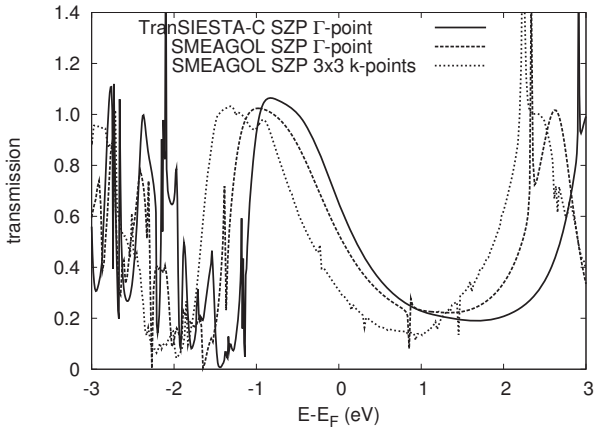

Figure 3.29: Transmission spectrum for the BDT junction, using SMEAGOL with only the Γ-point or 3x3 k-points in the transverse plane, and TranSIESTA-C with only the Γ-point. An SZP basis set is used for the gold atoms and a DZP basis set for the molecule. $\delta\varepsilon = 10$ mRy and $E_{\text{cut}} = 200$ Ry.

SMEAGOL and TranSIESTA-C using only the Γ-point are compared with the spectrum obtained with SMEAGOL using 3x3 k-points in the transverse plane. While the spectra have the same overall shape, the two codes clearly do not produce identical results. Also, the inclusion of modest k-point sampling reduces the transmission function at the Fermi energy and hence the zero biasconductance by a factor of 1.7. The importance of including k-point sampling will be further investigated in section 3.6.3.

3.6.3 XYL junction

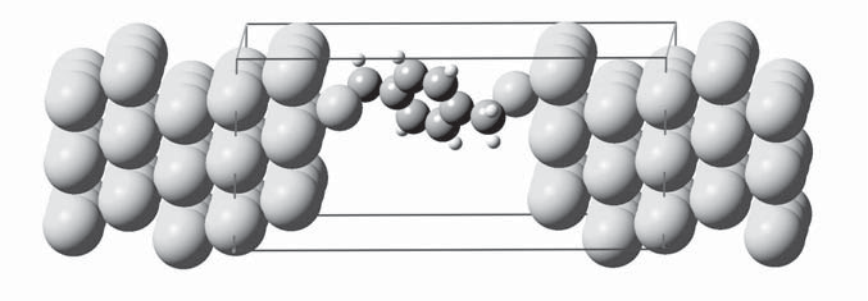

Figure 3.30: Computational setup of the twoprobe transport calculations for the Au(111)-XYL-Au(111) junction.

Figure 3.30 shows the left electrode, device region and right electrode unit

cells for a Au(111)-XYL-Au(111) junction. The setup is similar to the BDT junction. Here we test the effect of the basis set size and orbital confinement as well as the k-point sampling grid on the conductance of the system at zero bias. We have already seen in the case of a gold chain that the choice of basis set has a much larger effect on the conductance than on the current. A DZP basis set will be used throughout on the atoms in the molecule and the basis set on the gold atoms will be interchanged between SZP ($\zeta_{\mathrm{Au}} = 1$) and DZP ($\zeta_{\mathrm{Au}} = 2$). The orbital confinement on all atoms will be varied simultaneously through the energyshift parameter, $\delta\varepsilon$.

In the present system the k-point sampling grid in the transverse direction also becomes important. It has been demonstrated by the TranSIESTA-C authors [174] that more k-points are needed for convergence of the transmission function than the electronic structure. This will be very important for transport calculations and we quantify such behaviour in this section.

We will thus distinguish two k-point grids. The electronic structure is calculated self-consistently on an $N_{\mathrm{E}} \times N_{\mathrm{E}}$ grid and the density matrix given by equation (2.108). The current is then evaluated from equation (2.119) after the Hamiltonian, equation (2.56), and hence the Green's function, is calculated on a finer grid of $N_{\mathrm{T}} \times N_{\mathrm{T}}$ k-points. This is not equivalent to performing the electronic structure calculation on an $N_{\mathrm{T}} \times N_{\mathrm{T}}$ grid, since self-consistency is not achieved in the transmission function calculation. For this reason N_{T} has a much smaller effect on the total calculation time than N_{E}. This can be seen in figure 3.31, where the SCF calculation time is compared to that of the post-SCF calculation of the transmission function.

Figure 3.32 shows the convergence of the total energy and HOMO and LUMO eigenenergies with respect to N_{E}. Here $\zeta_{\mathrm{Au}} = 1$ and $\delta\varepsilon = 20$ mRy are fixed, while N_{E} is varied between 1 and 13. At $N_{\mathrm{E}} = 2$ the total energy is converged to within 1 eV (or 0.01 eV/atom) and at $N_{\mathrm{E}} = 3$ the HOMO and LUMO eigenenergies to within 0.005 eV of the limiting values. More reliable total energy results are obtained by including the gamma point in the k-space integration and this is achieved by using an odd number of k-points along the transverse directions. We therefore use $N_{\mathrm{E}} = 3$ for most of the transport calculations in chapter 5.

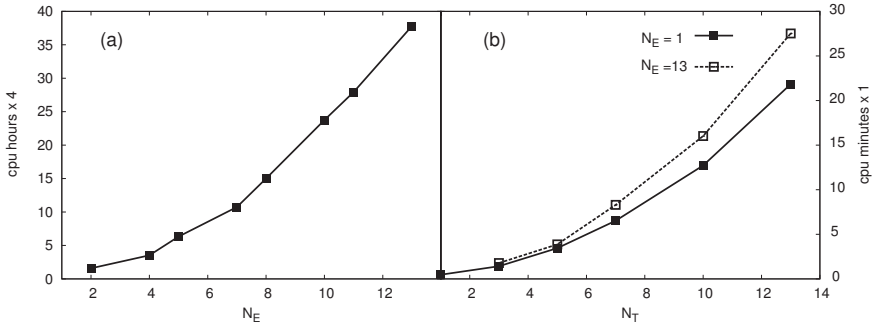

Figure 3.31: (a) Number of hours required on 4 cpu's in parallel to complete the SCF calculation of the electronic structure of the XYL junction with an increasing k-point grid. (b) Number of minutes required on 1 cpu to calculate the transmission function after the electronic structure has been converged with either a 1x1 or 13x13 k-point grid.

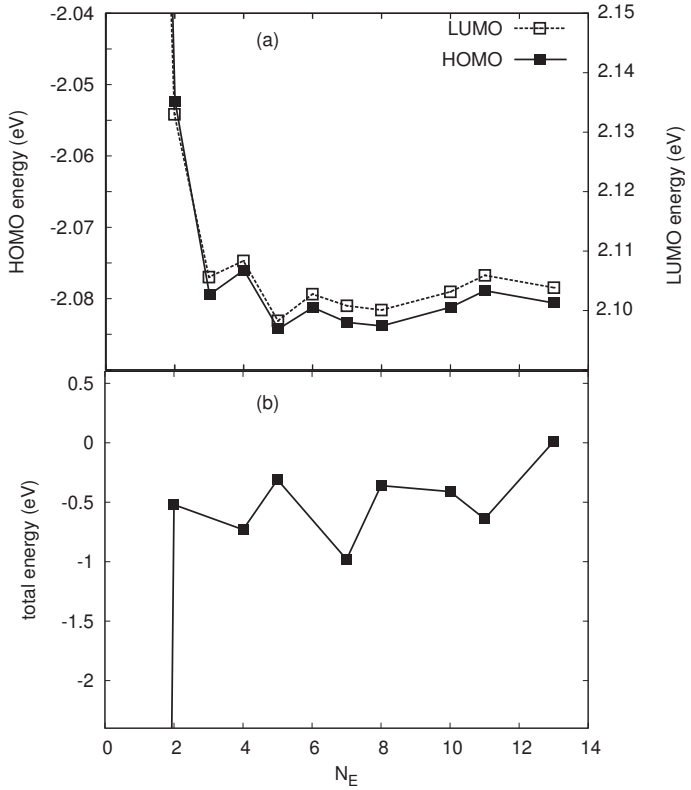

Figure 3.32: (a) HOMO and LUMO eigenenergies and (b) total energy of the XYL junction with different k-point grids for the self-consistent electronic structure calculation.

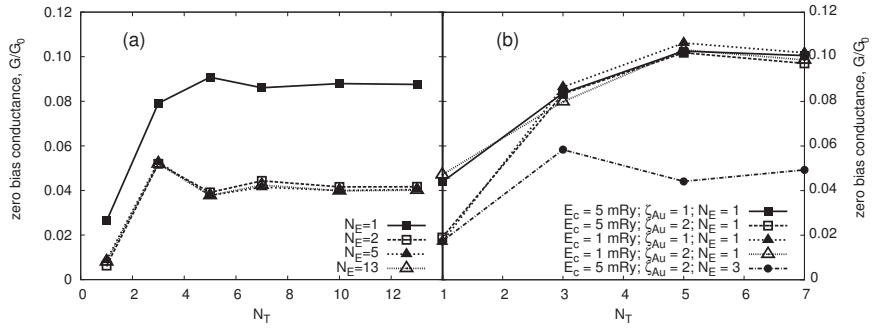

Figure 3.33: Convergence of zero bias conductance results of the XYL junction with the size of the k-point grid used to evaluate the transmission function, (a) for different SCF k-point grids and (b) with different sets of parameters.

For efficiency only the 0 V transmission function was calculated for the XYL junction. The conductance at zero bias was therefore calculated from equation (3.2), since the finite-bias current needed in equation (3.4) was not available. The use of a finite temperature avoids the problem of a discontinuous transmission spectrum.

Figure 3.33 shows the convergence of the zero bias conductance results calculated from equation (3.2) using $T = 300$ K, as a function of N_{T} for various choices of ζ_{Au}, $\delta\varepsilon$ and N_{E}. In figure 3.33a the basis set parameters are kept fixed, $\zeta_{\mathrm{Au}} = 1$ and $\delta\varepsilon = 20$ mRy, while N_{E} and N_{T} are varied. The converged conductance value at $N_{\mathrm{E}} = N_{\mathrm{T}} = 13$ is $G = 0.0401\ G_0$. With $N_{\mathrm{T}} = 5$ and $N_{\mathrm{E}} = 2$, G is converged to within 10% of this limiting value. In chapter 5 we use $N_{\mathrm{T}} = 13$, since increasing N_{T} has very little effect on the computational time, see figure 3.31.

In figure 3.33b ζ_{Au}, $\delta\varepsilon$ and N_{E} are varied simultaneously. For $N_{\mathrm{T}} = 1$, G changes by up to a factor of three depending on the other parameters, although the errors introduced by the basis set size and energyshift appear to cancel. However when convergence is reached with respect to N_{T}, it seems that the basis set parameters do not affect the converged value, whereas the k-point sampling used for the electronic structure does have an effect.

Finally in figure 3.34 the convergence of both the total energy and zero bias-conductance with the energyshift parameter is tested, while $\zeta_{\mathrm{Au}} = 1$ and $N_{\mathrm{E}} = 1$ are fixed. Taking the values at $\delta\varepsilon = 0.01$ mRy to be converged, the total energy at

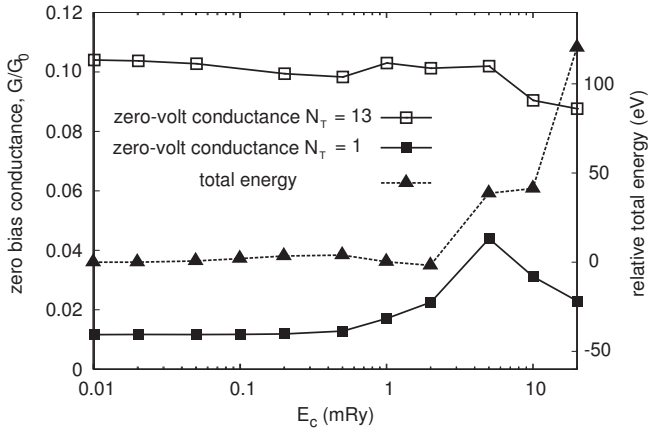

Figure 3.34: Convergence of zero bias conductance and total energy of the XYL junction as a function of $\delta\varepsilon$.

$\delta\varepsilon = 2$ mRy is converged to within 4 eV (or 0.04 eV/atom) of the limiting value. At $\delta\varepsilon = 5$ mRy, G evaluated with $N_\mathrm{T} = 13$ is converged to within 6%. However, G evaluated with $N_\mathrm{T} = 1$, is only well converged at $\delta\varepsilon = 5$ mRy, to within 10% of the limiting value. This is consistent with the finding from figure 3.33b, i.e. when convergence is reached with respect to N_T, the basis set parameters have a much smaller effect on the converged value of G.

Based on the extensive testing presented in this section, table 3.8 lists a set of reference parameters used for transport calculations. The meshcutoff was reduced to 150 Ry in most cases due to the large memory requirements of these calculations. LDA and GGA functionals were used, although interchanging these did not have a large effect, as shown in figure 3.23. The TranSIESTA-C authors also find very little effect on the transmission function of the Au(111)-BDT-Au(111) junction when changing the XC functional [125].

3.7 Summary

Our pseudopotential based DFT calculations of the cohesive energy, lattice constant and bulk modulus of gold produce results that compare favourably to pseudopotential and all-electron calculations as well as experimental data in the literature. For the organic elements used in this work, our calculated bond lengths and interaction energies of the corresponding dimers as well as first and second

parameter	reference value
basis set size on molecule	DZP
basis set size on gold	SZP
energyshift $\delta\varepsilon$	5 mRy
MP grid for electronic structure	3x3x1
MP grid for post-SCF transmission calculation	13x13x1
meshcutoff E_{cut}	150 Ry
electronic temperature T	300 K

Table 3.8: Default set of parameters to use for transport calculations.

ionisation energies are in good agreement with accurate calculations in the literature. These results instill confidence in the pseudopotentials used and the level of accuracy of the parameters describing the other approximations, i.e. details of the basis set and the k-space and real-space integration grids. Most calculated values are close to their experimental counterparts, which suggests that the exchange-correlation approximation is reasonable.

A default set of parameters (table 3.6) have been established for use in calculations of molecular adsorption on the Au(111) surface. In addition to the standard DFT parameters, this includes the size of the gold slab required to accurately represent a gold surface.

Several transport calculations were performed on a one-dimensional gold chain and molecular junctions consisting of a single BDT or XYL molecule sandwiched between three-dimensional gold electrodes. Table 3.8 lists the resulting set of recommended parameters for transport calculations. The calculated conductance and current were much more sensitive to the k-point sampling grid than the basis set.

Chapter 4

Molecular Surface Adsorption

In this chapter we use SIESTA to find the optimum adsorption geometry of various molecules on an Au(111) surface. In all cases low coverage is assumed and we use enough gold atoms per layer so that molecules in adjacent unit cells do not interact; usually 3x3 Au atoms per layer is sufficient.

The first step is a CG optimisation of the molecule in the gas phase within a large unit cell. The optimised molecule is then placed on the surface, in some cases after removal of a terminal hydrogen atom. The total energy of the system is minimised by a coordinate optimisation of the molecule on the surface using either the CG or BFGS algorithm. Usually the surface atoms are fixed in their bulk positions. The geometry is considered relaxed when the maximum force on any atomic coordinate is less than a certain tolerance level, usually $l_{\mathrm{tol}} = 0.04$ eV/Å for lengths and $\theta_{\mathrm{tol}} = 0.0009$ eV/deg for angles.

Alternatively a manual scan of the position of the molecule relative to the surface is performed to obtain a detailed description of the PES. The latter is defined by the binding site, the height above the surface and the angles of rotation of the molecule relative to the surface.

Figure 4.1 shows a top view of the Au(111) surface. The triangle with its vertices at the ontop, fcc and hcp sites contains all distinct binding sites, and any other position on the surface is symmetrically equivalent to some point in this triangle.

The interaction energies of molecules on the Au(111) surface reported here,

are calculated according to

$$E_{\mathrm{I}} = E_{\mathrm{tot}} - E_{\mathrm{surf}} - E_{\mathrm{mol}}. \tag{4.1}$$

E_{tot} refers to the total energy of the optimised molecule-surface system; E_{surf} and E_{mol} are the energies of the surface and molecule subsystems with the same geometry as in the combined system. The basis set is kept fixed in the calculation of all three energies, i.e. the basis functions associated with all atoms in the total systems are retained in the calculation of the subsystem energies. This constitutes the counterpoise correction [149] to the basis set superposition error (see section 2.2.1).

Based on the tests in chapter 3, we use a DZP basis set on all atoms with an energyshift parameter of $\delta\varepsilon = 5$ mRy for orbital confinement, a meshcutoff of $E_{\mathrm{cut}} = 300$ Ry to define the real-space grid and 4 slab layers to approximate the surface. An MP grid of 5x5x1 k-points is generally used for the k-space integration in surface calculations. Where computational efficiency is of greater concern, this is reduced to 3x3x1. Calculations on the isolated molecules use only the Γ-point with a unit cell sufficiently large to rule out interactions of the molecule with its periodic images. Unless otherwise stated, calculations in this chapter use the GGA-PBE XC functional.

4.1 Surface properties of Au(111)

It is important to assess how well the present level of theory can describe the properties of a surface, before molecular adsorption is investigated.

4.1.1 Surface relaxation and reconstruction

A surface does not have the same crystalline and electronic structure as the corresponding bulk material. To achieve the minimum energy structure, the upper layers of surfaces can reconstruct due to the lower coordination of the surface atoms. STM measurements of a gold (111) surface [175] have revealed a $(22 \pm 1) \times \sqrt{3}$ reconstruction, resulting in a contraction of 4.2 % in the $[1\bar{1}0]$

direction. The position of the top layer of atoms varies along the fcc-bridge-hcp direction, with a corrugation height between fcc and bridge sites of 0.15 Å [175]. Although *ab-initio* studies of this reconstruction are not feasible due to the large unit cell needed, Takeuchi *et al.* [176] used DFT to show that the surface energies of atoms in fcc, hcp and bridge sites are very close in magnitude, which is a prerequisite for reconstruction. Another necessary condition for reconstruction, is the tendency for the outer layer to contract to a higher density than a bulk Au(111) layer. We provide evidence for this effect in figure 4.2. The lattice constant (both normal and perpendicular to the surface) was calculated for ultra-thin films with different numbers of layers, in the same way as in section 3.3.2. As the number of layers increases, the lattice constant approaches that of bulk Au, but for a single layer, we observe a 5% contraction.

In addition to the reconstruction of the top layer, the distance between the outer layers of a surface may contract relative to the bulk interlayer distance. This is very difficult to observe experimentally due to the lack of ordered structure on the surface; Van Hove and Tong summarised low energy electron diffraction (LEED) measurements for various surfaces and report no change in the bond length and hence surface interlayer distance of unreconstructed gold (111) [177]. There is some variation in *ab-initio* results of interlayer relaxation. Masens *et al.* [178] find contractions of 1.43% and 2.35% for the outer and second layer spacings respectively, using the SIESTA code. Grönbeck *et al.* [173] report a 1% contraction of the outer layer using DFT with various XC potentials. Yourdshahyan *et al.* [179] on the other hand calculate a 1% expansion of the outer layer together with a 0.5% contraction of the second layer using plane-wave DFT. Our results in general indicate an expansion of the outer layer and a contraction of the second layer; however the behaviour was found to dependent on the computational parameters used.

4.1.2 Surface energy

DFT results for the surface energy of Au(111) also show large variation [179–182], suggesting that the calculation of surface properties at this level of theory presents a significant challenge.

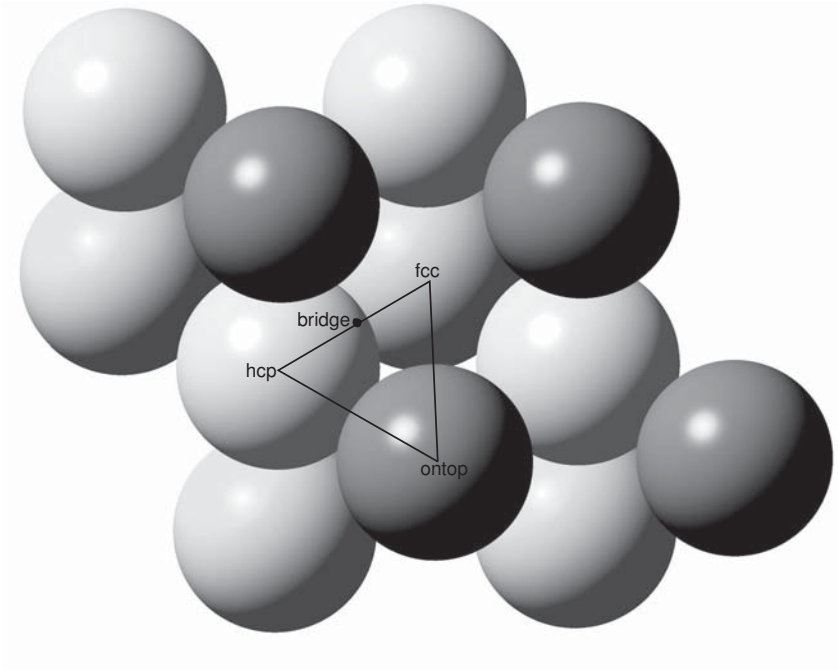

Figure 4.1: Top view of the Au(111) surface. The triangle includes all the inequivalent binding sites.

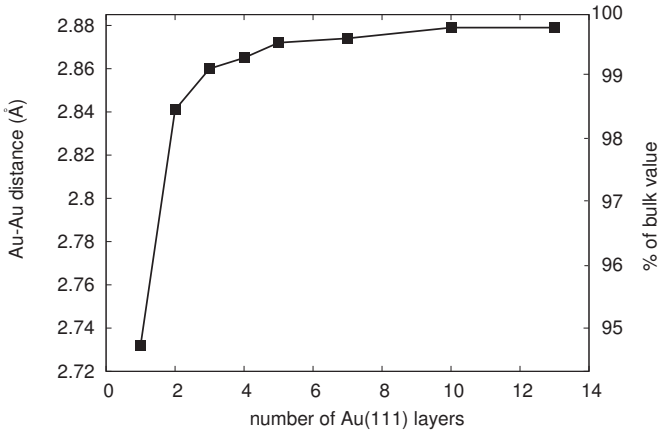

Figure 4.2: The optimum lattice constant of Au(111) slabs approach that of bulk gold.

The surface energy of an n-layer slab with total energy E_n is given by

$$E_{\mathrm{S}}(n) = \frac{1}{2}(E_n - nE_{\mathrm{bulk}}). \tag{4.2}$$

The factor $\frac{1}{2}$ accounts for the fact that the slab has two surfaces. E_{bulk}, the bulk energy per layer, can be taken from an independent calculation of the bulk material or estimated as the difference in energy between n- and $(n-1)$-layer slabs, as proposed by Boettger [1].

In an electronic structure calculation of a bare surface, it is only necessary to use one atom per layer. This is repeated periodically to represent the surface. A denser k-point grid is therefore needed to sample the Brillouin zone accurately. Figure 4.3 shows the surface energy of Au(111) calculated from equation (4.2) using the total energy of slabs with varying thickness. The slab calculations use a 19x19 k-point grid in the plane parallel to the surface and an energyshift parameter of 0.1 mRy.

We find $E_{\mathrm{S}}(n) = 0.31$ eV/atom, or 41 meV/Å^2, when the bulk energy is calculated independently. The method of estimating the bulk energy from successive slab calculations produce large variations in the surface energy evaluated with different slab thicknesses. The experimental value of ~ 96 meV/Å^2 is much larger than our calculated result, but is an extrapolation of high-temperature data averaged over the faces of polycrystalline gold [183]. It may be expected that the (111) surface has lower energy. Crljen *et al.* [182] and Yourdshahyan *et al.* [180] both find $E_{\mathrm{S}} \sim 50$ meV/Å^2 using plane-wave DFT with a GGA XC functional.

4.1.3 Work function

The surface work function is calculated as the difference between the electrostatic potential in vacuum (i.e. at a position in the unit cell far above the surface) and the Fermi level,

$$\phi = V_{\mathrm{vac}} - E_{\mathrm{F}}. \tag{4.3}$$

Although very accurate work function calculations are possible when using plane-wave basis sets [184], the situation is more challenging when using local orbital

basis sets and results tend to be highly basis set dependent [185]. This is because the localised basis functions do not extend naturally beyond the edge of a surface as plane waves do. Doll [186] introduced a scheme of adding basis functions to the vacuum region in the same way that basis functions are added to correct for the basis set superposition error (see section 2.2.1). This method showed improved results.

We test for convergence of the work function with respect to three computational parameters: the number of layers used to estimate the surface n, the energyshift $\delta\varepsilon$ and the k-point grid in the plane of the surface. The convergence tests are carried out independently for each parameter - the common set of parameters is indicated where the three curves in figure 4.4 cross, i.e. $n = 4$, $\delta\varepsilon = 5$ mRy and 13x13 k-points. One parameter at a time is then changed and the other two kept fixed at these values. We find that the work function is well converged for $n = 10$, $\delta\varepsilon = 0.1$ mRy and 15x15 k-points. Repeating the calculation with these three parameters used simultaneously yields a work function for Au(111) of $\phi_{\mathrm{Au}} = 5.13$ eV. Notably, the work function is very sensitive to the orbital confinement defined through $\delta\varepsilon$, whereas the number of slab layers and k-points do not have as large an effect. Our calculated value is in reasonable agreement with the experimental result of 5.31 eV measured using the photoelectric effect [187]. The systematic improvement in basis set obtained by varying the SIESTA energyshift parameter appears to be a very effective technique leading to calculated work functions at a level of accuracy not previously achieved with local orbital basis sets. In order to obtain a converged solution a very small cutoff energy of $\delta\varepsilon = 0.1$ mRy should be used. This is in contrast with typical cutoff energies of $\delta\varepsilon = 5$ mRy which are usually sufficient for surface adsorption studies. It would be interesting to investigate the effect of improving the basis set size beyond the DZP approximation used here.

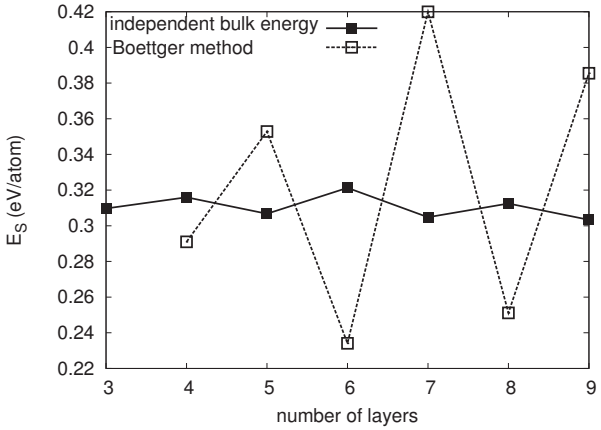

Figure 4.3: Au(111) surface energy calculated using a GGA XC potential, 19x19x1 k-point grid, DZP basis set with $\delta\varepsilon = 0.1$ mRy. The bulk energy per atom was calculated independently and used throughout (solid data points) or estimated from consecutive slab calculations according to the method of Boettger [1] (hollow data points).

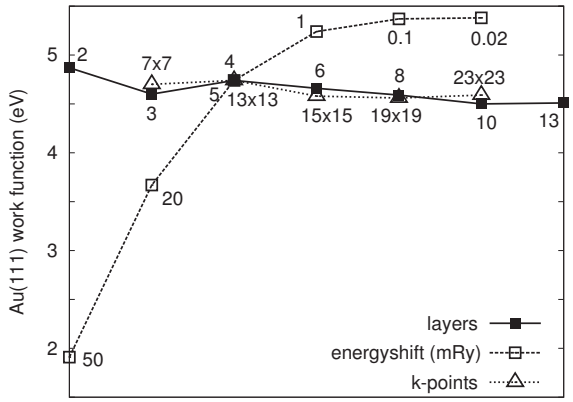

Figure 4.4: Convergence of Au(111) work function with computational parameters.

4.2 Implementation of a Z-matrix optimiser in the SIESTA code

In section 2.3.3 the use of Z-matrix internal coordinates was discussed as a technique for optimising nuclear geometries. This coordinate system is particularly intuitive for molecules. For the atomic coordinates of surfaces that consist of a lattice of points, Cartesian coordinates seem more intuitive. When the aim is to calculate adsorption geometries of molecules on surfaces, it is therefore appropriate to describe the geometry with a mixture of Cartesian and Z-matrix coordinates.

In many cases it is desirable to fix molecular coordinates relative to the surface, or to freeze certain atomic coordinates during an optimisation. This facilitates surface scans of the molecule, when a full CG or BFGS optimisation is not feasible or does not find the global minimum. Furthermore, it enables transition state searches by coordinate driving, i.e. fixing a certain variable stepwise at increasing values and relaxing the remaining geometry.

4.2.1 Algorithm and code

A module named ZMATRIX was added to the SIESTA code to handle most tasks related to the Z-matrix optimiser [61]. In addition, the conjugate gradients optimiser was modified to handle Z-matrix coordinates, as discussed below.

Input

A block of atomic coordinates as well as a number of parameters related to the Z-matrix optimisation are read from the input file. The coordinate block consists of any number of separate Z-matrix and Cartesian blocks, specified with the MOLECULE and CARTESIAN keywords respectively. For example, many molecules can be specified with separate Z-matrices. Each coordinate, whether part of a Z-matrix or Cartesian block, may be specified numerically or symbolically. All defined symbols must be given initial values in one of three seperate blocks, CONSTANTS, VARIABLES or CONSTRAINTS, and will accordingly either be included in the optimisation or fixed. For the coordinates specified numerically, flags are

set to state whether the coordinate is a constant or variable. Symbols initialised in the CONSTRAINTS block are fixed by a linear relation to another symbol, e.g. coordinate y may be given by $Ax+B$ where x is another symbol and A and B are numerical values. The input is checked for circular and inconsistent definitions and appropriate error messages displayed if needed. This style of input is useful for fixing certain symmetries in the geometry, a function which is not otherwise available in SIESTA.

Parameters are read from the input file that specify the coordinate units, the maximum coordinate displacement in a CG step and the force tolerance below which a coordinate is considered to be relaxed. Each coordinate is classified as being either a length or an angle and these three parameters are given seperately for angles and lengths. All Cartesian coordinates as well as bond lengths in a MOLECULE block are classified as lengths, whereas all angles and torsions in a MOLECULE block are classified as angles.

For a detailed description of the Z-matrix input, see the SIESTA manual [188].

Z-matrix to Cartesian coordinate conversion

Before the self-consistent calculation of the electronic structure at each iteration of the optimisation, the coordinates must be converted from Z-matrix to Cartesian format. This is done by looping over all Cartesian and Z-matrix blocks and over all atoms within each independent block. The coordinates of atoms in the Cartesian blocks remain unchanged. In each Z-matrix block, the fourth atom onwards is specified by a bond length, angle and torsion relative to three other atoms defined earlier in the same block. Given the Cartesian coordinates of these three atoms (already calculated), standard mathematical expressions are used to convert the coordinates of the current atom. The first three atoms in each Z-matrix block are handled separately, as their coordinate formats are different. The first atom is given in Cartesians and its coordinates remain unchanged. The second atom is given by spherical coordinates relative to the position of the first atom. The third atom torsion is given relative to a dummy atom positioned 1 unit above the second atom in the z-direction. The bond length and angle for the third atom are given relative to the first two atoms in the same way as the

subsequent atoms.

The onus is on the user to check that atoms are not specified relative to three collinear atoms.

Cartesian to Z-matrix force conversion

After the self-consistent electronic structure calculation at each CG iteration, the forces are calculated as the partial derivatives of the total energy with respect to the Cartesian coordinates of the atoms (see section 2.3). These Cartesian forces must be converted to the equivalent forces on the Z-matrix coordinates, using equation (2.83) in section 2.3.3. The matrix of partial derivates, $M_{mn} = \frac{\partial R_n}{\partial Z_m}$, is calculated by finite differences.

In light of the way in which the Z-matrix coordinates can be specified as fixed, variable or dependent on another coordinate, care has to be taken when setting up the array of optimisation variables to pass to the CG routine. In what follows we refer to this array as Z, while the full set of input coordinates is labeled $\mathcal{Z}$. Each coordinate that is allowed to vary and given numerically in the input, is included in Z. Each symbol x defined in the input that is initialised in the VARIABLES block, is included in Z. However, when this symbolic variable is updated in the method of finite differences, all its dependent coordinates must also be updated. This includes all Z-matrix coordinates defined by x or any other symbol which is dependent on x through a linear relation specified in the CONSTRAINTS block. Linked lists are used in the implementation to keep track of the set of coordinates dependent on each symbol.

Each variable $Z_m \in Z$ in turn is incremented and decremented by a specified small amount h^m, where $h^m = 10^{-6} Z_m$ if $Z_m \neq 0$ and $h^m = 10^{-6}$ if $Z_m = 0$. The linked lists are used to find all coordinates dependent on Z_m and these coordinates are updated accordingly, either by adding and subtracting h^m if the coordinate is defined by the symbol x underlying the variable Z_m, or by adding and subtracting $Ah^m + B$ if the coordinate is defined by another symbol y, dependent on x through a linear relation, $y = Ax + B$. This yields two full sets of Z-matrix coordinates, $\mathcal{Z}^{m+}$ and $\mathcal{Z}^{m-}$, obtained by adding and subtracting respectively. The Z-matrix to Cartesian coordinate conversion can now be used to find the two corresponding

sets of Cartesian coordinates R^{m+} and R^{m-}. The matrix M is then evaluated by

$$M_{mn} = \frac{R_n^{m+} - R_n^{m-}}{2h^m} \tag{4.4}$$

for each pair of forwards and backwards difference Cartesian coordinates $R_n^{m+} \in R^{m+}$, $R_n^{m-} \in R^{m-}$. In practice it is not necessary to recalculate all the Cartesian coordinates. In each Z-matrix input block only atoms after and including the first atom affected by the change in Z_m need to have their Cartesian coordinates updated. In Cartesian input blocks only atoms directly affected by a change in Z_m need their Cartesian coordinates updated.

Conjugate gradients optimisation of Z-matrix variables

The CG algorithm is independent of the set of coordinates being optimised. A small difference in the implementation for Z-matrix coordinates is needed to allow the maximum displacement and tolerance parameters to be specified independently for length and angle variables, as discussed above for the input. In the original SIESTA implementation these parameters are passed as real numbers to the CG routine, to be used for all coordinates equivalently. This is replaced by an array for each parameter, specifying individual tolerances and maximum displacements for each variable. Before invoking the CG routine, the arrays are filled up according to the length/angle classification of each variable.

A linear relation specified between symbols with different length/angle classification will be honoured, but the maximum displacement and tolerance of the dependent symbol will not correspond to its classification.

4.2.2 Testing

In order to assess the soundness and usefulness of the implementation, geometry optimisations were performed for three representative molecules, water, benzene and hexanedithiol, as well as two molecular adsorption problems, methanethiol on Au(111) and benzenethiol on Au(111).

Molecule	No of atoms	Coordinates	No of variables	No of CG steps I	II	III
Water	3	Cartesian	6	15	15	15
			9	35	37	40
		Z-matrix	2	6	8	8
			3	3	6	9
			6	3	6	9
			9	4	19	21
Benzene	12	Cartesian	33	25	33	36
			36	7	9	9
		Z-matrix	2	7	11	18
			11	12	14	20
			30	47	57	69
			33	45	58	63
			36	44	55	66
Hexanedithiol	22	Cartesian	63	76	108	171
			66	44	46	81
		Z-matrix	60	20	33	44
			63	24	39	115
			66	32	397	-

Table 4.1: Number of CG steps required to optimise the geometry of three molecules in Z-matrix and Cartesian coordinates. Columns I, II and III represent progressively stricter convergence criteria for lengths and angles, namely I: (0.04 eV/Å,0.0009 eV/deg); II: (0.02 eV/Å,0.0004 eV/deg); III: (0.01 eV/Å, 0.0002 eV/deg). For Cartesian coordinate optimisations only the length tolerance is relevant.

Isolated molecules

CG optimisations were performed for the three molecules, using either Cartesian or Z-matrix coordinates. Identical initial geometries were used for the two methods and represent a reasonable guess at the optimum geometry for each molecule. The number of CG steps required to reach a relaxed geometry was recorded for three increasingly strict tolerance levels, as described in table 4.1. Table 4.1 also lists the number of steps needed to reach the relaxed geometry at each tolerance level for different numbers of optimisation variables. The number of internal degrees of freedom of an isolated molecule with N atoms is $3N-6$. In the Cartesian implementation, the only available constraint is fixing the position of any atom. The position of one atom can be fixed, leaving $3N-3$ optimisation variables, but

fixing the position of two or more atoms restricts the internal degrees of freedom. Cartesian geometry optimisations are thus performed with either $3N$ or $3N-3$ variables.

In the Z-matrix implementation any of the optimisation variables can be fixed. Hence exactly $3N-6$ variables are needed to relax the internal degrees of freedom. This is achieved by fixing the Cartesian coordinates of the first atom (translational degrees of freedom) and the second and third coordinates of the second atom together with the third coordinate of the third atom (rotational degrees of freedom). Symmetry arguments may lead to a reduction of optimisation variables, for example by setting the O-H bonds in water as equivalent. Thus Z-matrix optimisations are performed with $3N$, $3N-3$, $3N-6$ and possibly a further reduced number of variables.

The Z-matrix optimisation completes in far fewer steps in the case of water, although the use of symmetry does not improve the performance any further.

For the chain-like hexanedithiol the Z-matrix optimisation outperforms the Cartesian case at tolerance level I. At stricter tolerance levels, the Z-matrix performance remains good if the external degrees of freedom are fixed. However, when the rotational degrees of freedom are relaxed (63 variables), the optimisation requires significantly more steps, and when the translational degrees of freedom are relaxed (66 variables), the optimisation at stricter tolerances is very troublesome. Fixing the translational degrees of freedom in the Cartesian optimisation significantly *increases* the number of optimisation steps needed at all tolerance levels.

In the case of the cyclic benzene molecule, the Cartesian optimisation performs better than the Z-matrix optimisation. This is to be expected for cyclic molecules due to coupling between non-redundant internal coordinates [189,190]. However, using the symmetry of the molecule to reduce the number of variables greatly improves the Z-matrix performance, making it comparable with the Cartesian case. Again fixing the translational degrees of freedom in the Cartesian optimisation, hampers the performance. This is not surprising for a method such as CG that does not utilise a Hessian matrix [61].

The final geometries of the molecules are not sensitive to the coordinate sys-

tem, the tolerance level or number of optimisation variables. The maximum geometry variation is about 0.002 Å for lengths and 1.5° for angles.

Surface adsorption

Comparison of the optimisation of methanethiol and benzenethiol on an Au(111) surface using either Z-matrix or Cartesian coordinates, revealed some important advantages of the Z-matrix optimiser specific to surface adsorption calculations [61, 62]. The surface was specified in Cartesian coordinates and the molecules in the Z-matrix format. For both methanethiol and benzenethiol the Z-matrix CG optimisation resulted in the correct final geometry, i.e. with the sulphur atom slightly offset from the bridge site towards the fcc site (see Ref. [180] and also section 4.3). The correct tilt angles for both molecules were also obtained from the Z-matrix optimisations. When the entire system was specified in Cartesian coordinates, the molecule remained upright and failed to move to the correct binding site; this was the case for all starting positions tested - bridge, fcc and hcp - and remained unchanged even when the force tolerance was reduced from 0.04 eV/Å to 0.01 eV/Å [62]. Furthermore, the Z-matrix optimisation resulted in the fcc and hcp sites being local maxima, whereas Cartesian optimisations classify these as local minima [61, 180].

The reason for the increased success of the Z-matrix over the Cartesian optimisation is a very flat PES with respect to the tilt angle of the molecule [61, 62]. This is overcome in Z-matrix coordinates by the decoupling of the tilt angle from all other variables and specifying a strict tolerance for angles. Also the ability to relax the molecule in a fixed binding site (i.e. fixing the x-y coordinates of the sulphur atom, but relaxing its z-coordinate together with the rest of the molecule) results in a much more detailed mapping of the PES than performing a scan of the fixed molecule across the surface [61, 62], as was the case in previous work [180]. It appears that Cartesian optimisations of this type are more susceptible to terminating in local minima.

The optimum binding geometry and barrier to dissociation of dimethyl disulphide and diphenyl disulphide were also calculated with the Z-matrix optimiser. Again a more favourable final geometry was obtained with Z-matrix coordinates

and the result was robust with respect to the starting geometry [62]. The dissociation barrier was estimated by fixing the S-S bond at increasing lengths and relaxing the remaining geometry. This approach can only give an estimate to the true barrier since multi-reference methods are required to desribe the interaction at intermediate geometries where the bond is "nearly broken" [62]. However in a Cartesian representation such coordinate driving would be much more troublesome.

4.3 Phenylenedimethanethiol on Au(111)

The 1,4-phenylenedimethanethiol (XYL) molecule shown in figure 4.5 was CG optimised in the gas phase. The hydrogen atom was removed and the radical placed on the Au(111) surface. It is generally accepted that thiols can chemisorb to the gold surface after cleavage of the S-H bond (see for example Refs. [180] and [173]). We shall refer to such a bond as thiolate; an alternative physisorbed state where the hydrogen is retained (thiol bond) will also be investigated.

A CG optimisation of the molecule with the surface atoms fixed resulted in a sulphur binding height of 2.10 Å above the surface, slightly offset from the bridge site towards the fcc site. The angle between the phenyl ring and the surface normal in the optimum geometry was 21°. This geometry is shown in figure 4.8c. The interaction energy corrected for the BSSE, is $E_{\mathrm{I}} = -30$ kcal/mol. This is close to the calculated interaction energy for methanethiol on gold of $E_{\mathrm{I}} \sim -40$ kcal/mol (see for example [180] and references therein). The optimisation was performed in Cartesian coordinates with a force tolerance of 0.04 eV/Å.

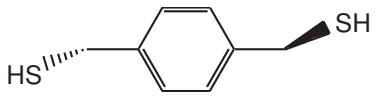

Figure 4.5: 1,4-phenylenedimethanethiol

A surface scan of the rigid molecule at different binding sites was performed in combination with a scan for the optimal height at each site. This confirmed that the CG optimisation terminated in a global minimum with respect to the position of the sulphur atom above the surface. Figure 4.6 shows the PES with

respect to the surface scan, where the interaction energy at each site corresponds to the optimal height of the molecule at that site. The optimal position and interaction energy are the same as that found from the CG optimisation. The most favourable binding sites are concentrated around the bridge site and along the path between fcc and hcp sites. Towards the ontop position the interaction is less favourable, although the difference in interaction energy between the bridge and ontop sites is only 8 kcal/mol. The optimal height at the ontop site is 2.5 Å and in positions between the fcc-bridge-hcp line and the ontop site, the height is intermediate between 2.1 Å and 2.5 Å.

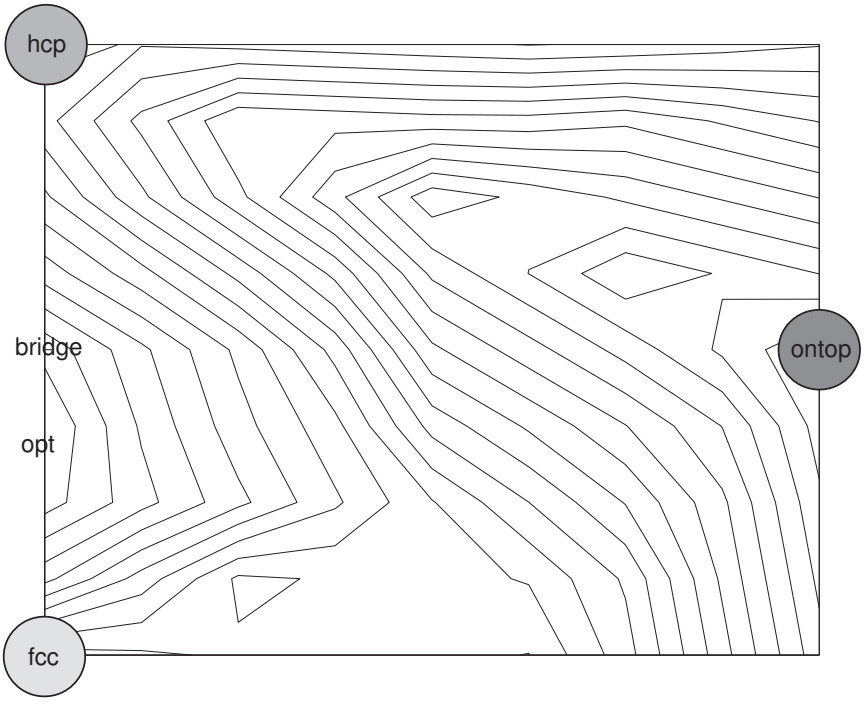

Figure 4.6: Potential energy surface of XYL on Au(111). The interaction energies are given as at the optimum binding height at each site. The optimum binding site is between the fcc and bridge sites.

Figure 4.7 shows the interaction energy of XYL at positions along the fcc-bridge-hcp path. Molecules can move along this path over the surface with a barrier to diffusion of 3.5 kcal/mol.

At the optimum binding site and height, the interaction energy was calculated as the molecule was scanned over different angles of rotation. Two angles were varied independently while the other was kept fixed at the CG optimised value.

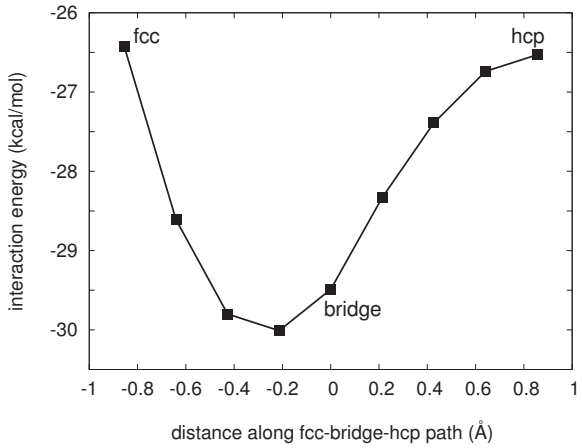

Figure 4.7: Interaction energy of XYL on Au(111) along the fcc-bridge-hcp path, indicating a barrier to diffusion of 3.5 kcal/mol.

Firstly the molecule was rotated perpendicular to the plane of the phenyl ring, with the surface normal making an angle of θ with the plane of the ring (figure 4.8a). Secondly the molecule was rotated in the plane of the ring, with the surface normal making an angle of σ with the vector joining the carbon atoms in the 1 and 4 positions on the ring (figure 4.8b). This confirmed that the CG optimisation resulted in a global minimum with respect to the rotation of the molecule on the surface.

At $\theta = -90°$ another shallow local minimum emerges due to the slight additional interaction of the ring with the surface (figure 4.8a). However DFT does not provide a reliable description of this dispersive interaction [65]. The optimum perpendicular rotation is $\sigma = 0°$. The rotations are clarified in the inserts on figures 4.8a and 4.8b. The optimum geometry is shown in figure 4.8c.

An additional CG optimisation was started from the optimal scan geometry, where the upper two slab layers were allowed to relax along with the molecule. The resulting interaction energy was $E_{\mathrm{I}} = -39.4$ kcal/mol, 30% stronger than the case where all gold atoms were fixed. The position of the molecule on the surface remained essentially unchanged.

A Mulliken population analysis at the optimal binding geometry revealed a charge transfer of 0.15 electrons from the gold surface to the molecule. The total overlap population of the sulphur with the two nearest gold atoms is $0.32|e|$. The

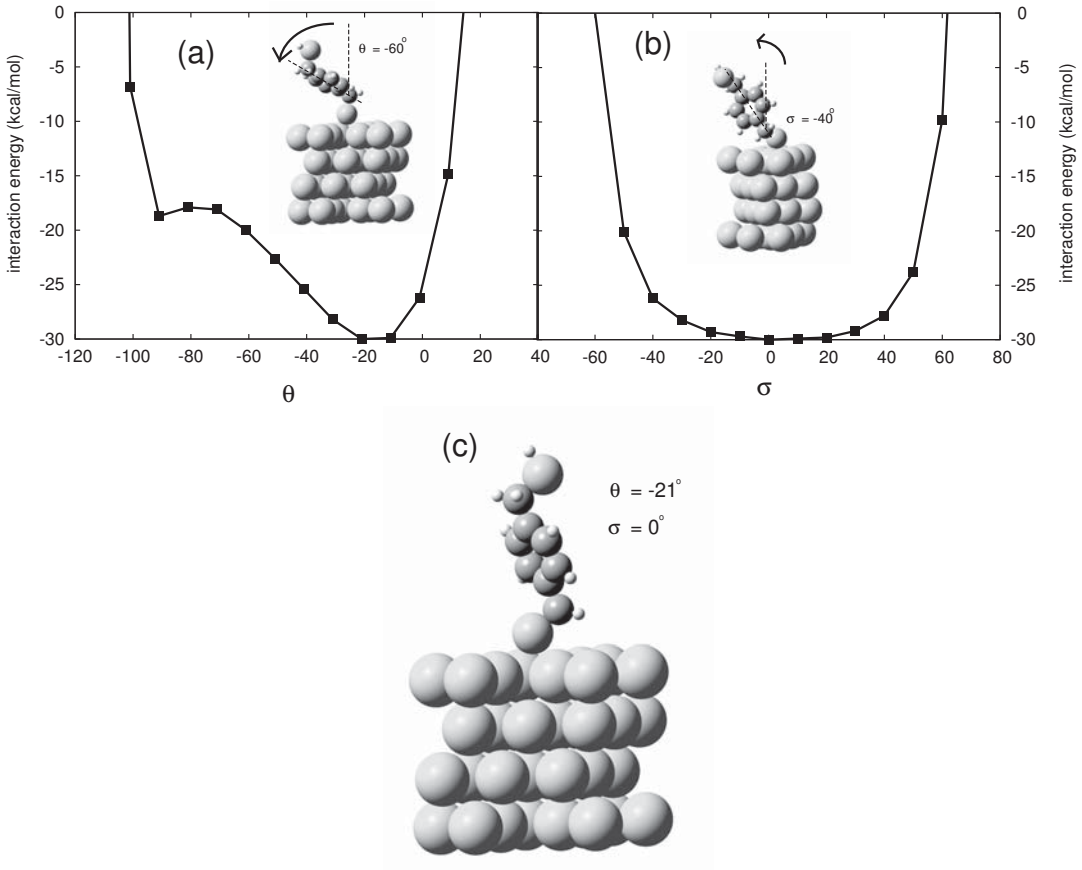

Figure 4.8: Change in interaction energy with rotation of the molecule (a) perpendicular to the plane of the phenyl ring and (b) in the plane of the ring. (c) Optimum binding geometry ($\theta = -21°$, $\sigma = 0°$).

large overlap indicates a strong covalent character for the bond. For the S-H bond on the upper side of the molecule, the charge transfer is 0.20 electrons from the molecule onto the hydrogen and the overlap population is $0.43|e|$. As expected, this bond also has strong covalent character.

Figure 4.9a shows how the sharp energy levels of the sulphur 3s and 3p orbitals become diffuse when mixed with the gold orbitals after adsorption. Smaller changes are also seen for the 5d and 6s orbitals of the gold atoms involved in the Au-S bond (figure 4.9b and 4.9c).

The scan of the molecule over the surface sites was repeated using the LDA-PZ XC functional. As listed in table 3.7, the interaction energy changes significantly to $E_{\mathrm{I}} = -47.6$ kcal/mol. However, the PES retains the same features as in the GGA case. The optimal binding site is unchanged and the heights above the various surface sites are lowered slightly to 2.0 Å above the optimal site and 2.4 Å above the ontop site.

The physisorbed state of XYL thiol-bonded to the Au(111) surface, i.e. prior to cleavage of the S-H bond, was optimised using the CG algorithm. This geometry may be a precursor to the chemisorbed state [180]. When using the GGA-PBE XC functional, the sulphur atom binds in a position 2.8 Å above the surface, slightly offset from the ontop site towards hcp. The interaction energy is only $E_{\mathrm{I}} = -3.9$ kcal/mol, much lower than the experimental value of $E_{\mathrm{I}} \approx -11$ kcal/mol for the physisorbed methanethiol (see [180] and references therein); this is to be expected since DFT provides a poor description of the van der Waals interaction which may account for a large portion of the binding energy. Figure 4.10 shows the GGA optimised geometry.

The optimisation was repeated with an LDA XC functional, resulting in a much stronger interaction energy, $E_{\mathrm{I}} = -15.7$ kcal/mol. This is indicative of the overbinding generally expected from LDA functionals. The position of the sulphur in this case was 2.4 Å above the surface midway between the ontop and hcp sites.

The Mulliken population analysis in the GGA case yields a charge transfer of 0.10 electrons from the molecule onto the slab. The overlap population between the sulphur and the single gold atom involved in the bond is $0.10|e|$. By compar-

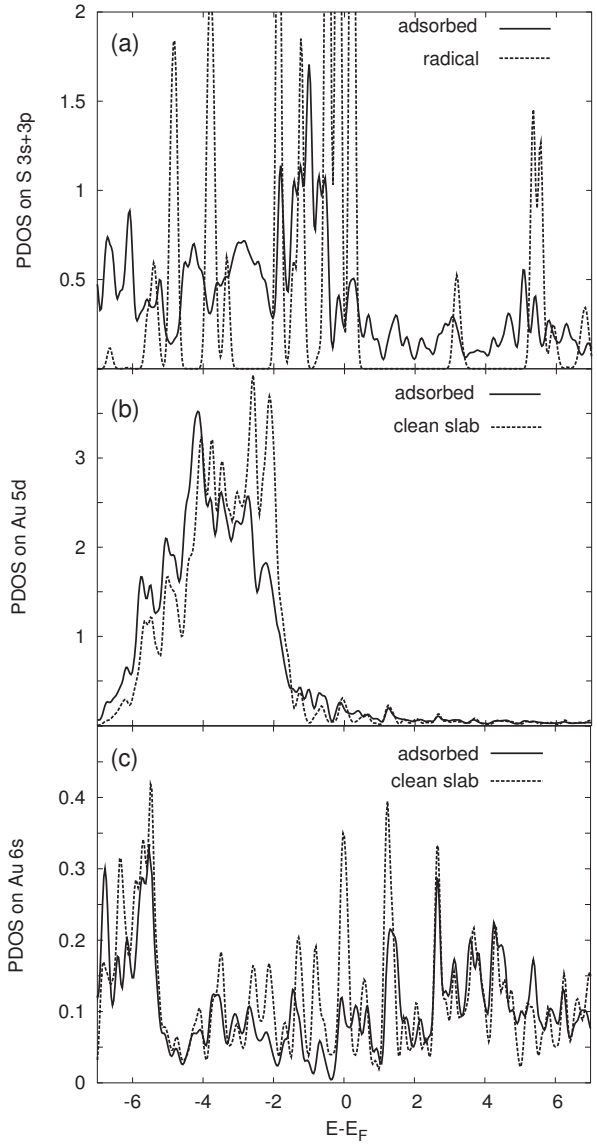

Figure 4.9: Change in the atomic orbitals after adsorption of XYL on Au(111) with the S-H bond cleaved: (a) S 3s and 3p orbitals, (b) Au 5d orbitals and (c) Au 6s orbitals.

Figure 4.10: Optimised geometry of thiol bonded XYL on Au(111).

ison to the thiolate bonded case, the interaction energies can be seen to follow the Mulliken charge transfer and overlap populations.

Figure 4.11 shows the PDOS on the 3s and 3p orbitals of the sulphur and the 5d and 6s orbitals of the gold atom involved in the bond, before and after adsorption. Even though the interaction is weak, significant differences are observed upon adsorption for each orbital.

4.4 Alkanedithiols on Au(111)

CG optimisations and surface scans of decanedithiol and dodecanedithiol on the Au(111) surface after cleavage of the S-H bond yield very similar results to the above analysis for XYL, using both LDA and GGA functionals. The backbone of each alkane chain makes an angle of 18° with the normal to the surface.

The Mulliken population analysis predicts a charge transfer of 0.17 electrons from the surface to the molecule. The total overlap between the sulphur and the two gold atoms involved in the bond is $0.32|e|$. Figure 4.12 indicates the changes in the sulphur 3s and 3p orbitals and the 5d and 6s orbitals of the two gold atoms involved in the bond. The PDOS on the sulphur and gold orbitals after adsorption is only slightly different from the case of XYL adsorption. The Mulliken charge transfer and overlap populations for the bond are also almost

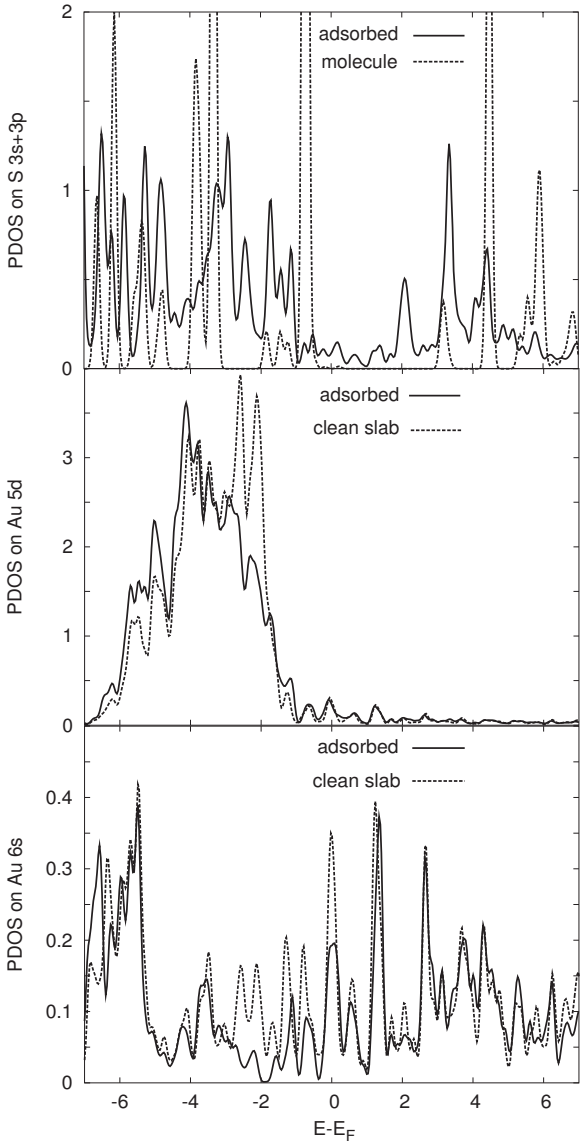

Figure 4.11: Change in the atomic orbitals after adsorption of XYL on Au(111) with the S-H bond in place: (a) S 3s and 3p orbitals, (b) Au 5d orbitals and (c) Au 6s orbitals.

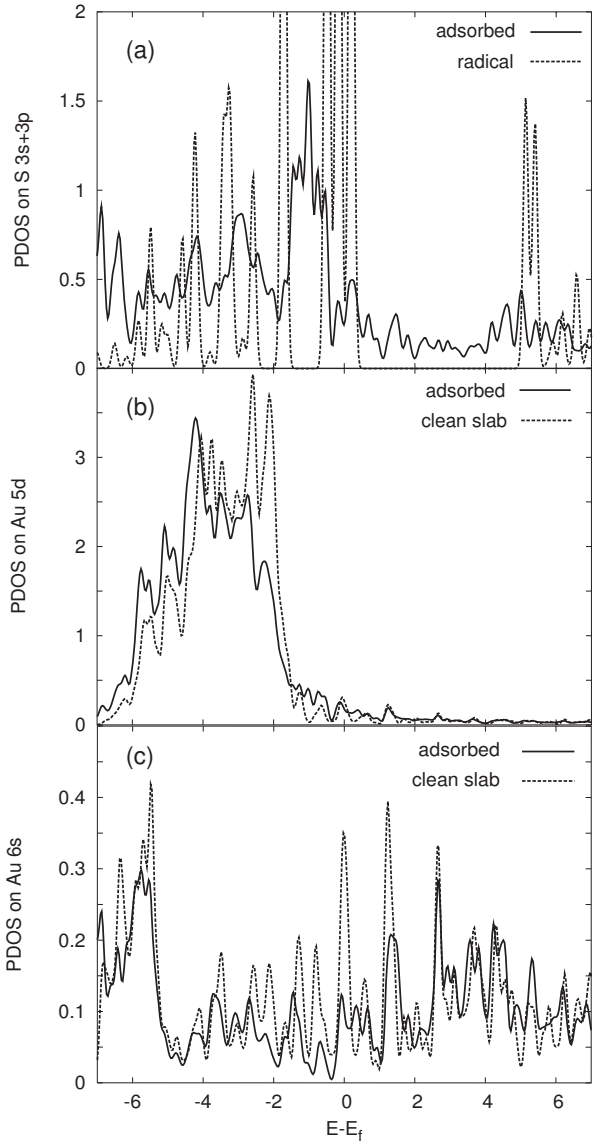

Figure 4.12: Change in the atomic orbitals after adsorption of decanedithiol on Au(111): (a) S 3s and 3p orbitals, (b) Au 5d orbitals and (c) Au 6s orbitals.

identical. The strong sulphur-gold bond is responsible for the resulting adsorption geometry and we therefore do not reoptimise each of the alkane chains used in the following chapter. Figure 4.13 shows the structure of hexanedithiol; the other alkane chains differ only in the number of carbon atoms in the chain.

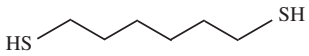

Figure 4.13: Hexanedithiol molecule.

4.5 Ethynylbenzene on Au(111)

The adsorption energetics of the ethynylbenzene (EB) molecule (figure 4.14) on the Au(111) surface was calculated with SIESTA [64]. After cleavage of the terminal C-H bond, the radical was predicted to bind to the surface through a strong carbon-gold interaction. In the calculated adsorption geometry the carbon atom lies 1.3 Å above the surface in the fcc hollow site with an interaction energy of $E_{\mathrm{I}} = -69$ kcal/mol. The interaction strength is notably larger than for the XYL-gold case presented in section 4.3. This is consistent with a comparison of the Au-C and Au-S interaction energies calculated for gold complexes [64].

Initial optimisation of the Cartesian coordinates resulted in an upright geometry of the radical on the sulface with a very shallow minimum with respect to the tilt angle, see figure 4.15. However subsequent Z-matrix optimisation resulted in a slightly tilted geometry [63].

The barrier to diffusion along the fcc-bridge-hcp path was calculated as 5 kcal/mol, suggesting that this molecule may form self-assembled monolayers driven by tail-tail dispersive interactions [64]. Using Z-matrix optimisations to map the PES of this path more thoroughly, resulted in a barrier of only 3.2 kcal/mol [63]. The alkynyl group should provide unbroken π-conjugated linkage to the gold surface [64], unlike thiol-terminated molecules where the conjugation is broken by the sulphur atom. Therefore this may be an important class of molecules from the point of view of molecular electronics. Monolayers of ethynylbenzene on gold have recently been observed [82].

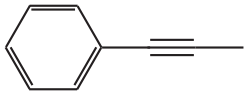

Figure 4.14: Ethynylbenzene molecule.

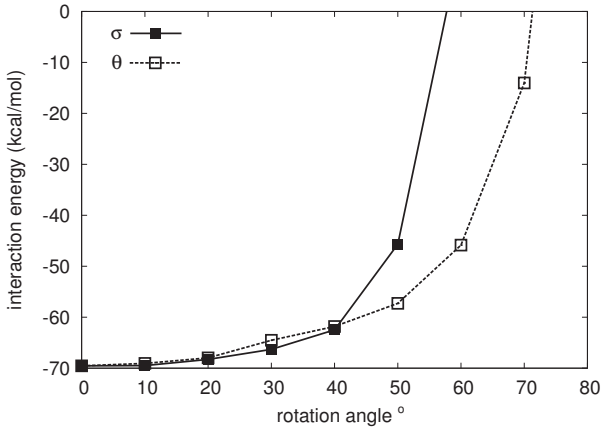

Figure 4.15: Interaction energy of EB on Au(111) when the molecule is rotated on the surface. The rotations are in the same sense as in figure 4.8.

4.6 Amines on Au(111)

Amine compounds have recently been studied in experiments that aim to probe the conductance of individual molecules [14–16, 19]. The conductance measurements for amines were more reproducible than for their widely studied thiol counterparts, as discussed in section 1.2.3. Characterisation of the adsorption energetics of amine compounds on the Au(111) surface is therefore important alongside the wide literature on thiol-Au(111) interactions.

Bilic *et al.* [84] studied the ammonia-Au(111) interaction at the plane-wave DFT level. They found a relatively weak interaction energy of $E_{\mathrm{I}} = -7.6\,\mathrm{kcal/mol}$ at 1/9 monolayer coverage with the nitrogen atom placed in the ontop site. In the bridge, fcc and hcp hollow sites very weak or no binding was indicated [84]. Li and Kosov [191] studied the aniline-Au(111) interaction in a relaxed geometry as well as in a stretched junction. They found that when the molecule is oriented perpendicular to the surface, lending itself to molecular junction formation, the aniline binds preferentially in an "adatom" geometry, shown in figure 4.17a. The nitrogen atom binds directly above an additional gold atom, placed in the fcc

position above the (111) slab. A large interaction energy was also calculated for the flat-lying molecule with the nitrogen atom in the ontop site; however, this may be due to neglect of the BSSE [192]. The preference of the molecule in the perpendicular orientation to bind in the adatom geometry was put forward as an explanation for the well-defined nature of the molecular conductance of amine- as compared with thiol compounds [191].

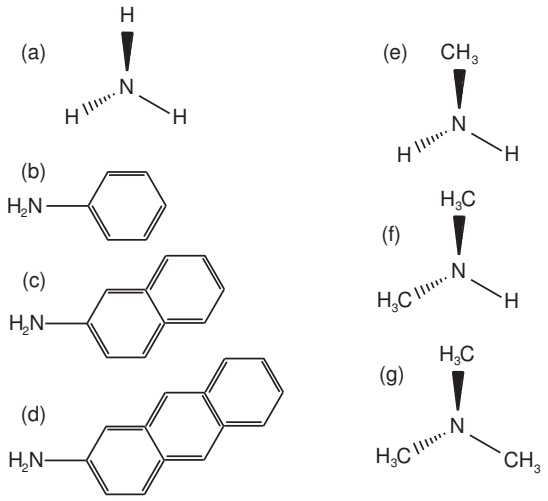

Figure 4.16: Amines included in this study: (a) ammonia - NH_3, (b) aniline - $NH_2C_5H_6$, (c) 2-aminonapthalene - $NH_2C_{10}H_7$, (d) 2-aminoanthracene - $NH_2C_{14}H_9$, (e) methylamine - NH_2CH_3, (f) dimethylamine - $NH(CH_3)_2$ and (g) trimethylamine - $N(CH_3)_3$.

Here we expand on this work by considering the adsorption of a series of amine compounds (figure 4.16) on Au(111).

CG optimisations of the amines on an Au(111) surface were performed with the molecules described in the Z-matrix format and the gold surface in Cartesians. The unit cell contained four Au(111) surface layers with 3x3 gold atoms per layer, implying a 1/9 monolayer coverage. The length and angle force tolerances were 0.02 eV/Å and 0.0003 eV/deg respectively. An MP grid of 5x5 k-points was used in the plane of the surface.

For each molecule separate optimisations were performed with the nitrogen atom fixed in one of five binding sites. In all cases the rest of the molecule as well as the height of the nitrogen above the surface were relaxed, while the gold atoms were fixed in their bulk positions. The ontop, bridge, fcc and hcp binding sites

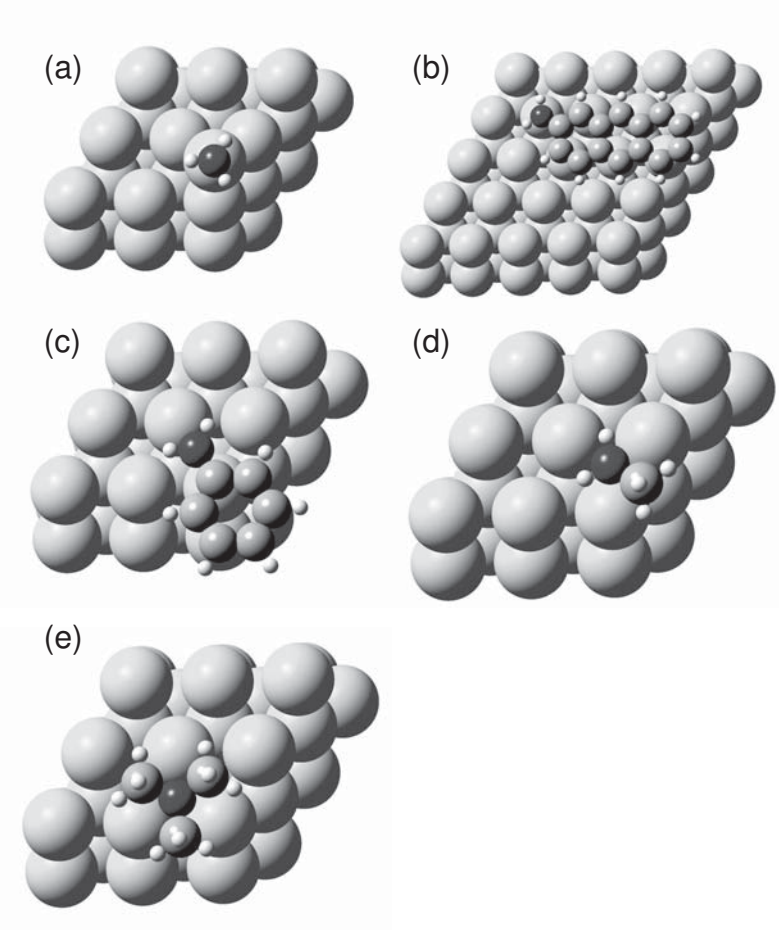

Figure 4.17: Some representative adsorption geometries of the amines on Au(111): (a) Ammonia in adatom geometry, (b) 2-aminoanthracene in ontop site, (c) aniline in bridge site, (d) methylamine in fcc site and (e) trimethylamine in hcp site.

were used as starting positions, as well as the adatom geometry described above. Figure 4.17 shows the relaxed geometries for these five starting configurations for a selection of the amines.

In the case of the aromatic ligands, the optimisation of the molecular coordinates is troublesome when using the Z-matrix description. This is because of the cyclic nature of the phenyl ring, as discussed in section 4.2.2. Thus for aniline, the phenyl ring was fixed in the gas-phase optimised structure, whereas the NH_2 component together with the rotation of the ring with respect to NH_2, was allowed to relax. For 2-aminonapthalene and 2-aminoanthracene, BFGS optimisations were

performed with both molecule and slab described in Cartesian coordinates. Even in the Cartesian representation, the CG algorithm did not converge to forces below the tolerance level. The unit cell contained 4x4 and 5x5 gold atoms per layer for these two molecules respectively. Larger unit cells are necessary to ensure negligible interactions between these larger molecules and their periodic images. For these two molecules only the ontop position was considered for nitrogen atom binding.

The interaction energies and heights of the nitrogen atom above the surface are summarised in table 4.2. For all molecules the sites with high coordination (bridge, fcc, hcp) are unfavourable and produce negligible interaction energies, $|E_{\mathrm{I}}| < 2$ kcal/mol. The binding energies in the ontop site are larger, but still weak, $2 < |E_{\mathrm{I}}| < 7$ kcal/mol. Significant binding is only observed in the adatom geometry, $8 < |E_{\mathrm{I}}| < 14$ kcal/mol.

	ontop		bridge		fcc		hcp		adatom	
molecule	E_{I}	h	E_{I}	h	E_{I}	h	E_{I}	h	E_{I}	h
NH_3	-5.1	2.46	-0.8	2.75	-0.6	2.90	-0.5	2.81	-11.8	2.32
$NH_2C_6H_5$	-2.3	2.66	-0.8	3.20	-1.0	3.29	-1.0	3.28	-8.2	2.36
$NH_2C_{10}H_7$	-3.0	2.80	-	-	-	-	-	-	-	-
$NH_2C_{14}H_9$	-4.4	2.64	-	-	-	-	-	-	-	-
NH_2CH_3	-6.8	2.46	-1.9	2.78	-1.6	2.82	-1.7	2.81	-13.4	2.32
$NH(CH_3)_2$	-6.5	2.54	-2.0	2.82	-2.0	2.82	-1.9	2.83	-13.7	2.32
$N(CH_3)_3$	-4.9	2.71	-1.7	3.00	-1.5	3.02	-1.5	3.02	-13.2	2.33

Table 4.2: Interaction energies in kcal/mol and binding heights of the nitrogen atom above the Au(111) surface in Å.

Table 4.3 lists the mulliken populations for the charge on the ammonia molecule and gold surface as well as the overlap between the nitrogen and bonded gold atoms in the bridge, ontop and adatom geometries. The interaction energy follows the overlap and charge transfer populations. In the adatom geometry the overlap population is $0.09|e|$ and the charge transfer is 0.18 electrons from the ammonia to the gold surface. These values are small but not negligible, and are responsible for the interaction energy of $E_{\mathrm{I}} = -11.8$ kcal/mol. In the ontop geometry, the overlap population is $0.045|e|$ and the charge transfer 0.08 electrons from molecule to surface, consistent with the weaker interaction energy. The

interaction energy of ammonia in the ontop site is $E_{\mathrm{I}} = -5.1$ kcal/mol, comparable with the -7.6 kcal/mol obtained in Ref. [84]. The variation may be due to differences in the basis set and exchange correlation potential – in Ref. [84] a plane-wave basis is used with the PW91 XC functional.

	charge			
binding site	molecule	surface	Au-N overlap	E_{I} (kcal/mol)
bridge	+0.034	-0.034	0.033	-0.8
ontop	+0.084	-0.084	0.045	-5.1
adatom	+0.178	-0.178	0.090	-11.8

Table 4.3: Mulliken charges on ammonia and the gold surface and overlap populations of the Au-N bond at different binding sites.

Table 4.4 shows the Mulliken population analysis for ammonia and the series of aromatic amines in the ontop site. Again the interaction energy follows the overlap population between the nitrogen and gold atom directly below it, and the amount of charge transfer between molecule and surface. Substitution of one of the hydrogen atoms in ammonia with an aromatic group reduces the overlap and charge transfer, thereby reducing the interaction energy.

	charge						
	gas phase		adsorbed ontop			Au-N	E_{I}
molecule	NH_x	ligand	NH_x	ligand	surface	overlap	(kcal/mol)
$NH_2C_6H_5$	-0.002	+0.002	+0.106	-0.076	-0.030	0.022	-2.3
$NH_2C_{10}H_7$	+0.098	-0.098	+0.118	-0.068	-0.050	0.025	-3.0
$NH_2C_{14}H_9$	+0.106	-0.106	+0.114	-0.032	-0.082	0.026	-4.4
NH_3	0	-	+0.084	-	-0.084	0.045	-5.1

Table 4.4: Mulliken charges on the molecule and gold surface and overlap populations of the Au-N bond for ammonia and the aromatic amines in the ontop binding site.

Substitution of hydrogen atoms with methyl groups generally increase the interaction energy, however this trend does not strictly correlate with the number of methyl substitutions and there is no consistency across binding sites. For example the interaction energy of trimethylamine in the ontop site is lower than that of ammonia, but higher in the adatom geometry. We therefore do not observe the same trend that occurs in a similar series of phosphine compounds [80].

In the case of aniline, we obtain $E_{\mathrm{I}} = -8.2$ kcal/mol in the adatom geometry and -2.3 kcal/mol in the ontop site. The phenyl ring tends to lie quite flat on the surface. This is a general trend for aromatic molecules not limited to amines. The angle between the phenyl ring and the surface normal is $\theta = 73.6°$ in the ontop geometry and $\theta = 63.3°$ in the adatom geometry, with θ defined as in figure 4.8.

The energetically favoured flat geometry suggests that the aryl-gold interaction contributes to binding; if this is the case the effect should be accentuated by an increased number of rings. We therefore calculated the interaction energy of 2-aminoanthracene with the surface as the aromatic group is rotated. The flat geometry is energetically favoured, as seen in figure 4.18. The BSSE corrected PES is shallow with respect to the rotation. When the interaction energies are not corrected for the BSSE, a deeper PES is observed and the interaction strength increases from $E_{\mathrm{I}} = -4.4$ kcal/mol (at $\theta = 85°$) to $E_{\mathrm{I}} = -19.5$ kcal/mol (at $\theta = 95°$). Taking account of the BSSE is therefore seen to be essential for the present geometry. Furthermore, we do not observe any binding when $\theta < 45°$. The interaction energy of 2-aminonapthalene is $E_{\mathrm{I}} = -3.0$ kcal/mol in the optimised geometry with the nitrogen atom in the ontop site and $\theta = 80°$. The interaction energy does indeed increase systematically with the number of rings.

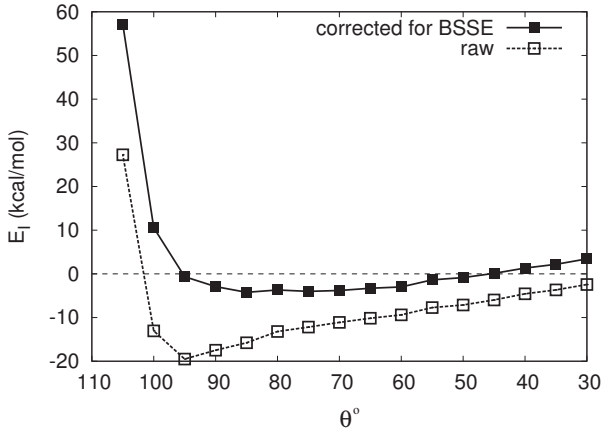

Figure 4.18: Raw and BSSE corrected interaction energies of 2-aminoanthracene on Au(111) as the molecule is rotated with the phenyl rings lying flat on the surface at $\theta = 90°$. The nitrogen is kept fixed at a height of 2.64 Å in the ontop position above the surface.

Note that it is evident from figure 4.18 that the BSSE has a significant effect not only on the interaction energy, but also on the optimised position of the molecule above the slab. Strictly speaking the BSSE should therefore be included at every step of a CG geometry optimisation. This would introduce significant computational overhead and complicate the calculation of the forces beyond the partial derivatives of the total energy with respect to atomic position, as described in section 2.3. The option is not included in SIESTA. However, for strongly bound systems such as the thiol-gold interactions considered in this chapter, the BSSE has a minimal effect on the binding geometry even though the effect on the interaction energy is significant.

4.7 Summary

A new module was implemented in the widely used SIESTA software package, to enable specification and optimisation of geometries using a Z-matrix coordinate system. A mixture of Z-matrix and Cartesian coordinates can be used. Any coordinate may be fixed, varied or coupled to another coordinate during an optimisation. This provides a very flexible optimisation tool, which is specifically useful for simulations of molecular adsorption on surfaces. Constrained optimisations may be performed by fixing certain molecular coordinates relative to the surface and coordinate driving can be used to simulate dissociation of molecules. Symmetries can be defined by specifying linear relations between coordinates – a tool not otherwise available in SIESTA.

Highly accurate DFT calculations of the surface energy and work function of gold Au(111) were performed. The work function obtained is in good agreement with experiment. This level of accuracy has not previously been obtained for work function calculations using local orbital basis sets. Reliable experimental values of the surface energy are not available, but the calculated value agrees with similar calculations in the literature. Although it is not possible to simulate the full reconstruction of the Au(111) surface within DFT, the tendency of the outer layer to contract in the plane of the surface was confirmed. The outermost interlayer distances of a surface are generally expected to contract. However

simulations of the Au(111) surface in the literature do not always support this and there is a lack of experimental evidence. Our calculated distances between the outermost surface layers depend on the computational parameters used, although usually an expansion rather than contraction is observed.

Optimisations of a range of small organic molecules on the Au(111) surface were performed with the SIESTA package. Aromatic- and alkanethiols were found to interact strongly with the surface through the sulphur-gold bond, when the S-H bond is cleaved prior to adsorption. A much weaker interaction is observed when the hydrogen is not removed. The results are in good agreement with similar calculations in the literature. The ethynylbenzene molecule interacts even more strongly with the surface through the gold-carbon bond, once the C-H bond has been cleaved. A series of amine compounds are found to bind preferentially to a gold adatom placed in the fcc position on the (111) surface. On a flat surface, the nitrogen atom binds weakly in the ontop site and not at all in sites with higher coordination. This supports experimental findings that the conductivity of amine-bound molecular junctions show less stochastic variation than their thiol counterparts.

More accurate adsorption geometries and barriers to diffusion could be calculated with a Z-matrix description, due to the shallow potential energy surface with respect to rotation of the molecules relative to the surface.

Table 4.5 provides a summary of the interaction energies together with the optimal binding heights and sites on the Au(111) surface for the molecules reported in this chapter as well as for a series of phosphine compounds reported in Ref. [80]. The ontop adsorption results for the amine compounds are also repeated for comparison, since the adatom geometry was not considered in the investigation of the other molecules. These results were all obtained with the same computational method and therefore provide a meaningful comparison of the relative adsorption strengths.

molecule	formula	binding site	height (Å)	E_I (kcal/mol)
ammonia	NH_3	ontop (adatom)	2.46 (2.32)	-5.1 (-11.8)
aniline	$NH_2C_6H_5$	ontop (adatom)	2.66 (2.36)	-2.3 (-8.2)
2-aminonapthalene	$NH_2C_{10}H_7$	ontop	2.80	-3.0
2-aminoanthracene	$NH_2C_{14}H_9$	ontop	2.64	-4.4
methylamine	NH_2CH_3	ontop (adatom)	2.46 (2.32)	-6.8 (-13.4)
dimethylamine	$NH(CH_3)_2$	ontop (adatom)	2.54 (2.32)	-6.5 (-13.7)
trimethylamine	$N(CH_3)_3$	ontop (adatom)	2.71 (2.33)	-4.9 (-13.2)
phosphine	PH_3	fcc	-	-
methylphosphine	PH_2CH_3	fcc	-	-
dimethylphosphine	$PH(CH_3)_2$	ontop	2.74	-13.5
trimethylphosphine	$P(CH_3)_3$	ontop	2.53	-20.6
methanethiol	SCH_3	bridge, towardsfcc	2.00	-42.7
benzenethiol	SC_6H_5	bridge	2.09	-33.0
phenylenedimethanethiol	$SCC_6H_4SH_2$	bridge, towards fcc	-30.0	
phenylenedimethanethiol	$HSCC_6H_4SH_2$	ontop	2.80	-3.9
ethynylbenzene	$C{\equiv}CC_6H_5$	fcc	1.32	-69.0

Table 4.5: Interaction energies and binding sites and heights of amines, phosphines, thiols and ethynylbenzene on the Au(111) surface calculated with SIESTA.

Chapter 5

DFT-NEGF Study of Transport Properties of Molecular Junctions

In this chapter the transport properties of molecular junctions are investigated with calculations that combine the DFT electronic structure solution of the system with the NEGF formalism to take into account the semi-infinite nature of the electrodes and the fact that the electrodes have different chemical potentials, $\mu_1 - \mu_2 = eV$. This formalism was presented in section 2.4. The transport results in section 5.4.4 were obtained with the SMEAGOL package. All other transport results in this chapter were calculated with the ATK/TranSIESTA-C packages.

In section 3.6 several test calculations were performed to find a set of parameters that yield well-converged conductance and current values. These are used where possible, but software restrictions as well as efficiency considerations sometimes necessitated these ideal parameter values to be relaxed. The basis set size is always SZP for the gold atoms and DZP for the molecular atoms. In all calculations two surface layers are included in the device region on either side of the molecule (see section 3.6). The LDA-PZ XC functional is employed, except for section 5.4.4 where the GGA-PBE XC functional is used. The calculations in sections 5.1, 5.2, 5.3, 5.4.1 and 5.4.2 were carried out with a 10 mRy energyshift parameter and no k-point sampling. In sections 5.4.3 and 5.4.4 more accurate

energyshift parameters were used and the k-space integrations carried out on a 3x3 grid in the plane of the surfaces. The seperate bulk electrode calculations always use 100 k-points in the transport direction as these are much more rapid than the transport calculation of the device region.

Junctions containing several different molecules are considered, but the electrodes are Au(111) surfaces in all cases. The adsorption geometries presented in chapter 4 are used as starting points for the electrode-molecule-electrode geometries. In most cases the molecule is assumed to bind to both surfaces in the minimum energy adsorption geometry for the molecule on a single Au(111) surface. The molecule is rotated in order to provide the symmetry needed to attain this geometry on both surfaces. Figures 4.8 and 4.15 indicate that the interaction energy is not affected significantly as long as the rotation angle is smaller than 20°. This suggests that the electronic structure and hence transport should not be unduly affected. In some cases this starting geometry is reoptimised using the BFGS algorithm. The junction setup is shown in figures 3.26 and 3.30 for the BDT and XYL molecules respectively. When asymmetric junctions are considered, the interface geometries on the two surfaces are purposefully different.

In order to obtain the $I(V)$ characteristics of a junction, the current is evaluated at various bias set points, -2.0 V $\leq V \leq$ 2.0 V in steps of 0.1 V. The conductance can then be evaluated from equation (3.4). When only the 0 V transmission function is calculated, the conductance is evaluated from equation (3.2).

5.1 $I(V)$ characteristics of alkane chains

The $I(V)$ curves for a series of alkanedithiols, S-C_n-S, for $4 \leq n \leq 12$, sandwiched between Au(111) electrodes are shown in figure 5.1. The optimised geometries of decanedithiol (C10) and dodecanedithiol (C12) on Au(111) from section 4.4 were used to construct symmetrical interface geometries on the left and right electrodes. It was assumed that both S-H bonds are cleaved. Each molecule is slightly rotated from its optimal position in order to obtain symmetric binding on the left and right electrodes. The symmetry is however not perfect, since the

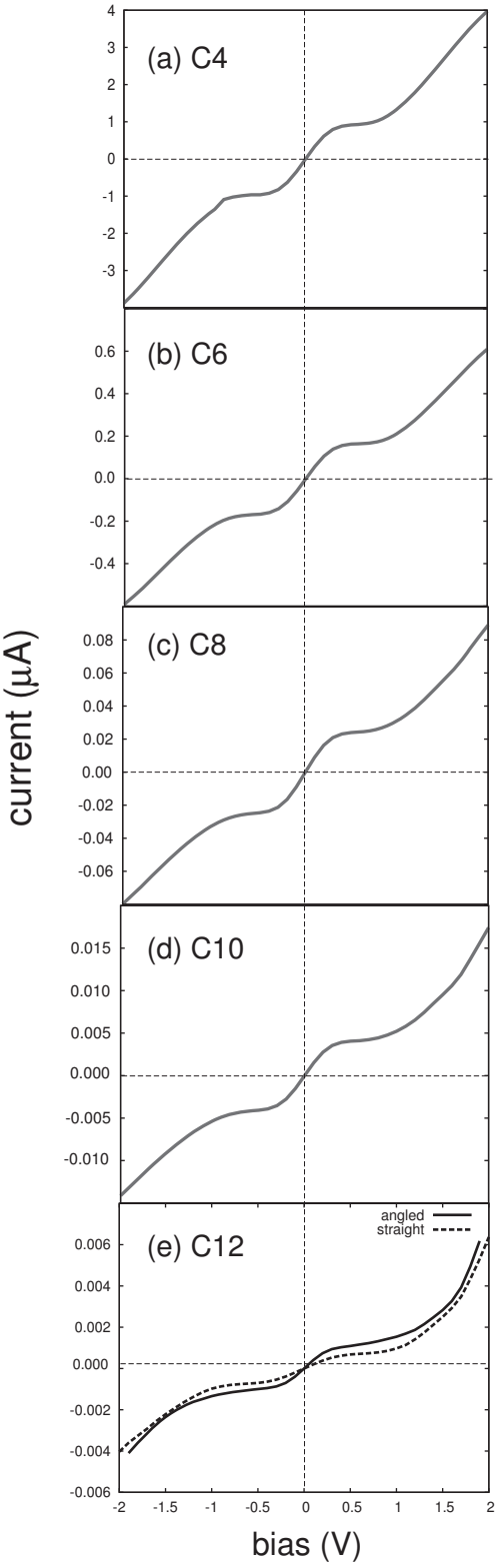

Figure 5.1: $I(V)$ curves for a series of alkane chain junctions, (a) butanedithiol (C4), (b) hexanedithiol (C6), (c) octanedithiol (C8), (d) decanedithiol (C10) and (e) dodecanedithiol (C12).

electrode configuration is such that the fcc site on the left electrode is directly opposite the hcp site on the right electrode. This can be seen from the slight asymmetries in the $I(V)$ curves. The junctions were not reoptimised.

The shapes of the $I(V)$ curves for the various alkane chains are fairly similar. It is clear by inspecting the scale of the current axis in figure 5.1a-e that the current decreases rapidly as the length of the chain increases. The relationship between the length and conductance of these chains will be investigated further in section 5.3.

Figure 5.1e compares the $I(V)$ curve for two different rotations of the C12 molecule between the electrodes. The effect on the overall $I(V)$ curve is small, however there is a more pronounced effect on the conductance at zero bias. The current is higher when the molecule is placed at an angle relative to the surface normal, than when the backbone of the molecule coincides with the normal. This is intuitive since the interaction energy with the surface is higher in the case of a tilted molecule (see section 4.4) and the coupling will therefore be greater.

5.2 $I(V)$ characteristics of aromatic dithiols and diethynylbenzene

The $I(V)$ curve for BDT was already presented in section 3.6.2. Here we repeat the current-voltage together with the conductance-voltage result (figure 5.2). There is good agreement between these results and those of the TranSIESTA-C authors [125]. The conductance reaches a maximum value of 0.6 G_0 at $V \approx \pm 1$ V.

Adsorption studies of XYL and EB on the Au(111) surface were presented in sections 4.3 and 4.5 respectively. As with the alkanedithiols in section 5.1, these molecules are placed in their optimum adsorption geometries and rotated slightly to obtain symmetric binding on the left and right electrodes. No reoptimisation of either junction is performed. The diethynylbenzene (DEB) molecule is assumed to bind to both surfaces in exactly the same configuration as the single ended EB. DEB is optimised in the gas phase before being placed between the electrodes.

Figure 5.4 shows the $I(V)$ characteristics of XYL and DEB as well as the 1-4-ethynylphenylmethanethiol (EPM) molecule, shown in figure 5.3. EPM is

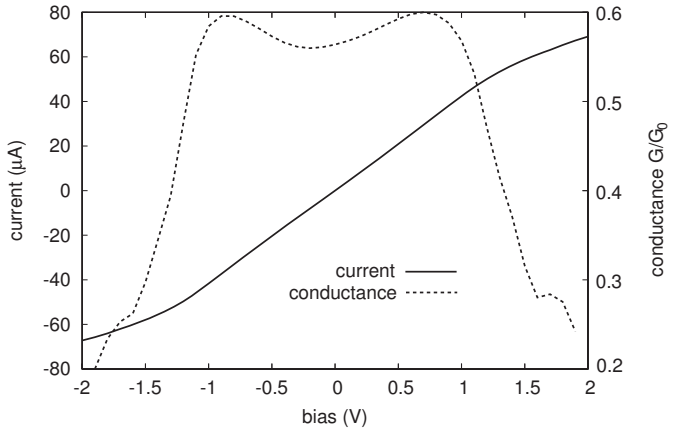

Figure 5.2: Current and conductance of a BDT junction.

in a sense a hybrid between XYL and DEB. Ethynyl and methanethiol groups are attached to the phenyl ring in the 1 and 4 positions. It is therefore rather intuitive that the $I(V)$ curve for EPM lies inbetween those of DEB and XYL.

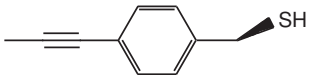

Figure 5.3: 1,4-ethynylphenylenemethanethiol (EPM) molecule.

The three molecules have very similar length and yet the current is notably larger in the DEB junction than in the XYL junction. This will be discussed in more detail in section 5.3.

CG optimisations were performed of the EPM molecule adsorbed on a single Au(111) surface. When the molecule is attached to the surface on the ethynyl side, the interaction energy and geometry is very similar to that obtained for EB in section 4.5. When the molecule is attached on the methanethiol side, the adsorption energy and geometry is likewise similar to that obtained for XYL in section 4.3. EPM is placed between the electrodes with the ethynyl group attached to the left electrode and the methanethiol group to the right electrode. The interface geometries are taken from the surface optimisations.

The EPM $I(V)$ curve is asymmetric due to the asymmetric nature of the molecule, the current being 2.7 times larger at 2.0 V than at -2.0 V. Asymmetries in the various $I(V)$ characteristics presented in this work will be discussed in

section 6.2.4. For consistency with the results in chapter 6 we use the convention throughout that positive current/voltage corresponds to electrons flowing from left to right across the junction.

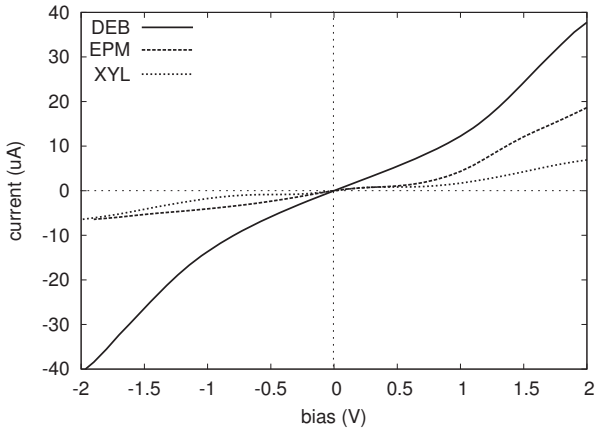

Figure 5.4: $I(V)$ characteristics of XYL, DEB and EPM junctions.

5.3 Comparison of zero bias conductance results

Figure 5.1 suggests that the current and hence the conductance of the alkane chains decreases exponentially with the length of the chain. This is quantified in figure 5.5 where the zero bias conductance results of all the molecules discussed in sections 5.1 and 5.2 are plotted against the interelectrode distance, d_{E}. d_{E} is taken as the distance between the centres of two gold atoms on the surface layers of opposite electrodes, measured perpendicular to the surfaces. For comparison the experimental data of Tao *et al.* [2, 3] is included on figure 5.5.

Exponential fits to the alkanedithiol conductance data (d_{E}, G) from our work as well as experiment are calculated from

$$G = Ae^{-\beta d_{\mathrm{E}}} \tag{5.1}$$

and indicated on figure 5.5. This yields decay parameters of $\beta = 0.72$ Å^{-1} for our data and $\beta' = 0.94$ Å^{-1} for the experimental data. These exponential fits can be extrapolated to direct contact between the left and right electrodes. This amounts

to setting $d_{\mathrm{E}} = 2.36$ Å, the interlayer distance of bulk gold in the (111) direction. The result is $G(d_{\mathrm{E}} = 0) = 10.9\ G_0$ for our data and $G'(d_{\mathrm{E}} = 0) = 25.4\ G_0$ for the experimental data. Even though our calculated conductances are larger than the experimental values, the larger β for the fit to the experimental data causes the fitted lines to cross before $d_{\mathrm{E}} = 2.36$ is reached, resulting in a larger extrapolated conductance value at $d_{\mathrm{E}} = 2.36$ for the experimental fit.

Alternatively the data can be plotted as a function of chain length N (figure 5.6), and fitted to

$$G = A_N^{-\beta_N N}. \tag{5.2}$$

This yields $\beta_N = 0.90$ for our data and $\beta'_N = 1.02$ for the experimental data. When these fits are extrapolated to $N = 0$, indicating direct contact between the electrodes, the values are $G(N = 0) = 1.56\ G_0$ for the calculated data and $G'(N = 0) = 0.65\ G_0$ for the experimental data.

The conductance of a one-dimensional metallic contact is expected to be G_0 (see section 3.6.1). One may therefore expect the extrapolated conductance from the data for the alkane chains to be G_0 at contact, since transport through the chain is essentially one-dimensional. The extrapolated values from the (N, G) data are much closer to this expectation than from the (d_{E}, G) data. This is not surprising, since the interelectrode distance is not a well-defined quantity and introduces an additional uncertainty into equation 5.1.

It is interesting to compare the zero bias conductance results of the series of alkane chains with those of the aromatic molecules on figure 5.5. Due to the delocalised phenyl π-orbitals, the aromatic molecules are expected to be more conductive than the alkane chains with predominantly σ-type orbitals along the backbone. The calculated conductances of the aromatics indeed lie above the exponential fit to the alkane data. However the experimental data from Refs. [2, 3] indicate lower conductance values for the aromatic molecules than the alkane chains, relative to the interelectrode distance. The difference between the calculated and experimental results is about two orders of magnitude for the aromatic molecules, but closer to one order of magnitude for the alkanes.

The DEB and XYL molecules are very similar in length. The smaller interelectrode distance in the case of DEB is due to the smaller height of the

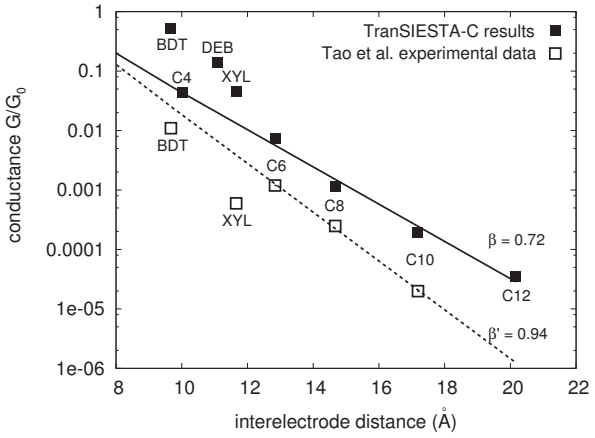

Figure 5.5: Zero bias conductance results for junctions with a series of alkane chains as well as the aromatic molecules BDT, XYL and DEB. Our TranSIESTA-C DFT-NEGF results are compared with experimental data from Refs. [2, 3].

carbon atoms above the respective surfaces in the optimum binding geometry, as compared with the sulphur atoms in XYL. It is therefore significant that the conductance at zero bias is 3.5 times higher for DEB than for XYL. This results in a much larger current for the DEB junction than the XYL junction, as seen in figure 5.4. The increased conductivity may be due to the unbroken conjugation provided by the C-C triple bonds on either side of the phenyl ring in the case of DEB [64].

5.4 Effect of interface geometry on transport properties

The results presented in sections 5.1-5.3 were obtained with the molecules attached in the equilibrium geometry on each electrode. In an actual physical system this ideal situation is not realistic and an ensemble of many contact geometries is likely to occur. Measurements of the conductance of single-molecule junctions are expected to vary accordingly.

In this section the effect of changing the molecule-electrode interface is investigated. Several studies have been done in this regard and the current or conductance of molecular junctions are known to be quite sensitive to the inter-

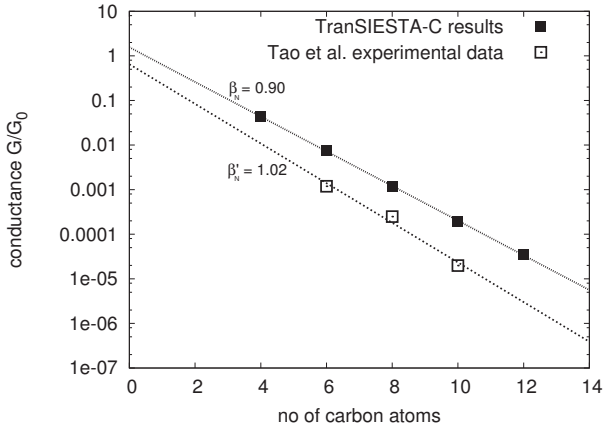

Figure 5.6: Zero bias conductance results of a series of alkane chain junctions plotted againts the number of carbon atoms in the chain. Our TranSIESTA-C DFT-NEGF results are compared with experimental data from Refs. [2, 3].

face geometry (see section 1.2.4).

5.4.1 Binding site

The $I(V)$ curve for XYL in section 5.2 was obtained with the sulphur atoms attached in the minimum energy positions close to the bridge site on either electrode. This site is marked "opt" on figure 4.6. The optimal height at this site is 2.0 Å when using an LDA XC functional. To test the effect of the binding site on the $I(V)$ characteristics, the XYL molecule was attached to the gold electrodes with the sulphur atom placed slightly removed from the ontop site towards the hcp site. On figure 4.6 this position corresponds to the energy maximum near the ontop site. The optimal height at this site is 2.4 Å when using an LDA XC functional. $I(V)$ curves were calculated with the sulphur atoms of XYL attached in this position on both electrodes, at the optimal height of $h = 2.4$ Å as well as a height of $h = 2.0$ Å. These $I(V)$ curves are shown in figure 5.7 together with the $I(V)$ for the optimal position, as in figure 5.4.

It may be expected that the current will be largest when the molecule is attached in its energetically most favourable (optimal) binding site. In this position the overlap between the molecule and electrode should be at a maximum - a situation that is conducive to a higher current. Furthermore, the current is *lower*

when the sulphur-gold distance is decreased in the non-optimal site, even though this decreases the interelectrode distance. Again the more favourable binding between the molecule and electrodes at the height of 2.4 Å on this site facilitates greater current.

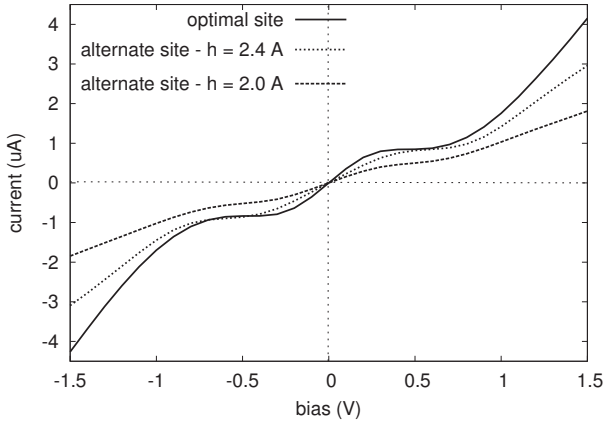

Figure 5.7: $I(V)$ characteristics of XYL junctions, where the molecule has been placed in three distinct interface geometries. All three junctions are symmetrical.

The binding site is seen to have an effect on the current, but does not account for the orders of magnitude difference between calculated and experimental values. In the remaining part of this chapter, the effect of introducing a gap between the molecule and one of the electrodes, or alternatively stretching the molecular junction, is investigated. This is a realistic scenario in recent experiments, where an STM tip is plunged into a substrate in a solution of molecules, and subsequently retracted to form single-molecule junctions (see section 1.2.3).

5.4.2 Gap between molecule and electrode

In STS measurements of the current passing through a dithiol molecule adsorbed on a substrate, it is not clear whether the S-H bond on the side of the STM tip is cleaved. If a chemical bond is formed between the tip and the upper end of the molecule, the junction is of the form investigated in section 5.4.1. Here we calculate the current and conductance characteristics of junctions where the S-H bond on the methanethiol or the C-H bond on the ethynyl group on one end of the molecule is *not* cleaved. The molecule-tip distance d on this end is allowed to

vary. d is taken as the distance from the centre of the S or C atom to the centre of the first layer of gold atoms, measured perpendicular to the surface as shown in figure 5.8.

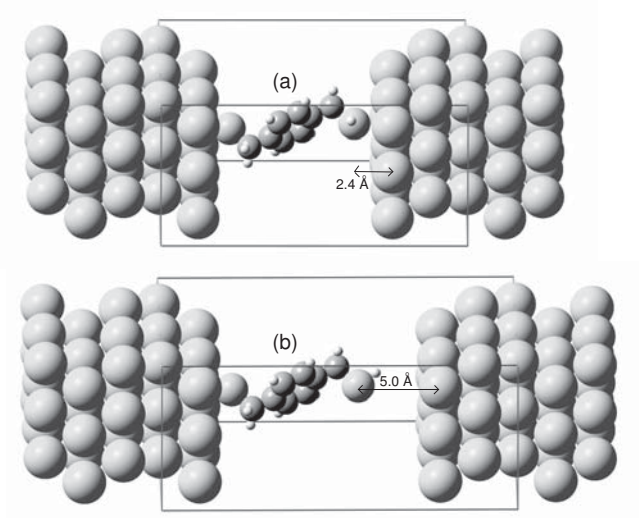

Figure 5.8: Geometry of the XYL junction where the S-H bond on the right side of the molecule is not cleaved. (a) The S-H end of the molecule is physisorbed to the right gold surface, with a sulphur-gold distance of $d = 2.4$ Å. (b) There is no interaction between the S-H end of the molecule and the right surface, $d = 5.0$ Å.

In section 4.3 the optimal binding geometry of the physisorbed thiol on the Au(111) surface was calculated using a GGA XC functional. The sulphur was located at a height of 2.8 Å above the surface, slightly removed from the ontop site. When using an LDA XC functional as in the present transport calculations, the binding site does not change but the optimal height decreases to 2.4 Å. Here we assume a chemisorbed bond on the left electrode as in the previous sections of this chapter. On the right electrode the sulphur-gold distance is varied between $d = 2.4$ Å and $d = 5.0$ Å. At $d = 2.4$ Å the physisorbed geometry from section 4.3 is used, reoptimised with an LDA XC functional (figure 5.8a). At larger values of d the presence of the right electrode is assumed not to influence the molecular geometry.

Figure 5.9 shows the conductance at zero bias for this junction with different values of d. Two sets of calculations were performed with different parameters. In the first set the energyshift parameter is 10 mRy and only the Γ-point is used,

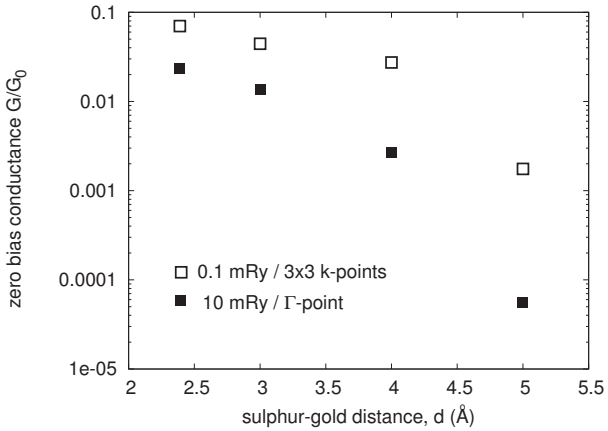

Figure 5.9: Zero bias conductance results of the XYL junction, where the S-H bond on the right end of the molecule is not cleaved (figure 5.8). The conductance decays as the sulphur-gold distance on the right is increased.

as in the previous calculations in this chapter. In the second set the energyshift paramer is 0.1 mRy and a 3x3 k-point grid is used in the plane of the surfaces. The conductance is larger when the orbital confinement is reduced ($\delta\varepsilon = 0.1$ mRy), since the overlap between the electrode and molecular orbitals is increased. The difference between the results for the two sets of calculations increases with d, since the error introduced by the finite spatial extent of the orbitals becomes more severe as atoms are stretched further apart. The conductance decay with increasing d is more rapid than exponential decay. This again is because of the larger effect of the orbital confinement as the molecule-electrode distance is increased. Note that the difference in k-point grids used for the two sets of results will also have an influence over and above the effect of the different orbital confinement. However, as shown in section 3.6.3, using only the Γ-point leads to an overestimation of the conductance (see figure 3.33). If the more accurate 3x3 k-point grid had been used for the 10 mRy results in figure 5.9, it is therefore expected that the conductance results for the 10 mRy and 0.1 mRy series would have been shifted further apart.

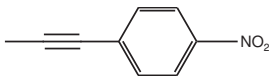

Figure 5.10: 1-ethynyl-4-nitrobenzene (ENB) molecule

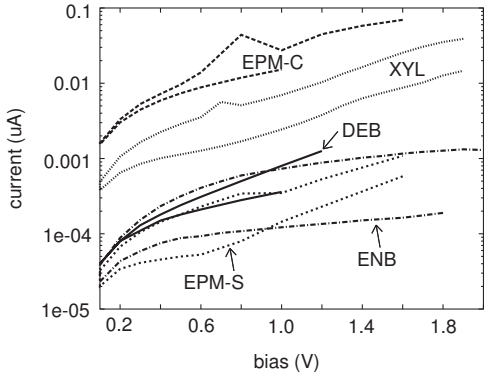

Figure 5.11: $I(V)$ curves for various molecular junctions, where the hydrogen on the right end of the molecule has not been removed and the distance between the S/C/N atom on the molecule and right electrode is $d = 5.0$ Å (figure 5.8b).

Figure 5.11 shows $I(V)$ curves calculated for XYL and other molecules in the geometry shown in figure 5.8b with $d = 5.0$ Å, the distance between the right sulphur/carbon/nitrogen atom and the right electrode. EPM-C and EPM-S refer to the EPM molecule attached to the left electrode on the ethynyl and methanethiol sides respectively.

1-ethynyl-4-nitrobenzene (ENB) shown in figure 5.10, is bound to the left electrode via an ethynyl linker and an NO_2 group is attached to the right end of the phenyl ring in the 4 position. The 5 Å distance is measured from the electrode to the nitrogen atom. A measurement to the oxygen atoms increases the overall interelectrode distance by about 1 Å to 14.3 Å, in closer agreement with the other molecular junctions calculated in figure 5.11. However, this reduces the conductance by three orders of magnitude. Although this behaviour makes comparison difficult, it is worth noting that the interelectrode distance for the ENB result in figure 5.11 is shorter than for the other molecules. This points to a lower conductance for ENB than its counterparts with the same ethynyl linker on the left electrode, but different endgroups on the gap side.

The negative side of the $I(V)$ curves have been folded over to illustrate the large asymmetries resulting from this molecule-gap geometry. For all molecules

the positive current (electrons flowing from left to right) is larger than the negative current. These asymmetries will be discussed further in section 6.2.4.

5.4.3 Gap between radical and electrode

Next the effect of increasing the sulphur-gold distance d on the right electrode is tested in the case where the S-H bond *has* been cleaved. Since a strong chemical bond is formed between the sulphur and gold atoms after cleavage of the S-H bond, the process of increasing d is equivalent to breaking this bond. Bond breaking is a phenomenon that is not well-described by single-configuration techniques such as DFT, and for an accurate description multi-configuration methods should be employed. However by performing spin-polarised DFT calculations the range of d-values over which the results are not reliable can be identified. The spin-polarisation γ, is defined as the excess number of α-spin electrons over β-spin electrons. It is given in the standard SIESTA output and calculated from equation (2.46).

We find that for $d \leq 3.0$ Å, $\gamma = 0$, i.e. the system is in a spin singlet state and the sulphur-gold bond is in tact, albeit stretched from the equilibrium distance, $d = 2.0$ Å. For $d \geq 4.5$ Å, $0.9 < \gamma < 1.0$ and the system is in a spin doublet state. The sulphur-gold bond has been broken and an unpaired α-spin electron remains on the right sulphur atom, free from the right electrode. For 3.0 Å $< d < 4.5$ Å the DFT electronic structure is not in a pure spin state, but is a mixture between singlet and doublet states. In this region the DFT results are not reliable. However this does not invalidate the results for $d \leq 3.0$ Å and $d \geq 4.5$ Å.

The transport calculations in this section are necessarily also spin-polarised. As discussed in section 5.4.2, the increased sulphur-gold distance makes the spatial extent of the orbitals more critical. Therefore an energyshift parameter of 0.1 mRy is used. This ensures that the 5d orbitals on gold and 3s orbitals on sulphur will overlap for gold-sulphur distances of up to 7.5 Å (see table 2.1). Note that the latter refers to the Au-S bond length, different from d, the sulphur-gold surface distance. Better quantitative reliability is obtained by using a 3x3 k-point grid in the plane of the electrodes. This set of parameters yields well converged

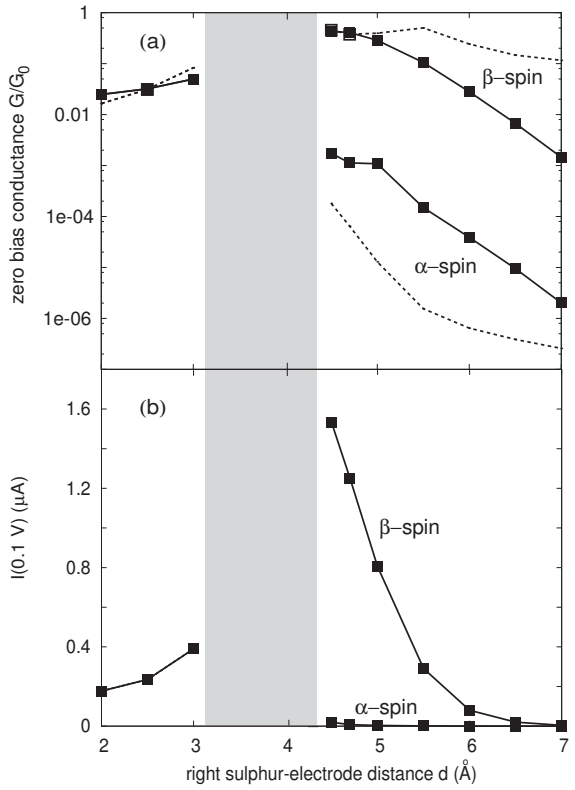

Figure 5.12: (a) Zero bias conductance and (b) 0.1 V current results for the XYL junction, where the S-H bond on the right end of the molecule has been cleaved. The shaded region indicates d-values where the electronic structure is not in a pure spin state. Solid lines indicate the DFT-NEGF calculations and dashed lines are results of a simple one-level model (see text).

results within the DFT level of theory (see section 3.6).

From the spin-polarised transport calculations (for all values of d), separate transmission functions and hence conductances and currents are obtained for α-spin and β-spin electrons. These are identical for $d \leq 3.0$ Å, but different for the spin doublet system with $d \geq 4.5$ Å. Figure 5.12a shows the zero bias conductance results as a function of d. The range of d-values where the electronic structure is not in a pure spin state is indicated by the shaded region.

Counterintuitively, the conductance rises as the sulphur-gold distance is increased from $d = 2.0$ Å to $d = 3.0$ Å, in confirmation of previous DFT results [53, 57, 59]. Furthermore the conductance for β-spin electrons continues to rise *after the bond is broken* before decaying to zero for large d. Conductance for

α-spin electrons decays rapidly to zero once the bond is broken. The same trend is obtained for the current at 0.1 V, shown in figure 5.12b.

The rise in conductance as d is increased can be understood by examining the transmission function, figure 5.13a. At $d = 2.0$ Å a broad resonance is seen at ~ 0.75 eV below the Fermi level. When d is increased to 3.0 Å, this resonance becomes sharper and moves towards the Fermi level, centred at ~ 0.3 eV below E_{F}. For the spin-polarised system at $d = 4.5$ Å, the resonance becomes sharper again and splits into α-spin and β-spin components. The α-spin component is situated in the same position as the resonance in the $d = 2.0$ Å case. The β-spin component is located at the Fermi level and gives rise to the high conductance for β-spin electrons.

The origin of the resonance peaks in the transmission function can be traced back to the projected density of states (PDOS) onto the orbitals of the XYL molecule, shown in figure 5.13b. At the equilibrium bond length there is strong hybridisation between the gold and sulphur orbitals, stabilising the bond. The PDOS on the sulphur atom becomes sharper as d is increased due to reduced mixing with the gold orbitals. When the bond is broken, the PDOS takes a form similar to the radical adsorbed on a single gold surface (the left electrode).

Figure 5.14 presents SIESTA density of states calculations, using the same parameters as the present transport calculations, except the energyshift parameter which was changed to 5 mRy in the interest of computational speed. For the equilibrium bond lengths considered here, a value of 5 mRy should be sufficient and will not affect the results.

Figure 5.14a shows the DOS of an isolated XYL molecule and figure 5.14d shows the corresponding PDOS onto one of the S atoms. The occupied levels of XYL closest to E_{F} with energies -2.02 eV and -2.07 eV have their weight mainly divided between the two sulphur atoms on either end of the molecule. The lowest lying unoccupied levels with energies 1.56 eV and 1.84 eV have negligible weight on the sulphur. The HOMO-LUMO gap of the isolated molecule is 3.58 eV. The sharp energy levels have been broadened with a Gaussian function as in equation (2.67) with the integral of the DOS between $-\infty$ and 0 recovering the number of valence electrons in the molecule.

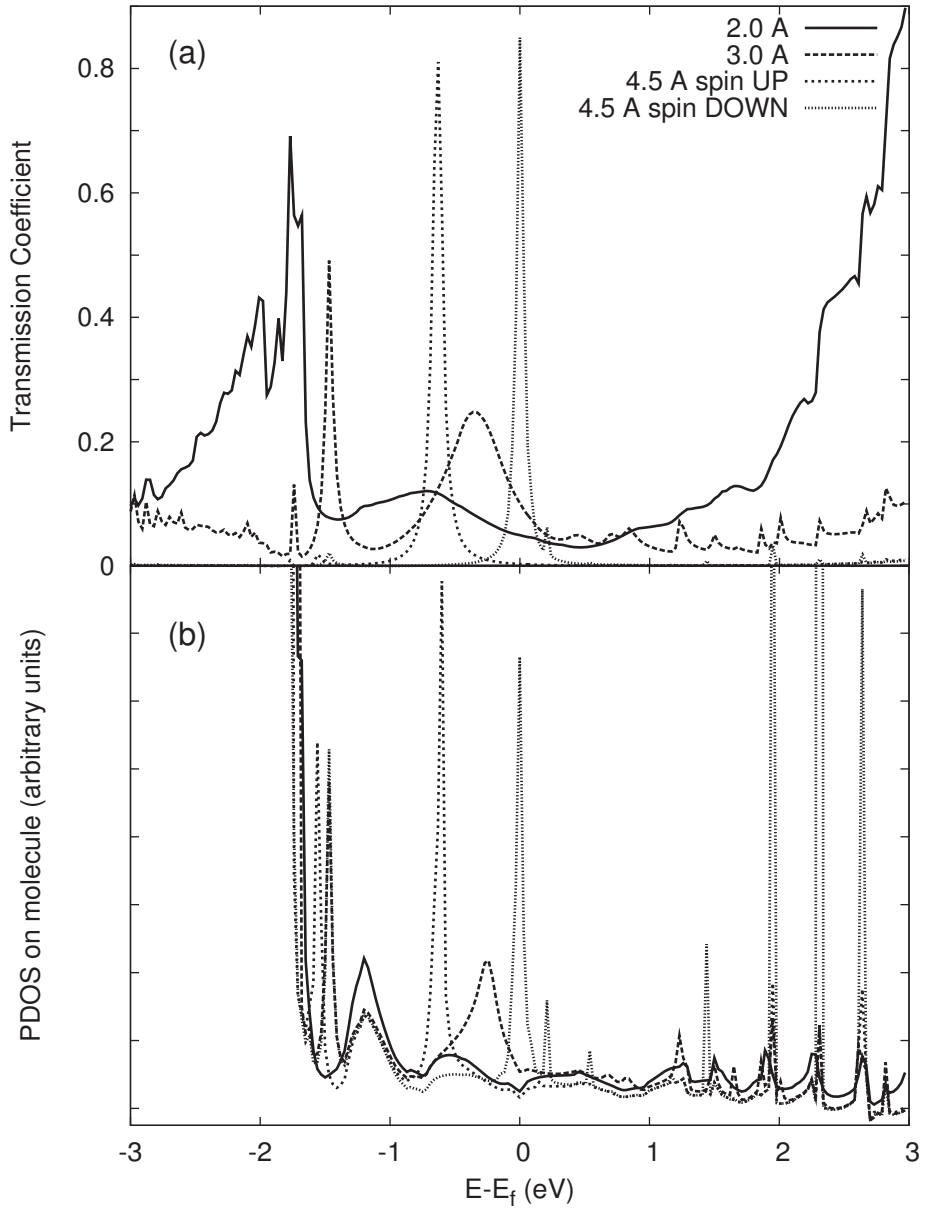

Figure 5.13: (a) Transmission function and (b) PDOS on the molecule for XYL junctions with right sulphur-electrode distances of 2.0 Å, 3.0 Å and 4.5 Å.

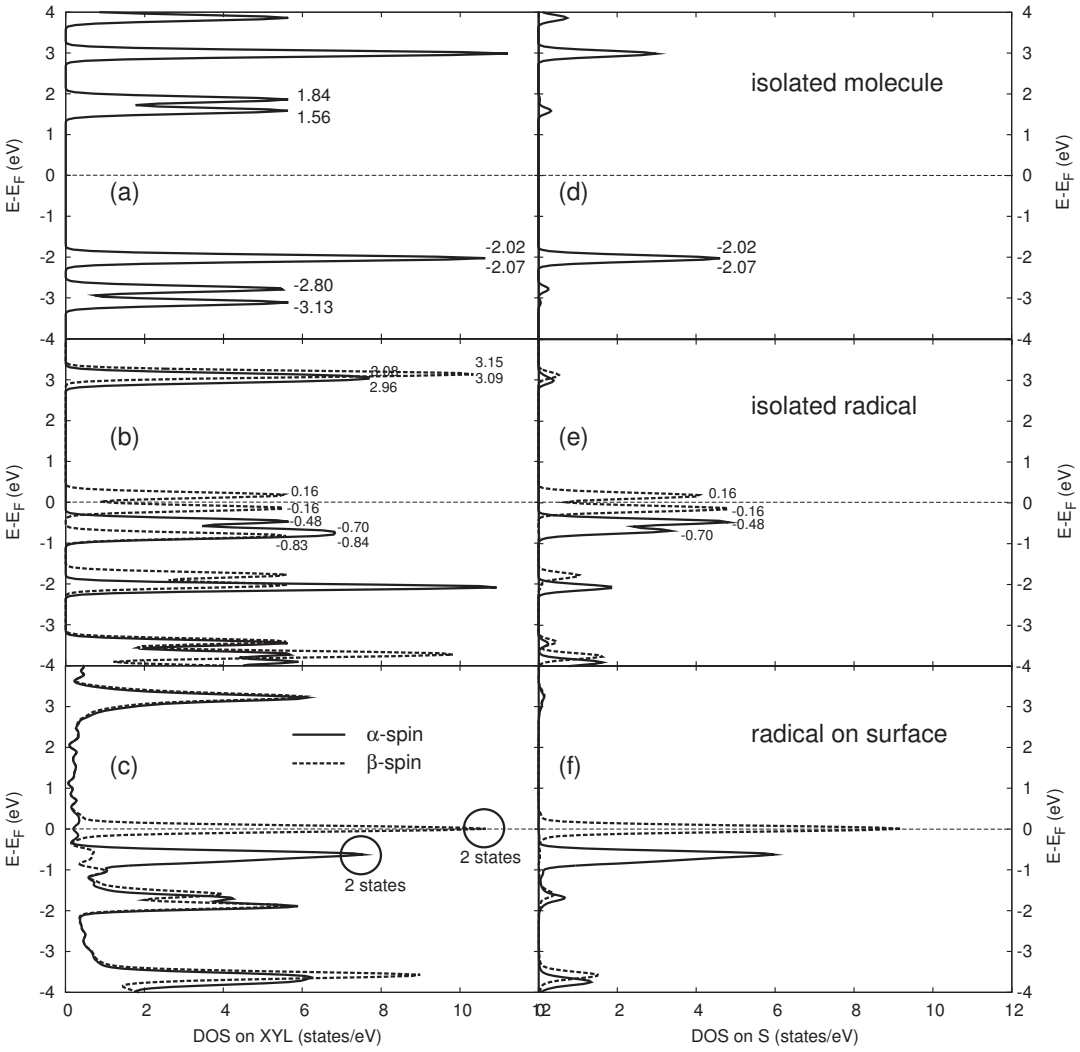

Figure 5.14: (a,d) DOS for isolated XYL molecule, (b,e) isolated XYL radical and (c,f) XYL radical adsorbed onto an Au(111) surface. (a-c) The DOS is projected onto the entire molecule/radical or (d-f) onto the right sulphur atom.

Figures 5.14b and 5.14e represent calculations on the isolated XYL radical, where the hydrogen on the right sulphur atom has been removed. The radical is in a spin doublet state and the DOS is distinct for α-spin and β-spin electrons. A Mulliken population analysis reveals that the extra α-spin electron resides largely on the right sulphur atom, which has an occupancy of 3.5 α-spin and 2.7 β-spin electrons. The Fermi level shifts to push one β-spin level above E_{F} and in general moves closer to the highest lying occupied states. The β-spin LUMO is now one of the states with its weight largely on the right sulphur atom and the β-spin HOMO-LUMO gap reduces to 0.32 eV. The occupied α-spin levels also lie close to the Fermi level, but the α-spin HOMO-LUMO gap is 3.44 eV.

Figure 5.14c shows the PDOS onto the orbitals of the XYL radical adsorbed on an Au(111) surface, i.e. the remaining terminal hydrogen on the XYL radical has been replaced by a gold surface. The effect on the orbitals of the radical is to move the HOMO and LUMO β-spin levels closer together so that they lie virtually on the Fermi level. The two occupied α-spin states with their weight on the right sulphur atom are also moved closer together. Integrating under the peaks indicated on figure 5.14c reveals that both peaks represent two states. The β-spin peak lying on the Fermi level is occupied by only one electron since it is essentially centred at E_{F}. Figure 5.14c can be compared with the $d = 4.5$ Å curve on figure 5.13b to confirm that the second electrode has little effect on the molecular density of states.

The TranSIESTA/ATK package provides a feature whereby the eigenvalues of the selfconsistent Hamiltonian of the molecule in the presence of the electrodes can be found [120]. For large d these eigenvalues will correspond to the peaks on figure 5.14c. Figure 5.15a shows a trace of the eigenvalues of the two highest occupied states as d is increased from the equilibrium value. At $d = 2.0$ Å the terminal hydrogens on both ends of the molecule have been replaced by gold surfaces and the eigenvalues are simlar to those found in figure 5.14a. As d increases they move closer to the Fermi level. For $d \geq 4.5$ Å when the system is in a spin doublet state, the two levels for α-spin and β-spin electrons correspond to the circled peaks in figure 5.14c.

The location of the two β-spin levels close to the Fermi level is responsible

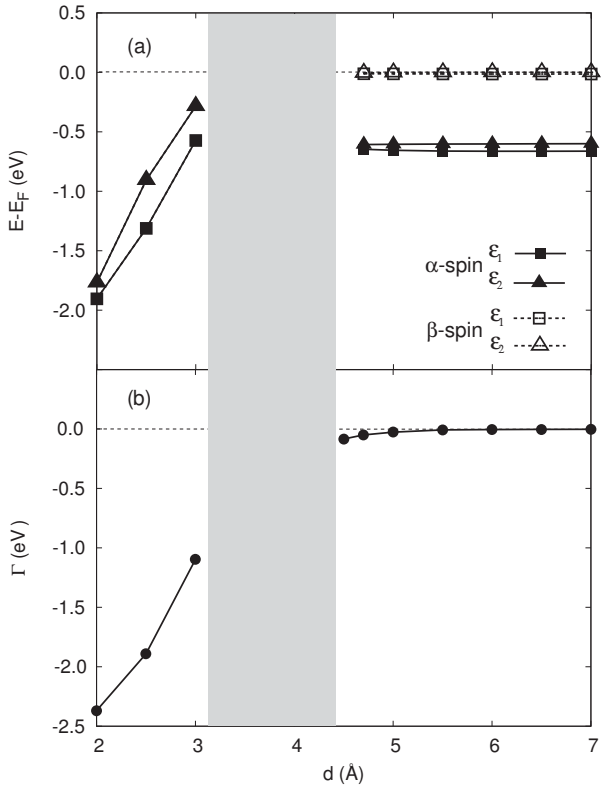

Figure 5.15: (a) Eigenvalues of the two highest occupied molecular levels. For $d \geq 4.5$ Å one of the β-spin levels becomes unoccupied. (b) Interaction energy between the molecule and right electrode at various molecule-electrode separation distances, d.

for the increased conductance when d is large. However it may be surprising that this effect is able to overcome the decreased coupling between the molecule and right electrode. In order to investigate the competition between the effects of orbital alignment with E_{F} and reduced coupling, a simple one-level model is used to obtain a qualitative description of the current through the junction. The current through a channel with a single level of energy ε between two electron reservoirs is given by [168]

$$i(V) = \frac{e}{h}\gamma_1\gamma_2 \int_{-eV/2}^{eV/2} \left[(E-\varepsilon)^2 + \gamma^2\right]^{-1} \mathrm{d}E \tag{5.3}$$

where zero-temperature and a Lorentzian density of states have been assumed. γ_1 and γ_2 are the coupling strengths of the energy level to the left and right reservoirs

and $\gamma = \frac{1}{2}(\gamma_1 + \gamma_2)$. E is the energy relative to the Fermi level. Equation (5.3) can be integrated to obtain the current or differentiated to find the conductance as a function of voltage, once γ_1, γ_2 and ε are known.

The conductance of the Au(111)-XYL-Au(111) junction is estimated for various values of d, by adding the conductances obtained from equation (5.3) for the two energy levels shown in figure 5.15a. An approximation needs to be made for the coupling strengths, γ_1 and γ_2, of each energy level to the two electrodes, as it is not clear how these quantities may be obtained from the SIESTA or ATK results. One available measure of the coupling strength at various distances, d, is the interaction energy between the molecule and electrode. A possible approximation for $\gamma_1(d)$ and $\gamma_2(d)$ is therefore to set them proportional to the interaction energies of the molecule with the left and right electrodes, $\Gamma_1(d)$ and $\Gamma_2(d)$. Since only the right electrode is pulled away from the molecule, the coupling of the molecule with the left electrode remains constant, $\Gamma_1(d) = \Gamma(2.0\text{Å})$. In figure 5.16 the solid lines indicate the conductance obtained when using $\gamma_1 = \alpha\Gamma(2.0\text{Å}), \gamma_2(d) = \alpha\Gamma(d)$, for $\alpha = 0.1$. It is also assumed that γ_1 and γ_2 are unchanged for the two energy levels.

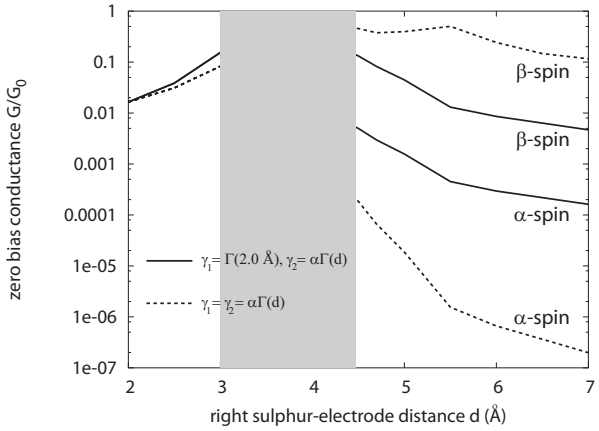

Figure 5.16: One-level model conductance results using equation (5.3) with $\gamma_1(d) = \Gamma(2.0\text{Å}), \gamma_2(d) = \alpha\Gamma(d)$ (solid lines) and $\gamma_1(d) = \gamma_2(d) = \alpha\Gamma(d)$ (dashed lines). The shaded region indicates the range of d-values where the system is not in a pure spin state.

A shortcoming of this approximation is that the coupling of the specific two energy levels contributing to the conductance does not necessarily behave in the

same way as the interaction energy of the *entire molecule* with the electrodes. The two energy levels, ε_1 and ε_2, are in fact seen to be delocalised across the molecule in the equilibrium geometry, but become localised on the right sulphur atom as the right electrode is pulled away (not shown). For the two energy levels to which we are applying equation (5.3), it is thus the coupling to *both* electrodes and not only the right electrode which decays as d is increased. It is precisely this weak coupling that allows the eigenvalues to approach the Fermi level so closely. It therefore seems more correct to choose $\gamma_1(d)$ and $\gamma_2(d)$ in a way that causes both values to decay with increasing d. For this reason we use $\gamma_1(d) = \gamma_2(d) = \alpha\Gamma(d)$, plotted as the dashed curve on figure 5.16 and repeated in figure 5.12a. It is again assumed that the coupling strengths of the two energy levels are identical.

The interaction energies, $\Gamma(d)$, are calculated with SIESTA in the same way as in chapter 4 and plotted in figure 5.15b.

α is used as a fitting parameter to obtain the best quantitative agreement between this one-level conductance and the DFT-NEGF results. The one level model data in figures 5.16 and 5.12a are calculated with $\alpha = 0.1$. The qualitative behaviour does not change if α is varied. As evidenced by figure 5.16, the high conductance for β-spin electrons is not dependent on the assumption $\gamma_1 = \gamma_2$, although relaxing this constraint may cause the conductance peak to shift. $\alpha = 0.1$ corresponds to a coupling energy of about 240 meV when $d = 2.0$ Å, which is reasonable compared with values used by Datta [168]. This simple model confirms the increase in conductance with d, both when the bond is stretched ($d \leq 3.0$ Å) and broken ($d \geq 4.5$ Å).

5.4.4 Stretching a molecular junction

In section 5.4.3 the right sulphur-surface distance in an Au(111)-XYL-Au(111) junction was fixed at increasing values d. This is a powerful computational technique for investigating junction stretching behaviour in a controlled manner. A more realistic representation of the experimental scenario may be obtained by allowing the junction geometry to fully relax at incremental stretching distances. This is achieved with the SIESTA code by performing BFGS geometry opti-

misations of the atomic coordinates in a series of stages. The XYL system is considered again, as well as a Au(111)-DEB-Au(111) junction.

The optimisations are similar to the molecular adsorption calculations of chapter 4. The molecule is positioned on a gold surface represented by four layers of 3x3 atoms in the optimised adsorption geometry from chapter 4. As an initial guess at the equilibrium junction geometry, the unit cell length in the z-direction (labeled z) is reduced such that the top end of the molecule forms a bond with the periodic image of the bottom slab layer, with the same molecule-surface distance at both interfaces (figures 5.17b and 5.21b). The molecule as well as the top and bottom gold slab layers are allowed to relax, while the middle two layers are fixed. The optimisation is complete when the maximum force on any atomic coordinate does not exceed 0.04 eV/Å.

The junction is stretched by increasing z in steps of 0.2 - 0.5 Å and reoptimising the geometry at each step, or "squeezed" by reducing z in steps of 0.2 - 0.3 Å and reoptimising. A 5x5 k-point grid was used in the plane of the surface. For geometries where the system is in a spin-singlet state a 5 mRy energyshift parameter is used, but where the system is in a spin doublet state this is reduced to 0.1 mRy. The size of the basis set is DZP on all atoms. The calculations in this section make use of the GGA-PBE XC functional.

For the transport calculations the k-point grid is reduced to 3x3 and the basis set on the gold atoms is reduced to SZP. The energyshift parameter is set to 0.5 mRy for all transport calculations.

Au(111)-XYL-Au(111) junction

On optimisation of the initial junction geometry (figure 5.17b) the XYL molecule stretches slightly. The heights of the sulphur atoms above the respective surfaces are reduced from the single-surface adsorption height to $d_1 = d_2 = 1.9$ Å.

Decreasing the unit cell size z (and hence the interelectrode distance) causes the SCC angles on the methanethiol endgroups to tighten as the sulphur atoms are pushed towards the phenyl ring and the ring becomes more tilted (figure 5.17a).

When the interelectrode distance is stretched, the two gold atoms (Au_{1a} and

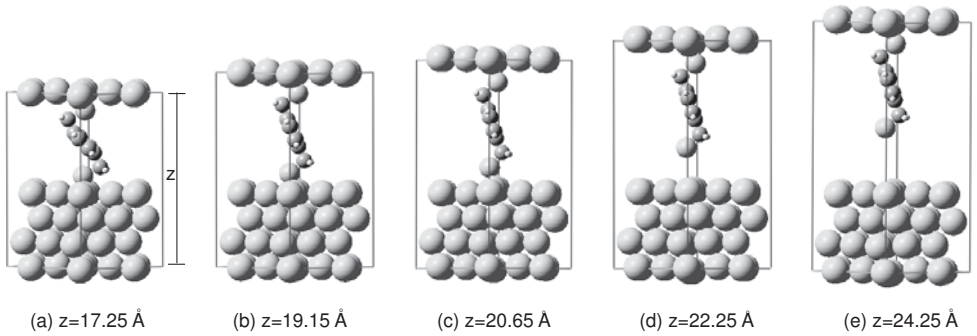

Figure 5.17: Unit cells of the XYL junction at selected intervals of stretching. The equilibrium junction geometry is shown in panel (b) where $z = 19.15$ Å.

Au_{1b}) bound to the lower sulphur atom (S_1) are initially pulled out of registry with the rest of the surface. However the gold-sulphur bond breaks before any gold atoms are detached from the surface. Subsequently Au_{1a} and Au_{1b} return to registry with the rest of the surface. As in section 5.4.3 the system remains in a spin singlet state as the Au-S bond is initially stretched, $z \leq 21.45$ Å. Once the bond is broken the system is in a spin doublet state, $z \geq 22.25$ Å. For 21.45 Å $< z <$ 22.25 Å the system is not in a pure spin state and multi-configurational methods are needed for a proper description.

Just prior to breaking of the Au-S bond, the junction is stretched 2.3 Å beyond the equilibrium value. At this point the height of S_1 above Au_{1a} and Au_{1b} is $d_1 = 2.69$ Å, while Au_{1a} and Au_{1b} are out of registry by $\Delta Au_1 = 0.48$ Å. The sulphur (S_2) on the other end of the junction stays attached to the gold surface. Nevertheless at $z = 21.45$ Å, S_2 has moved to a height of $d_2 = 2.07$ Å above the two gold atoms (Au_{2a} and Au_{2b}) to which it is bonded and Au_{2a} and Au_{2b} have moved out of registry by $\Delta Au_2 = 0.26$ Å.

When the Au-S bond is stretched the SCC angles on the endgroups increase and the phenyl ring tilts towards the surface normal. After the bond is broken, the molecule returns to its equilibrium configuration. The geometric parameters at each stage of the stretching process are summarised in table 5.1.

When the bond is broken the XYL radical contains an unpaired α-spin electron on S_1, as in section 5.4.3. The bond breaking occurs at a smaller sulphur-surface distance than in section 5.4.3, since a GGA rather than LDA XC func-

z (Å)	d_1 (Å)	ΔAu_1 (Å)	ΔAu_2 (Å)	d_2 (Å)	$z_{S\text{-}S}$ (Å)	θ_{SCC} (deg)
16.65	1.75	-0.07	-0.04	1.76	5.97	90.7
16.95	1.77	-0.06	-0.04	1.78	6.22	92.6
17.25	1.79	-0.06	-0.03	1.80	6.47	94.4
17.55	1.79	-0.05	-0.02	1.82	6.73	96.2
17.85	1.81	-0.03	0.00	1.84	6.96	98.6
18.15	1.83	-0.02	0.02	1.87	7.17	100.5
18.45	1.83	-0.01	0.04	1.90	7.40	102.7
18.75	1.85	0.02	0.07	1.93	7.61	105.0
18.95	1.85	0.03	0.08	1.95	7.76	106.8
19.15	1.91	0.08	0.09	1.95	7.84	108.7
19.35	1.93	0.12	0.11	1.97	7.95	109.9
19.65	1.96	0.16	0.15	1.99	8.11	112.0
19.95	2.08	0.22	0.16	1.99	8.22	114.6
20.25	2.13	0.31	0.17	2.01	8.34	116.8
20.65	2.17	0.41	0.24	2.06	8.49	118.3
21.05	2.23	0.50	0.26	2.08	8.62	120.8
21.25	2.37	0.59	0.30	2.12	8.57	119.2
21.45	2.69	0.48	0.26	2.07	8.63	122.0
22.25	4.18	0.14	0.33	1.98	8.22	116.5
22.75	4.75	0.12	0.31	1.98	8.19	116.1
23.25	5.27	0.13	0.31	1.97	8.18	116.0
23.75	5.79	0.12	0.30	1.97	8.16	115.8
24.25	6.30	0.12	0.29	1.97	8.16	115.8
24.75	6.80	0.12	0.29	1.97	8.16	115.8
25.25	7.31	0.12	0.29	1.97	8.15	115.7

Table 5.1: Geometric parameters for relaxed XYL junctions. d_1 is the height of the sulphur above the two gold atoms to which it is bonded on the lower side of the molecule. ΔAu_1 is the height of these two gold atoms above the rest of the surface. d_2 and ΔAu_2 are similarly defined on the upper end of the molecule. $z_{S\text{-}S}$ is the distance between the sulphur atoms on opposite ends of the molecule along the z-axis. θ_{SCC} is the angle made between the sulphur and carbon on the lower methanethiol endgroup and the carbon to which it is bonded on the ring.

tional is used. The range of z-values where the system is not in a pure spin state is smaller due to the geometry relaxation at each step as well as the change in XC functional.

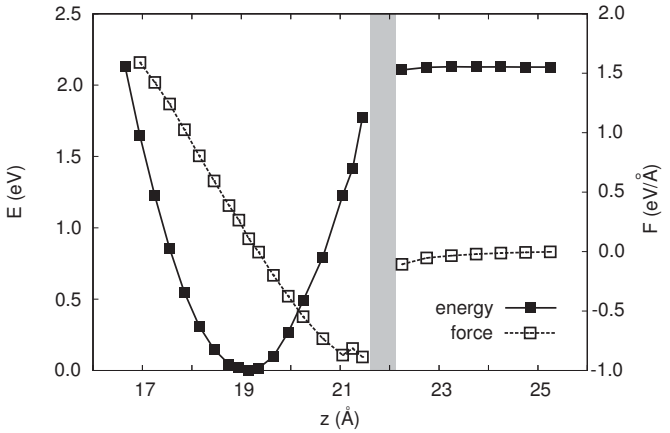

Figure 5.18: Relative total energy E, and force, $F = -\frac{\mathrm{d}E}{\mathrm{d}z}$ vs unit cell size z, for the XYL junction. The shaded region indicates the range of z-values where the system is not in a pure spin state.

Figure 5.18 shows the total energy $E(z)$, and the restoring force, $F = -\frac{\mathrm{d}E}{\mathrm{d}z}$, acting on the junction under stress. Since the z-axis is normal to the base of the unit cell, the restoring force can be calculated as $F = A(\sigma_{zz} - R)$, where A is the xy-area of the unit cell and σ_{zz} is the zz-component of the stress tensor given by SIESTA. R is the residual stress inside the slab as a result of fixing the middle slab layers and is not associated with the junction stretching. R can be found as the limiting value of σ_{zz} once the S-Au bond is broken, $R = \lim_{d\to\infty} \sigma_{zz} = 0.17$ eV/Å. Because the residual stress is subtracted out, the zero of the force curve does not correspond exactly to the energy minimum. Alternatively F can be found by numerically differentiating the E vs z curve, but this makes the force very sensitive to a lack of smoothness in the latter.

The equilibrium length of the junction is $z = 19.15$ Å. Below this value the restoring force is positive and acting to open up the junction (i.e. increase z). Above $z = 19.15$ Å the restoring force is negative, acting to close the junction (i.e. decrease z). The minimum restoring force is reached at $z = 21.45$ Å, when the sulphur-gold bond is broken. This breaking force of $|F| = 0.89$ eV/Å ($= 1.42$ nN) is close to the value of 1.25 nN calculated in Ref. [127], where the gold-sulphur

bond is also predicted to break before gold atoms are pulled out of the surface. For $z \geq 22.25$ Å when the bond is broken, the restoring force returns to 0.

The PDOS on the XYL molecule is shown in figure 5.19a-d for different junction sizes. As in section 5.4.3, the two highest lying occupied states move closer to the Fermi level as the junction is stretched. When the bond is broken the α-spin and β-spin states are distinct (figure 5.19d). There is one less occupied β-spin state and hence the two pertinent β-spin states straddle the Fermi level. These two levels are not as close together as in section 5.4.3 and two distinct peaks can be identified.

The transmission spectra (figure 5.19e-g) and hence zero bias conductances results were calculated for some cell sizes. The conductance is shown in figure 5.20 as a function of the S-Au height, d_1. The conductance decreases as d_1 increases prior to bond-breaking, contrary to the behaviour in section 5.4.3. The transport calculation in the spin-polarised case after the Au-S bond is broken proved to be troublesome and thus far we have been unable to obtain a converged self-consistent Hamiltonian. The position of the PDOS peaks in figure 5.19d close to the Fermi level suggest that a transmission resonance will lie very close to the Fermi level and produce an enhanced conductance for β-spin electrons. The effect may be less pronounced than for the unrelaxed junction in section 5.4.3, since the two peaks for $z = 22.25$ Å in figure 5.19d are not degenerate as the peaks for $d = 4.5$ Å in figure 5.13b.

It is surprising that in the squeezed junction with $z = 17.25$ Å ($d_1 = 1.8$ Å), the conductance is a factor of three larger than in the equilibrium case. The PDOS on the molecule is very similar in the vicinity of the Fermi level (compare figures 5.19a and 5.19b) and the enhanced conductance is not due to a resonance in the PDOS. The broad feature in the transmission spectrum around the Fermi level is enhanced when the junction is squeezed (compare figures 5.19e and 5.19f). This is presumably due to enhanced overlap between the sulphur and gold orbitals. The Mulliken overlap population on either side of the junction between the sulphur and each of the two bonded gold atoms is $0.17|e|$ for the equilibrium junction and $0.19|e|$ for the squeezed junction.

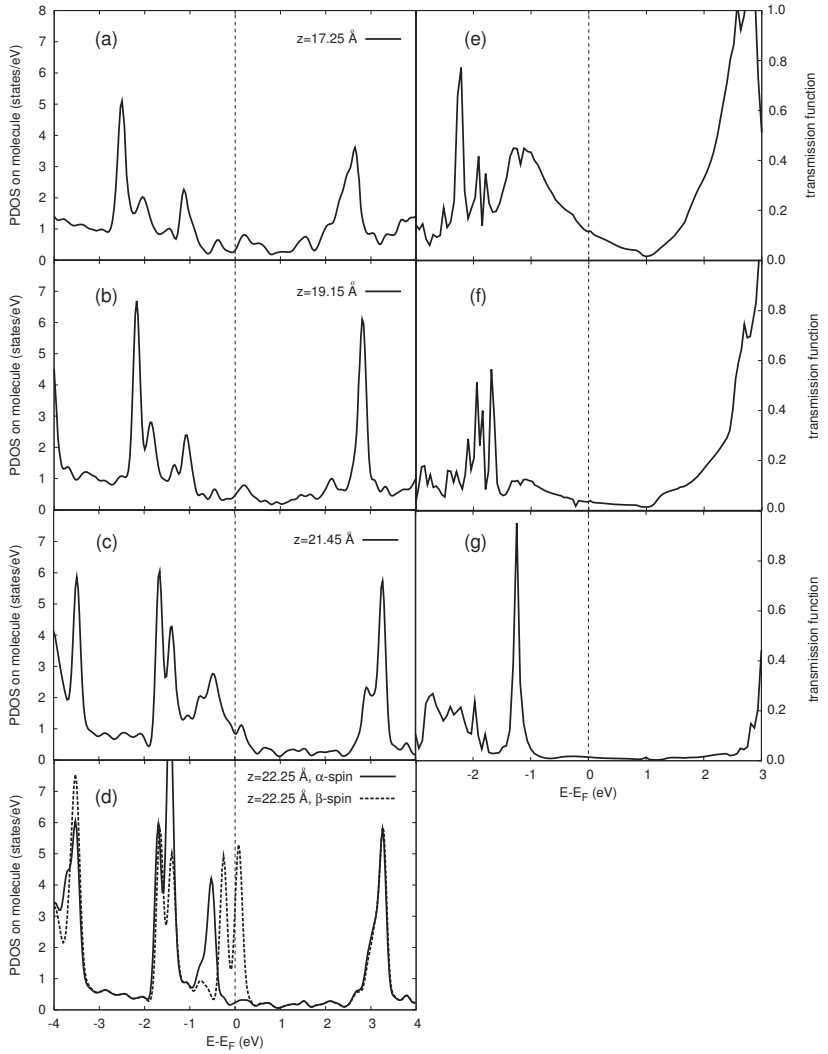

Figure 5.19: (a-d) PDOS on molecule and (e-g) transmission spectra for XYL junctions: (a,e) a squeezed junction ($z = 17.25$ Å), (b,f) the equilibrium junction length ($z = 19.15$ Å), (c,g) just before the Au-S bond is broken ($z = 21.45$ Å) and (d) after the bond is broken ($z = 22.25$ Å). The transmission function was not evaluated for the latter case.

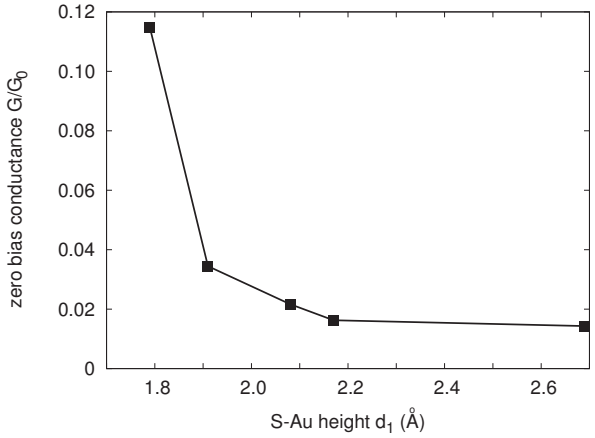

Figure 5.20: Zero bias conductance results for the XYL junction for different unit cell lengths, z. The conductance was only calculated for spin singlet states where the Au-S bond is stretched, but not broken.

Au(111)-DEB-Au(111) junction

The DEB junction is shown in figure 5.21 at various stages of stretching. The equilibrium junction geometry (panel b) has a unit cell size of $z = 18.25$ Å. The carbon atoms on either end of the molecule are initially placed in fcc sites on the surfaces at heights of 1.3 Å, the optimised position for adsorption on a single surface (see section 4.5). After optimisation of the $z = 18.25$ Å junction, the three gold atoms bonded to each carbon move out of registry with the surface by $\Delta\text{Au} = 0.1$ Å. The height of the carbon above these three gold atoms is slightly reduced from 1.3 Å, but the carbon remains in the same binding site.

The ethynyl endgroups are more rigid than the methanethiol endgroups of XYL. The junction can be squeezed by 1.1 Å to $z = 17.15$ Å, but any further reduction in the unit cell size did not lead to a converged solution.

When the junction is stretched a single gold atom is pulled out of the surface. As a result the system remains in a spin singlet state throughout the stretching process. The strong carbon-gold bond which measures a higher interaction energy than the sulphur-gold bond (see chapter 4) does not break during stretching. However, the carbon is initially placed in a three-fold hollow site and in the stretched geometry (figures 5.21d-g) it is bound only to the single gold atom detached from the surface. It is perhaps surprising that a chain of Au atoms is not pulled out from the surface, as in the MD simulations of a thiolate molecule

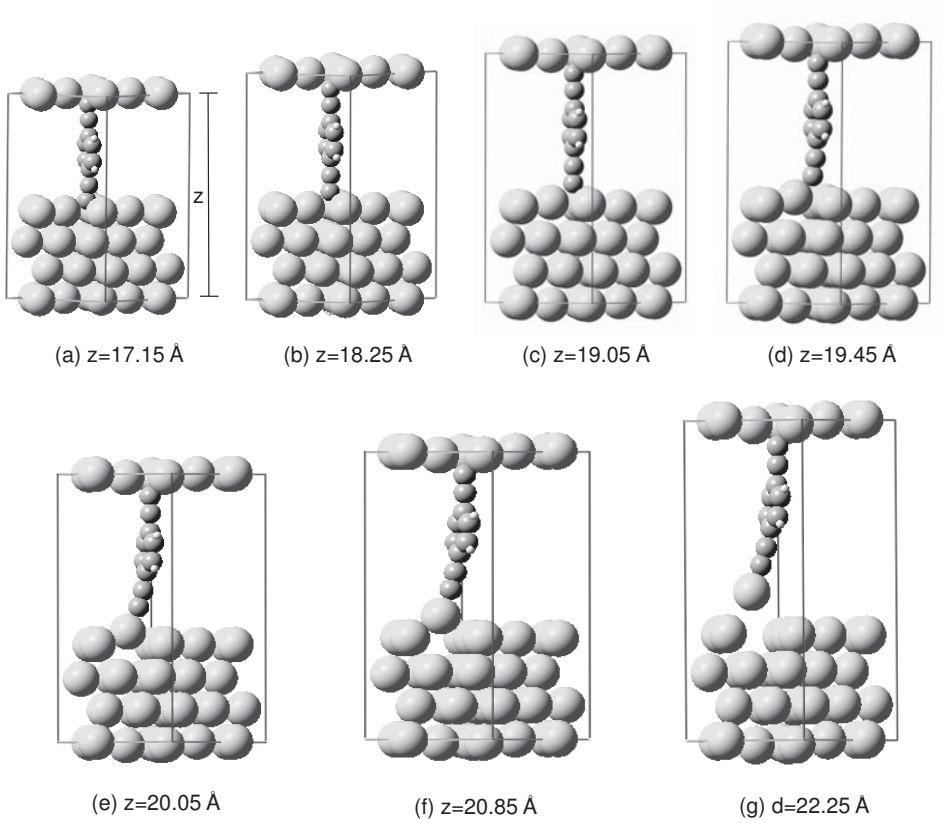

Figure 5.21: Unit cells of the DEB junction at selected intervals of stretching. The equilibrium junction geometry is shown in panel (b) where $z = 18.25$ Å.

in Ref. [128]. The geometric parameters of the junction at various unit cell sizes are defined in the same way as for XYL and summarised in table 5.2. $\Delta\mathrm{Au}_1$ and d_1 are measured with respect to the single Au atom pulled out of the surface. $\Delta\mathrm{Au}_2$ and d_2 are measured with respect to the three Au atoms closest to the carbon atom at the upper end of the molecule.

Figure 5.22 shows the total energy of the junction and the restoring force on the unit cell size as a function of z. The limiting value of σ_{zz} was not explicitly found, but since the electrode geometry is identical to the XYL case, the same value of $R = 0.17$ eV/Å was used as the residual stress.

The equilibrium unit cell size is $z = 18.25$ Å. Below this size the restoring force is positive and acts to increase z. Above the equilibrium value, the restoring force is negative acting to reduce z. Two minima can be identified for the force.

z (Å)	d_1 (Å)	$\Delta\mathrm{Au}_1$ (Å)	$\Delta\mathrm{Au}_2$ (Å)	d_2 (Å)	$z_{\text{C-C}}$ (Å)
17.15	0.92	-0.02	-0.03	0.93	8.04
17.45	1.04	-0.01	0.00	1.02	8.10
17.75	1.13	0.02	0.03	1.11	8.16
18.05	1.19	0.05	0.08	1.22	8.22
18.25	1.29	0.10	0.08	1.23	8.27
18.45	1.33	0.15	0.11	1.28	8.30
18.75	1.44	0.21	0.14	1.32	8.35
19.05	1.53	0.27	0.17	1.39	8.40
19.45	1.75	0.39	0.20	1.42	8.38
19.84	1.84	0.78	0.22	1.42	8.29
20.05	1.87	0.95	0.22	1.43	8.29
20.25	1.88	1.13	0.23	1.43	8.29
20.45	1.92	1.28	0.22	1.43	8.30
20.85	1.93	1.62	0.23	1.45	8.30
21.25	1.94	1.95	0.25	1.47	8.31
21.65	1.93	2.32	0.26	1.49	8.31
21.85	1.92	2.53	0.28	1.50	8.31
22.25	1.86	3.01	0.31	1.49	8.25

Table 5.2: Geometric parameters for relaxed DEB junctions. d_1 is the height of the carbon above the gold atom being pulled out of the surface. $\Delta\mathrm{Au}_1$ is the height of this gold atom above the rest of the surface. d_2 is the height of the carbon atom at the upper end of the molecule below the three gold atoms on the top surface to which it is bonded. $\Delta\mathrm{Au}_2$ is the distance of these three atoms below the rest of the top surface layer. $z_{\text{C-C}}$ is the distance between the carbon atoms on opposite ends of the DEB molecule along the z-axis.

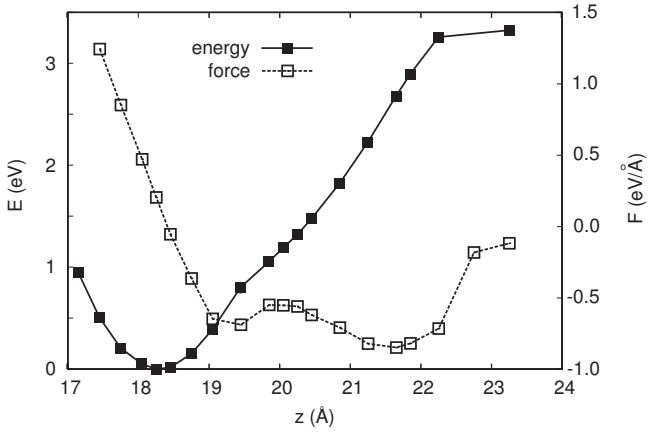

Figure 5.22: Relative total energy E, and force, $F = -\frac{\mathrm{d}E}{\mathrm{d}z}$ vs unit cell size z, for the DEB junction.

The first minimum, $|F(19.45\ \text{Å})| = 0.69\ \text{eV/Å} = 1.10\ \text{nN}$, is the force required to pull the gold atom out of registry with the rest of the surface and reduce the number of gold atoms coordinated to the carbon from three to one. The second minimum, $|F(21.65\ \text{Å})| = 0.85\ \text{eV/Å} = 1.36\ \text{nN}$ is the force required to break the Au-Au bond and pull the single gold atom free from the surface. Since stretching the XYL junction did not succeed in pulling a gold atom free from the surface, it is surprising that the Au-Au breaking force calculated here is smaller than the S-Au breaking force calculated in the XYL case. The result could be improved by performing optimisations at more regular intervals and with stricter convergence criteria.

The zero bias results of the conductance of the DEB junction is plotted in figure 5.23 as a function of the unit cell size z. The conductance decays rapidly both initially as the carbon atom is detached from the surface and binds to a single gold atom, and finally as the gold atom is detached from the surface. The conductance is higher for the squeezed junction than the equilibrium junction.

The PDOS on the DEB molecule *including* the detached gold atom is plotted in figure 5.24a-d for various junction sizes. The corresponding transmission functions are shown in figure 5.24e-h. Changes in the PDOS upon stretching are significant only for energies more than 1 eV below the Fermi level. The lowering of the broad transmission feature around E_{F} for the stretched junctions is due to the reduced coupling between the carbon and gold atoms as well as between the

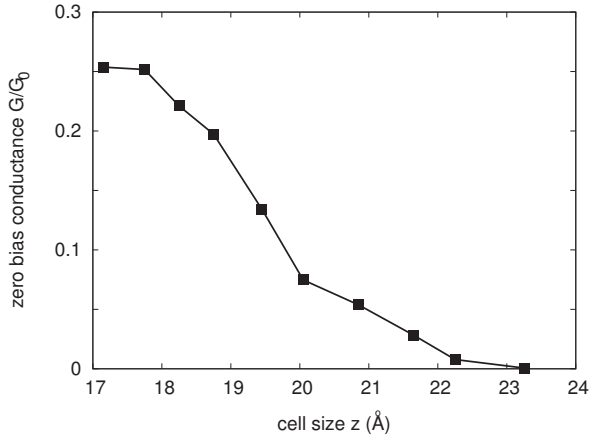

Figure 5.23: Zero bias results of the conductance for the DEB junction as a function of the unit cell size z.

detached gold atom and the rest of the surface. The transmission resonance close to the Fermi level in the XYL case, is not observed here since the Au-C bond is not broken and there are no unpaired electrons giving rise to states close to the Fermi level.

5.5 Summary

In this chapter the DFT electronic structure theory combined with the non-equilibrium Green's functions technique was used to study the transport properties of several molecular junctions. $I(V)$ characteristics and zero bias conductance results were calculated for junctions both in their equilibrium (minimum energy) geometry and in several alternate geometries. The junctions consist of one molecule sandwiched between Au(111) electrodes.

The $I(V)$ curves for a series of alkane chains as well as four aromatic molecules were calculated. The asymmetric EPM molecule yields an asymmetric $I(V)$ characteristic; the size of the current is inbetween that of XYL and DEB. DEB is notably more conductive than XYL.

The zero bias conductances results for the alkane chains and aromatic molecules were compared with experimental values in the literature. Extrapolating the alkane data to contact between the electrodes showed that the decay curve for the zero bias conductance results is more reliable when the data is plotted as

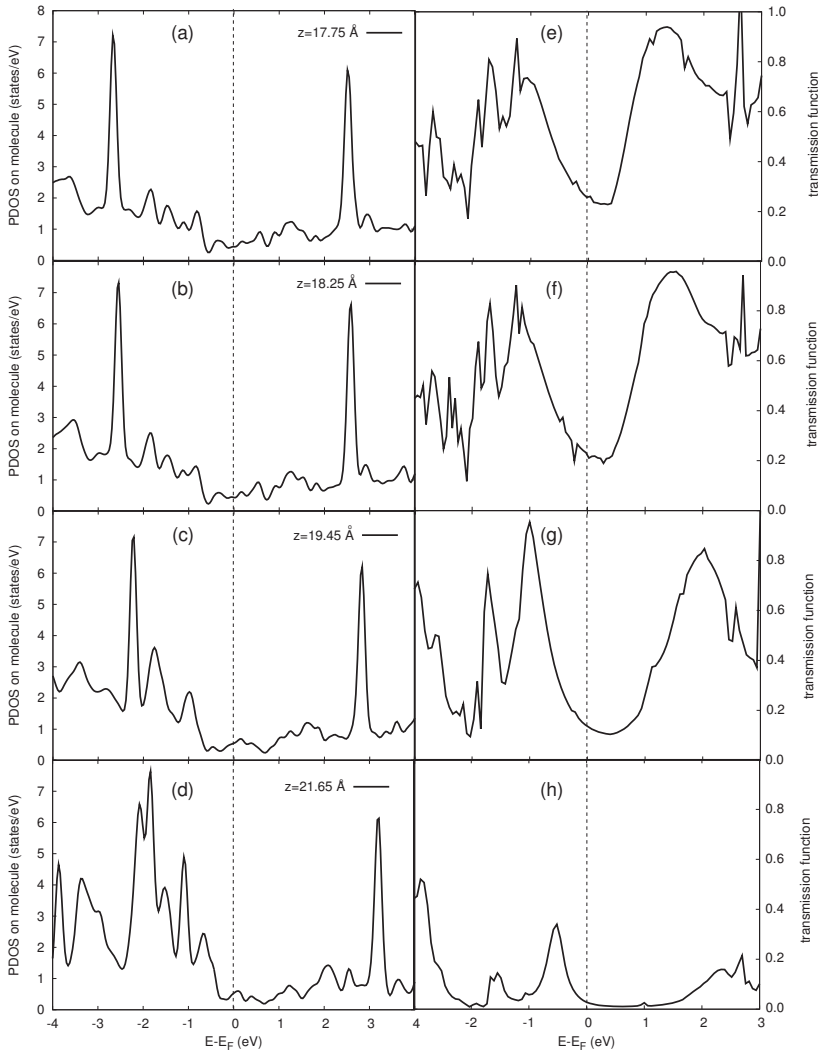

Figure 5.24: (a-d) PDOS on the DEB molecule including the detached gold atom. (e-h) Transmission functions for various junction sizes.

a function of the number of carbon atoms in the chain, rather than the inter-electrode distance. The calculations predict the aromatic molecules to be more conductive than the alkane chains, in line with expectation, whereas the experimental data suggest the opposite.

Changing the binding site of XYL on both electrodes reduced the current as the interaction between the molecule and surfaces became less favourable. The change in current was marginal compared with the orders of magnitude difference in conductance between our calculations and experimental data from the literature. Introducing a gap between the molecule and one of the electrodes indeed reduces the conductance by orders of magnitude when the hydrogen atom attached to the sulphur on the gap side is not removed.

Comparison between the currents across junctions with different molecules in this molecule-gap geometry was difficult due to the sensitivity of the current on the exact gap distance. This sensitivity can be reduced by using a more accurate energyshift parameter for orbital confinement. The results did point to the ENB molecule being less conductive than its counterparts.

The zero bias conductance results were calculated for an XYL junction with various distances between the right sulphur atom and right electrode, where the right S-H bond has been cleaved. These calculations were performed with a more accurate energyshift parameter to better describe the large interatomic distances. The conductance at zero bias *increased* both as the S-Au bond was stretched and broken, before eventually decaying to zero for large Au-S distances. This behaviour could be ascribed to a resonance in the density of states on the molecule in the vicinity of the Fermi level. When the Au-S bond is broken the system is in a spin doublet state and the conductance increase only occurs for electrons of one spin-type. The behaviour was qualitatively confirmed with a one-level model.

The geometries of XYL and DEB junctions were investigated as the junctions were systematically stretched and optimised in a series of steps. The Au-S bond was cleaved before any gold atoms were removed from the surface. However the strong Au-C bond was not broken and a single Au atom was detached from the surface as the junction was stretched. The presence of the gold atom bonded to

the terminal carbon precludes a resonance in the PDOS and transmission function and hence the conductance decays rapidly as the DEB junction is stretched. The conductance of the XYL junction decreased as the Au-S bond length increased, contrary to the observation for the unoptimised XYL junctions. A resonance did appear in the PDOS close to the Fermi level once the Au-S bond was broken with the system in a spin doublet state. However the transmission function and conductance could not be obtained in this case.

Chapter 6

Transport Calculations Using a Tunnel Barrier Model

In this chapter the problem of electron transport across a molecular junction is approached by modelling the junction as a tunnel barrier. It is assumed that semi-infinite electrodes exist to the left and right of the device region and are separated by a distance d_{E}. When an external bias is applied to the electrodes, electrons flow from source to drain by tunnelling through the barrier, the form of which is determined by the molecule occupying the device region. The problem is treated as one-dimensional.

This empirical model serves as a comparison to the DFT results in chapter 5 and experimental measurements in the literature. Furthermore, the increased speed with which these lower level calculations can be completed, allows for systematic variation of the fundamental junction parameters, which is not feasible in the DFT approach. Hence desirable properties of molecular junctions may be identified by scanning over a large parameter space, after which a small subset of junctions can be investigated at a higher level of theory.

6.1 Implementation of a WKB tunnel barrier approximation

The WKB approximation to the Schrödinger equation was used to calculate the transmission function $T(E)$, and tunnelling current $I(V)$, between the electrodes. The derivation of these quantities is given in section 2.5. They can be computed from equations (2.129) and (2.130) after specifying the form of the tunnel barrier, $U(x)$.

Fortran code was written to evaluate the integrals in equations (2.129) and (2.130) using Simpson's rule. Evaluation of the transmission function requires as input the barrier function and the relevant energy point. The mass m, is taken as the mass of an electron. Evaluation of the current proceeds from knowledge of the transmission function and specification of the input voltage.

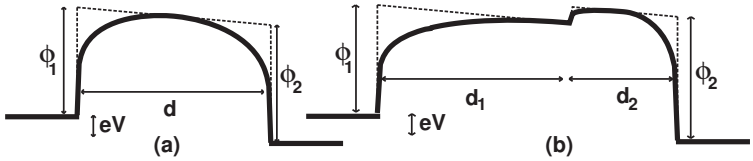

Figure 6.1: (a) Trapezoid and (b) double rectangle barriers. Solid lines indicate the barriers with a rounding parameter, $\alpha = 0.2$ and broken lines show the barriers with no rounding, $\alpha = 0.0$.

In principle any barrier function can be implemented and the function call linked to the remaining code. Thus far trapezoid and double rectangle barriers with sinusoidal rounding have been implemented and are shown in figure 6.1. The trapezoid shape is described by

$$U_{\mathrm{T}}(x) = eV(1 - \frac{x}{d}) + \left[\phi_1 + \frac{x}{d}(\phi_2 - \phi_1)\right] \cdot \left[\sin\left(\frac{\pi x}{d}\right)\right]^{\alpha}. \qquad (6.1)$$

The α parameter is responsible for rounding the edges of the barrier to account for image charging [47]. We use either $\alpha = 0.0$ (no rounding) or $\alpha = 0.2$ (as in Ref. [47]). ϕ_1 and ϕ_2 are the heights of the trapezoid on the left and right. $d = d_{\mathrm{E}}$ is the interelectrode distance or width of the barrier.

The rounding of the double rectangle is set to match the electrode potentials

at $x = 0$ and $x = d$, as in the trapezoid case. At the interface of the two rectangles, the barriers on the left and right are set to approach the height of the lower rectangle, as seen in figure 6.1b. This complicates the expression for the double rectangle; the case where $\phi_2 > \phi_1$ (figure 6.1b) is given by

$$U_{\mathrm{DR}}(x) = \begin{cases} eV\left(1-\frac{x}{d}\right) + \phi_1\left[\sin\left(\frac{\pi}{2}\cdot\frac{x}{d_1}\right)\right]^{\alpha} & \text{if } 0 < x < d_1 \\ eV\left(1-\frac{x}{d}\right) + \phi_1 + (\phi_2-\phi_1)\cdot\left[\sin\left(\pi\frac{x-d_1}{d_2}\right)\right]^{\alpha} & \text{if } d_1 < x < d_1 + \frac{d_2}{2} \\ eV\left(1-\frac{x}{d}\right) + \phi_2\left[\sin\left(\pi\frac{x-d_1}{d_2}\right)\right]^{\alpha} & \text{if } d_1 + \frac{d_2}{2} < x < d \end{cases} \tag{6.2}$$

where d_1, ϕ_1 and d_2, ϕ_2 are the widths and heights of the left and right rectangles with $d_1 + d_2 = d$. The case where $\phi_1 > \phi_2$ is obtained by a suitable modification.

To avoid confusion, we do not refer to conventional current, but rather to electron flow. A positive bias and current corresponds to the situation in figure 6.1 with electron flow being from left to right.

6.2 Single molecule acting as tunnel barrier

The WKB tunnel barrier model is used to calculate the current across the junctions studied in chapter 5. Each molecule should be identified with a unique barrier shape, $U(x)$. In the present work this is achieved by considering the modification of the left and right surface work functions due to adsorption of the molecule. The results from this model are compared with the *ab-initio* results from chapter 5 and the results when solving $T(E)$ exactly according to the Schrödinger equation [72].

More sophisticated barrier shapes may be used in future work. In principle the WKB solution to the transmission function can be found for barriers of arbitrary shape. Exact solutions to the Schrödinger equation can be obtained when the barrier is assumed to consist of a series of (unrounded) retangles.

6.2.1 Modified surface work functions

The interelectrode region is modelled with a trapezoid or double rectangle barrier, where the barrier heights on the left and right correspond to the respective surface

work functions. The molecules are viewed as altering this barrier simply by changing the work function of the surface on which it is adsorbed. Reduction of the work function of an electrode by surface layers is well-known. For example, coating tungsten [193, 194] and other cathodes [194] with BaO can significantly reduce the cathode work function. In this case the reduction of the cathode work function has been correlated with the density of BaO dipoles [194].

In section 4.1.3, we presented highly accurate DFT calculations of the work function of a bare Au(111) surface, giving $\phi_{\mathrm{Au}} = 5.13$ eV. These calculations were repeated at the same level of theory for a Au(111) surface with the adsorbed molecules already encountered in chapters 4 and 5. As in the majority of the adsorption calculations in chapter 4, 3x3 gold atoms per layer are included in the unit cell to avoid interactions between molecules in adjacent cells. These calculations were therefore much more computationally intensive than the calculation of the bare gold work function, where only one gold atom per layer was needed. Nevertheless, the calculations were performed with 10 Au(111) surface layers and an energyshift parameter of 0.1 mRy. In the plane of the surface a sampling grid of 5x5 k-points was used. This is equivalent to the 15x15 grid used in the bare surface calculations, since the unit cell has been scaled by a factor of three in the dimensions parallel to the surface.

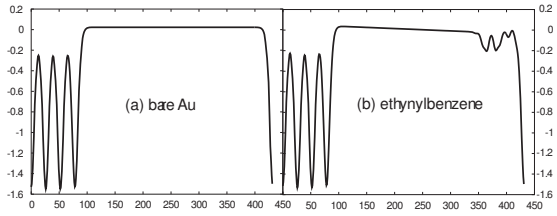

Figure 6.2: Electrostatic potential averaged over xy-plane for unit cells containing (a) a bare gold slab and (b) a gold slab with adsorbed ethynylbenzene.

The work function is given by equation (4.3) in section 4.1.3. The average electrostatic potential in each xy-slice parallel to the surface was calculated and the electrostatic potential in the vacuum, V_{vac}, taken as the converged value far away from the slab. As seen in figure 6.2a, this works for the case of a bare surface. However, when a molecule is adsorbed on one of the two surfaces of the thin slab, the electrostatic potential in the vacuum is sloped as shown in

figure 6.2b. This is due to the periodic boundary conditions enforced by the calculation. The problem can be overcome by adding a dipole correction energy to the DFT total energy [195] or by symmetrically adsorbing a molecule on both surfaces of the slab. However, in the present calculations the vacuum electrostatic potential was directly read off the sloping potential profile of figure 6.2b. This was done by observing the start of the straight line portion of the V_{vac} vs z profile on the molecule side of the vacuum and taking the desired vacuum electrostatic potential at this point. As a check the method was used to read V_{vac} values for the bare slab off the potential profile on the bare slab side of the unit cells with adsorbed molecules. These values were compared with the V_{vac} values obtained from the bare slab calculation and the error was found to be at most 0.04 eV. Effectively the dipole correction of Ref. [195] is being applied *a posteriori* and possible changes in atomic geometry and electronic charge density due to the spurious electric field are not accounted for.

The resulting work functions calculated from equation (4.3) are listed in table 6.1. EPM-S and EPM-C indicate the ethynylphenylenemethanethiol molecule attached to the gold surface on the methanethiol and ethynyl sides respectively.

The surface work function can be viewed as the energy required to remove an electron from the Fermi level of the surface, plus the energy required to move the electron through the surface dipole to a position far removed from the surface. Table 6.1 lists the surface dipole moment per unit area for a gold slab and some adsorbed molecules. While SIESTA does provide the total dipole moment in each direction in the unit cell, this is not what is required, since the slab geometry has two surfaces and the corresponding dipole moments are oriented in opposite directions. Fortran code was written to calculate the dipole moment of a surface by integrating the charge density given by SIESTA between positions in the centre of the slab and in the vacuum region far removed from the slab. Accordingly the dipole moment per unit area is given by

$$P_\sigma = \frac{1}{A}\int_{z_0}^{z_{\text{vac}}} \left(\int_{\mathcal{A}} q(\vec{r})\mathrm{d}x\mathrm{d}y\right) z\mathrm{d}z \tag{6.3}$$

where the surface normal is in the z-direction. The charges inside a z-slice of area A are summed to give the total charge of the slice, before multiplying by the

z-position of the slice. A negative dipole moment indicates orientation towards the surface.

Apart from 1-ethynyl-4-nitrobenzene (ENB), the molecules studied have no appreciable internal dipole moment and the change in work function is largely due to the change in dipole moment induced by the charge distribution at the surface bond. It is therefore not surprising that the molecules attached via a gold-sulphur bond yield very similar work functions, $\phi_S \approx 4.9$ eV. The DEB and EPM-C molecules act to reduce the surface dipole moment more effectively through the gold-carbon bond. The ENB molecule has a large internal dipole moment pointing towards the surface and hence increases the surface work function.

Adsorbed molecule	ϕ (eV)	P_σ (10^{-2} e/a_0)
bare Au(111)	5.13	-1.14
XYL	4.92	-0.97
C6	4.90	-
EPM-S	4.91	-
EPM-C	4.50	-
DEB	4.31	-0.78
ENB	5.77	-1.60

Table 6.1: Work functions and surface dipole moments for various molecules adsorbed on the Au(111) surface, calculated from equation (4.3).

6.2.2 $I(V)$ curves

The modified surface work functions are used to define the tunnel barrier in two scenarios, shown in figure 6.3. When the molecule spans the entire interelectrode region (figure 6.3a), a trapezoid barrier is used with the barrier heights on the left and right defined by the work functions of the left and right surfaces as modified by the adsorbed molecule. If the molecule is symmetric the barrier heights will be equal. For the asymmetric EPM molecule, the barrier heights on the left and right correspond to the work functions modified by EPM-C and EPM-S respectively. The ENB molecule was not considered in this geometry, since the adsorption of the NO_2 group on gold was not characterised.

When a gap is present between the molecule and right electrode (figure 6.3b), a double rectangle barrier is used with the heights on the left and right given by

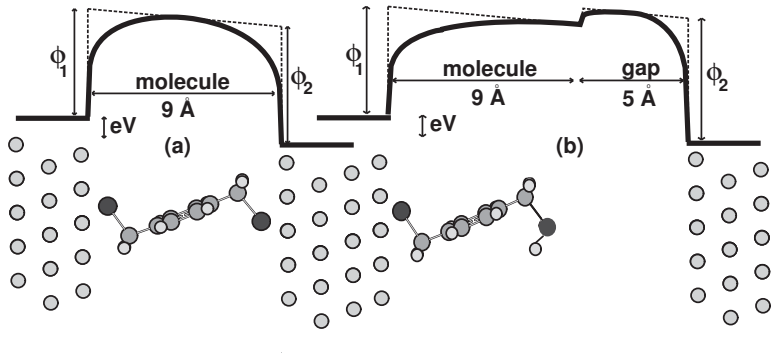

Figure 6.3: (a) Trapezoid barrier describing a molecule spanning the interelectrode region. (b) Double rectangle barrier used to desribe the interelectrode region consisting of a molecule plus gap.

the work functions of the surface with attached molecule, and bare gold surface respectively. The length of the barrier due to the molecule was assumed to be 9 Å, the approximate length of all the molecules considered here. The gap distance was assumed to be 5 Å. The sinusoidally rounded ($\alpha = 0.2$) barrier shapes are used, unless otherwise stated.

The resulting $I(V)$ curves for the molecules spanning the interelectrode region are shown in figure 6.4a. The reduction in surface work function of 0.8 eV with adsorption of DEB, increases the current by a factor of 6 at 2.0 V bias. For C6 and XYL the modest 0.2 eV reduction in surface work function, results in a 60% increase in current at 2.0 V compared with the current for the bare gold slab. The percentage increase in current due to a lower work function tends to increase with voltage, but not significantly. For example, the ratio of currents for DEB vs C6, $I_{\mathrm{DEB}}/I_{\mathrm{C6}} = 3.8$, at 2.0 V and $I_{\mathrm{DEB}}/I_{\mathrm{C6}} = 3.3$ at 0.1 V.

The negative current for the asymmetric EPM molecule was folded onto the positive side to show the asymmetric nature of the $I(V)$ characteristic. This is repeated in figure 6.4b and compared to the case where the barrier is not rounded ($\alpha = 0$). The absolute currents are obviously much larger for the rounded barrier, since the area under the barrier is smaller. In both cases the negative current (electron flow from right to left) is larger. Quite surprisingly, the asymmetry is more pronounced for the rounded barrier, but in both cases the effect is very small. At 2.0 V bias the asymmetry is about 4% for the sharp barrier and 6%

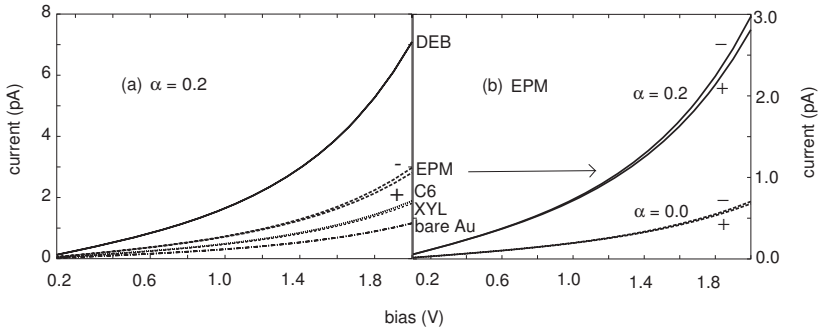

Figure 6.4: (a) $I(V)$ curves calculated with the WKB approximation using the trapezoid barrier shown in figure 6.3a. (b) Comparison of the $I(V)$ curves for the asymmetric EPM molecule using a rounded ($\alpha = 0.2$) or sharp ($\alpha = 0.0$) barrier.

for the rounded barrier.

Figure 6.5 shows a similar comparison between the $I(V)$ curves for the geometries with a gap between the right end of the molecule and the electrode, as shown in figure 6.3b. Here we have included the ENB molecule. The NO_2 group is on the gap side and there is no chemical bonding between this end and the right electrode. The work function of ENB is 0.85 eV higher than that of XYL, causing the current to be a factor of 6.3 smaller at 2.0 V and a factor of 6.4 smaller at 0.1 V. Again the influence of the bias on the relative currents is minor.

Because of the asymmetric nature of the geometry, all the curves in figure 6.5 show a slight asymmetry. In figure 6.4b, the $I(V)$ curves for rounded and sharp barriers are compared in the case of DEB. Again the rounded barrier ($\alpha = 0.2$) produces a more asymmetric response. In this case the excess negative bias current over positive bias current at 2.0 V is 60%, whereas the excess is only 20% when using a sharp barrier.

6.2.3 Comparison with exact solution to Schrödinger equation and *ab-initio* results

A comparison of the $I(V)$ curves for DEB resulting from the WKB approximation and the exact solution to the Schrödinger equation for the sharp barriers shown in figure 6.3 [72], revealed that the exact solution gives a current 3-4 times larger at 2.0 V bias. For a much longer barrier, the WKB result is closer to the

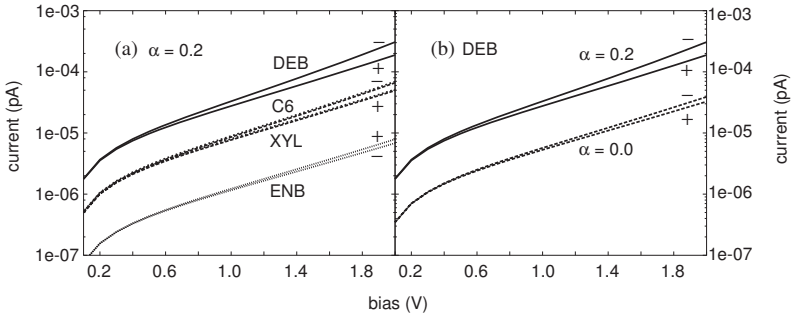

Figure 6.5: (a) $I(V)$ curves calculated with the WKB approximation using the double rectangle barrier shown in figure 6.3b. (b) Comparison of the $I(V)$ curves for the DEB molecule with a gap, using a rounded ($\alpha = 0.2$) or sharp ($\alpha = 0.0$) barrier.

exact solution, since the approximation is more appropriate in this regime [72]. Nonetheless, the asymmetry predicted by both methods is almost identical – the excess negative current over positive current for the DEB+gap geometry is about 20%.

The currents calculated with the DFT-NEGF formalism in chapter 5 are several orders of magnitude larger than those presented here for the WKB tunnel barrier model. As discussed in chapter 1, experimental currents are also generally much smaller that DFT-NEGF currents, while there is certainly a large spread among experimental values. The tunnel barrier model currents presented here are similar in size to those recently reported for large area molecular junctions [31]. However, the latter results were obtained with the decanedithiol molecule, about 17 Å in length. Considering the spread in experimental data for single-molecule currents, summarised in figure 5 of Ref. [31], it is fair to say that most experimental data lie between the WKB tunnel barrier results presented in this section and the DFT-NEGF results presented in chapter 5.

6.2.4 Implications for asymmetry and rectification

Here we discuss the asymmetry in the $I(V)$ characteristics (rectifying effects) caused by the spatial asymmetry of the molecular junctions studied. The spatial asymmetry arises either from the inherent asymmetry of the molecule or from different interface geometries at the electrodes.

In chapter 5, the DFT-NEGF calculated $I(V)$ curves for the asymmetric junctions with a gap between the molecule and right electrode (figure 5.11), show quite pronounced asymmetry. At 1.0 V the positive current (electron flow from left to right) is a factor of 5-10 times larger than the negative current for the molecules studied. The $I(V)$ curve for the asymmetric EPM molecule chemically bound to both electrodes (figure 5.4) also shows significant asymmetry, however the sense of the asymmetry reverses at 1.0 V. Below 1.0 V the negative current is larger and above 1.0 V the positive current is larger.

On the other hand, the current calculated with the double rectangle tunnel barrier model in section 6.2.1 is larger when electrons tunnel first through the higher and second through the lower barrier. In Appendix B we prove that this is a general result when using the WKB expression, equation (2.129), with either a trapezoid or double rectangle barrier with no rounding ($\alpha = 0.0$). The proof holds only when the applied bias is smaller than both barrier heights, $eV < \phi_1, \phi_2$. Outside this regime the validity of the WKB approximation becomes doubtful, since the transmission function has to be truncated at incident energies larger than the barrier $U(x)$.

Since the work function on the gap side is larger than on the molecule side for the molecules studied in chapter 5, the asymmetry predicted in section 6.2.1 is in the opposite sense as that calculated with the DFT-NEGF theory.

To quantify this result, we define the rectification $r(V)$, at a particular bias voltage as

$$\begin{aligned} r(V) &= \frac{I_f(V) - I_r(V)}{I_f(V) + I_r(V)} \\ I_f(V) &= \left|I(|V|)\right| \\ I_r(V) &= \left|I(-|V|)\right| \end{aligned} \tag{6.4}$$

The rectification for the Au(111)-XYL-gap-Au(111) junction calculated from the DFT-NEGF $I(V)$ data in chapter 5 is $r(0.1\text{ V}) = 0.13$ and $r(0.5\text{ V}) = 0.44$. From the tunnel barrier model, $r(0.1\text{ V}) = -0.005$ and $r(0.5\text{ V}) = -0.025$.

Rectification based on an exact solution to the Schrödinger equation for a double rectangle barrier is in agreement with the WKB results [72].

6.2.5 Possible improvements on the model

The large disparity between the currents obtained with the WKB tunnel barrier model and the DFT-NEGF full electronic structure method, points to the fact that the effect of the molecule is indeed more complicated than a simple change of the surface work function. The alignment of the HOMO and LUMO energy levels of the molecule relative to the Fermi level of the electrodes has a large effect on the transport properties of the molecular junction in simple toy models [168] and self-consistent Green's function models [196] alike. In Ref. [73] a double tunnelling barrier is conceptually associated with an electrode-molecule-gap-electrode geometry in the same way as in this chapter, but taking the local density of states of the molecule into consideration.

In this work it has been demonstrated that the WKB tunnel barrier approximation is unable to capture important resonance behaviour in transmission spectra, leading for example to the enhanced conductance of stretched junctions described in section 5.4.3. However, the model can capture some qualitative behaviour of molecular junctions and the orders of magnitude speed improvement it brings over more sophisticated electronic structure methods thus makes it an attractive alternative.

The model deviates from the real-life scenario in that the complicated interplay between the electronic structure of a molecule and large electron reservoirs is approximated by an effective potential barrier. Furthermore the three-dimensional problem is reduced to one dimension. In improving the model these issues should be addressed without reverting to a full electronic description.

More complete tunnelling theories are available which go beyond the WKB approximation and consider the degrees of freedom perpendicular to the direction of transport [197–199]. Furthermore in approximating the potential profile between electrodes, we have thus far averaged over the dimensions perpendicular to tranport. A more detailed description of the three-dimensional local potential can be obtained from a SIESTA electronic structure calculation of the system. Although the object is to avoid a full self-consistent calculation, such a potential profile could be obtained once and suitably modified for different molecular geometries. In figure 6.6 the electostatic potential inside the device region is plot-

ted for the same geometry as shown in figure 6.3b. The potential is shown for parallel slices at various distances normal to the electrode surfaces. Slices near the left electrode (larger d-values) indicate a clear lowering of the potential in the central region due to the presence of the molecule. This is indicated by the dark areas on the contour plots for panes with $d \geq 4.64$ Å. The potential for slices near the right electrode ($d < 4.64$ Å) rapidly reduce to the flat vacuum level. Replacing the averaged one-dimensional potential profile with the more complete three-dimensional description should enhance tunnelling since the local potential in the region of binding is reduced more effectively than the planar averaged potential. Asymmetry should also be enhanced since the barrier is effectively lowered on the molecule side, but not on the gap side. Results may thus agree more closely with the DFT-NEGF results of chapter 5.

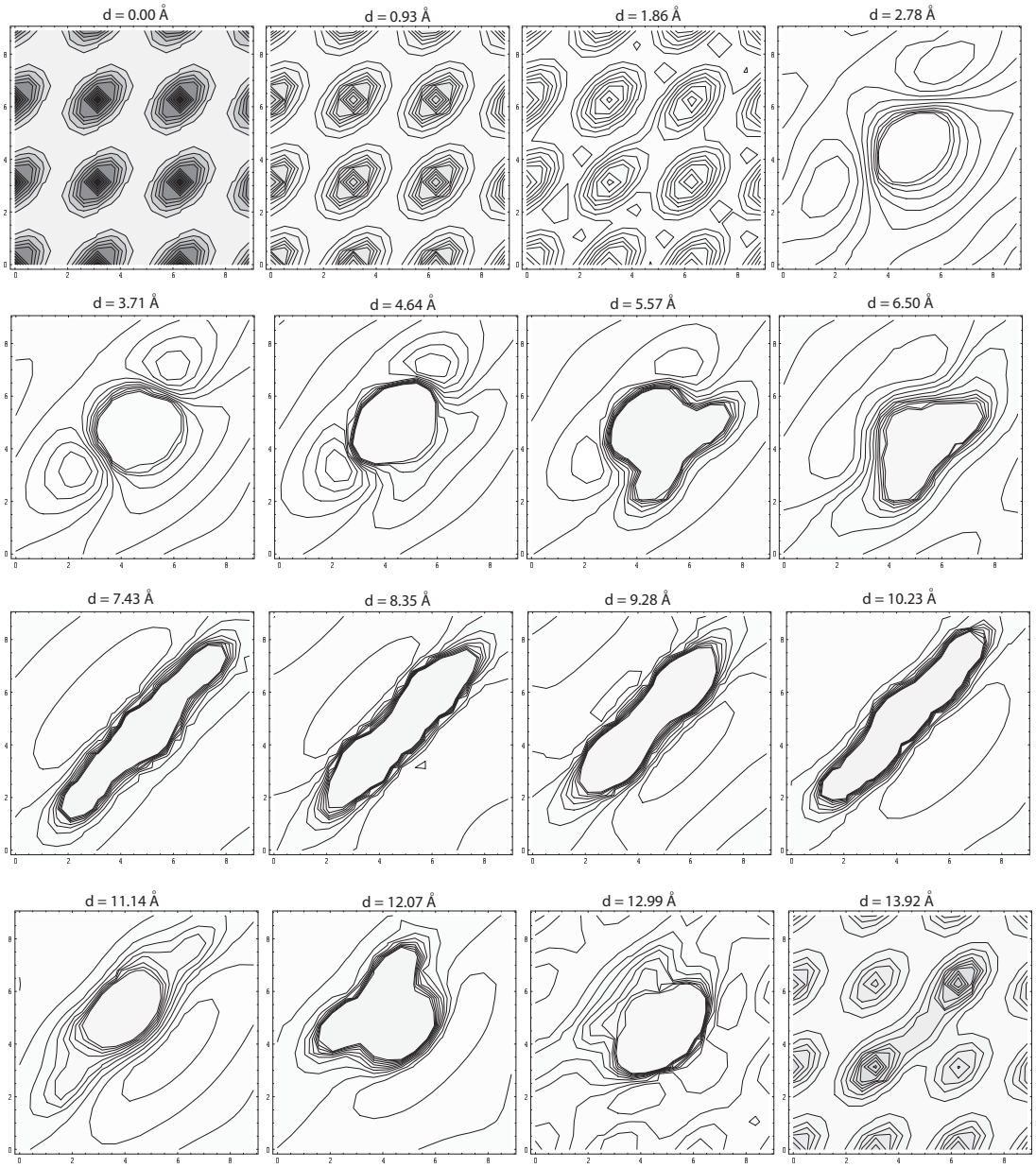

Figure 6.6: Electrostatic potential inside the device region of an electrode-XYL-gap-electrode system (shown in figure 6.3b). Each pane represents a contour plot of the potential in a slice parallel to the transport direction a distance d from the *right* electrode surface. The separation between the electrode surfaces is 14.85 Å.

6.3 Modelling a tunnel gap in STM experiments

In this section the WKB tunnel barrier model is used to describe a typical experimental setup. An STM tip is lowered onto a molecular monolayer adsorbed on a gold surface. Gold nanoparticles are attached to the top of the monolayer, as shown in figure 6.7. A gap of distance d exists between the STM tip and a gold nanoparticle. In the model this gap will be varied, but is generally unknown in STM experiments. We assume that the particles are large enough that the Coulomb blockade effect can be neglected, but that only one molecule is attached to each particle. This is certainly possible, for example if dithiol molecules are embedded in a matrix of single-ended thiols [22]. Current flow occurs through two resistors in series, namely the molecule attached to the nanoparticle and the gap between tip and nanoparticle.

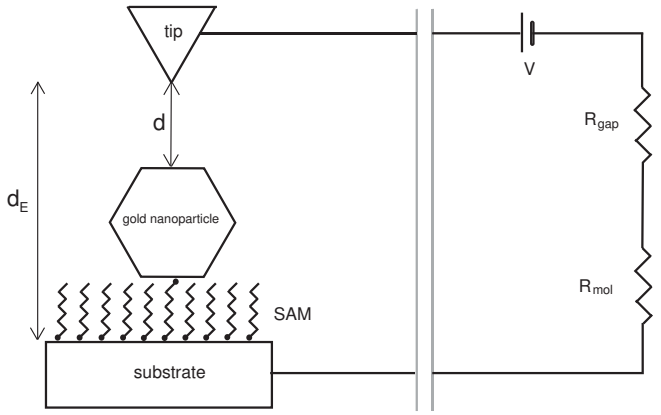

Figure 6.7: Schematic of STM setup.

The current through the molecule I_{mol}, is taken from the DFT-NEGF results in chapter 5 as a function of the bias between substrate and nanoparticle, $V_{\mathrm{mol}} = V_{\mathrm{substrate}} - V_{\mathrm{particle}}$, in steps of 0.1 eV. The current through the gap, I_{gap}, is given by the tunnel barrier model as a function of the bias between nanoparticle and tip, $V_{\mathrm{gap}} = V_{\mathrm{particle}} - V_{\mathrm{tip}}$, and the gap distance, d. The prefactor $\frac{2e}{h}$ in equation (2.130) is valid for an ideal tip with one atom at the apex, so that a point contact is formed when the tip touches the nanoparticle ($d = 0$). $I_{\mathrm{gap}}(V_{\mathrm{gap}}, d)$ is calculated in steps of 0.1 eV and 0.1 Å using a single rectangle barrier, equation (6.1) with $\alpha = 0.2$ and $\phi_1 = \phi_2 = 5$ eV, approximately the work function of gold. In order to

find the relation $I_{\text{tot}}(V_{\text{tot}}, d)$ for the current-voltage characteristic of the combined system, we use $I_{\text{tot}} = I_{\text{mol}} = I_{\text{gap}} = I$ and $V_{\text{tot}} = V_{\text{mol}} + V_{\text{gap}}$ for resistors in series. Rewriting with the current as independent variable, we have

$$V_{\text{tot}}(I, d) = V_{\text{mol}}(I) + V_{\text{gap}}(I, d). \tag{6.5}$$

The terms on the right hand side were calculated in voltage steps of 0.1 eV. For a suitable set of current points I and gap distances d, these data can be interpolated to give the corresponding V_{mol} and V_{gap} values, which are added to give $V_{\text{tot}}(I, d)$. This is inverted to give $I(V_{\text{tot}}, d)$ and interpolated for arbitrary voltages.

6.3.1 Combined molecule-gap $I(V)$ characteristics

Figure 6.8 shows the resulting current for various molecules at a fixed tip-substrate bias of 0.5 V, as the gap distance is increased. The pure WKB result is shown for comparison, where there is no molecule present and the substrate voltage is assumed equal to the nanoparticle voltage. For each molecule we see initially a slow response as the gap is introduced where the resistance of the molecule dominates. However, as soon as the gap distance dominates, the current decays exponentially with d. The onset of exponential decay occurs at larger gap distances for more resistive molecules; for the most resistive molecule, C12, exponential decay starts at $d \approx 5$ Å. With this model, experimental and theoretical results can be reconciled for reasonably small gap distances, which are likely to be present in actual experiments. The shaded region in figure 6.8 shows the range of experimental currents at 0.5 V found in the literature for BDT and XYL [3, 13, 23, 43, 45]. The presence of such a gap is a realistic scenario in some experiments and this can obscure high conductances and interesting features in current-voltage characteristics of molecules. The results in figure 6.8 also clearly show that for STS measurements to be able to distinguish between molecules as different as alkanethiols and alkynethiols, the gap between tip and substrate must be less than about 6 Å. To distinguish between molecules with similar values of conductance, such as DEB and BDT, this gap must be less than about 2 Å.

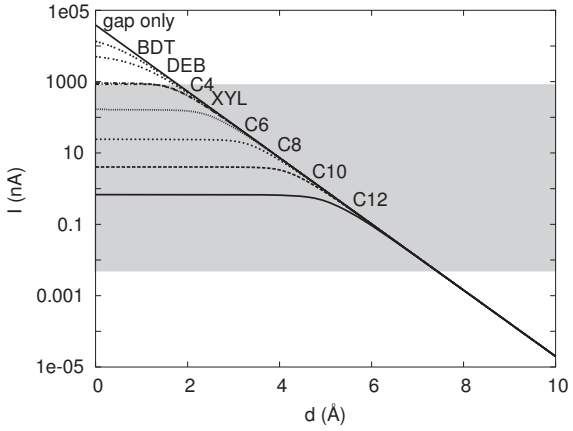

Figure 6.8: Current at different gap distances for the STM setup shown in figure 6.7 for various molecules. The bias between tip and substrate is fixed at 0.5 V.

6.3.2 Apparent molecule heights in STM measurements

From the results presented in figure 6.8, some insight can be gained into the problem of measuring molecule heights in STM experiments. As analysed by Weiss *et al.* [44], if an STM tip is scanned from a region of one type of molecule to another, or from a region of SAM to bare substrate, the tip does not necessarily follow the true contours of the sample, but measures the apparent height. The reason for this is that the different regions will have different conductances and the tip will move to maintain constant current.

Define h_{STM} as the height of the STM tip above the substrate, h_{mol} as the thickness of the SAM, d the gap distance between the STM tip and the SAM and Δh_{STM}, Δh_{mol} and Δd as the change in these quantities as the STM tip is moved at a fixed current from one type of molecule to another or to a bare surface. Then

$$\Delta h_{\mathrm{STM}} = \Delta h_{\mathrm{mol}} + \Delta d. \tag{6.6}$$

Δh_{STM} is the apparent height difference and is a known quantity in STM experiments. Δh_{mol} is the true height difference and the quantity we aim to determine. If the tip moves from a monolayer to a bare surface, then $h_{\mathrm{mol}} = \Delta h_{\mathrm{mol}}$.

From figure 6.8, if $d > 6$ Å, then as the tip moves from one molecule to another, for example from C12 to XYL, constant current can be maintained

without altering d. In other words, $\Delta d = 0$ and hence $\Delta h_{\mathrm{STM}} \approx \Delta h_{\mathrm{mol}}$. In this regime the gap dominates the resistance and the difference in heights of the STM tip above the molecules reflects the actual geometric height differences between the molecules. For tip-SAM distances less than 6 Å this is no longer the case and the apparent height deviates from the true height of the molecule. This is illustrated in figure 6.9 for an STM tip scanning at constant current from a C12 molecule to bare substrate. The apparent height measured by the STM minus the true height is plotted as a function of the set point current, i.e. Δd vs I. For set point currents less than about 0.5 nA, which from figure 6.8 corresponds to a gap of about 6 Å, the apparent height is approximately equal to the true height. This is the regime described above. However, for currents greater than 0.5 nA, i.e. gaps of $d < 6$ Å, the apparent height diverges rapidly from the true height.

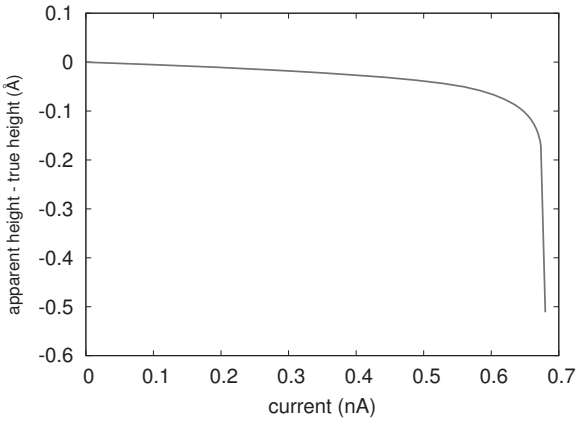

Figure 6.9: Offset of the apparent height from the true height of a C12 molecule when an STM tip is moved from a self-assembled monolayer of C12 to a bare gold surface.

Figure 6.8 shows that if the tip is above the C12 molecule, the tunnelling current is approximately independent of the tip-molecule distance for distances less than about 6 Å. In this regime, if the tip now moves onto one of the other molecules studied here, the current can only be maintained by moving the tip to a gap of 5.1 Å above the molecule. This is inferred from figure 6.8 by extrapolating the plateau region of C12 until it intersects the current-distance curves for the other molecules. If the tip is started at a distance of d_{C12} above the C12 molecule, then the apparent height is given by $\Delta h_{\mathrm{STM}} \approx \Delta h_{\mathrm{mol}} + (0.51 - d_{\mathrm{C12}})$. In order to

determine the true height of the molecule, the initial height of the tip above the C12 molecule would need to be known.

6.3.3 Deconvoluting STS $I(V)$ curves

For a fixed bias and various current setpoints, the apparent height difference Δh_{STM} between an adsorbed monolayer and the bare slab can be measured. Substituting $\Delta h_{\mathrm{mol}} = h_{\mathrm{mol}}$ and $\Delta d = d_{\mathrm{mol}} - d_{\mathrm{bare}}$ into equation (6.6) gives the relation

$$\Delta h_{\mathrm{STM}} = h_{\mathrm{mol}} + d_{\mathrm{mol}} - d_{\mathrm{bare}}. \tag{6.7}$$

For low current setpoints $\Delta h_{\mathrm{STM}} = h_{\mathrm{mol}}$ as discussed in section 6.3.2. Thus h_{mol} can be measured as the converged value of Δh_{STM} as the current setpoint is systematically reduced and the tip scanned from molecule to bare surface, at each setpoint. For any current setpoint, the current and voltage are known and the gap distance between the tip and bare slab d_{bare}, can be calculated from the WKB approximation by substituting equation (2.129) into equation (2.130) and inverting. Thus for various current setpoints, Δh_{STM} can be measured and hence d_{mol}, the gap between the tip and monolayer, calculated from equation (6.7). With this knowledge, the bias across the gap V_{gap}, can be calculated, again by inverting the WKB equations for tunnelling across the gap. Thus the total voltage can be deconvoluted into voltages across the gap and across the molecule. The voltage across the molecule together with the setpoint current define the $I(V)$ characteristic of the molecule alone.

6.4 Summary

In this chapter a tunnel barrier model was used to evaluate the $I(V)$ characteristics of molecular junctions. A WKB solution was implemented to solve the tunnelling problem for barriers with trapezoid and double rectangle shapes. The model facilitates rapid calculation of full $I(V)$ curves and may be used to provide comparative results for different junctions and to identify junction parameters that yield desirable $I(V)$ characteristics, e.g. rectification.

DFT calculations of the modified surface dipole moments and work functions of Au(111) with various adsorbed molecules were presented. The change in work function was shown to follow the change in dipole moment, as expected. The surface work function increased upon adsorption of ENB, but decreased with adsorption of all other molecules studied. Tunnel barriers were constructed where the barrier heights are based on the modified work functions.

Despite large absolute size differences, the relative sizes of the currents for different molecules predicted by the tunnel barrier model follow the same trend as in chapter 5 with the DFT-NEGF method.

The currents obtained with the tunnel barrier model where a gap forms part of the barrier are in the $10^{-6} - 10^{-3}$ pA range and not measurable by an STM. However, these currents correspond to single-molecule tunnelling, whereas an STM is likely to measure current through multiple molecules.

The rectification obtained from the WKB solution to the tunnelling problem always favours tunnelling first through the larger side and second through the smaller side of the trapezoid or double rectangle barrier. The rectification predicted with the tunnel barrier model was much more limited than with the DFT-NEGF method in chapter 5. If the barrier heights are assumed to follow the modified surface work functions, the asymmetry predicted with the DFT-NEGF method in chapter 5 for the molecule-gap geometries, appears to be in the opposite sense as that predicted by the tunnel barrier model for all molecules that reduce the surface work function. More work is needed to assign barrier shapes that are more representative of the different molecules.

A typical STM experimental setup where a gold nanoparticle is adsorbed on a dithiol molecule embedded in a matrix of single-ended thiols, was modelled by combining the WKB tunnelling current through the tip-nanoparticle gap with the DFT-NEGF predicted current through the molecule. The large spread in available experimental data can be reconciled with this model for realistic gap distances between the tip and nanoparticle. A method is suggested whereby the true heights of molecules adsorbed on the surface can be measured. Moreover the $I(V)$ characteristic of the molecular junction alone could be extracted from the measured STS curve, using this method.

Chapter 7

Conclusion

The main aim of this work was a computational investigation of the transport properties of single-molecule junctions, in particular focusing on the effect of changing the interface geometry between the molecule and electrodes on either side of the junction. This was achieved by studying the $I(V)$ characteristics and zero-volt conductances of a series of junctions using both an *ab-initio* DFT and an empirical computational technique. The DFT electronic structure was used in combination with non-equilibrium Green's functions to describe the semi-infinite system and obtain the transmission function. Alternatively the molecular junction was described by a tunnel barrier and the WKB approximation used to calculate the transmission function.

The DFT-NEGF theory was used to calculate the $I(V)$ curves and zero-volt conductances of a series of alkane chains, aromatic dithiols and diethynylbenzene in their respective equilibrium junction geometries. The results indicate that the alkane chains are less conductive than the aromatic dithiols which are in turn less conductive than DEB. This could be attributed to the relative degrees of localisation of the electrons in the molecules. The current and conductance through the alkane junctions were shown to decay exponentially with chain length. Comparing the calculations with recent experimental results in the literature revealed an excess conductance of one order of magnitude in the case of the alkanes and two orders of magnitude in the case of the aromatic molecules. This reflects the experimental prediction of larger conductance for the alkane chains than the

aromatic molecules, contrary to expectation.

Orders of magnitude discrepancies between experimental and calculated results and indeed among different experimental results are common. The role of the geometric variation of junctions likely to occur in experiments in causing this lack of reproducibility, was investigated. Altering the binding site of the XYL molecule on either electrode from the equilibrium geometry, reduced the conductance by about a factor of two. Changing the S-Au chemical bond on one end of the molecule to a physisorbed interaction where the S-H bond on the thiol linker had not been cleaved, reduced the conductance by a similar amount. However, when the distance between the thiol linker and electrode was increased by about 2 Å beyond the physisorbed distance, the conductance decreased by an order of magnitude, bringing the results closer to experimental observation.

Stretched XYL junctions where the Au-S distance is increased after the S-H bond has been cleaved, were also investigated at the DFT-NEGF level. When the Au-S bond was broken, an unpaired electron was located on the sulphur and the system was in a spin doublet state. Counterintuitively, the conductance *increased* when the Au-S distance was increased at fixed values, without allowing the junction to relax. The conductance was essentially determined by an interplay between the coupling of the molecule to the electrodes and the location of the molecular energy levels relative to the Fermi level of the system. The effect of a resonance in the energy spectrum of the molecule close to the Fermi level in increasing the conductance was larger than the effect of the reduced coupling with the electrodes in decreasing the conductance, causing a net increase in conductance as the junction was stretched.

When the junction was allowed to relax at each incremental stretching step, similar resonances in the molecular density of states were observed. The relaxation of the geometry resulted in these resonances being slightly further removed from the Fermi level and the interplay between the energy spectrum and coupling was altered sufficiently to cause the conductance to decrease with junction stretching.

Whether or not the junction was allowed to relax after the Au-S bond was broken, the resonance in the molecular density of states appeared close to the

Fermi level only for electrons of the spin type with one less occupied state. The conductance was therefore greatly enhanced for one spin type relative to the other - by a factor of 250 in the unrelaxed case. This suggests that the junction acts as a spin filter. Although the geometry is an idealistic representation of a real experimental setup, this is an interesting observation. It is conceivable that an electrode or tip may be brought into contact with a layer of thiol molecules, thereby cleaving the S-H bond, and subsequently retracted to beak the Au-S bond. In another DFT study it was suggested that the Au-Au bond would break before the Au-S bond and hence the molecule would extract a chain of gold atoms from the surface [128]. Other authors predicted that the Au-S bond would break before the Au-Au bond [127], in agreement with the present results.

The junction stretching analysis was repeated for Au(111)-DEB-Au(111) in the case where the junction was allowed to relaxed at successive steps. The Au-C bond was strong enough to extract a gold atom from the surface. As a result the density of states of the molecule did not exhibit the resonance structure of the XYL junction and the conductance decayed rapidly with stretching. The system remained in a spin singlet state throughout the stretching process.

As computational resources are rapidly improving, more realistic simulations of molecular junctions will become possible. As a first extension of the present work, a more detailed analysis of junction stretching could be performed. The relaxations could be repeated at smaller incremental stretching steps and the force tolerance tightened to obtain a better prediction of the stretching behaviour. This scenario is particularly relevant for the most recent experimental measurements of the conductance of single-molecule junctions. Simulations of rough surfaces or pyramid-like electrode structures that occur in break junction experiments may also become standard if the number of atoms included in the unit cell can be increased substantially.

When studying molecular junctions from an *ab-initio* perspective, it is important to understand the interaction of the molecule with the surfaces or electrodes. Density functional theory calculations of the adsorption of alkane and aromatic molecules bonded to the Au(111) surface with thiol, ethynyl and amine linkers were performed. This allowed prediction of the minimum energy geometry of the

junctions and served as a starting point for the DFT-NEGF transport calculations.

Some surface properties of Au(111) were studied at the DFT level. Highly accurate work functions could be calculated, both of the bare surface and for the surface with an adsorbed monolayer. This is in contrast to previous DFT studies where the use of local orbital basis sets led to highly basis set dependent work functions. Calculations of the relaxation and reconstruction of the Au(111) surface were troublesome, but some results were suggestive of the contraction observed experimentally.

The potential energy surface of the adsorption of phenylenedimethanethiol on the Au(111) surface was mapped. This molecule as well as alkanedithiols of several lengths were found to interact strongly with the Au(111) surface through the sulphur-gold bond once the S-H bond is cleaved. The interaction of the uncleaved S-H bond with the Au(111) surface was calculated to be much weaker. The carbon-gold bond responsible for the adsorption of ethynylbenzene on Au(111) was found to be even stronger than the S-Au bond.

The adsorption geometries and interaction energies for a series of amine compounds were calculated. The results confirmed that these molecules bind preferentially to an adatom on the gold surface. This had been put forward previously as an explanation of the experimental observation that amine bound junctions exhibit a much smaller spread in conductance values than their thiol counterparts [16]. Transport calculations were not performed for amine junctions, but this is an interesting avenue for future work, as there is less uncertainty in the junction geometry. The weak amine-gold bond will almost certainly break before extracting any gold atoms from the surface.

The interaction energy with the Au(111) surface of the series of molecules studied here, together with results in the literature obtained with the same level of theory, provide a meaningful comparison of DFT results for several molecules.

A module was added to the widely used SIESTA DFT code to enable geometry optimisation using a Z-matrix coordinate system. The input format is flexible and adds functionality not previously available in SIESTA. Any of the coordinates may either be fixed or varied. Linear relationships between coordinates allow for

specification of symmetries. Z-matrix optimisations are particularly appropriate for surface adsorption calculations, since shallow minima are more accessible and mapping of the potential energy surface is more reliable. This module may therefore be used in future for more sophisticated characterisation of the geometry of molecular junctions.

The motivation for predicting $I(V)$ curves with a tunnel barrier model is the tremendous increase in computational efficiency. When using the WKB approximation to evaluate the transmission function, full $I(V)$ curves can be computed in a few minutes. The DFT-NEGF method on the other hand would take about two to three weeks at best. In some cases obtaining a converged self-consistent solution is troublesome. Furthermore, care has to be taken to use a set of parameters that produce converged results within the level of theory. A detailed analysis of the convergence behaviour when using DFT for both transport and electronic structure calculations, was presented in this work. The computational parameters recommended by this analysis are more accurate than those usually used in transport calculations and lead to very computationally intensive simulations.

The WKB tunnel barrier model can be used to scan over a large range of junction geometries. More sophisticated computational methods such as the DFT-NEGF combination used in this work, can then be focused on potentially interesting junctions, e.g. those that produce rectification. To validate this approach the junction parameters varied in the tunnelling model calculations should be connected with the actual geometric properties of the junction, e.g. the type of molecule or the length of a gap between the molecule and electrode. An attempt at this connection was made by using a double rectangle barrier to represent junctions with a molecule-gap geometry. The DFT calculated work functions of the bare gold surface or surface with adsorbed molecule were used as the barrier heights of the two rectangles.

The relative sizes of the junction currents predicted with this model agree with those obtained using the DFT-NEGF theory - molecules that act to reduce the surface work function form more conductive junctions. The absolute currents

are much lower than their DFT-NEGF counterparts and even underestimate experimental data. The asymmetry in the resulting $I(V)$ characteristics differ in the direction of the larger current and is much less pronounced than predicted by the DFT-NEGF theory. It was proved in this work that when using the WKB tunnel barrier model with a trapezoid or double rectangle barrier, the larger flow of current carriers will *always* be from the side with higher barrier to the side with lower barrier. The DFT-NEGF $I(V)$ results for the molecule-gap geometries consistently predict a larger electron flow, first through the molecule side and then through the gap side. However, all molecules studied except for ENB act to reduce the surface dipole moment and hence work function, thereby placing the lower barrier on the molecule side. While this method of constructing the barrier may potentially provide a fast technique for predicting the relative conductances of junctions, more subtle predictions such as the direction and degree of asymmetry do not seem possible. For this model to become more useful, tunnel barriers should be constructed that more accurately reflect the properties of individual molecules. The model could also be improved by using tunnelling theories more sophisticated than WKB and solving the problem in three dimensions by making use of the three-dimensional local potential, especially at the molecule-electrode interfaces.

Finally, a typical STM setup was modelled where a gold nanoparticle is adsorbed onto a molecular monolayer and current measurements taken with the tip scanning above the nanoparticle. The *ab-initio* calculations for the substrate-molecule-nanoparticle junction were combined with WKB tunnel barrier model results for the nanoparticle-tip gap. It was shown that the molecular junction resistance may dominate the gap resistance for small gaps. However, for large enough tip-nanoparticle separation, the gap resistance becomes significant and increasing the gap by 1 Å may decrease the current by an order of magnitude. STS data from the literature could be reconciled with calculated currents using this model.

Appendix A

Pseudopotential Plots

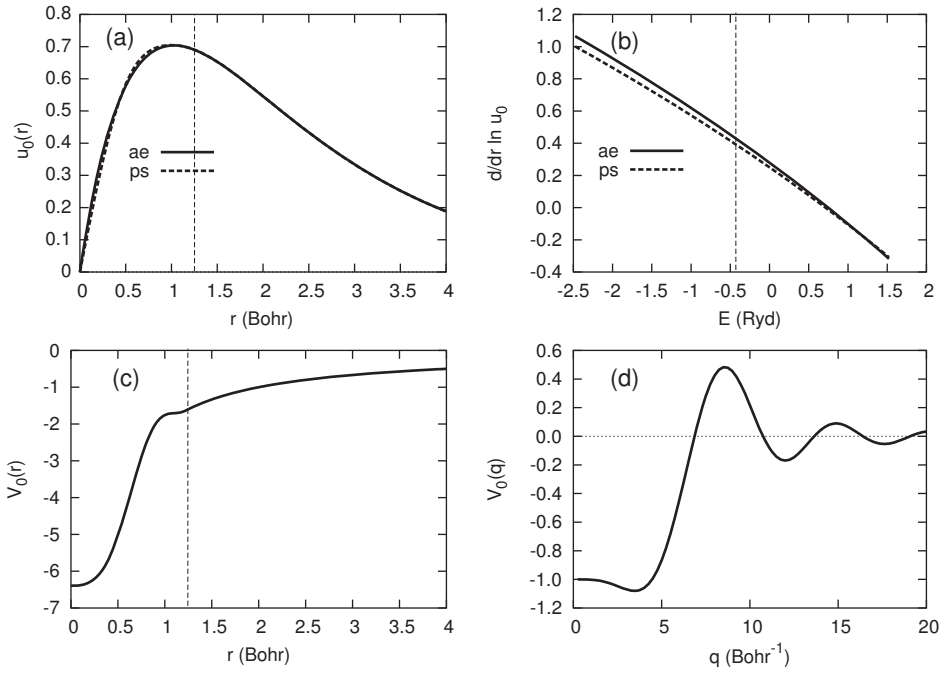

Figure A.1: Hydrogen GGA pseudopotential for $l = 0$

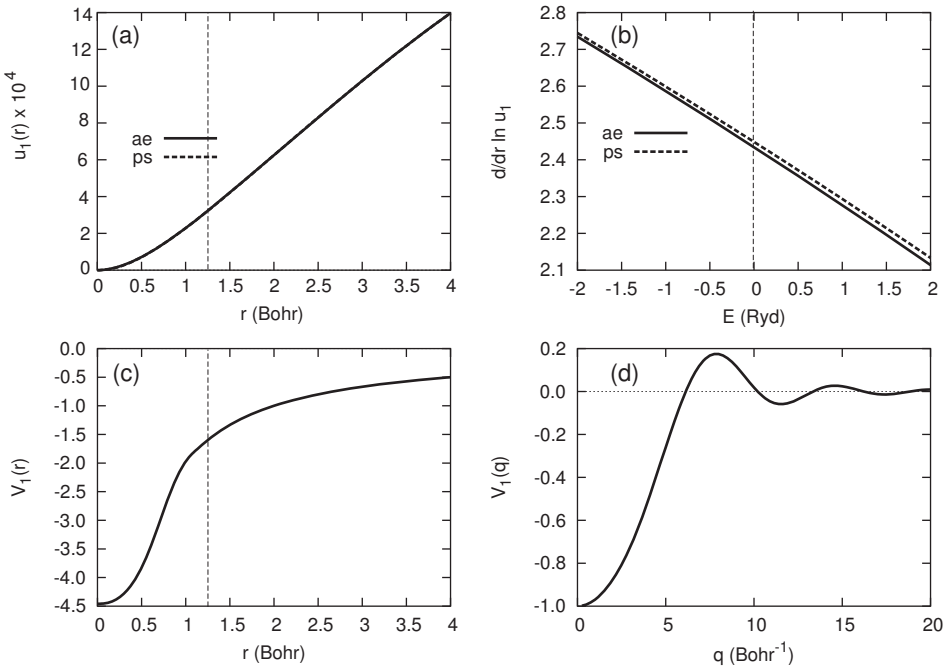

Figure A.2: Hydrogen GGA pseudopotential for $l = 1$

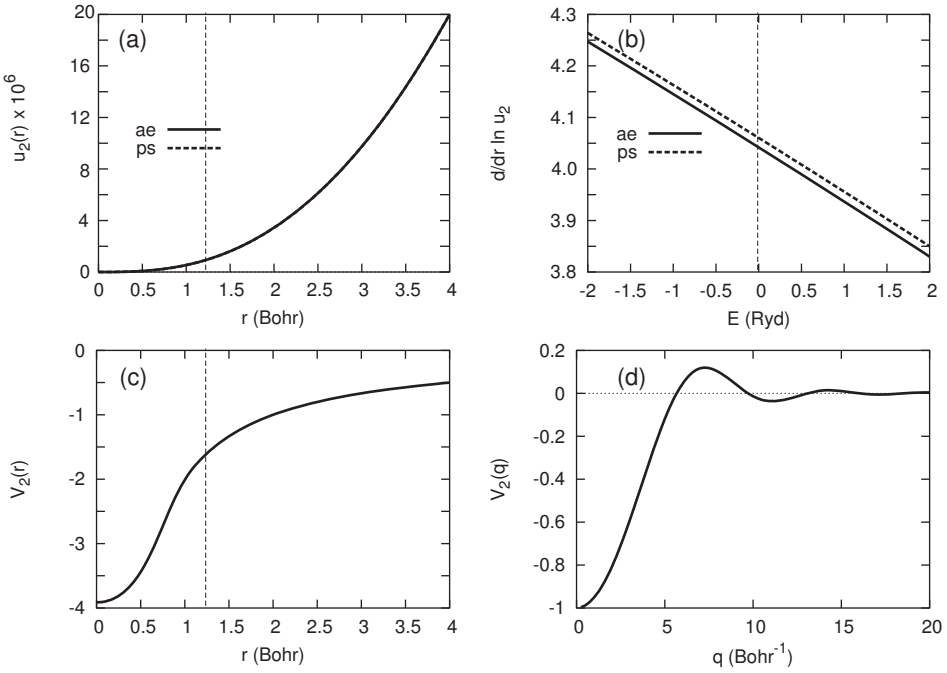

Figure A.3: Hydrogen GGA pseudopotential for $l = 2$

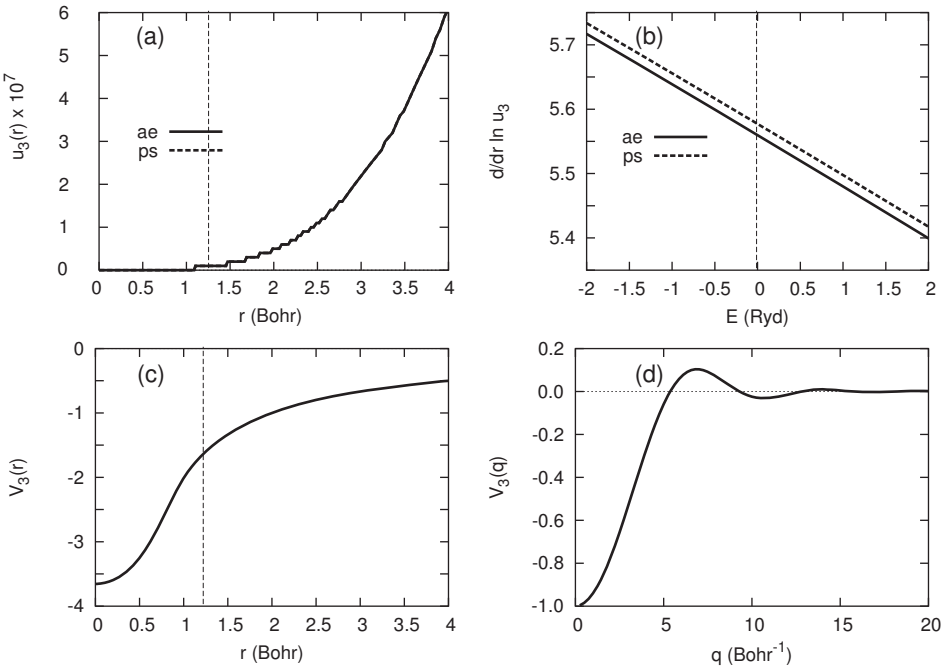

Figure A.4: Hydrogen GGA pseudopotential for $l = 3$

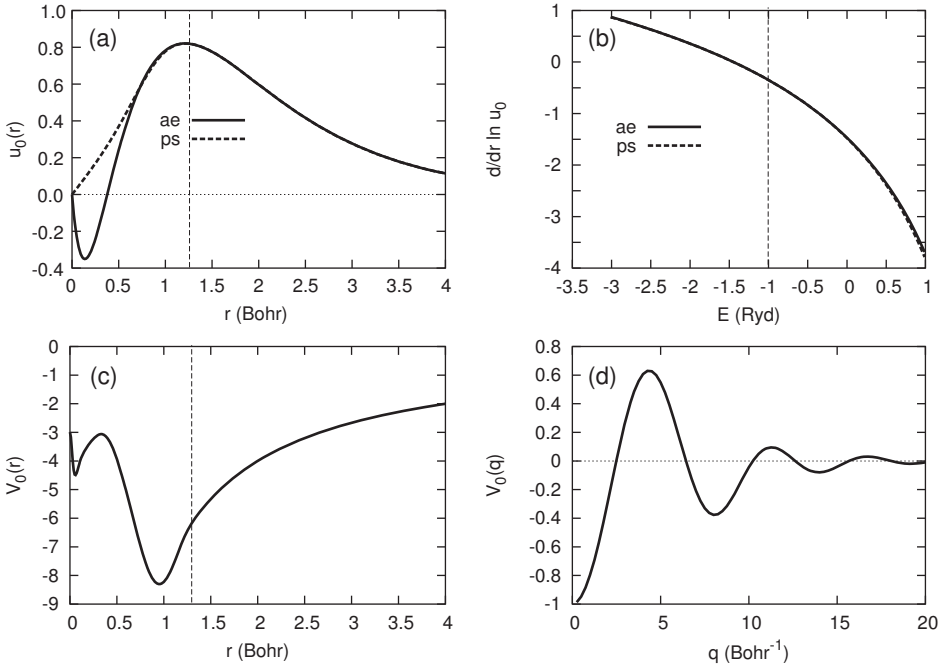

Figure A.5: Carbon GGA pseudopotential for $l = 0$

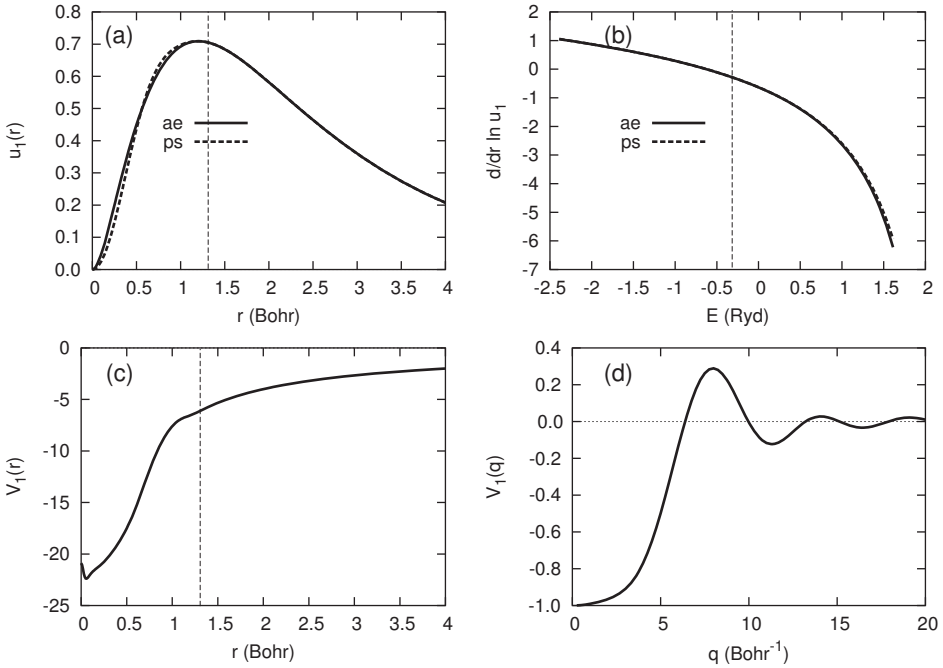

Figure A.6: Carbon GGA pseudopotential for $l = 1$

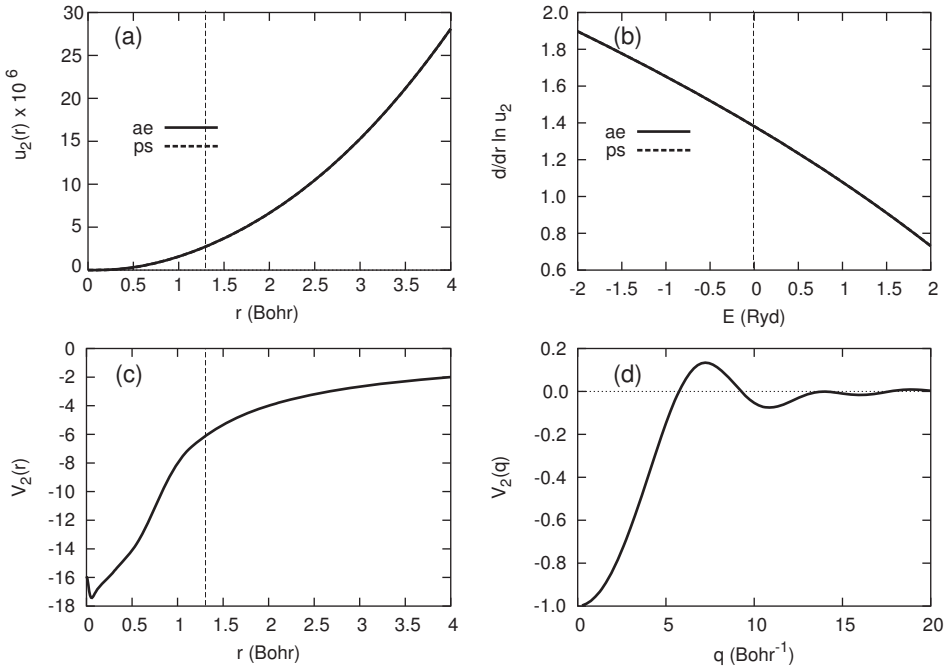

Figure A.7: Carbon GGA pseudopotential for $l = 2$

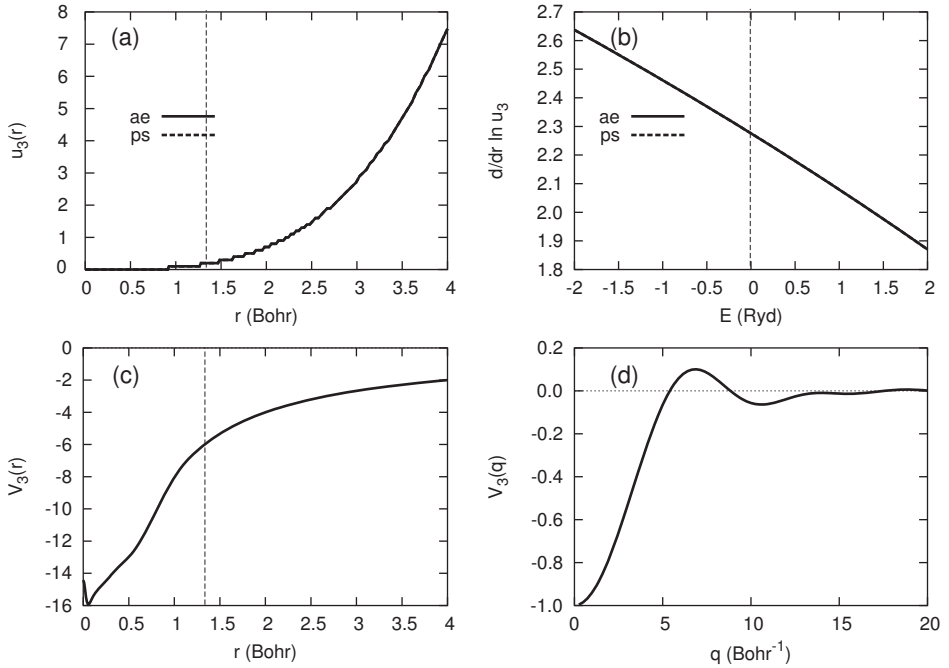

Figure A.8: Carbon GGA pseudopotential for $l = 3$

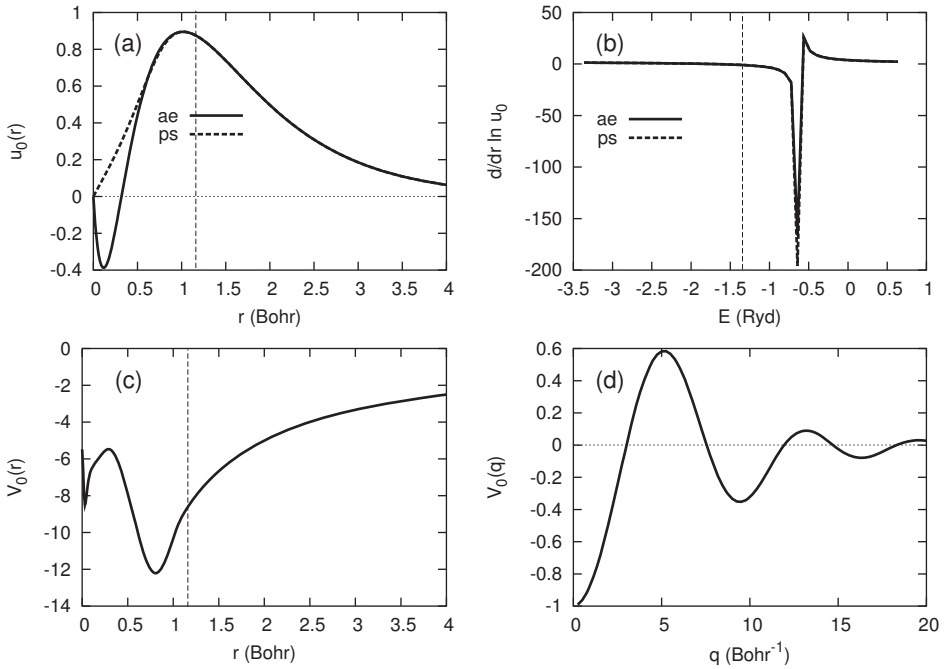

Figure A.9: Nitrogen GGA pseudopotential for $l = 0$

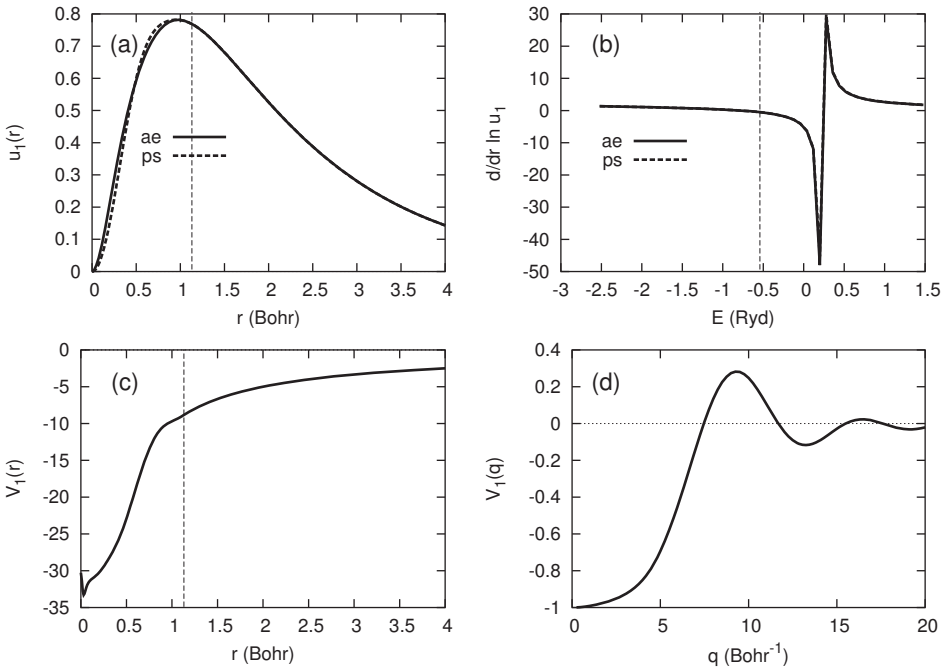

Figure A.10: Nitrogen GGA pseudopotential for $l = 1$

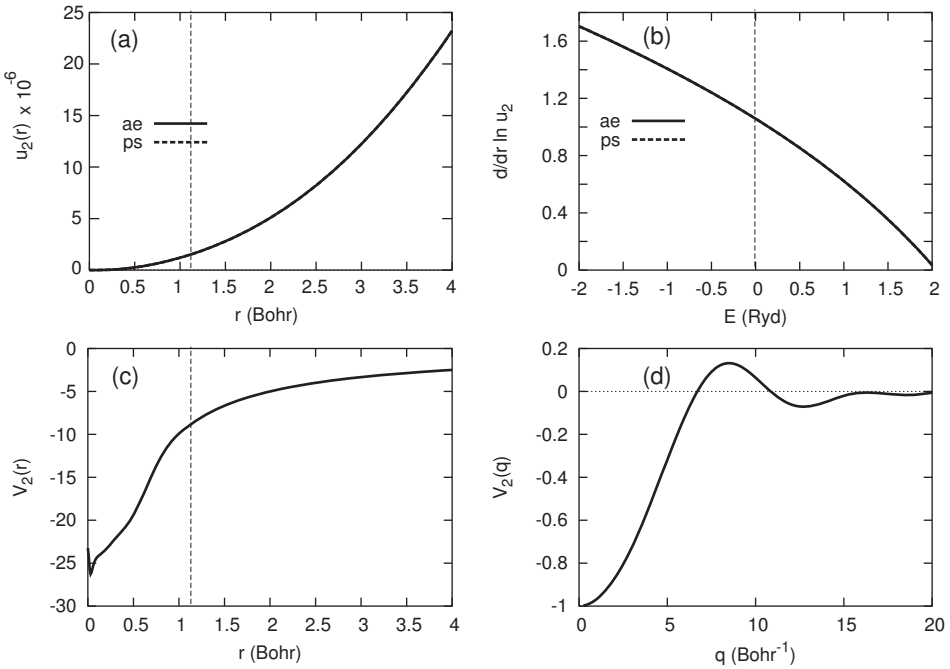

Figure A.11: Nitrogen GGA pseudopotential for $l = 2$

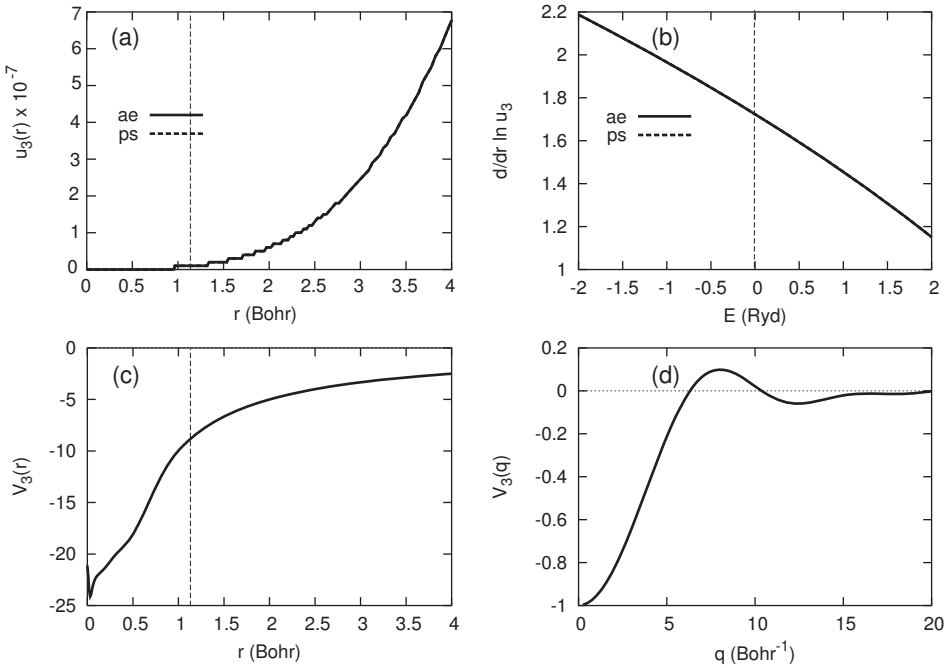

Figure A.12: Nitrogen GGA pseudopotential for $l = 3$

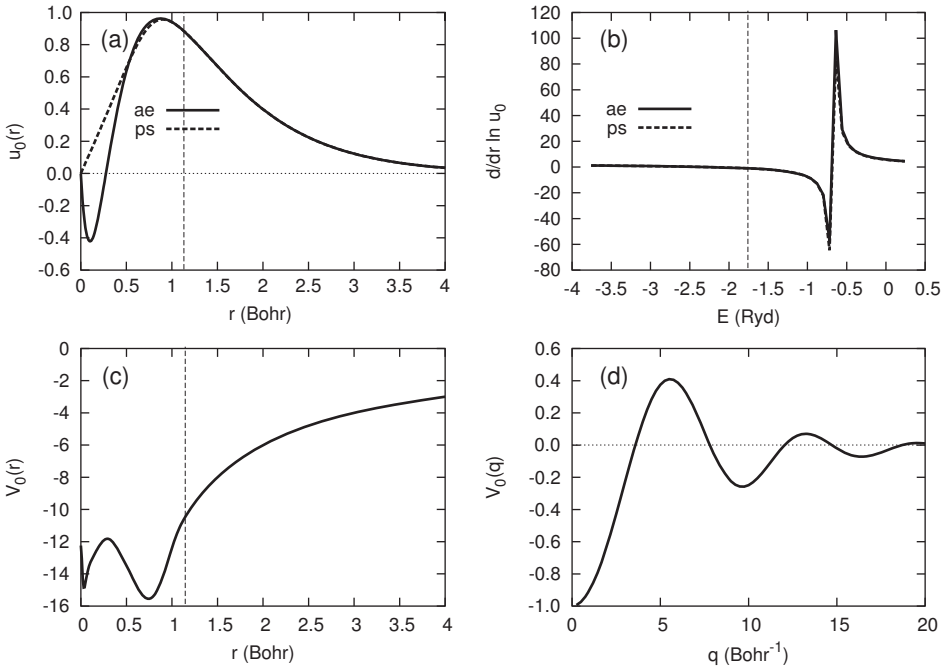

Figure A.13: Oxygen GGA pseudopotential for $l = 0$

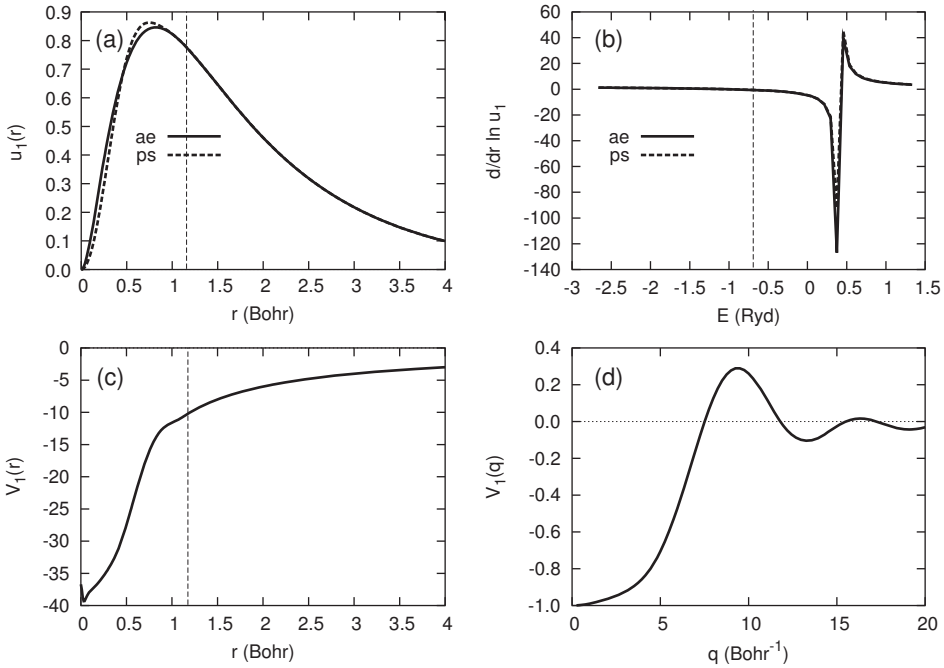

Figure A.14: Oxygen GGA pseudopotential for $l = 1$

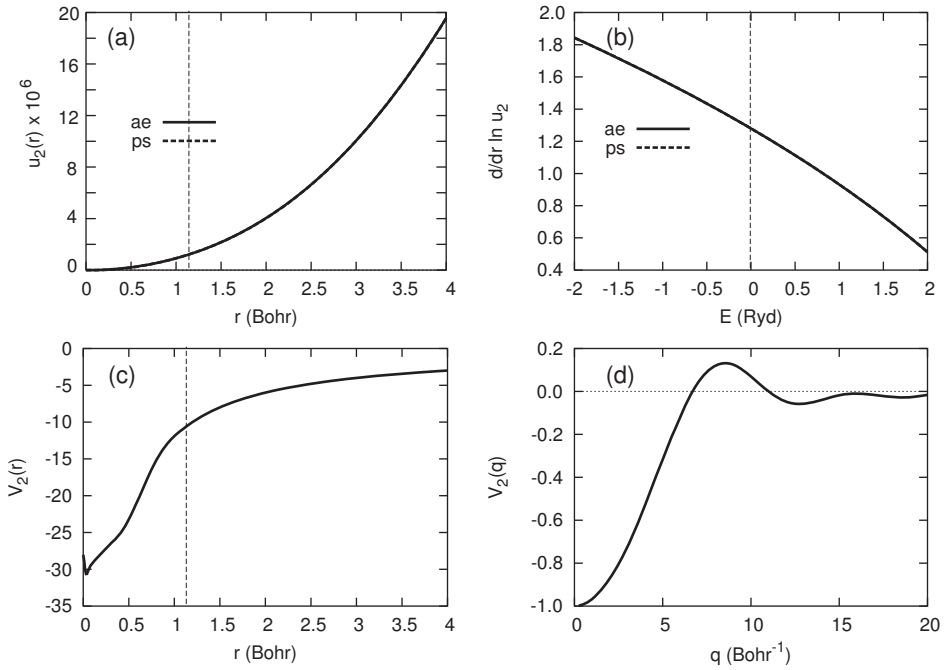

Figure A.15: Oxygen GGA pseudopotential for $l = 2$

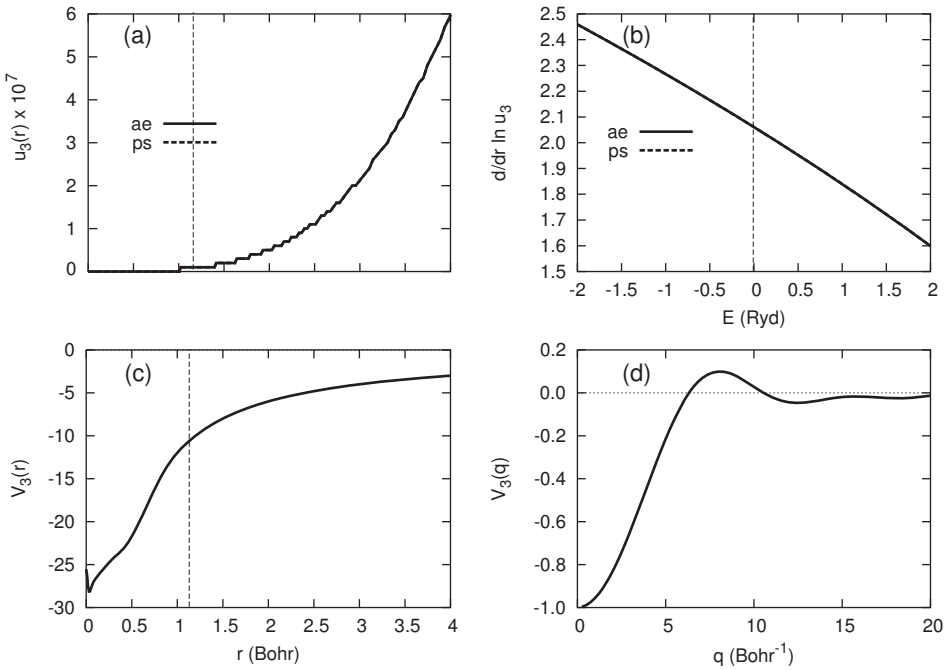

Figure A.16: Oxygen GGA pseudopotential for $l = 3$

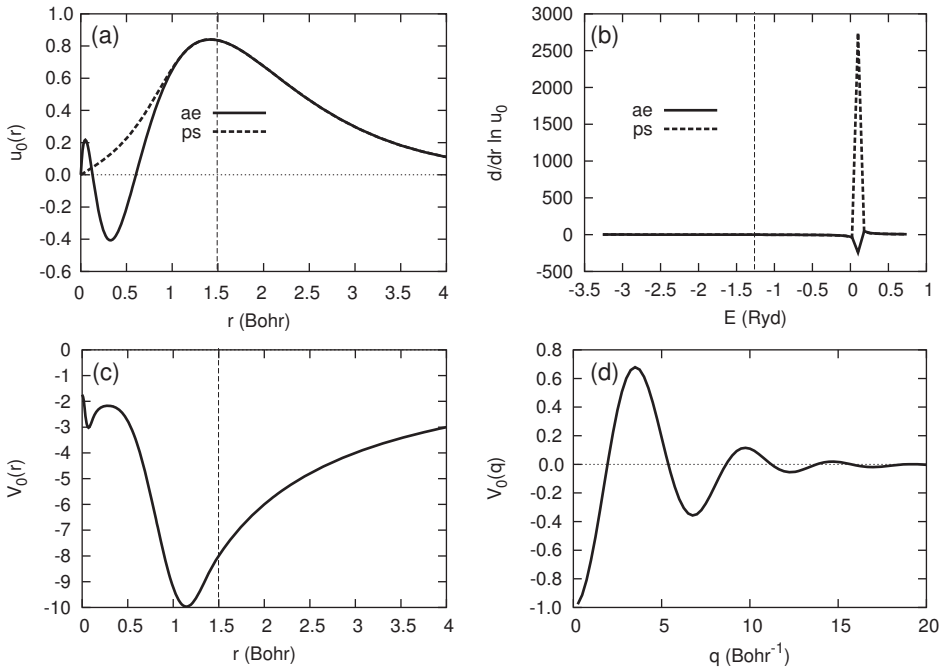

Figure A.17: Sulphur GGA pseudopotential for $l = 0$

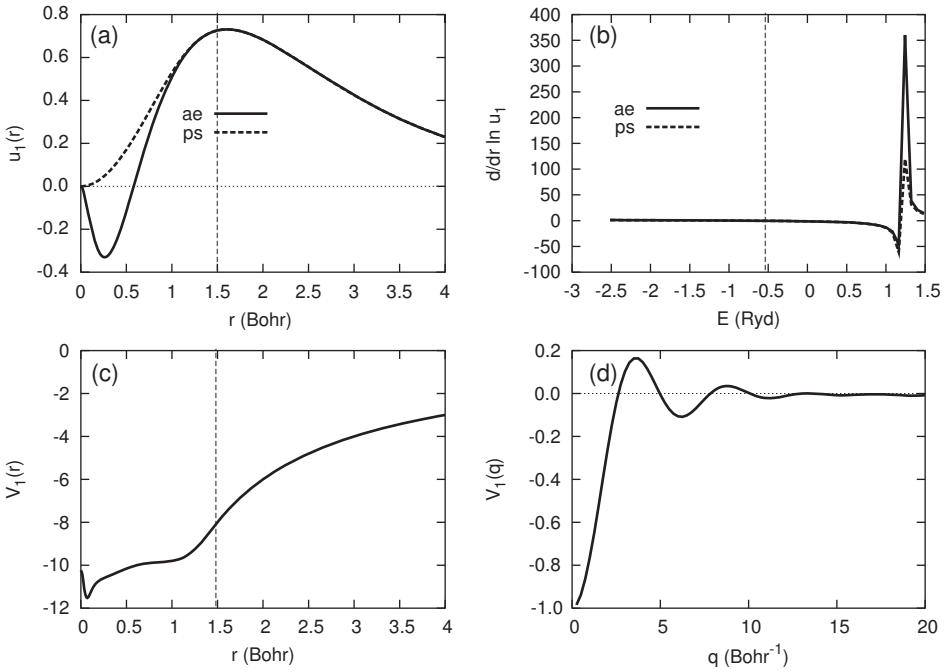

Figure A.18: Sulphur GGA pseudopotential for $l = 1$

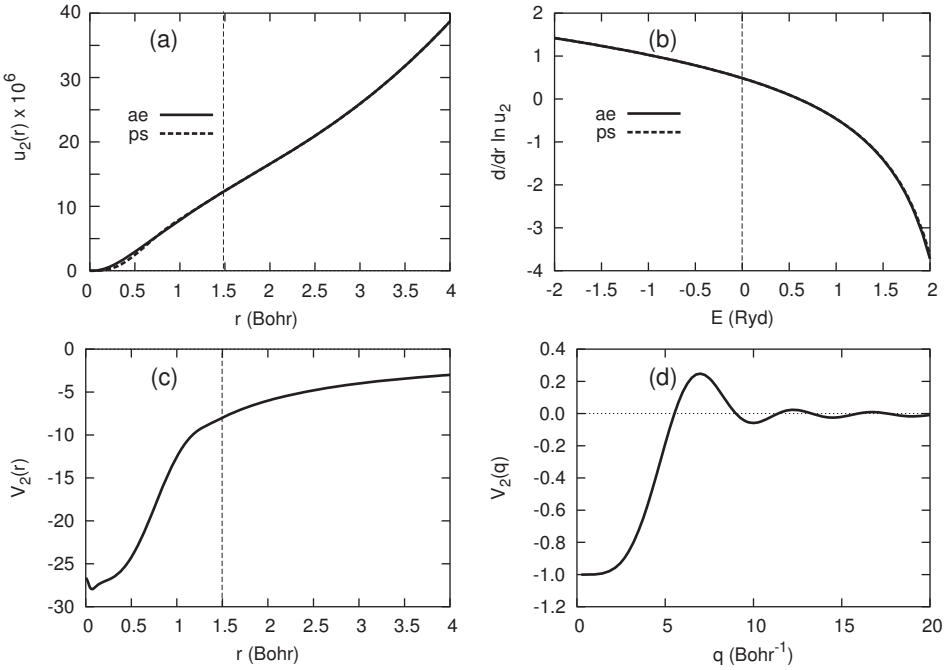

Figure A.19: Sulphur GGA pseudopotential for $l = 2$

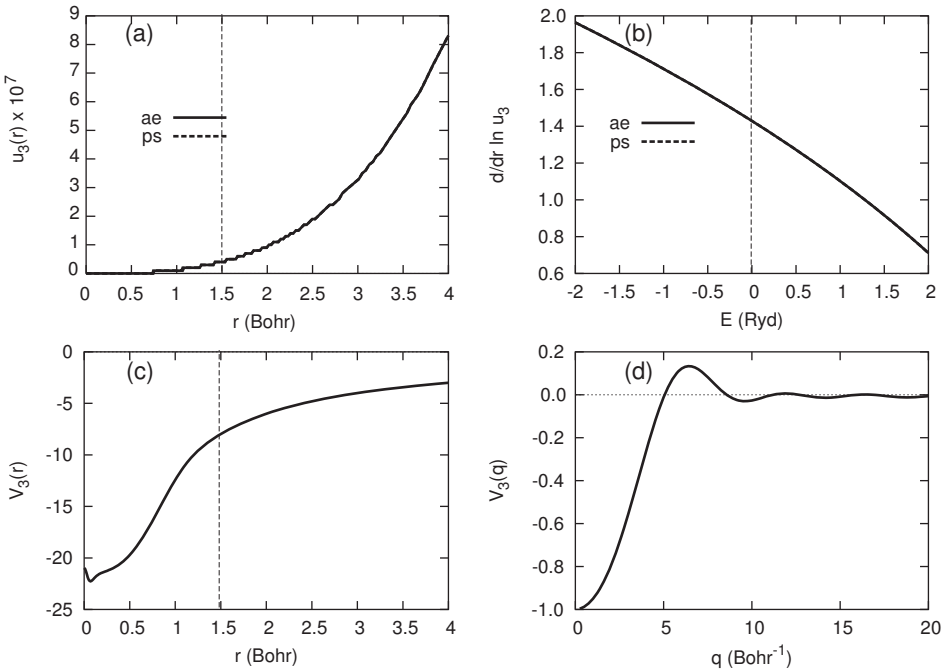

Figure A.20: Sulphur GGA pseudopotential for $l = 3$

Appendix B

Sign of Rectification in WKB Tunnel Barrier Model

We give a proof of the assertion in section 6.2.4 that the asymmetry in the $I(V)$ curve obtained when applying the WKB approximation to the trapezoid or double rectangle barriers with $\alpha = 0.0$, is always such that the larger electron flow occurs first through the higher side of the barrier and second through the lower side. It is assumed that both barrier heights are larger than the applied voltage, $\phi_1, \phi_2 > eV$. If this is not the case the WKB approximation is invalid, since for part of the energy range $0 < E < eV$, a negative number appears inside the square root of the integrand of equation (2.129).

B.1 Double rectangle barrier

Assume that $\phi_2 > \phi_1$ and $eV > 0$. Then the forward and reverse currents are given by

$$\begin{aligned} I_{\mathrm{f}} = |I(eV)| &= \frac{2e}{h}\int_0^{eV} T(E, eV)\mathrm{d}E \\ &\equiv \frac{2e}{h}\int_0^{eV} e^{-\frac{2\sqrt{2m}}{\hbar}A^{+}(E)}\mathrm{d}E \end{aligned} \tag{B.1}$$

and

$$\begin{aligned} I_{\rm r} = |I(-eV)| &= \frac{2e}{h}\left|\int_0^{-eV} T(E,-eV)\mathrm{d}E\right| \\ &= \frac{2e}{h}\int_0^{eV} T(E-eV,-eV)\mathrm{d}E \\ &\equiv \frac{2e}{h}\int_0^{eV} e^{-\frac{2\sqrt{2m}}{\hbar}A^-(E)}\mathrm{d}E \end{aligned} \tag{B.2}$$

We proceed to prove that $A^+(E) > A^-(E)$ for all $0 < E < eV$ from where it follows that $I_{\rm r} > I_{\rm f}$. The case where $\phi_1 > \phi_2$ similarly leads to $I_{\rm f} > I_{\rm r}$. Inserting equation (6.2) with $\alpha = 0.0$ into equation (2.129), yields

$$\begin{aligned} A^+(E) &= \int_0^{d_1}\sqrt{eV\Big(1-\frac{x}{d}\Big)+\phi_1-E}\;\mathrm{d}x + \int_{d_1}^{d}\sqrt{[eV\Big(1-\frac{x}{d}\Big)+\phi_2-E}\;\mathrm{d}x \\ &= -\frac{2d}{3eV}\Big[eV\Big(1-\frac{x}{d}\Big)+\phi_1-E\Big]^{\frac{3}{2}}\Big|_0^{d_1} - \frac{2d}{3eV}\Big[eV\Big(1-\frac{x}{d}\Big)+\phi_2-E\Big]^{\frac{3}{2}}\Big|_{d_1}^{d} \\ &= \frac{2d}{3eV}\Big[\Big(eV+\phi_1-E\Big)^{\frac{3}{2}} - \Big(eV(1-\frac{d_1}{d})+\phi_1-E\Big)^{\frac{3}{2}} \\ &\quad +\Big(eV(1-\frac{d_1}{d})+\phi_2-E\Big)^{\frac{3}{2}} - \Big(\phi_2-E\Big)^{\frac{3}{2}}\Big] \end{aligned} \tag{B.3}$$

Comparison of (B.1) and (B.2) shows that $A^-(E)$ is obtained from $A^+(E)$ by swapping $eV \leftrightarrow -eV$ and $E \leftrightarrow E - eV$ (or equivalently $1 - \frac{d_1}{d} \leftrightarrow \frac{d_1}{d}$ and $\phi_1 \leftrightarrow \phi_2$)

$$A^-(E) = \frac{2d}{3eV}\Big[-\Big(\phi_1-E\Big)^{\frac{3}{2}}+\Big(eV\frac{d_1}{d}+\phi_1-E\Big)^{\frac{3}{2}}-\Big(eV\frac{d_1}{d}+\phi_2-E\Big)^{\frac{3}{2}}+\Big(eV+\phi_2-E\Big)^{\frac{3}{2}}\Big] \tag{B.4}$$

Then

$$\begin{aligned} A^-(E) - A^+(E) &= \frac{2d}{3eV}\Bigg\{\Bigg(\Big[\Big(eV+\phi_2-E\Big)^{\frac{3}{2}} - \Big(eV+\phi_1-E\Big)^{\frac{3}{2}}\Big] \\ &\quad -\Big[\Big(eV\frac{d_1}{d}+\phi_2-E\Big) - \Big(eV\frac{d_1}{d}+\phi_1-E\Big)\Big]\Bigg) \\ &\quad -\Bigg(\Big[\Big(eV\big(1-\frac{d_1}{d}\big)+\phi_2-E\Big)^{\frac{3}{2}} - \Big(eV\big(1-\frac{d_1}{d}\big)+\phi_1-E\Big)\Big] \\ &\quad -\Big[\Big(\phi_2-E\Big)^{\frac{3}{2}} - \Big(\phi_1-E\Big)^{\frac{3}{2}}\Big]\Bigg)\Bigg\} \end{aligned} \tag{B.5}$$

Define the following functions:

$$\begin{aligned} f(x) &= x^{\frac{3}{2}} - \big(x-(\phi_2-\phi_1)\big)^{\frac{3}{2}} \\ g(x) &= f(x) - f\big(x - eV(1-\frac{d_1}{d})\big) \\ h(x) &= g(x) - g\big(x - eV\frac{d_1}{d}\big). \end{aligned}$$

Taking the derivative of $g(x)$,

$$\begin{aligned} g'(x) &= f'(x) - f'\big(x - eV(1-\frac{d_1}{d})\big) \\ &= \frac{3}{2}\sqrt{x} - \frac{3}{2}\sqrt{x-(\phi_2-\phi_1)} - \frac{3}{2}\sqrt{x-eV(1-\frac{d_1}{d})} \\ &\quad +\frac{3}{2}\sqrt{x-eV(1-\frac{d_1}{d})-(\phi_2-\phi_1)} \\ &= \frac{3}{2}\Big(\sqrt{x}+\sqrt{x-a-b}-\sqrt{x-a}-\sqrt{x-b}\Big) \end{aligned} \tag{B.6}$$

where $a = \phi_2 - \phi_1 > 0$ and $b = eV(1-\frac{d_1}{d}) > 0$. Applying Jensen's inequality to the *concave* square root function reveals

$$\begin{aligned} \frac{2a}{b+a}\sqrt{x-\frac{a+b}{2}} + \frac{b-a}{b+a}\sqrt{x} &\leq \sqrt{\frac{2a}{b+a}\left(x-\frac{a+b}{2}\right)+\frac{b-a}{b+a}x} \\ &= \sqrt{x-a} \end{aligned} \tag{B.7}$$

and

$$\begin{aligned}\frac{2a}{b+a}\sqrt{x-\frac{a+b}{2}}+\frac{b-a}{b+a}\sqrt{x-a-b} &\leq \sqrt{\frac{2a}{b+a}\left(x-\frac{a+b}{2}\right)+\frac{b-a}{b+a}(x-a-b)} \\ &= \sqrt{x-b} \end{aligned} \tag{B.8}$$

Adding (B.7) and (B.8) and again using Jensen's inequality,

$$\begin{aligned}\sqrt{x-a}+\sqrt{x-b} &\geq \frac{b-a}{b+a}\left(\sqrt{x}+\sqrt{x-a-b}\right)+\frac{4a}{b+a}\sqrt{x-\frac{a+b}{2}} \\ &\geq \frac{b-a}{b+a}\left(\sqrt{x}+\sqrt{x-a-b}\right)+\frac{2a}{b+a}\left(\sqrt{x}+\sqrt{x-a-b}\right) \\ &= \sqrt{x}+\sqrt{x-a-b}. \end{aligned} \tag{B.9}$$

Thus from equation (B.6), $g'(x) < 0$ or $g(x)$ is decreasing; hence $h(x) < 0$. Notising that $A^-(E) - A^+(E) = h(eV + \phi_2 - E)$ completes the proof.

B.2 Trapezoid barrier

Assume $\phi_2 > \phi_1 > eV > 0$. Inserting equation (6.1) into equation (2.129) with $A^+(E)$ and $A^-(E)$ defined as in the double rectangle case, leads to

$$\begin{aligned}A^+(E) &= \int_0^d \sqrt{eV\Big(1-\frac{x}{d}\Big)+\phi_1+\frac{x}{d}\Big(\phi_2-\phi_1\Big)-E}\;\mathrm{d}x \\ &= \frac{2d}{3(\phi_2-\phi_1-eV)}\left[\frac{x}{d}(\phi_2-\phi_1-eV)+eV+\phi_1-E\right]^{\frac{3}{2}}\Bigg|_0^d \\ &= \frac{2d}{3(\phi_2-\phi_1-eV)}\Big[(\phi_2-E)^{\frac{3}{2}}-(eV+\phi_1-E)^{\frac{3}{2}}\Big] \end{aligned} \tag{B.10}$$

when $\phi_2 - \phi_1 - eV \neq 0$ and $A^+(E) = d\sqrt{eV + \phi_1 - E}$ otherwise. Swapping $E \leftrightarrow E - eV$ and $eV \leftrightarrow -eV$ yields

$$A^-(E) = \frac{2d}{3(\phi_2-\phi_1+eV)}\Big[(\phi_2-E+eV)^{\frac{3}{2}}-(\phi_1-E)^{\frac{3}{2}}\Big]. \tag{B.11}$$

Let $f(x) = x^{\frac{3}{2}}$ and define the central difference estimate of $f'(x_0)$ by $\delta[f(x_0)](\omega) \equiv \delta_{x_0}(\omega)$ where the variable ω is the size of the finite difference increment;

$$\delta_{x_0}(\omega) = \frac{f(x_0+\omega) - f(x_0-\omega)}{2\omega}. \tag{B.12}$$

$\delta_{x_0}(\omega)$ is an even function, $\delta_{x_0}(\omega) = \delta_{x_0}(|\omega|)$, so it is safe to assume $\omega \geq 0$. The Taylor series expansion of $f(x_0)$ gives

$$\delta_{x_0}(w) = \sum_{n=0}^{\infty} \omega^{2n} \frac{f^{2n+1}(x_0)}{(2n+1)!} \tag{B.13}$$

A quick inspection of the derivatives of the function $f(x) = x^{\frac{3}{2}}$ reveals that

$$f^n(x) = (-1)^n \cdot \frac{3}{2} \cdot \frac{1}{2} \cdot \frac{3}{2} \cdots \frac{2n-3}{2} \cdot x^{\frac{3}{2}-n} \tag{B.14}$$

which is always negative for odd $n > 1$. Thus from equation (B.13), $\delta_{x_0}(\omega)$ is a decreasing function for $x_0 > 0$. From (B.10) and (B.11), one can write

$$\begin{aligned} x_0 &= \frac{\phi_1 + \phi_2 + eV}{2} - E > 0 \\ A^+(E) &= \frac{2d}{3}\delta_{x_0}\left(\frac{\phi_2 - \phi_1 - eV}{2}\right) \\ A^-(E) &= \frac{2d}{3}\delta_{x_0}\left(\frac{\phi_2 - \phi_1 + eV}{2}\right). \end{aligned} \tag{B.15}$$

Note that when $\phi_2 - \phi_1 - eV = 0$,

$$A^+(E) = \frac{2d}{3}\delta_{x_0}(0) = \frac{2d}{3}f'(x_0) = d\sqrt{\frac{\phi_1 + \phi_2 + eV}{2} - E} = d\sqrt{\phi_1 + eV - E} \tag{B.16}$$

as required. Now $\phi_2 > \phi_1$ and $eV > 0$ implies $|\phi_2 - \phi_1 + eV| > |\phi_2 - \phi_1 - eV|$, so by virtue of the fact that $\delta_{x_0}(\omega)$ is decreasing, we have $A^+(E) > A^-(E)$ for all $0 < E < eV$, which completes the proof for the trapezoid case.

Appendix C

Publication Report

C.1 Peer reviewed journal articles

- "Theoretical study of ethynylbenzene adsorption on Au(111) and implications for a new class of self-assembled monolayer", M. J. Ford, R. C. Hoft and A. McDonagh, *Journal of Physical Chemistry B* **109**, 20387 (2005).

- "Adsorption of benzene on copper, silver and gold surfaces", A. Bilic, J. Reimers, N. Hush, R. C. Hoft and M. J. Ford, *Journal of Chemical Theory and Computation* **2**, 1093 (2006).

- "Implementation of a Z-matrix approach within the SIESTA periodic boundary conditions code and its application to surface adsorption", R. C. Hoft, J. D. Gale and M. J. Ford, *Molecular Simulation* **32**, 595 (2006).

- "Prediction of increased tunneling current by bond length stretch in molecular break junctions", R. C. Hoft, M. J. Ford and M. B. Cortie, *Chemical Physics Letters* **429**, 503 (2006).

- "Adsorption and dimerisation of thiol molecules on Au(111) using a Z-matrix approach in density functional theory", M. J. Ford, R. C. Hoft and J. D. Gale, *Molecular Simulation* **32**, 1219 (2006).

- "Ab-initio and empirical studies on the asymmetry of molecular current-voltage characteristics", R. C. Hoft, N. Armstrong, M. J. Ford and M. B. Cortie, *Journal of Physics: Condensed Matter* **19**, 215206 (2007).

- "Adsorption of amine compounds on the Au(111) surface: A density functional study", R. C. Hoft, M. J. Ford, A. McDonagh and M. B. Cortie, *Journal of Physical Chemistry C* **111**, 13886 (2007).

- "Exploring the performance of molecular rectifiers: Limitations and factors affecting molecular rectification", N. Armstrong, R. C. Hoft, A. McDonagh, M. B. Cortie and M. J. Ford, *Nano Letters* **7**, 3018 (2007).

- "The effect of reciprocal-space sampling and basis set quality on the calculated conductance of a molecular junction", R. C. Hoft, M.J. Ford and M. B. Cortie, *Molecular Simulation* **33**, 897 (2007).

- "Electron tunneling in the presence of adsorbed molecules", R. C. Hoft, M. J. Ford and M. B. Cortie, *Surface Science* (in press), doi:10.1016/J.SUSC.2007.06.049.

- "The effect of stretching thiyl- and ethynyl-Au molecular junctions", R. C. Hoft, M. J. Ford, V. M. Garcia-Suarez, C. J. Lambert and M. B. Cortie, *Journal of Physics-Condensed Matter* (accepted).

C.2 Peer reviewed full conference papers

- "Electron tunneling through alkanedithiol molecules", R. C. Hoft, M. J. Ford and M. B. Cortie, in *Proc. SPIE: BioMEMS and Nanotechnology II*, ed. D. V. Nicolau, **6036**, 603603 (2006).

- "Effect of dipole moment on current-voltage characteristics of single molecules", R. C. Hoft, M. J. Ford and M. B. Cortie, in *Proceedings of the International Conference on Nanoscience and Nanotechnology (ICONN)*, eds. C. Jagadish and G. Q. M. Lu, p. 695 (Brisbane, 2006, IEEE).

- "A new class of self-assembled monolayers on gold using an alkynyl group as linker", M. J. Ford, R. C. Hoft, J. D. Gale and A. McDonagh, in *Proceedings of the International Conference on Nanoscience and Nanotechnology (ICONN)*, eds. C. Jagadish and G. Q. M. Lu, p.396 (Brisbane, 2006, IEEE)

C.3 Poster presentations

- "Single molecules on gold surfaces and molecular conduction", R. C. Hoft, M. J. Ford, and M. B. Cortie, Australian Institute of Physics (AIP) Congress, February 2005, Canberra, Australia.

- "Electron tunnelling in the presence of adsorbed molecules", R. C. Hoft, M. J. Ford and M. B. Cortie, 30$^{\text{th}}$ Annual Condensed Matter and Materials Meeting, February 2006, Wagga-Wagga, Australia.

- "Dimerisation of surface bound thiol molecules using a Z-matrix approach in density functional theory", R. C. Hoft, J. D. Gale and M. J. Ford, Molecular Modelling, April 2006, Perth, Australia.

- "Theoretical investigation of surface adsorption and transport properties of individual molecules", R. C. Hoft, M. J. Ford, M. B. Cortie, J. D. Gale and N. Armstrong, GRC: Electron donor-acceptor interactions, August 2006, Newport, R.I., USA.

C.4 Oral presentations

- "Electron tunnelling in the presence of adsorbed molecules", R. C. Hoft, M. J. Ford and M. B. Cortie, Australian Research Council – Nanotechnology Network (ARCNN) postgraduate symposium, July 2005, Perth, Australia.

- "Electron tunneling across alkanedithiol molecules", R. C. Hoft, M. J. Ford, J. Liu and M. B. Cortie, SPIE: BioMEMS and Nanotechnology II, December 2005, Brisbane, Australia.

- "Effect of surface dipole moment on molecular conduction", R. C. Hoft, M. J. Ford and M. B. Cortie, International Conference on Nanoscience and Nanotechnology (ICONN), July 2006, Brisbane, Australia.

Bibliography

[1] J. C. Boettger, Physical Review B **49**, 16798 (1994).

[2] B. Q. Xu and N. J. Tao, Science **301**, 1221 (2003).

[3] X. Y. Xiao, B. Q. Xu, and N. J. Tao, Nano Letters **4**, 267 (2004).

[4] *Computational Chemistry Comparison and Benchmark Database, release 12* (National Institute of Standards and Technology, 2005), http://srdata.nist.gov/cccbdb.

[5] C. Kittel, *Introduction to Solid State Physics*, 7 ed. (John Wiley and Sons inc., New York, 1996).

[6] C. Joachim, J. K. Gimzewski, and A. Aviram, Nature **408**, 541 (2000).

[7] N. Hush, Nature Materials **2**, 134 (2003).

[8] G. Binnig, H. Rohrer, C. Gerber, and E. Weibel, Applied Physics Letters **40**, 178 (1982).

[9] L. A. Bumm *et al.*, Science **271**, 1705 (1996).

[10] R. P. Andres *et al.*, Science **272**, 1323 (1996).

[11] R. P. Andres *et al.*, Science **273**, 1690 (1996).

[12] Y. Q. Xue *et al.*, Physical Review B **59**, R7852 (1999).

[13] S. Datta *et al.*, Physical Review Letters **79**, 2530 (1997).

[14] J. Herrmann *et al.*, Contact effects in single-molecule conduction, in *Proceedings of the International Conference On Nanoscience and Nanotechnology*, edited by C. Jagadish and G. Q. M. Lu, p. 314, Brisbane, Australia, 2006, IEEE.

[15] L. Venkataraman *et al.*, Nano Letters **6**, 458 (2006).

[16] L. Venkataraman, J. E. Klare, C. Nuckolls, M. S. Hybertsen, and M. L. Steigerwald, Nature **442**, 904 (2006).

[17] X. L. Li *et al.*, Journal of the American Chemical Society **128**, 2135 (2006).

[18] J. He *et al.*, Faraday Discussions **131**, 145 (2006).

[19] F. Chen, X. L. Li, J. Hihath, Z. F. Huang, and N. J. Tao, Journal of the American Chemical Society **128**, 15874 (2006).

[20] T. W. Kelley, E. L. Granstrom, and C. D. Frisbie, Advanced Materials **11**, 261 (1999).

[21] G. Leatherman *et al.*, Journal of Physical Chemistry B **103**, 4006 (1999).

[22] X. D. Cui *et al.*, Science **294**, 571 (2001).

[23] M. A. Reed, C. Zhou, C. J. Muller, T. P. Burgin, and J. M. Tour, Science **278**, 252 (1997).

[24] J. Reichert *et al.*, Physical Review Letters **88**, 176804 (2002).

[25] T. Böhler, J. Grebing, A. Mayer-Gindner, H. V. Löhneysen, and E. Scheer, Nanotechnology **15**, S465 (2004).

[26] C. Zhou, M. R. Deshpande, M. A. Reed, L. Jones, and J. M. Tour, Applied Physics Letters **71**, 611 (1997).

[27] J. Chen, M. A. Reed, A. M. Rawlett, and J. M. Tour, Science **286**, 1550 (1999).

[28] J. Chen *et al.*, Applied Physics Letters **77**, 1224 (2000).

[29] W. Y. Wang, T. Lee, I. Kretzschmar, and M. A. Reed, Nano Letters **4**, 643 (2004).

[30] A. S. Blum *et al.*, Nature Materials **4**, 167 (2005).

[31] H. B. Akkerman, P. W. M. Blom, D. M. de Leeuw, and B. de Boer, Nature **441**, 69 (2006).

[32] A. W. Ghosh and S. Datta, Journal of Computational Electronics **1**, 515 (2002).

[33] A. Nitzan and M. A. Ratner, Science **300**, 1384 (2003).

[34] P. Hohenberg and W. Kohn, Physical Review **136**, B864 (1964).

[35] W. Kohn and L. J. Sham, Physical Review **140**, A1133 (1965).

[36] A. W. Ghosh, P. Damle, S. Datta, and A. Nitzan, MRS Bulletin **29**, 391 (2004).

[37] Y. Q. Xue and M. A. Ratner, International Journal of Quantum Chemistry **102**, 911 (2005).

[38] S. M. Lindsay and M. A. Ratner, Advanced Materials **19**, 23 (2007).

[39] M. Di Ventra and T. N. Todorov, Journal of Physics-Condensed Matter **16**, 8025 (2004).

[40] N. Sai, M. Zwolak, G. Vignale, and M. Di Ventra, Physical Review Letters **94**, 186810 (2005).

[41] N. Bushong, N. Sai, and M. Di Ventra, Nano Letters **5**, 2569 (2005).

[42] P. Delaney and J. C. Greer, Physical Review Letters **93**, 036805 (2004).

[43] M. Dorogi, J. Gomez, R. Osifchin, R. P. Andres, and R. Reifenberger, Physical Review B **52**, 9071 (1995).

[44] L. A. Bumm, J. J. Arnold, T. D. Dunbar, D. L. Allara, and P. S. Weiss, Journal of Physical Chemistry B **103**, 8122 (1999).

[45] J. J. W. M. Rosink, M. A. Blauw, L. J. Geerligs, E. van der Drift, and S. Radelaar, Physical Review B **62**, 10459 (2000).

[46] K. Moth-Poulsen *et al.*, Nano Letters **5**, 783 (2005).

[47] M. B. Cortie, M. H. Zareie, S. R. Ekanayake, and M. J. Ford, IEEE Transactions on Nanotechnology **4**, 406 (2005).

[48] G. C. Solomon, J. R. Reimers, and N. S. Hush, Journal of Chemical Physics **121**, 6615 (2004).

[49] G. C. Solomon, J. R. Reimers, and N. S. Hush, Journal of Chemical Physics **122**, 224502 (2005).

[50] C. Toher, A. Filippetti, S. Sanvito, and K. Burke, Physical Review Letters **95**, 146402 (2005).

[51] F. Evers, F. Weigend, and M. Koentopp, Physical Review B **69**, 235411 (2004).

[52] P. S. Krstic *et al.*, Computational Materials Science **28**, 321 (2003).

[53] Y. Q. Xue and M. A. Ratner, Physical Review B **68**, 115407 (2003).

[54] H. Basch, R. Cohen, and M. A. Ratner, Nano Letters **5**, 1668 (2005).

[55] Y. B. Hu, Y. Zhu, H. J. Gao, and H. Guo, Physical Review Letters **95**, 156803 (2005).

[56] K. H. Muller, Physical Review B **73**, 045403 (2006).

[57] S. H. Ke, H. U. Baranger, and W. T. Yang, Journal of Chemical Physics **122**, 074704 (2005).

[58] F. Jiang *et al.*, Physical Review B **72**, 155408 (2005).

[59] G. Speyer, R. Akis, and D. K. Ferry, IEEE Transactions on Nanotechnology **4**, 403 (2005).

[60] E. G. Emberly and G. Kirczenow, Physical Review Letters **87**, 269701 (2001).

[61] R. C. Hoft, J. D. Gale, and M. Ford, Molecular Simulation **32**, 595 (2006).

[62] M. Ford, R. C. Hoft, and J. D. Gale, Molecular Simulation **32**, 1219 (2006).

[63] M. Ford, R. C. Hoft, J. D. Gale, and A. McDonagh, A new class of self-assembled monolayers on gold using an alkynyl group as a linker, in *Proceedings of the International Conference on Nanoscience and Nanotechnology (ICONN2006)*, edited by C. Jagadish and G. Q. M. Lu, p. 695, Brisbane, 2006, IEEE.

[64] M. J. Ford, R. C. Hoft, and A. McDonagh, Journal of Physical Chemistry B **109**, 20387 (2005).

[65] A. Bilic, J. R. Reimers, N. S. Hush, R. C. Hoft, and M. J. Ford, Journal of Chemical Theory and Computation **2**, 1093 (2006).

[66] R. C. Hoft, M. J. Ford, A. M. McDonagh, and M. B. Cortie, Journal of Physical Chemistry C **111**, 13886 (2007).

[67] R. C. Hoft, M. J. Ford, and M. B. Cortie, Surface Science (in press) , doi:10.1016/J.SUSC.2007.06.049.

[68] R. C. Hoft, M. Ford, and M. B. Cortie, Chemical Physics Letters **429**, 503 (2006).

[69] R. C. Hoft, M. J. Ford, V. M. Garcia-Suarez, C. J. Lambert, and M. B. Cortie, Journal of Physics-Condensed Matter (accepted).

[70] R. C. Hoft, J. Liu, M. B. Cortie, and M. Ford, Electron tunneling through alkanedithiol molecules, in *Proc. of SPIE: BioMEMS and Nanotechnology II*, edited by D. V. Nicolau Vol. 6036, p. 603603, 2006.

[71] R. C. Hoft, M. Ford, and M. B. Cortie, Effect of dipole moment on current-voltage characteristics of single molecules, in *Proceedings of the International Conference On Nanoscience and Nanotechnology (ICONN2006)*, edited by C. Jagadish and G. Q. M. Lu, p. 395, Brisbane, 2006, IEEE.

[72] R. C. Hoft, N. Armstrong, M. J. Ford, and M. B. Cortie, Journal of Physics: Condensed Matter **19**, 215206 (2007).

[73] N. Armstrong, R. C. Hoft, A. McDonagh, M. B. Cortie, and M. J. Ford, Nano Letters **7**, 3018 (2007).

[74] R. C. Hoft, M. Ford, and M. B. Cortie, Molecular Simulation **33**, 897 (2007).

[75] A. Aviram and M. A. Ratner, Chemical Physics Letters **29**, 277 (1974).

[76] R. G. Nuzzo and D. L. Allara, Journal of the American Chemical Society **105**, 4481 (1983).

[77] A. Ulman, Chemical Reviews **96**, 1533 (1996).

[78] J. M. Tour *et al.*, Journal of the American Chemical Society **117**, 9529 (1995).

[79] J. C. Love, L. A. Estroff, J. K. Kriebel, R. G. Nuzzo, and G. M. Whitesides, Chemical Reviews **105**, 1103 (2005).

[80] M. Ford, C. Masens, and M. B. Cortie, Surface Review and Letters **13**, 1 (2006).

[81] J. I. Henderson, S. Feng, G. M. Ferrence, T. Bein, and C. P. Kubiak, Inorganica Chimica Acta **242**, 115 (1996).

[82] A. M. McDonagh *et al.*, Journal of the American Chemical Society **129**, 3533 (2007).

[83] H. Feilchenfeld and M. J. Weaver, Journal of Physical Chemistry **93**, 4276 (1989).

[84] A. Bilic, J. R. Reimers, N. S. Hush, and J. Hafner, Journal of Chemical Physics **116**, 8981 (2002).

[85] A. S. Martin, J. R. Sambles, and G. J. Ashwell, Physical Review Letters **70**, 218 (1993).

[86] R. M. Metzger *et al.*, Journal of the American Chemical Society **119**, 10455 (1997).

[87] J. G. Kushmerick, C. M. Whitaker, S. K. Pollack, T. L. Schull, and R. Shashidhar, Nanotechnology **15**, S489 (2004).

[88] S. Datta, *Electronic Transport in Mesoscopic Systems* (Cambridge University Press, Cambridge, 1995).

[89] C. P. Collier *et al.*, Science **285**, 391 (1999).

[90] D. I. Gittins, D. Bethell, D. J. Schiffrin, and R. J. Nichols, Nature **408**, 67 (2000).

[91] C. P. Collier *et al.*, Science **289**, 1172 (2000).

[92] Z. J. Donhauser *et al.*, Science **292**, 2303 (2001).

[93] D. Dulic *et al.*, Physical Review Letters **91**, 207402 (2003).

[94] J. M. Seminario, Nature Materials **4**, 111 (2005).

[95] J. G. Kushmerick *et al.*, Nano Letters **4**, 639 (2004).

[96] N. D. Lang, Physical Review Letters **55**, 230 (1985).

[97] N. D. Lang, Physical Review Letters **56**, 1164 (1986).

[98] N. D. Lang, Physical Review B **34**, 5947 (1986).

[99] V. Mujica, M. Kemp, and M. A. Ratner, Journal of Chemical Physics **101**, 6849 (1994).

[100] V. Mujica, M. Kemp, A. Roitberg, and M. Ratner, Journal of Chemical Physics **104**, 7296 (1996).

[101] M. P. Samanta, W. Tian, S. Datta, J. I. Henderson, and C. P. Kubiak, Physical Review B **53**, R7626 (1996).

[102] L. P. Kadanoff and G. Baym, *Quantum Statistical Mechanics* (W. A. Benjamin, New York, 1962).

[103] L. P. Keldysh, Sov. Phys. JETP **20**, 1018 (1965).

[104] E. G. Emberly and G. Kirczenow, Physical Review B **58**, 10911 (1998).

[105] C. Joachim and J. F. Vinuesa, Europhysics Letters **33**, 635 (1996).

[106] R. Landauer, Philosphical Magazine **21**, 863 (1970).

[107] M. Büttiker, Y. Imry, R. Landauer, and S. Pinhas, Physical Review B **31**, 6207 (1985).

[108] Y. Meir and N. S. Wingreen, Physical Review Letters **68**, 2512 (1992).

[109] M. P. Das and F. Green, Journal of Physics-Condensed Matter **15**, L687 (2003).

[110] M. P. Das and F. Green, Journal of Physics-Condensed Matter **17**, V13 (2005).

[111] W. D. Tian *et al.*, Journal of Chemical Physics **109**, 2874 (1998).

[112] S. N. Yaliraki, A. E. Roitberg, C. Gonzalez, V. Mujica, and M. A. Ratner, Journal of Chemical Physics **111**, 6997 (1999).

[113] N. D. Lang, Physical Review B **52**, 5335 (1995).

[114] M. Di Ventra, S. T. Pantelides, and N. D. Lang, Physical Review Letters **84**, 979 (2000).

[115] E. G. Emberly and G. Kirczenow, Physical Review B **64**, 235412 (2001).

[116] P. A. Derosa and J. M. Seminario, Journal of Physical Chemistry B **105**, 471 (2001).

[117] P. S. Damle, A. W. Ghosh, and S. Datta, Physical Review B **64**, 201403 (2001).

[118] P. Damle, A. W. Ghosh, and S. Datta, Chemical Physics **281**, 171 (2002).

[119] J. Taylor, H. Guo, and J. Wang, Physical Review B **63**, 245407 (2001).

[120] M. Brandbyge, J. L. Mozos, P. Ordejon, J. Taylor, and K. Stokbro, Physical Review B **65**, 165401 (2002).

[121] A. R. Rocha *et al.*, Physical Review B **73**, 085414 (2006).

[122] J. M. Soler *et al.*, Journal of Physics-Condensed Matter **14**, 2745 (2002).

[123] D. Sanchez-Portal, P. Ordejon, E. Artacho, and J. M. Soler, International Journal of Quantum Chemistry **65**, 453 (1997).

[124] A. I. Yanson, G. R. Bollinger, H. E. van den Brom, N. Agrait, and J. M. van Ruitenbeek, Nature **395**, 783 (1998).

[125] K. Stokbro, J. Taylor, M. Brandbyge, J. L. Mozos, and P. Ordejon, Computational Materials Science **27**, 151 (2003).

[126] G. Speyer, R. Akis, and D. K. Ferry, Superlattices and Microstructures **34**, 429 (2003).

[127] L. Romaner, G. Heimel, M. Gruber, J. L. Bredas, and E. Zojer, Small **2**, 1468 (2006).

[128] D. Krüger, H. Fuchs, R. Rousseau, D. Marx, and M. Parrinello, Physical Review Letters **89**, 186402 (2002).

[129] R. L. McCreery, Chemistry of Materials **16**, 4477 (2004).

[130] G. C. Solomon *et al.*, Journal of Chemical Physics **124**, 094704 (2006).

[131] M. Born and R. Oppenheimer, Annalen der Physik **389**, 457 (1927).

[132] J. C. Tully, Theoretical Chemistry Accounts **103**, 173 (2000).

[133] R. G. Parr and W. G. Yang, *Density-Functional Theory of Atoms and Molecules* (Oxford University Press, New York, 1989).

[134] W. Koch and M. C. Holthausen, *A Chemist's Guide to Density Functional Theory*, 2 ed. (Wiley-VCH, Weinheim, 2001).

[135] L. H. Thomas, Proc. Camb. Phil. Soc. **23**, 542 (1927).

[136] E. Fermi, Rend. Accad. Lincei **6**, 602 (1927).

[137] P. Dirac, Proceedings of the Cambridge Philosphical Society **26**, 376 (1930).

[138] D. M. Ceperley and B. J. Alder, Physical Review Letters **45**, 566 (1980).

[139] S. J. Vosko, L. Wilk, and M. Nusair, Canadian Journal of Physics **58**, 1200 (1980).

[140] J. P. Perdew *et al.*, Physical Review B **46**, 6671 (1992).

[141] J. P. Perdew and A. Zunger, Physical Review B **23**, 5048 (1981).

[142] J. P. Perdew, K. Burke, and M. Ernzerhof, Physical Review Letters **77**, 3865 (1996).

[143] P. J. Stephens, F. J. Devlin, C. F. Chabalowski, and M. J. Frisch, Journal of Physical Chemistry **98**, 11623 (1994).

[144] P. Ordejon, E. Artacho, and J. M. Soler, Physical Review B **53**, R10441 (1996).

[145] E. Artacho, D. Sanchez-Portal, P. Ordejon, A. Garcia, and J. M. Soler, Physica Status Solidi B-Basic Research **215**, 809 (1999).

[146] J. Junquera, O. Paz, D. Sanchez-Portal, and E. Artacho, Physical Review B **64**, 235111 (2001).

[147] D. Sanchez-Portal, P. Ordejon, and E. Canadell, Principles and Applications of Density in Inorganic Chemistry II: structure and bonding **113**, 103 (2004).

[148] O. F. Sankey and D. J. Niklewski, Physical Review B **40**, 3979 (1989).

[149] S. F. Boys and F. Bernardi, Molecular Physics **19**, 553 (1970).

[150] N. D. Mermin, Physical Review **137**, A1441 (1965).

[151] G. B. Bachelet and M. Schluter, Physical Review B **25**, 2103 (1982).

[152] D. R. Hamann, M. Schluter, and C. Chiang, Physical Review Letters **43**, 1494 (1979).

[153] D. Vanderbilt, Physical Review B **41**, 7892 (1990).

[154] M. Fuchs and M. Scheffler, Computer Physics Communications **119**, 67 (1999).

[155] S. G. Louie, S. Froyen, and M. L. Cohen, Physical Review B **26**, 1738 (1982).

[156] D. Porezag, M. R. Pederson, and A. Y. Liu, Physical Review B **60**, 14132 (1999).

[157] N. Troullier and J. L. Martins, Physical Review B **43**, 1993 (1991).

[158] L. Kleinman and D. M. Bylander, Physical Review Letters **48**, 1425 (1982).

[159] P. E. Blöchl, Physical Review B **41**, 5414 (1990).

[160] H. J. Monkhorst and J. D. Pack, Physical Review B **13**, 5188 (1976).

[161] V. R. Saunders *et al.*, Crystal98 1.0 user's manual, 1999.

[162] R. S. Mulliken, Journal of Chemical Physics **23**, 1833 (1955).

[163] M. C. Payne, M. P. Teter, D. C. Allan, T. A. Arias, and J. D. Joannopoulos, Reviews of modern physics **64**, 1045 (1992).

[164] W. H. Press, S. A. Teukolsky, W. T. Vetterling, and B. P. Flannery, *Numerical Recipes in C*, 2 ed. (Cambridge University Press, Cambridge, 1992).

[165] E. Polak, *Computational Methods in Optimization* (Academic Press, New York, 1971).

[166] M. Büttiker, IBM Journal of Research and Development **32**, 63 (1988).

[167] A. R. Rocha *et al.*, Nature Materials **4**, 335 (2005).

[168] S. Datta, *Quantum Transport: Atom to Transistor* (Cambridge University Press, Cambridge, 2005).

[169] N. Froman, *Physical Problems Solved by the Phase-Integral Method* (Cambridge University Press, Cambridge, 2002).

[170] F. D. Murnaghan, Proceedings of the National Academy of Sciences of the United States of America **30**, 244 (1944).

[171] T. Korhonen, M. J. Puska, and R. M. Nieminen, Physical Review B **51**, 9526 (1995).

[172] A. Khein, D. J. Singh, and C. J. Umrigar, Physical Review B **51**, 4105 (1995).

[173] H. Gronbeck, A. Curioni, and W. Andreoni, Journal of the American Chemical Society **122**, 3839 (2000).

[174] *Atomistix ToolKit Tutorial and Reference Guide* (Atomistix, 2005), http://www.atomistix.com.

[175] C. Wöll, S. Chiang, R. J. Wilson, and P. H. Lippel, Physical Review B **39**, 7988 (1989).

[176] N. Takeuchi, C. T. Chan, and K. M. Ho, Physical Review B **43**, 13899 (1991).

[177] M. A. Van Hove and S. Y. Tong, *Crystallography by LEED* (Springer, Berlin, 1979).

[178] C. Masens, M. J. Ford, and M. B. Cortie, Surface Science **580**, 19 (2005).

[179] Y. Yourdshahyan, H. K. Zhang, and A. M. Rappe, Physical Review B **63**, 081405(R) (2001).

[180] Y. Yourdshahyan and A. M. Rappe, Journal of Chemical Physics **117**, 825 (2002).

[181] L. Vitos, A. V. Ruban, H. L. Skriver, and J. Kollar, Surface Science **411**, 186 (1998).

[182] Z. Crljen, P. Lazic, D. Sokcevic, and R. Brako, Physical Review B **68**, 195411 (2003).

[183] W. R. Tyson and W. A. Miller, Surface Science **62**, 267 (1977).

[184] P. C. Rusu and G. Brocks, Journal of Physical Chemistry B **110**, 22628 (2006).

[185] K. Doll, Surface Science **544**, 103 (2003).

[186] K. Doll, Surface Science **600**, L321 (2006).

[187] *CRC handbook of chemistry and physics*, 87 ed. (CRC Press Inc., 2006).

[188] E. Artacho *et al.*, *SIESTA 1.5 User's Guide* (Fundacion General Universidad Autonoma de Madrid, 2005), http://www.uam.es/siesta.

[189] H. B. Schlegel, International Journal of Quantum Chemistry **44**, 243 (1992).

[190] J. Baker, Journal of Computational Chemistry **13**, 240 (1992).

[191] Z. Li and D. S. Kosov, Nature of well-defined conductance of amine anchored molecular junctions, arxiv:cond-mat/0702507v1, 2007.

[192] D. S. Kosov, 2007, Private communication.

[193] D. A. Gorodetsky and Y. P. Melnik, Surface Science **62**, 647 (1977).

[194] R. Cortenraad, A. W. D. van der Gon, H. H. Brongersma, G. Gartner, and A. Manenschijn, Applied Surface Science **191**, 153 (2002).

[195] L. Bengtsson, Physical Review B **59**, 12301 (1999).

[196] Y. Q. Xue and M. A. Ratner, Physical Review B **68**, 115406 (2003).

[197] J. Frenkel, Physical Review **36**, 1604 (1930).

[198] R. Stratton, Journal of Physics and Chemistry of Solids **23**, 1177 (1962).

[199] K. Hansen and M. Brandbyge, Journal of Applied Physics **95**, 3582 (2004).